

ADA48800

AD-E 300051

(12)

DNA 4377P-3

ADA 048800

PROCEEDINGS OF THE DICE THROW SYMPOSIUM 21-23 JUNE 1977

Volume 3

General Electric Company-TEMPO
DASIAC
816 State Street
Santa Barbara, California 93102

July 1977

Proceedings

CONTRACT No. DNA 001-75-C-0023

THIS WORK SPONSORED BY THE DEFENSE NUCLEAR AGENCY
UNDER RDT&E RMSS CODE B337076464P99QAXDC00803725900

APPROVED FOR PUBLIC RELEASE; DISTRIBUTION UNLIMITED

Prepared for

Director
DEFENSE NUCLEAR AGENCY
Washington, D.C. 20305

DDC FILE COPY

DDC
RECEIVED
JAN 19 1978
REGULATED
A

UNCLASSIFIED

SECURITY CLASSIFICATION OF THIS PAGE (When Data Entered)

19 REPORT DOCUMENTATION PAGE		READ INSTRUCTIONS BEFORE COMPLETING FORM	
1. REPORT NUMBER DNA 4377P-3	2. GOVT ACCESSION NO. (18) DNA	3. ABSTRACT CATALOG NUMBER S3TE	
4. TITLE (and Subtitle) PROCEEDINGS OF THE DICE THROW SYMPOSIUM 21-23 JUNE 1977, VOLUME 3		5. TYPE OF REPORT & PERIOD COVERED Proceedings	
7. AUTHOR(s)		6. PERFORMING ORG. REPORT NUMBER	
8. CONTRACT OR GRANT NUMBER(s)		(15) DNA 001-75 C-0923	
9. PERFORMING ORGANIZATION NAME AND ADDRESS General Electric Company-TEMPO DASIAC 816 State St., Santa Barbara, Ca., 93102		14. PROGRAM ELEMENT PROJECT TASK AREA & WORK UNIT NUMBERS (16) P99QAXI 00803	
11. CONTROLLING OFFICE NAME AND ADDRESS Director Defense Nuclear Agency Washington, D.C. 20305		(11) 12. REPORT DATE July 1977	
13. DISTRIBUTION STATEMENT (of the abstract entered in Block 20, if different from Report)		13. NUMBER OF PAGES	
14. SECURITY CLASS. (of this report)		15. SECURITY CLASS. (of this report)	
16. DISTRIBUTION STATEMENT (of the abstract entered in Block 20, if different from Report)		16. SECURITY CLASS. (of this report)	
17. DISTRIBUTION STATEMENT (of the abstract entered in Block 20, if different from Report)			
18. SUPPLEMENTARY NOTES			
19. KEY WORDS (Continue on reverse side if necessary and identify by block number)			
Airblast High Explosive Ammonium Nitrate Fuel Oil Nuclear Weapons Effects Dice Throw Simulation Ground Motion			
20. ABSTRACT (Continue on reverse side if necessary and identify by block number)			
This report contains the proceedings of the DICE THROW Symposium held 21-23 June at the Ballistic Research Laboratory, Aberdeen Proving Ground, Maryland. The presentations contained herein describe the experiments conducted, instrumentation used, and results obtained by the various participating projects from detonation of the 600-ton ANFO HE test 6 October 1976 at the White Sands Missile Range, N.M. The DICE THROW Event was sponsored by the Defense Nuclear Agency.			

DD FORM 1 JAN 70 1473 EDITION OF 1 NOV 65 IS OBSOLETE

UNCLASSIFIED

SECURITY CLASSIFICATION OF THIS PAGE (When Data Entered)

445

FOREWORD

This report contains the proceedings of the DICE THROW Symposium held 21-23 June 1977 at the Ballistic Research Laboratory (BRL), Aberdeen Proving Ground, Maryland. The report is divided into four volumes. Volumes 1 through 3 contain the unclassified presentations and Volume 4 contains the classified presentations.

The DICE THROW Event, which was conducted near the Giant Patriot site on the White Sands Missile Range (WSMR), 6 October 1976, was the final test of the DICE THROW Program. The charge for this test was composed of approximately 628 tons (570 metric tons) of ammonium nitrate fuel oil (ANFO). The charge configuration was a right-circular-cylinder base tangent to the surface with a hemispherical top, the same configuration as the second event in the Pre-DICE THROW II Series. The primary objectives of this test were to provide a simulated nuclear blast and shock environment for target response experiments that are vitally needed by the military services and defense agencies concerned with nuclear weapons effects, and to confirm empirical predictions and theoretical calculations for shock response of military structures, equipment, and weapon systems.

A complement of 33 experimenters and support agencies (including foreign governments) participated in Event DICE THROW. For details pertaining to the as-built experiment configurations, site and charge descriptions, and fielding requirements in support of this program, refer to the DICE THROW Test Execution Report, POR 6965.

Best Available Copy

iii

ACCESSION for	
NTIS	White Section <input checked="" type="checkbox"/>
DOC	Butt Section <input type="checkbox"/>
UNANNOUNCED	<input type="checkbox"/>
JUSTIFICATION	
BY	
DISTRIBUTION AVAILABILITY CODES	
Dist.	AVAIL. and/or SPECIAL
A	

TABLE OF CONTENTS

VOLUME 1

1. ANFO CHARGE DEVELOPMENT PROGRAM - PROGRAM SUMMARY - Capt. Thomas Y. Edwards, SAMSO.
2. DICE THROW OVERVIEW - LCDR J.D. Strode, Jr., CEC, USN, DNA Field Command.
3. CHARGE/DETONATION SYSTEM (DNA PROJECT 975) - M.M. Swisdak, Jr., Naval Surface Weapons Center, Explosion Dynamics Branch.
4. DICE THROW MAIN EVENT - EXPLOSIVE DIAGNOSTICS - Bernard Hayes and Ronald Boat, Lawrence Livermore Laboratory.
5. TECHNICAL PHOTOGRAPHY FROM DICE THROW EVENT - John Wisotski, Denver Research Institute.
6. INSTRUMENTATION NOISE PROBLEMS ENCOUNTERED ON DICE THROW - Noel Gantick, DNA Field Command.
7. FREE - FIELD AIRBLAST DEFINITION - EVENT DICE THROW - George D. Teel, Ballistic Research Laboratory.
8. DICE THROW PROJECT OFFICER'S REPORT - THEORETICAL AIR BLAST CALCULATIONS - C.E. Needham, Air Force Weapons Laboratory.
9. BLAST EFFECTS ON HELICOPTER - EVENT DICE THROW - Robert Mayerhofer, Ballistic Research Laboratory.
10. EVENT DICE THROW MOBILITY EXPERIMENTS - C.E. Green, U.S. Army Engineer Waterways Experiment Station.

VOLUME 2

11. BLAST EFFECTS ON THE CREWS OF U.S. ARMY TACTICAL EQUIPMENT - D.R. Richmond, J.T. Yelverton, E.R. Fletcher, W. Hicks, K. Saunders, and A. Trujillo, Lovelace Biomedical and Environmental Research Institute, Inc.
12. DICE THROW OFF-SITE BLAST PREDICTIONS AND MEASUREMENTS - Jack W. Reed, Sandia Laboratories, Environmental Research Division.
13. EVENT DICE THROW - INDUSTRIAL EQUIPMENT SURVIVAL/RECOVERY FEASIBILITY PROGRAM - Edwin N. York, The Boeing Aerospace Company.
14. FEDERAL REPUBLIC OF GERMANY STRUCTURES TEST PROGRAM - EVENT DICE THROW - James M. Watt, Jr., Major Gerhard Zahlmann, and Robert A. Cole, U.S. Army Engineer Waterways Experiment Station.
15. AIRCRAFT SHELTER TESTS IN THE DICE THROW EVENT - Capt. Harry T. Webster, Air Force Weapons Laboratory, Civil Engineering Research Division.

16. GROUP HELMET ARMY PERSONNEL SHELTERS - Golden E. Lane, Jr., Civil Engineering Research Facility.
17. PROJECT C-4, FREE-FLIGHT MEASUREMENT OF THE DRAG FORCES ON CYLINDERS - EVENT DICE THROW - A.W.M. Gibb and D.A. Hill, Defence Research Establishment Suffield.
18. PROJECT C-2, BLAST RESPONSE OF UHF POLEMAST ANTENNA - EVENT DICE THROW - C.G. Coffey and G.V. Price, Defence Research Establishment Suffield.
19. BLAST RESPONSE OF LATTICE MAST - EVENT DICE THROW - B.G. Laidlaw, Defence Research Establishment Suffield.
20. BLAST RESPONSE OF 35-FT FIBERGLASS WHIP ANTENNA - EVENT DICE THROW - G.V. Price and C.G. Coffey, Defence Research Establishment Suffield.
21. PROJECT C-5, CANADIAN AIR BLAST MEASUREMENTS - EVENT DICE THROW - F.H. Winfield, Defence Research Establishment Suffield.
22. UHF/SHF TRANSMISSION EXPERIMENT - Alan A. Burns, SRI International.
23. DICE THROW DUST CLOUD CALCULATIONS - Major Gary P. Ganong, Susan E. Check, and Charles E. Needham, Air Force Weapons Laboratory.
24. DICE THROW SEISMIC MEASUREMENTS - Laurence S. Melzer, Air Force Weapons Laboratory.
25. ARMY PERSONNEL SHELTERS - DNA PROJECT NO. 329 - William L. Huff, U.S. Army Engineer Waterways Experiment Station.

CONTENTS

VOLUME 3

26. NORWEGIAN BLAST DOOR - Golden E. Lane, Jr., Civil Engineering Research Facility.
27. BLAST TESTS OF EXPEDIENT SHELTERS IN THE DICE THROW EVENT - C.H. Kearny, Oak Ridge National Laboratory.
28. EXPERIMENTAL STUDY OF AIRCRAFT STRUCTURAL RESPONSE TO BLAST - DICE THROW PROJECT NO. 118 - Rudolf Friedberg and Peter Hughes, Naval Weapons Evaluation Facility.
29. BLAST DISPLACEMENT IN FIELD FORTIFICATIONS - B.R. Fletcher, D.R. Richmond, R.O. Clark, and J.T. Yehverton, Lovelace Biomedical and Environmental Research Institute, Inc.
30. DYNAMIC RESPONSE OF TWO TYPES OF GERMAN HOUSE CONSTRUCTION - C.K. Wiehle, J.R. Rempel, and J.E. Beck, Stanford Research Institute.
31. TEST SUMMARY - NIDS OPTICAL MEASUREMENTS - M. Oberst, Sandia Laboratory Albuquerque.

32. ~~RESULTS OF THE SPECIAL FORCES COMMUNICATIONS EXPERIMENT AT~~
THE DICE THROW MAIN EVENT - Capt. Alexander F. Wojcicki, SOC, USAOCCS.
33. ~~CRATER AND EJECTA ENHANCEMENT STUDIES~~ - R.W. Henny, Air Force
Weapons Laboratory and G.D. Jones, Civil Engineering Research Facility.

LIST OF ATTENDEES

ABRAHAMSSON, Eddy - Sweden
ALLISON, W. Don - BRL
ALTER, MAJ William A. - DNA
ALVAREZ, CPT Vicen A. - FCDMA
ATKINS, Marvin C. - DNA
AXELSSON, Hakan - Sweden
BACHMANN, Eberhard - Germany
BALLARD, James - WES
BALSARA, Jimmy P. - WES
BASHANT, MAJ Ronald W. - HQSAC
BELLIVEAU, Louis - HDL
BEZEMER, Ole R. - Canada
BRADSHAW, 1LT Joel C. - AFM
BREAZEAL, Norman - Sandia Labs
BROWN, Larry L. - DRI
BRUEGMANN, LTC Dieter - Germany
BRYANT, Edward - GE-TEMPO
BURNS, Alan A. - SRI
BUTALA, Edward - NSA
CARLSON, Roland - Boeing
CAULFIELD, Eugene - USASCA
CHAN, Warren - GE-TEMPO

CHAPYAK, Edward - TDA
CHECK, Susan - AFWL
CLARK, Robert O. - Lovelace
COFFEY, Clayton - Canada
COOPER, Henry - RDA
CRISCIONE, Emanuel - Kaman Avidyne
CRONK, Richard - KOA
DeBOY, William - NSA
DELANY, W. D. - ASWE
DeRAAD, CPT Robert G. - FCDMA
DYSART, Richard - WSMR
EDGERTON, LCDR E. W. - NSSC
EDWARDS, CPT Thomas - SANSO
ERLEMAN, COL Rudolf - Germany
ETHRIDGE, Noel - BRL
FLATHAU, William - WES
FLETCHER, E. Royce - Lovelace
FLUGER, Alvin - ARRADCOM
FREISBERG, Robert - USAECOM
FRIEDBERG, RUDOLF - NMWF
GANTICK, Noel - FCDMA
GIBB, Allan W. M. - Canada
GOMEZ, COL Robert - BRL
GRANT, G. A. - Canada
GREEN, Dale W. - WSMR

GUNBY, MAJ E. Neal - DNA
GUPTA, Aaron - BRL
GURKE, Gerhard - Germany
HAYES, Bernard - LLL
HEGGIE, R. M. - Canada
HEINTZEL, COL Hans-H. - Germany
HUFF, William L. - WES
HUGHES, Peter - NWEF
JACOBSON, John - BRL
JONES, Glen - CERF
KAUFMANN, LTC Ronald - WES/Germany
KEARNY, Cresson - ORNL
KEEFER, John - BRL
KELSO, Jack - GE-TEMPO
KENNEDY, Tom - DNA
KING, Vincent - BRL
KINGERY, Charles - BRL
KLIMMEK, LT Charles - FCDA
KNOWLES, Cyrus - RDA
LANE, Golden - CERF
LAIDLAW, Bryan - Canada
LIND, MAJ Alan - USANA
MAYERHOFER, Robert - BRL
McDONNELL, Michael - SAI
MELZER, Steve - AFML
MESZAROS, Julius J. - BRL

MUELLER, MAJ Edmund - HQDNA
NEEDHAM, Charles - AFWL
NOREN, Brig Gen Gunnar - Sweden
OLIVER, Lawrence - MHAF
PACHUTA, Michael A. - OCPA
PAHL, LTC Hermann - Germany
PARKER, Hassel - MIG
PASMAN, H. J. - Netherlands
PEARSON, Richard - BRL
PECKHAM, Phillip - NSWC/WOL
PERRY, Gerald - GE-TEMPO
PETERSON, Robert L. - BRL
PICKETT, Stephen - CERF
PETES, Joseph - NSWC/WOL
PFRENGLE, Herman - Germany
PLAMONDON, Maynard A. - AFWL
PYLE, Jay C. - Boeing
QUIGLEY, Ennis - BRL
RALEY, Robert J. - BRL
RAYOTTO, Martin - ARADCOM
REED, Jack - SLA
REICHENBACH, Heinz - Germany
REISLER, Ralph E. - BRL
ROECKER, Eugene - BRL
RICHMOND, Donald - Lovelace
RIGOTTI, David L. - BRL

RULA, Adam A. - WES
SCHILLING, Robert - Germany
SCHUMACHER, Robert - BRL
SCHUMAN, William J. - BRL
SHELTON, Russell - BRL
SKJELTORP, Arne - Norway
SMITH, Ross - Chrysler
STILL, LTC Edwin T. - DNA
STRODE, LCDR J. D. - FCDNA
SULLIVAN, John - BRL
SWISDAK, Michael - NSWC/WOL
TAYLOR, William - BRL
TEEL, George - BRL
UECKE, MAJ John - USANA
VAULT, William - HOL
VAN KUEREN, E. - RCA
WARD, Robert - EG&G
WARREN, LTC James - AFWL
WATSON, George - BRL
WATT, James - WES
WAXLER, Daniel - ARRADCOM
WEBSTER, Harry - AFWL
WIEHLE, Carl - SRI
WIERLE, Matthew - BRL
WISOTSKI, John - ORI
WOJCICKI, Alexander - USAOCCS

YORK, Edwin - Boeing

ZAKER, Thomas - DDESB

26. NORWEGIAN BLAST DOOR

by

Golden E. Lane, Jr.

Civil Engineering Research Facility

ABSTRACT

The Norwegian Defense Construction Service (NDCS) fielded an experiment in the DICE THROW Project. The NDCS experiment consisted of fabricating and exposing a concrete ammunition storage facility blast door to an overpressure of 1.4 MPa. The University of New Mexico's Civil Engineering Research Facility (LERF) was responsible for the construction, monitoring, instrumentation, and reporting of the experiment. The purpose of the experiment was to qualify the proposed blast door structure as a Norwegian, and possibly NATO, standard for ammunition storage facilities and civil defense protective installations. The door was instrumented with eight strain gages on the reinforcing steel, two accelerometers on the underside of the door, two accelerometers on the reaction frame of the door, and two active and four passive displacement gages to measure relative displacement between the door and the reaction base. The door survived the blast with a relatively small amount of permanent deformation and a moderate amount of cracking on the underside of the door.

TABLE OF CONTENTS

<u>Section</u>		<u>Page</u>
1	INTRODUCTION	3
2	EXPERIMENTAL PROGRAM	5
3	TEST RESULTS	13
	APPENDIX A: TEST DATA	17
	APPENDIX B: BLAST DOOR DAMAGE	45

LIST OF ILLUSTRATIONS

<u>Figure</u>		<u>Page</u>
1	Blast Door and Reaction Pit	6
2	Layout of Norwegian Experiment	8
3	Blast Door Frame	9
4	Damaged Anchor	9
5	Placement of Door	10
6	Casting of Reaction Pit	10
7	Preshot Norwegian Experiment	11
8	Blast Pressure	14

LIST OF TABLES

<u>Table</u>		<u>Page</u>
1	Measurement List	15

SECTION 1
INTRODUCTION

The Norwegian Defense Construction Service (NDCS) fielded an experiment in the DICE THROW Project, a 600-ton, high-explosive test conducted at the White Sands Missile Range in New Mexico on October 6, 1976. The NDCS experiment consisted of fabricating a reinforced concrete blast door and companion reaction support and exposing the unit to an overpressure of 1.4 MPa. The Defense Nuclear Agency's Field Command supported the experiment and the University of New Mexico's Civil Engineering Research Facility (CERF) was responsible for construction, monitoring, instrumentation, and reporting of the experiment.

The purpose of the Norwegian experiment in Project DICE THROW was to qualify the proposed blast door structure as a Norwegian, and possibly NATO, standard for ammunition storage facilities and civil defense protective installations.

SECTION 2

EXPERIMENTAL PROGRAM

The blast door was constructed of reinforced concrete encased in a steel frame. The reaction pit was also reinforced concrete with a steel bearing angle to support the door. The details of the door and reaction pit are shown in figure 1. Figure 2 shows the location of the blast door in the DICE THROW testbed.

The steel frame, reinforcing steel, and bearing angle were fabricated in Norway and shipped to CERF as one unit (fig. 3). The only apparent damage to the door during shipment was one bent anchor (fig. 4). After the strain gages and instrumentation mounting plates had been installed and the concrete had been cast and cured at CERF, the door was transported to the White Sands Missile Range to be positioned in the reaction pit forms before casting of the reaction pit. Figures 5 and 6 show the placement of the door and the casting of the reaction pit, respectively. After the reaction pit concrete had cured, the door was opened to assure proper operation. Figure 7 shows the Norwegian experiment just prior to the test. The compressive strength of the concrete in the door was 43.6 and 49.7 MPa at 28 days and shot day, respectively, based on the average of two 152.4 x 304.8 mm cylinders for each date. The average 28-day compressive strength of the reaction pit was 37.8 MPa based on an average of five 152.4 x 304.8 mm cylinders.

Active instrumentation consisted of eight strain gages on the reinforcing steel in the door, four accelerometers--two on the door and two on the reaction pit, and two displacement gages under the door. In addition, there were four passive displacement measurements made with scratch gages between the bottom of the door and the floor of the reaction pit. The strain gages used were Micro-Measurement Type EA-06-500GC-350 which had a gage length of 12.7 mm, a nominal resistance of 350 ohms, and a gage factor of 2.095. Accelerometers were Endevco 2264-A-2KR and CEC Type 4-202-0001. The Endevco accelerometers were full bridge with two active piezoresistive strain gages. The CEC accelerometers were full bridge with four active piezoresistive strain gages. The active displacement transducers were Celesco Model PT-101-10 pull-wire potentiometers with special features to allow relative acceleration magnitudes of ± 5.08 m/sec with displacements of ± 127 mm.

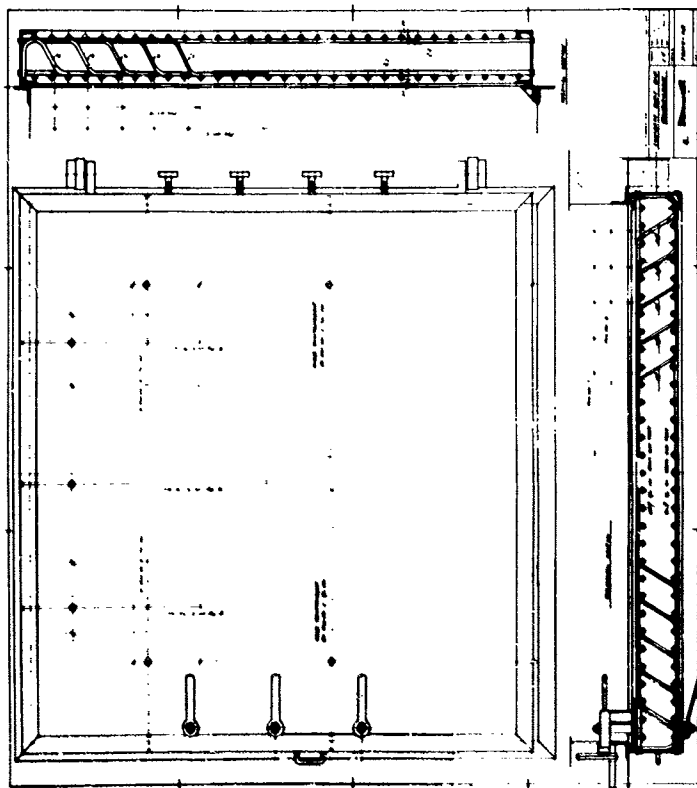


Figure 1. Blast Door and Reaction Pit (2 of 2)

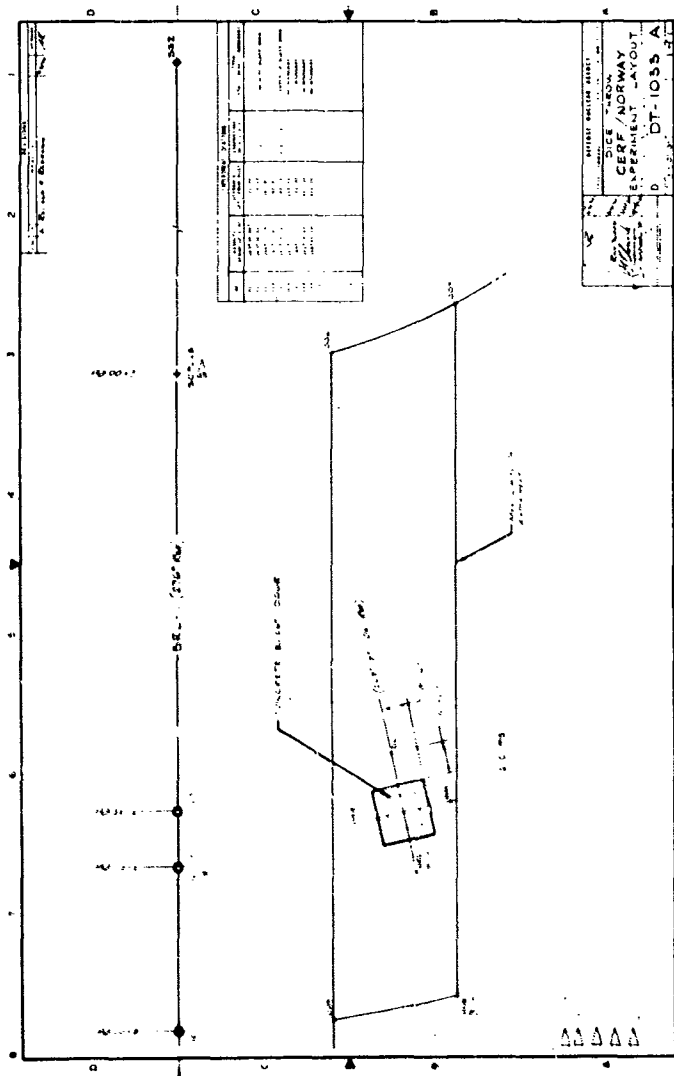


Figure 2. Layout of Norwegian Experiment

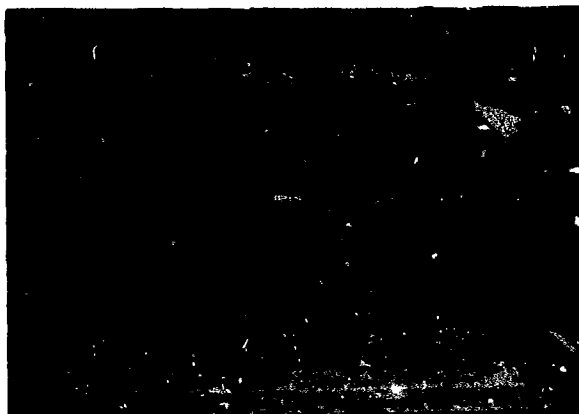


Figure 3. Blast Door Frame



Figure 4. Damaged Anchor



Figure 5. Placement of Door

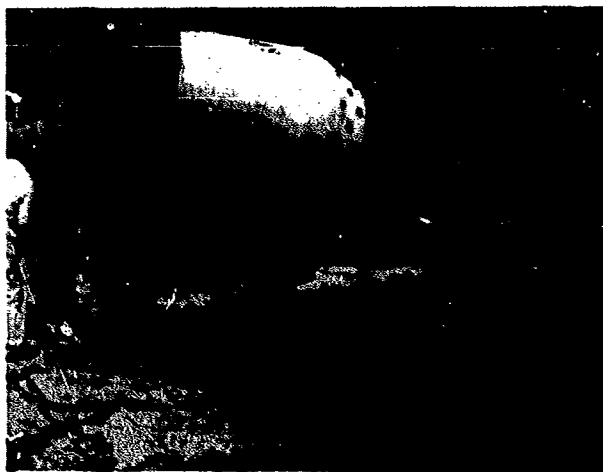


Figure 6. Casting of Reaction Pit

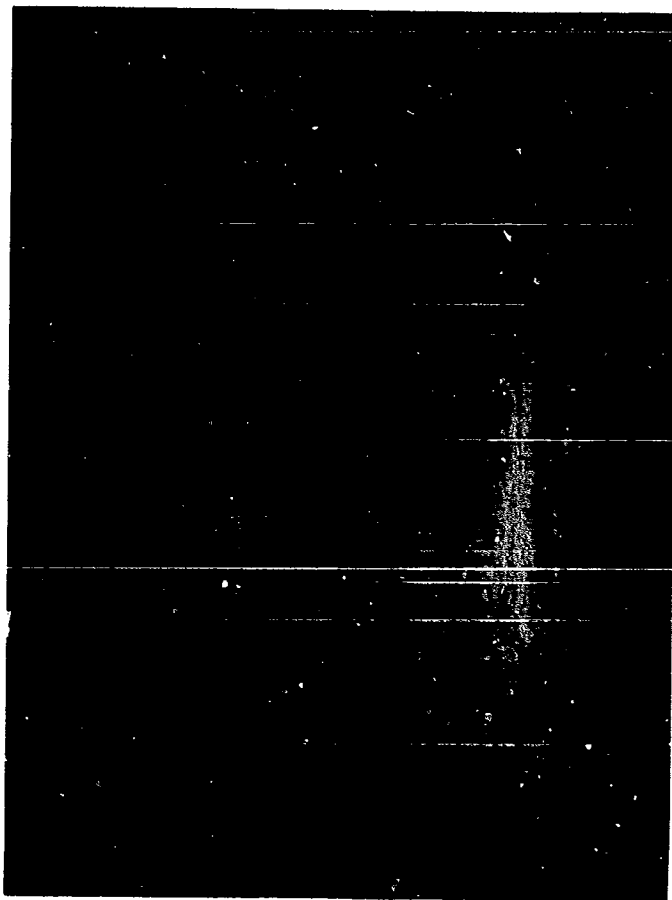


Figure 7. Preshot Norwegian Experiment

The scratch gages used for the passive displacement measurements were simply two aluminum pipes, one inside the other, one attached to the door and the other attached to the floor of the reaction pit. Displacement was indicated by a pointed screw through the outside pipe scratching the inside pipe.

The active gages were connected to a steel junction box located approximately 300 m from the shelters with 4-conductor lead wire buried 1.2 m deep. The junction box was connected to the recording van by 20-pair cables. The recording van was approximately 1800 m from the junction box.

The recording van used for data acquisition was supplied by DNA (Van No. 36040). In the van, the bridge type transducers were excited and conditioned by B&F 1-171 Signal Conditioners. The conditioned signals were amplified with Bay Labs 5503 Amplifiers (dc - 50 kHz). Recording was accomplished on Sangamo Type 4784 32-Track Tape Decks. Wideband FM recording (108 kHz center with ± 40 percent deviation) was used.

In addition to data, IRIG-B time code and fiducial signals were recorded on each tape deck. During the event, the van was operated remotely from the timing and firing van.

After the event, quick-look data were played back on O-graph paper. Final copy data were prepared at the Air Force Weapons Laboratory data-reduction facility.

A sampling rate of 20,000 points per second and a filter frequency of 5 kHz were used in digitizing the analog data. Each channel was scaled in engineering units and plotted against time.

SECTION 3 TEST RESULTS

Blast pressure was not measured at the exact location of the blast door. However, there was a blast pressure gage on gage line BRL-1 at the same radial distance from ground zero as the door. The relative location of the pressure measurement and the door can be seen in figure 2. The data from the pressure measurement are shown in figure 8.

Appendix A contains the time histories of the recorded data. Figure 1 and table 1 locate and describe the measurements, respectively. The sign convention used was as follows:

Acceleration	+ upward
Displacement	+ downward
Strain	+ compression

The displacements as indicated by the scratch gages were as follows:

<u>Gage Designation</u>	<u>Displacement, mm</u>
PD1	19.1
PD2	38.1
PD3	31.8
PD4	7.9

The door suffered some damage as can be seen in the posttest photographs in appendix B. After the test, the door was opened to determine the survivability of the hinges and locking mechanism. Although the door was opened with very little difficulty, it could not easily be reclosed because of distortions in the hinges.

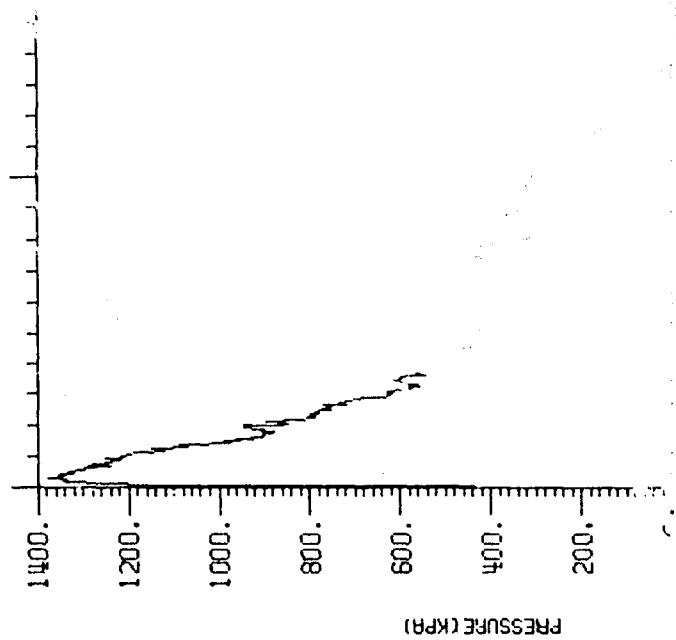
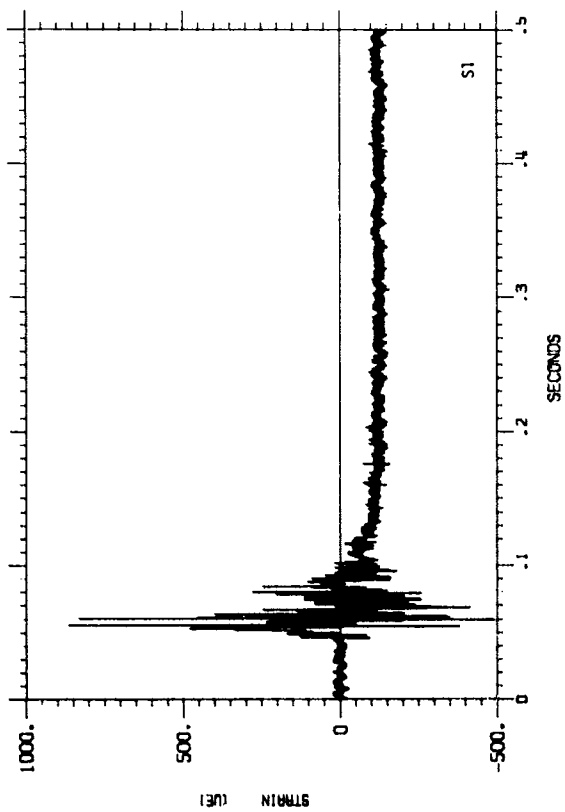


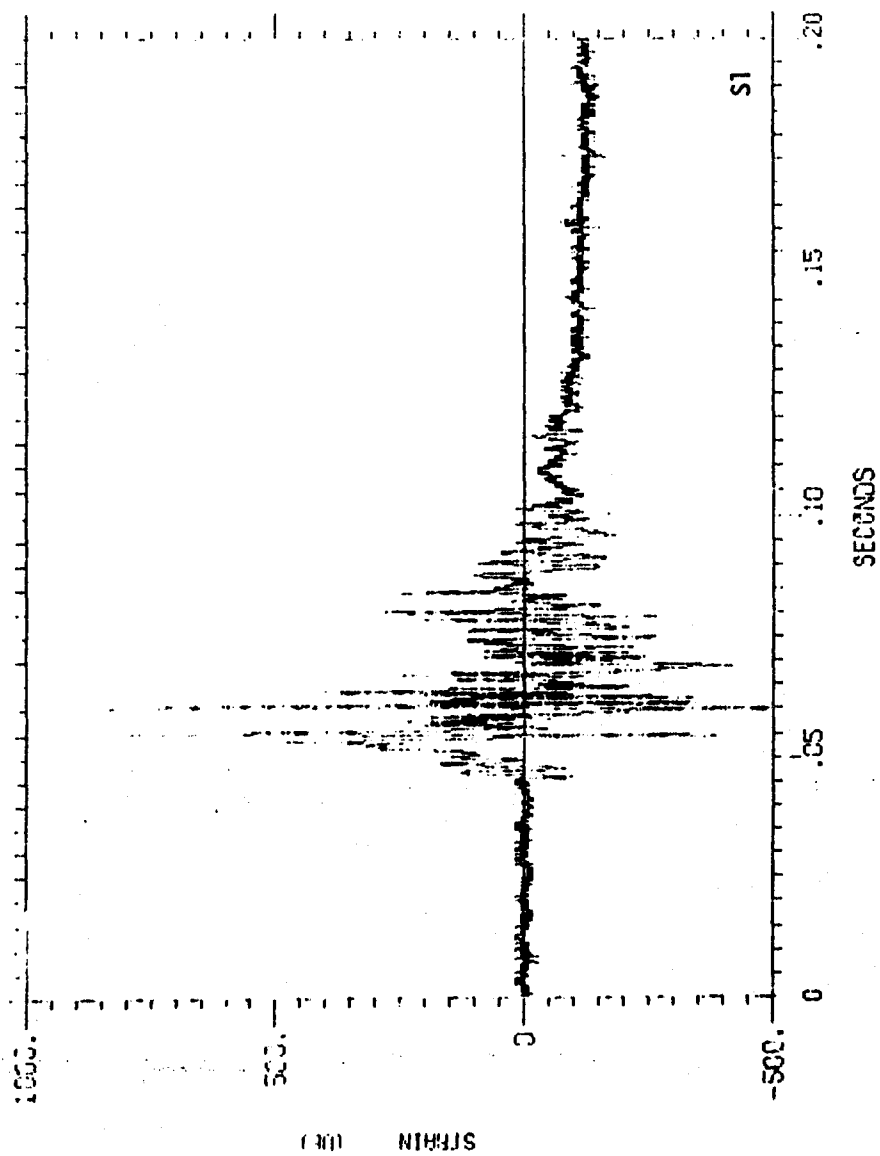
Table 1. Measurement List

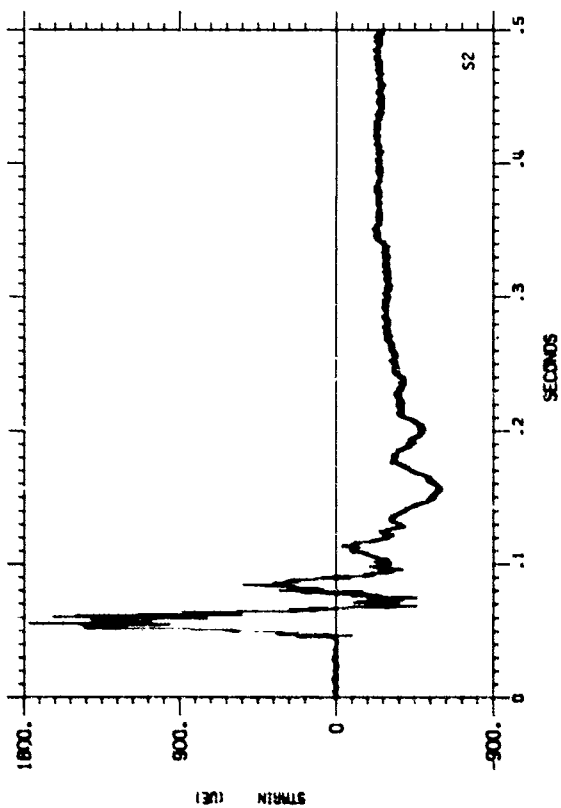
Designation	Type	Location	Measurement Number
S1	Strain	Rebar - Top	13
S2	Strain	Rebar - Top	14
S3	Strain	Rebar - Top	15
S4	Strain	Rebar - Top	16
S5	Strain	Rebar - Bottom	17
S6	Strain	Rebar - Bottom	18
S7	Strain	Rebar - Bottom	19
S8	Strain	Rebar - Bottom	20
A1	Acceleration	Door - Center	21
A2	Acceleration	Door - Edge	22
A3	Acceleration	Reaction Pit - Vertical	23
A4	Acceleration	Reaction Pit - Horizontal	24
D1	Displacement	Door - Center	25
D2	Displacement	Door - Edge	26
PD1	Passive Displacement	Door - Off Center	
PD2	Passive Displacement	Door - Off Center	
PD3	Passive Displacement	Door - Center	
PD4	Passive Displacement	Door - Edge	

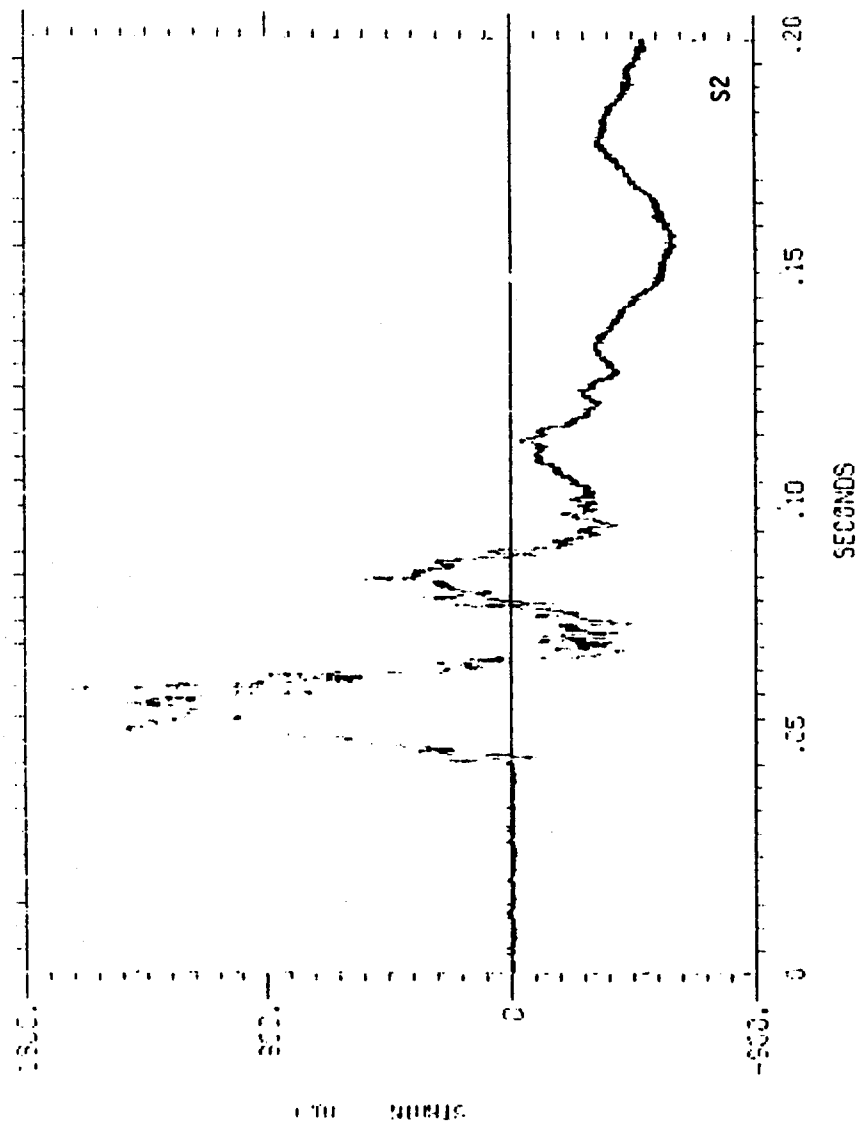
APPENDIX A

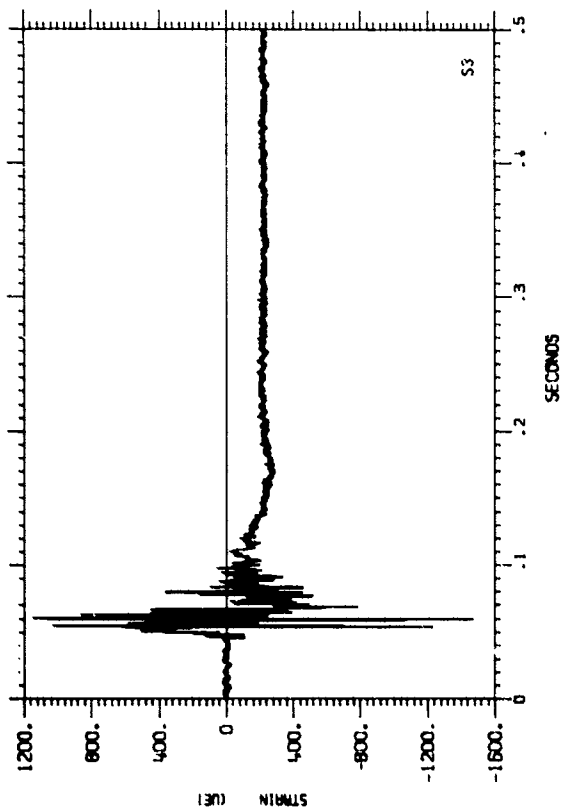
TEST DATA

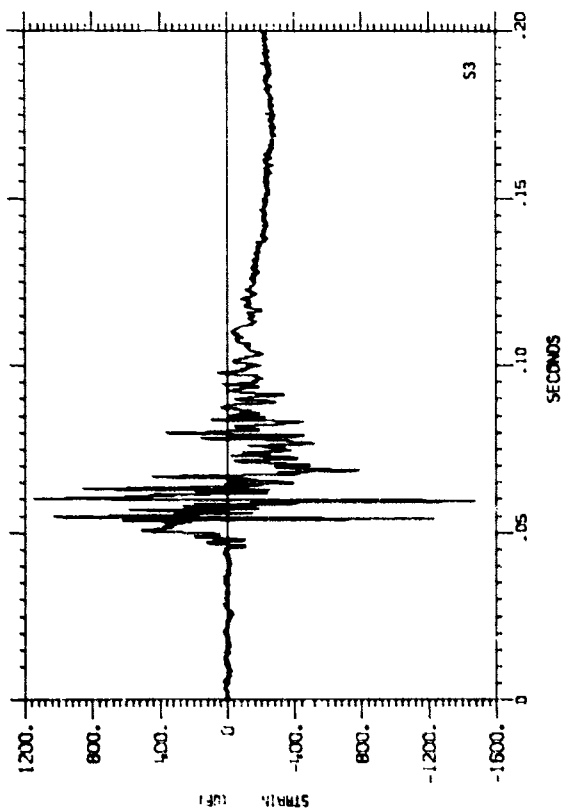


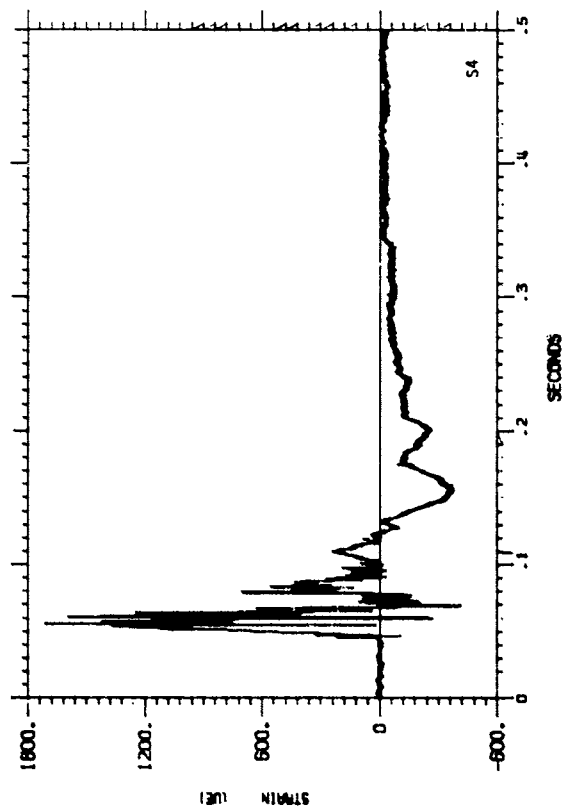


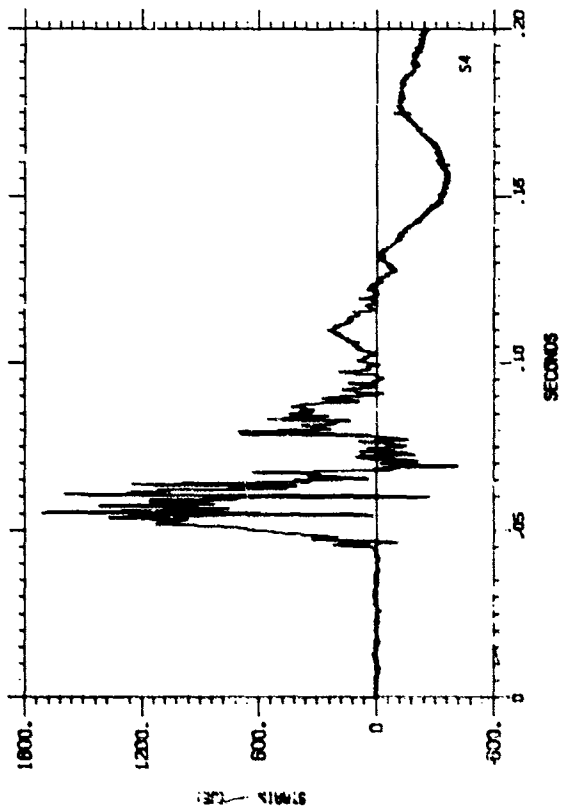


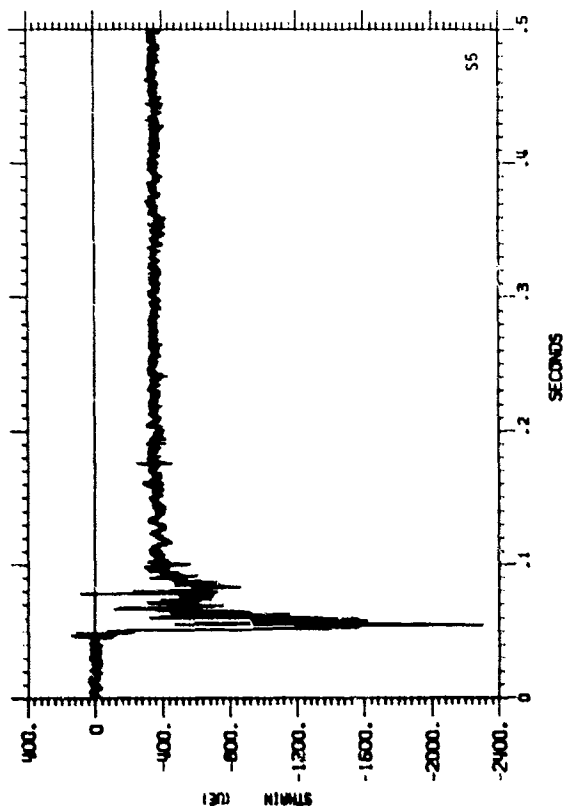


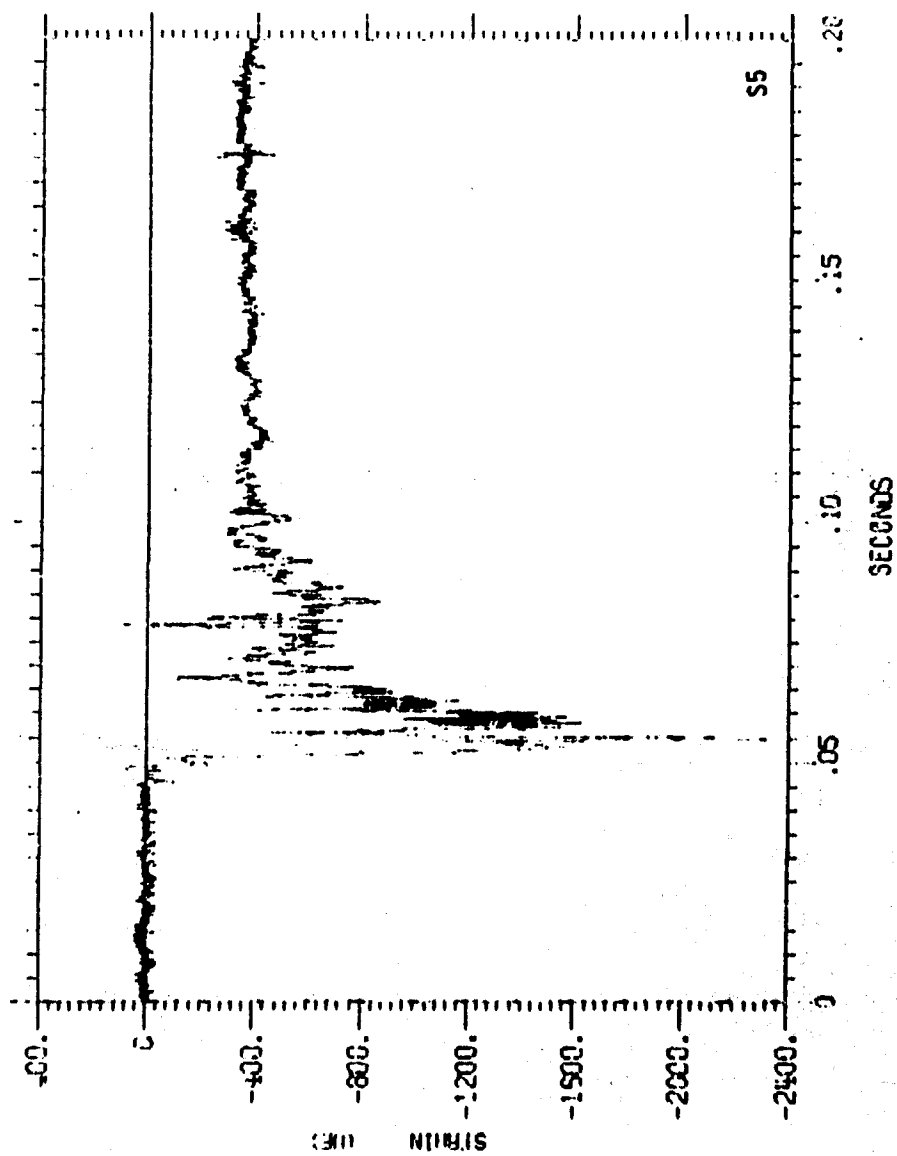


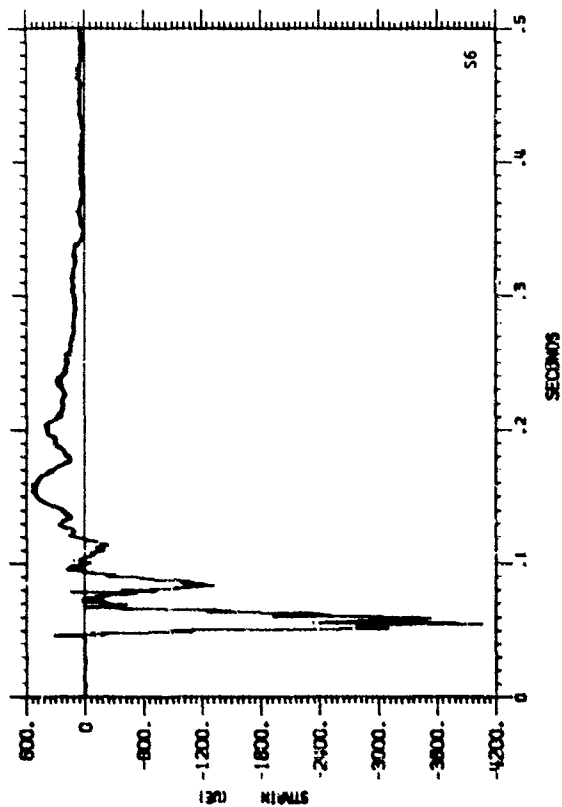


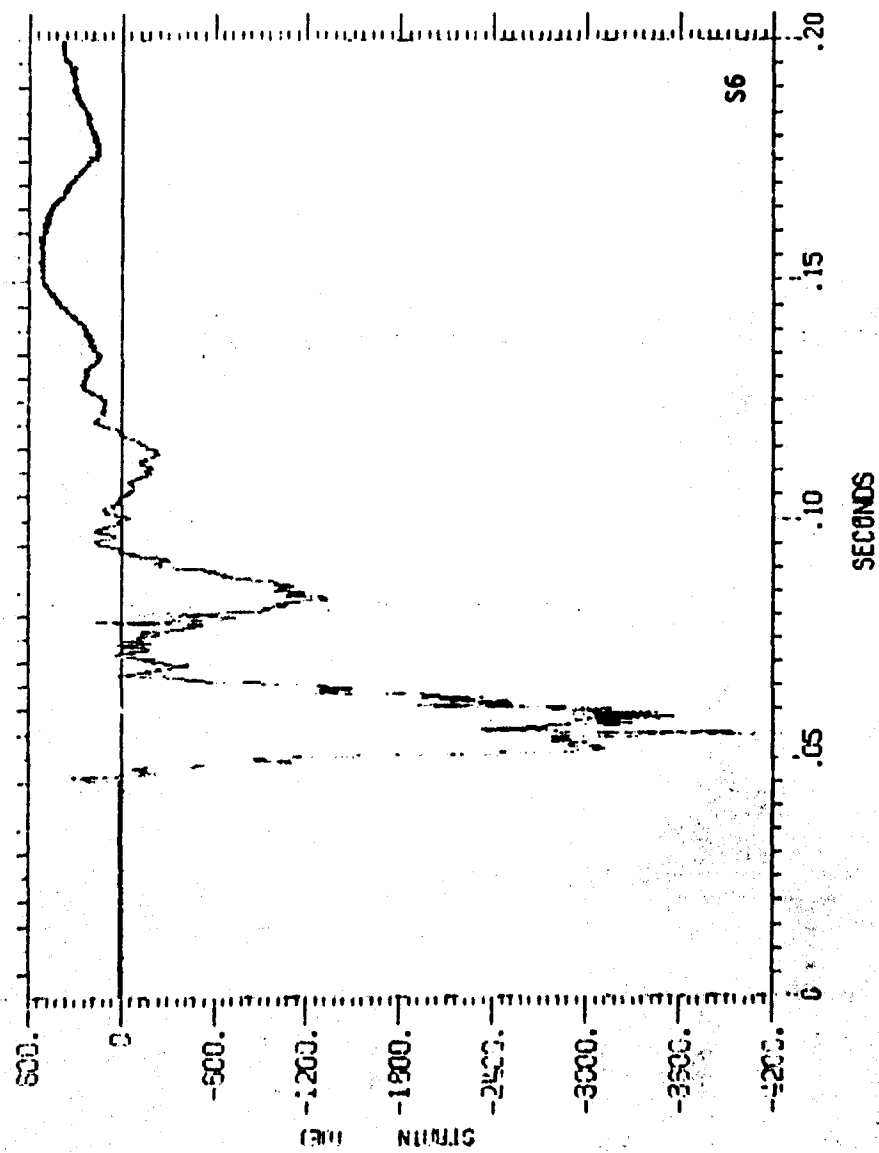


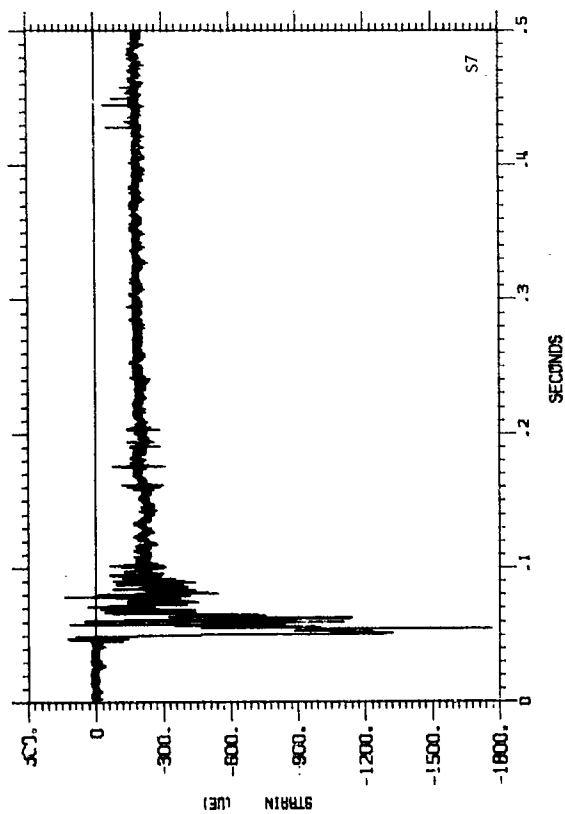


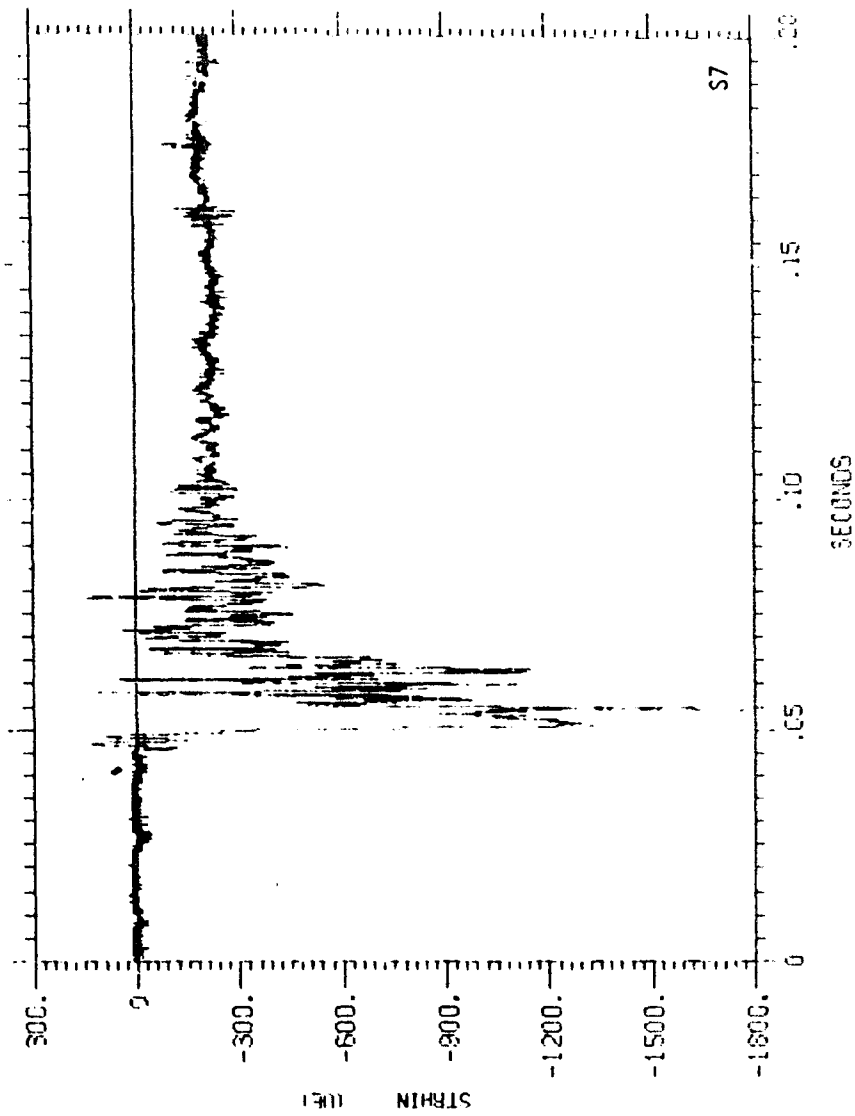


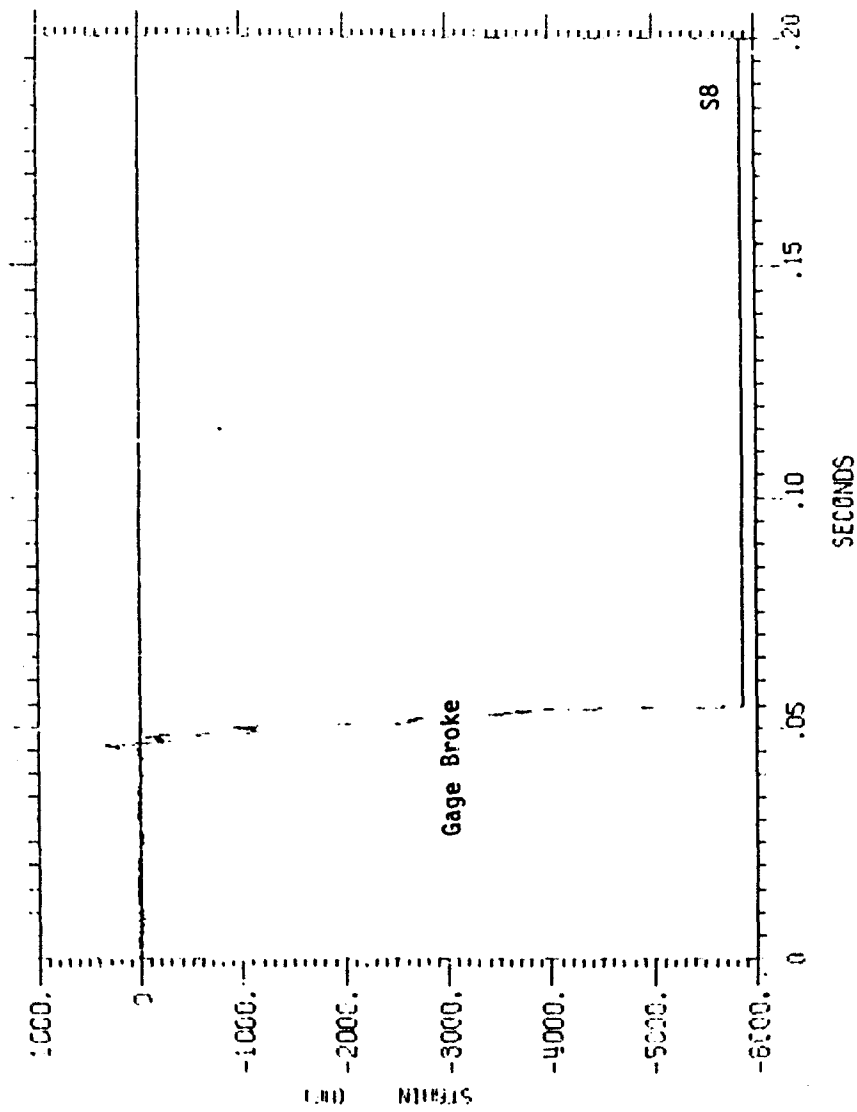


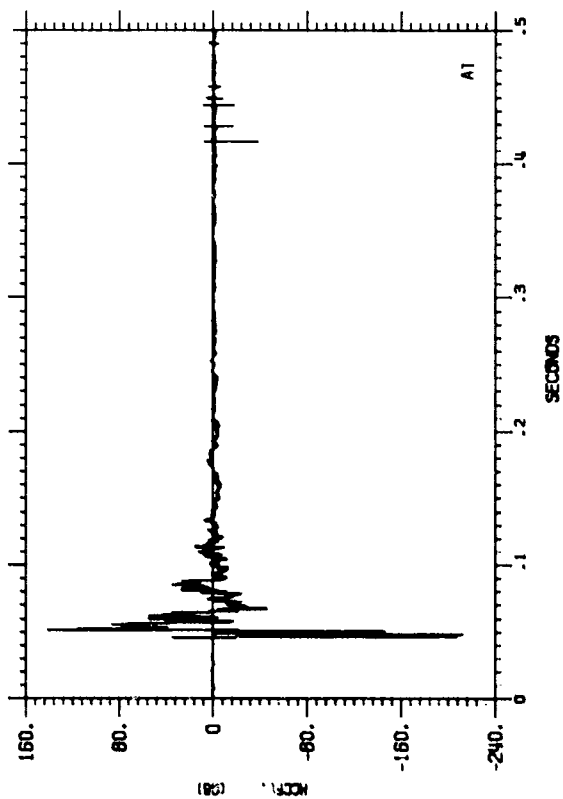


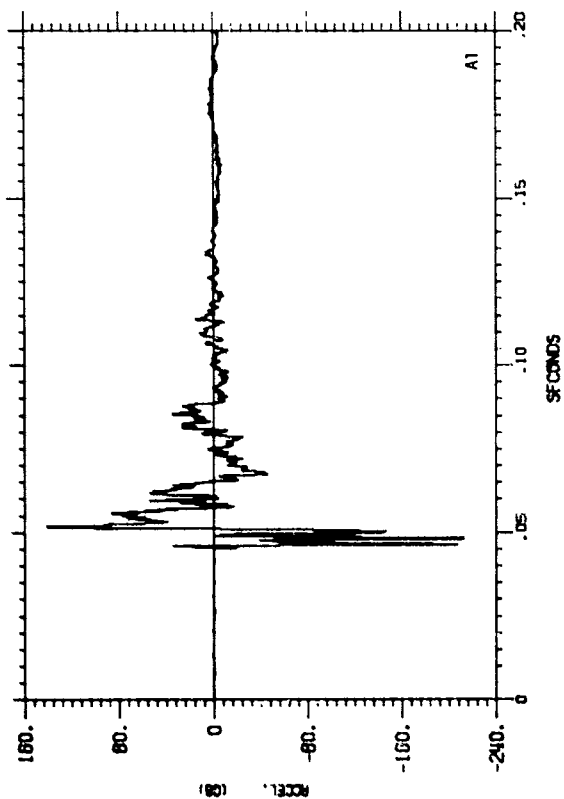


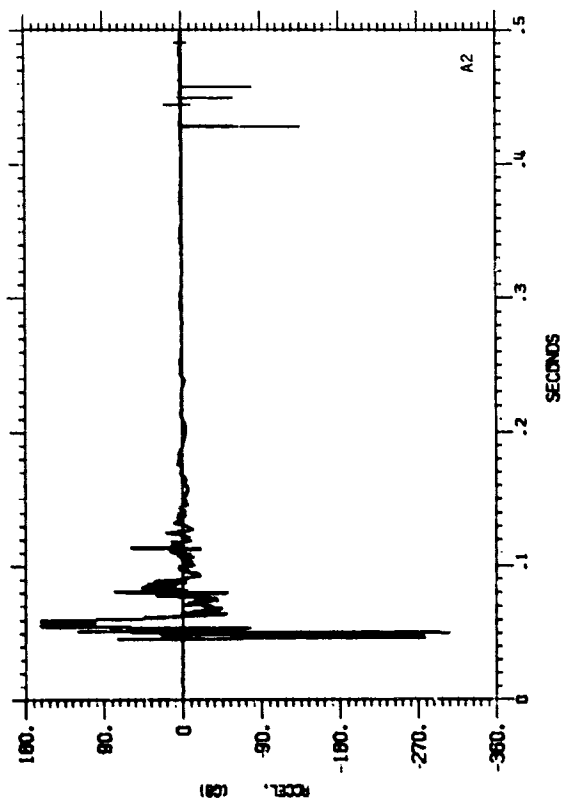


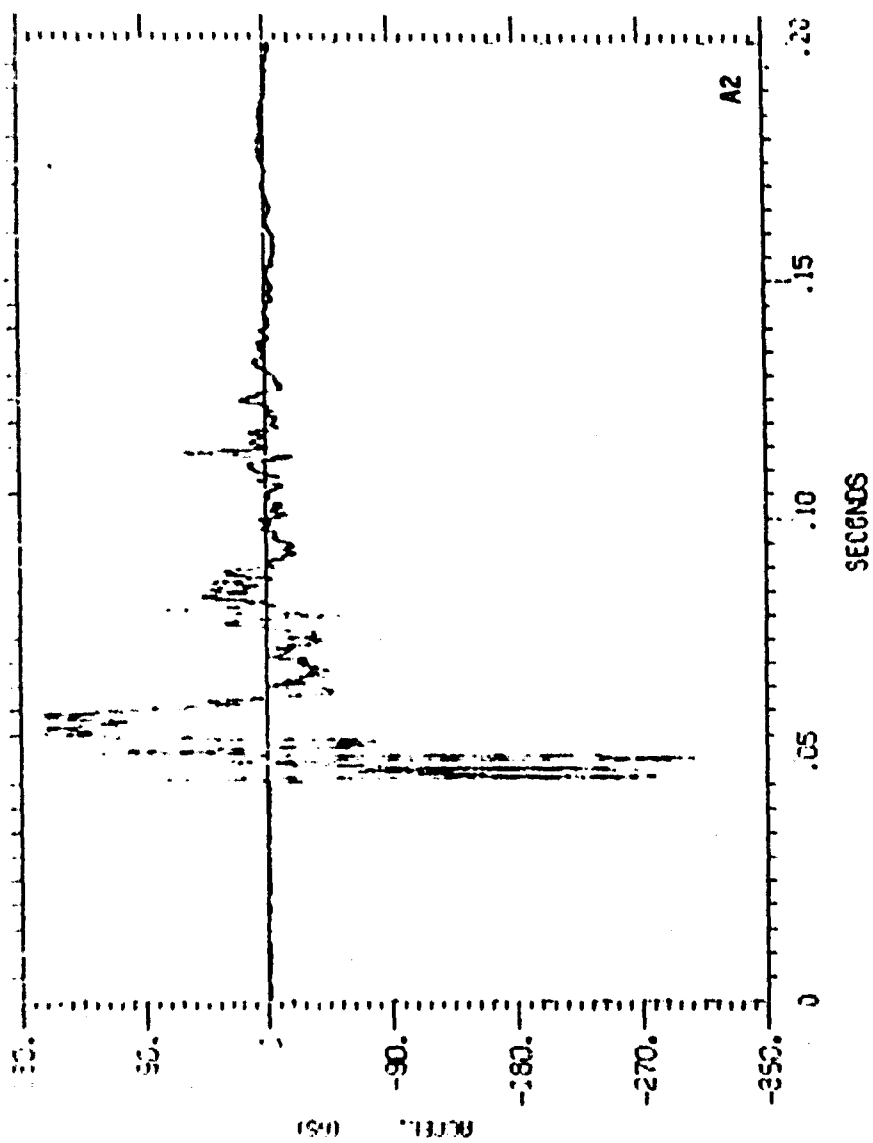


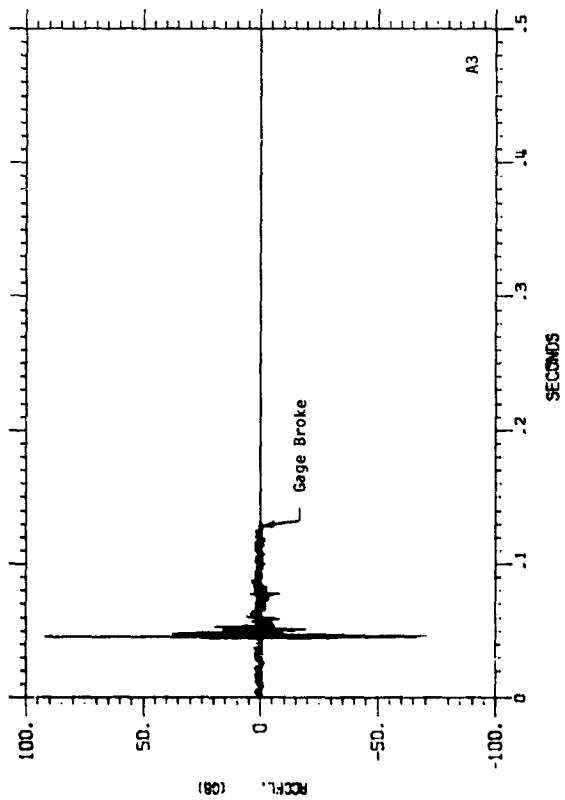


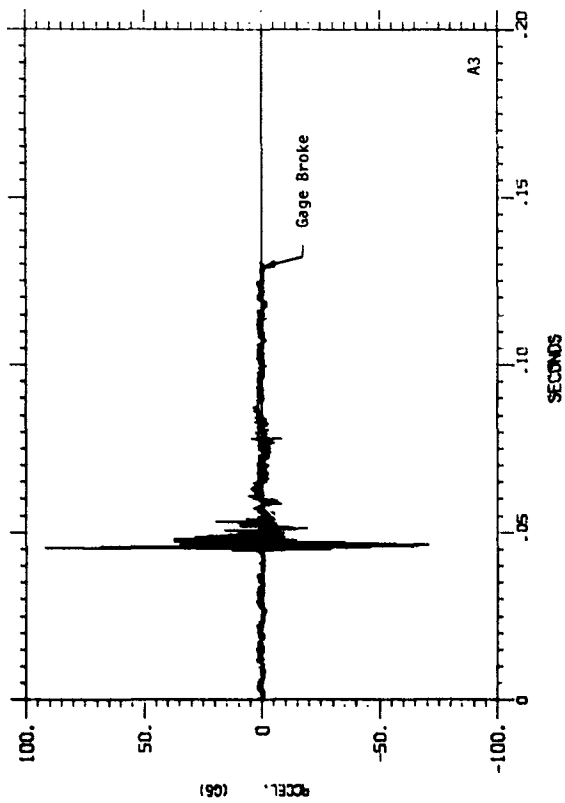


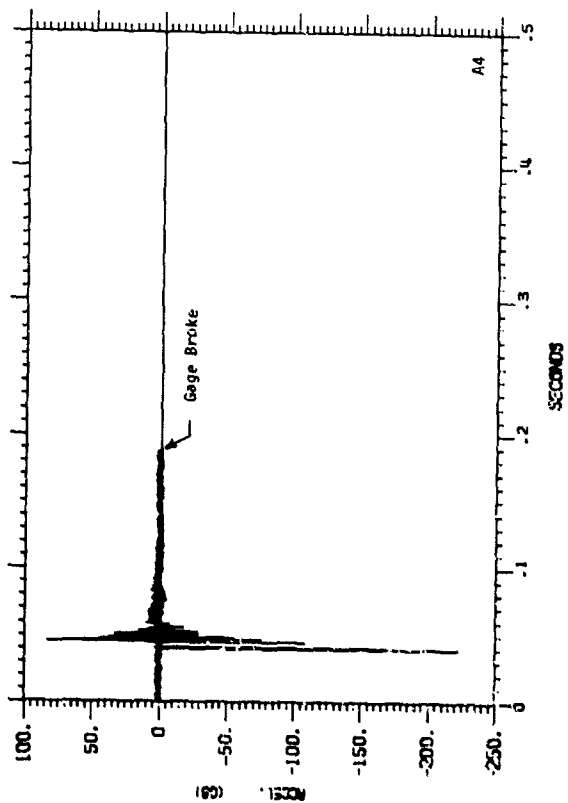


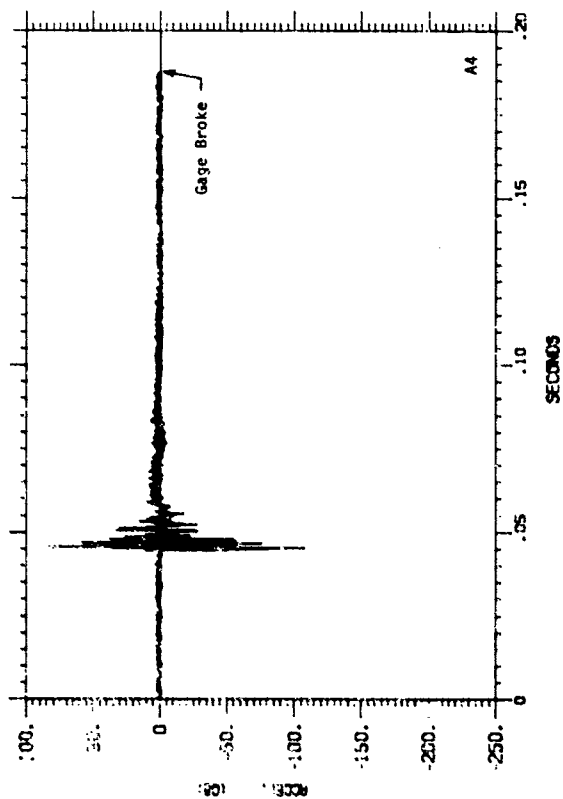


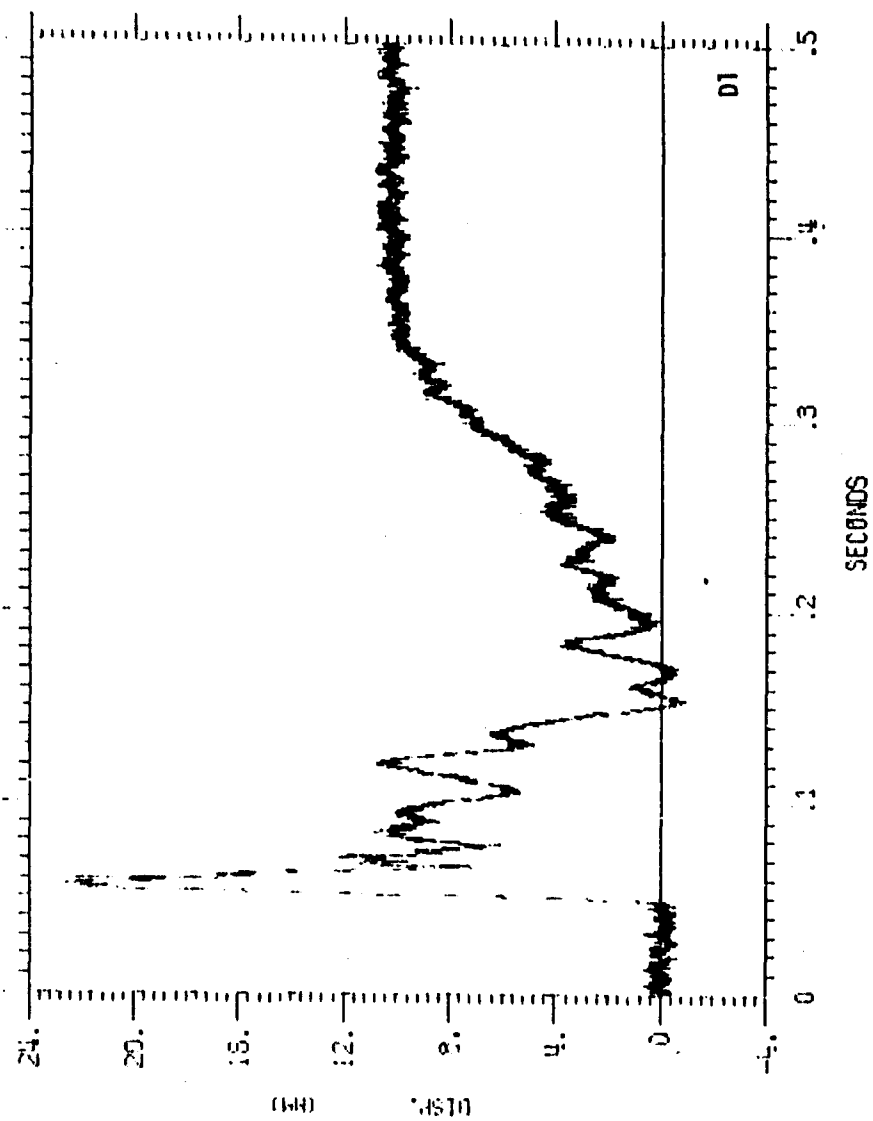


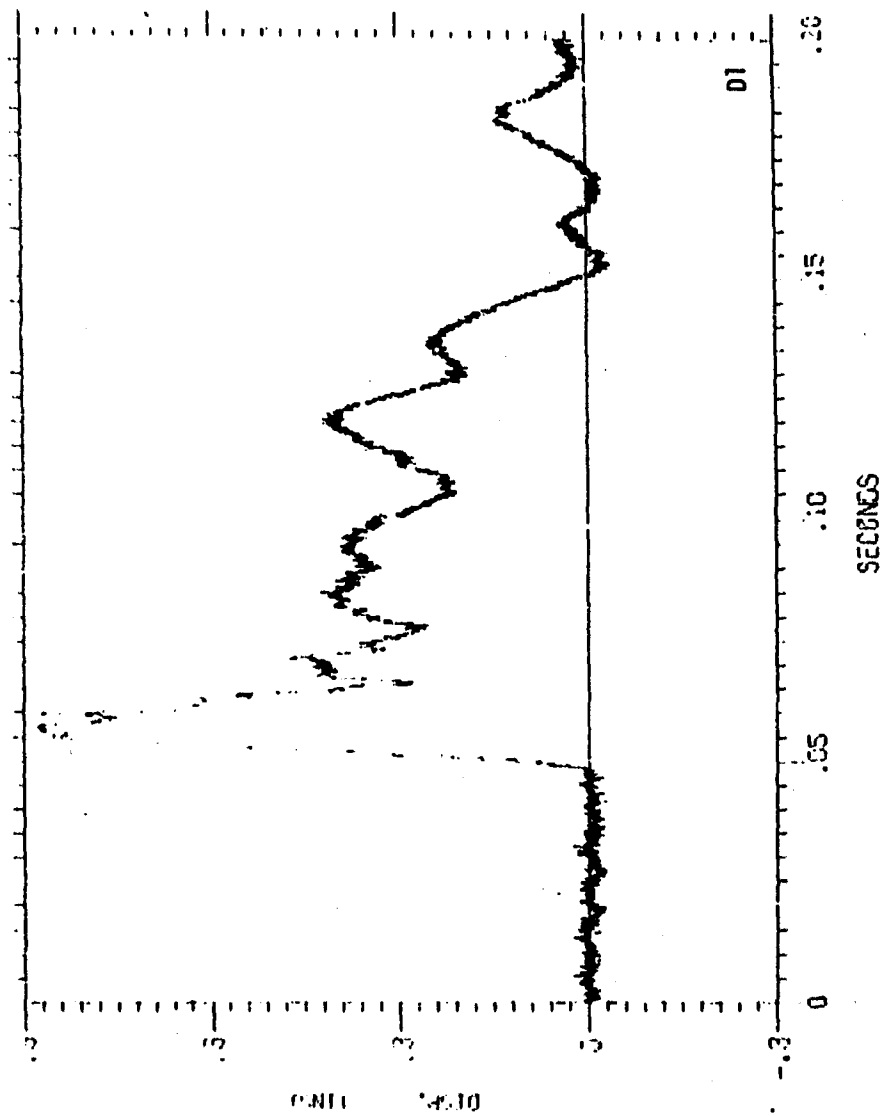


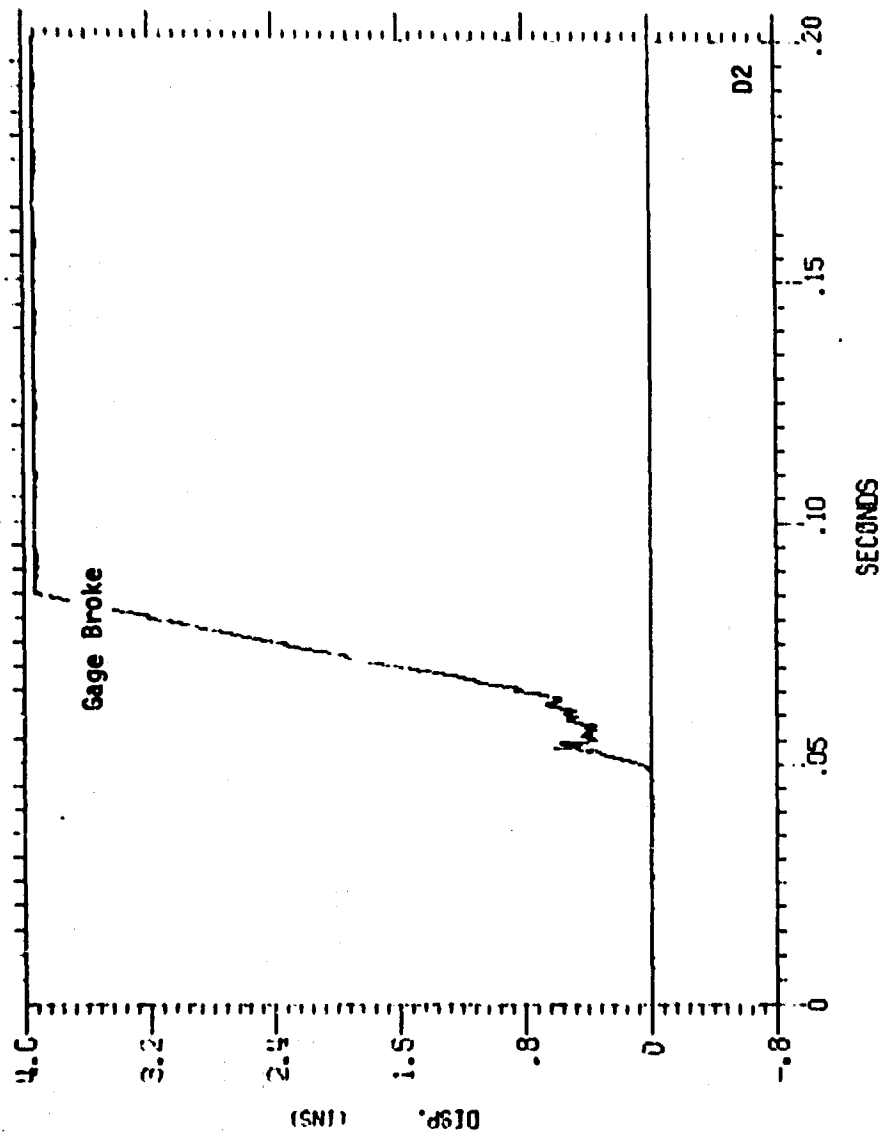












APPENDIX B

BLAST DOOR DAMAGE



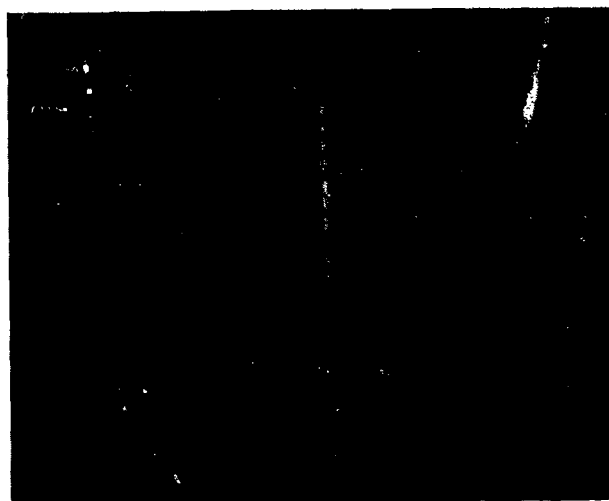
Door After Shot



Damage to Locking Handles



Hinge Area



Damage to Hinge



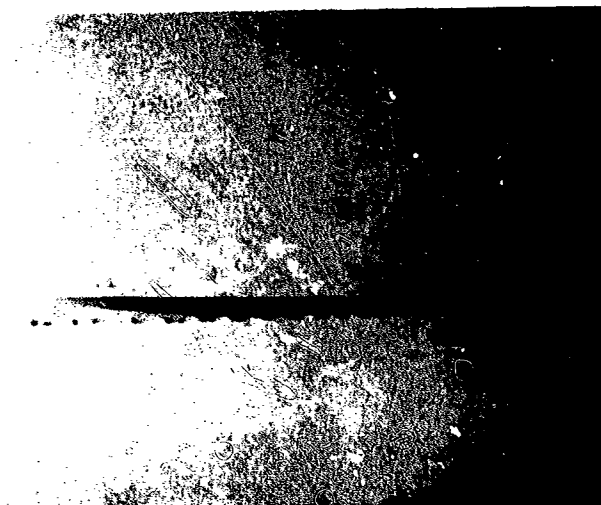
Damage to Hinge



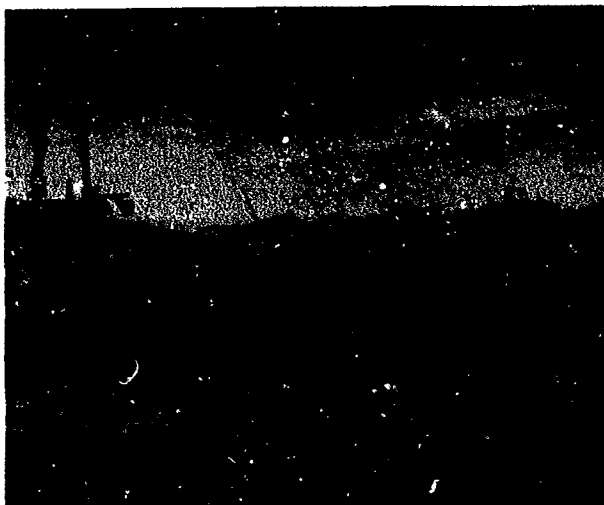
Top Surface Cracks



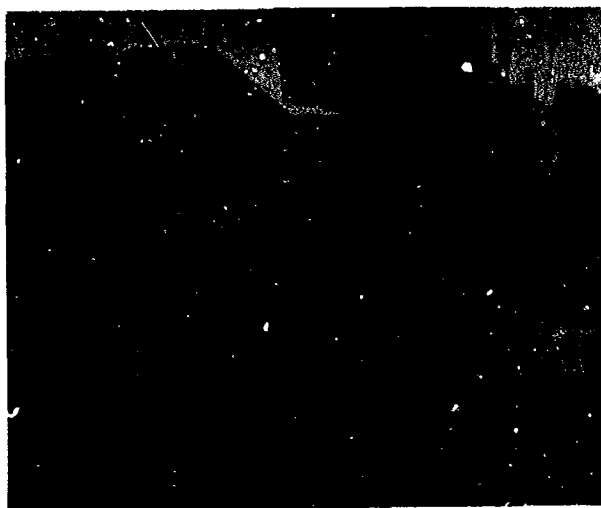
Top Surface Cracks



Damage to Seal Angle



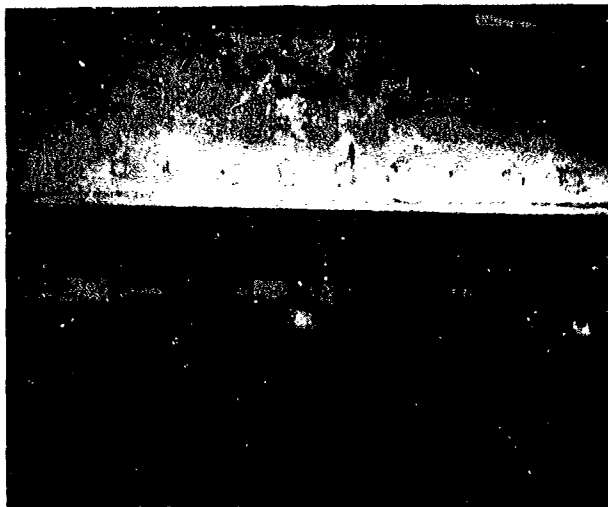
Lifting Door



Permanent Set in Door



Door Crack Pattern



Deformed Lock Mechanism

**27. BLAST TESTS OF EXPEDIENT SHELTERS
IN THE DICE THROW EVENT**

by

C.H. Kearny

Oak Ridge National Laboratory

BLAST TESTS OF EXPEDIENT SHELTERS IN THE DICE THROW EVENT*

C. H. Kearny

Emergency Technology Program, Energy Division
Oak Ridge National Laboratory, Oak Ridge, Tennessee 37830

1. BACKGROUND AND SCOPE

Civil defense research at Oak Ridge National Laboratory (ORNL) has always stressed the development of protection against blast effects. One reason for this emphasis is the fact that, if a population is able to occupy shelters affording good protection against blast effects at overpressures up to 7 psi, the area in which serious blast casualties would be suffered would be reduced by at least 75% compared to the situation in which a population takes shelter in homes that would be badly damaged at the 2 psi overpressure range by the blast effects of a large weapon. Another reason is the fact that even expedient shelters, if their walls are skillfully shored and their entrances equipped with expedient blast doors, can readily be built so as to protect occupants against all blast effects at peak overpressure ranges several times as high as 7 psi. Therefore, in 1973 ORNL participated in Defense Nuclear Agency's (DNA's) MIXED COMPANY Event. This test subjected various expedient shelter designs to the effects of an explosion of 500 tons of TNT. All of the ORNL expedient shelters survived with little or no damage.¹ As a result, it was decided that the most promising designs should be subjected to blast effects severe enough to indicate the worst blast environments that these shelters are capable of withstanding. The main event of DNA's recent DICE THROW series afforded the required blast environment. This event was a 630-ton ANFO (ammonium nitrate-fuel oil) explosion, producing airblast effects about equivalent to a 1-kiloton nuclear surface burst. This shot was detonated on October 6, 1976 at White Sands Missile Range, New Mexico. Eighteen expedient shelters (including four half-scale models) were subjected to the blast effects

* Research sponsored jointly by the Defense Civil Preparedness Agency and the Energy Research and Development Administration under contract with the Union Carbide Corporation.

at overpressures ranging from 53 psi to 5.8 psi, and expedient life-support equipment (mostly placed inside shelters) was exposed to overpressures of 53 psi to 1 psi. Several one-tenth-scale models of shelters were also tested, at overpressures of up to 180 psi.

2. PRINCIPAL OBJECTIVES

The principal objectives of ORNL's participation in DICE THROW were:

- a. To obtain field data useful in making more reliable estimates of the practical limitations of promising expedient shelter designs and expedient life-support equipment, as regards their capabilities for withstanding all blast effects from large explosions.
- b. To observe the relative effectiveness of several different ways of utilizing earth arching and trench-wall shoring to increase the blast protection afforded by lightly constructed shelters, in order to develop improved shelter designs that can be built using only widely available materials.

3. INSTRUMENTATION USED AND TEST DATA RECOVERED

3.1 Blast Overpressures

Blast overpressures were measured by yielding foil membrane blast gauges.² These passive gauges were developed at ORNL and performed well at the lower overpressures (less than 7 psi). However, the ORNL gauges that were installed adjacent to principal shelters to measure overpressures above 7 psi all recorded overpressures 28-60% higher than those recorded by the transducers at the same radial distances from ground zero on DNA's adjacent Gauge Line No. 1. Therefore, we have used the DNA measurements for all the aboveground overpressures to which the ORNL shelters were subjected, except for the DNA measurement at the predicted 100-psi range, which was obviously far too low.

The distances from ground zero (GZ) to the shelters, the predicted overpressures, and the measured overpressures at these distances are shown in the table below.

Table 3.1. Overpressures at Various Distances

Distance from Ground Zero	Predicted Overpressures	Measured Overpressures
440 ft	100 psi	106 psi
540 ft	50 psi	53 psi
640 ft	30 psi	31 psi
740 ft	20 psi	20 psi
820 ft	15 psi	15 psi
1140 ft	7 psi	6.7 psi
1370 ft	5 psi	5.8 psi

To simplify this report, only a few references to distances from GZ or predicted overpressures will be made. Measured peak overpressures will be used (e.g., "53 psi," "31 psi").

The ORNL pressure gauges inside the shelters recorded low overpressures. All these gauges functioned well except those inside the shelters at the 31-psi overpressure range. All the ORNL pressure gauges were recovered, and the overpressures they recorded inside the shelters are used in this report.

3.2 Elastic and Permanent Deformations

Elastic and permanent deformations of the roofs and some other parts of the shelters were measured by passive mechanical devices.¹ Over 90% of these functioned effectively. Linear measurements of distances between parts of a shelter were taken before and after the blast.

3.3 Blast-Wind Scouring

Blast-wind scouring of the earth mounded over shelters and around entryways was determined by driving 12-in. steel spikes into the earth until their heads were flush with the ground and measuring their exposures after the blast. (The duration of blast winds is proportional to the cube root of weapons yield;³ thus the depth of scouring by larger weapons can be estimated.) Also preblast and postblast depths of earth over and around shelters were recorded.

3.4 Blast Damage to Structures

Blast damage to all structural parts of shelters and to the earth walls of unshored shelters and of water-storage pits were determined primarily by observation. Numerous photographs were taken, both before and after the blast, to record blast damage--the most important part of the test data.

4. SMALL-POLE SHELTER AT 53 PSI

4.1 Purpose

The Small-Pole Shelter (see Figs. 4.1 and 4.2) has been developed for construction by unskilled workers in wooded areas (in stable or unstable earth, below or above ground). It provides excellent protection against radiation and much better protection against blast than does an unshored trench shelter or any poorly shored shelter. Untrained groups of families, using only muscle-powered tools, have succeeded in building this type shelter in less than 48 hours elapsed time from the time they received the instructions.⁴ A 24-man section of an infantry platoon of the 82nd Airborne Division, with no prior training and using only muscle-powered tools, built a 24-man model, without benches or bunks, in 18 elapsed hours.⁵

4.2 Construction

The main room and the horizontal part of the entryway at the east end were of unmodified Russian design,^{6,7} except that the excavation in

Fig. 4.1. Plan and Elevation of Small-Pole Shelter.

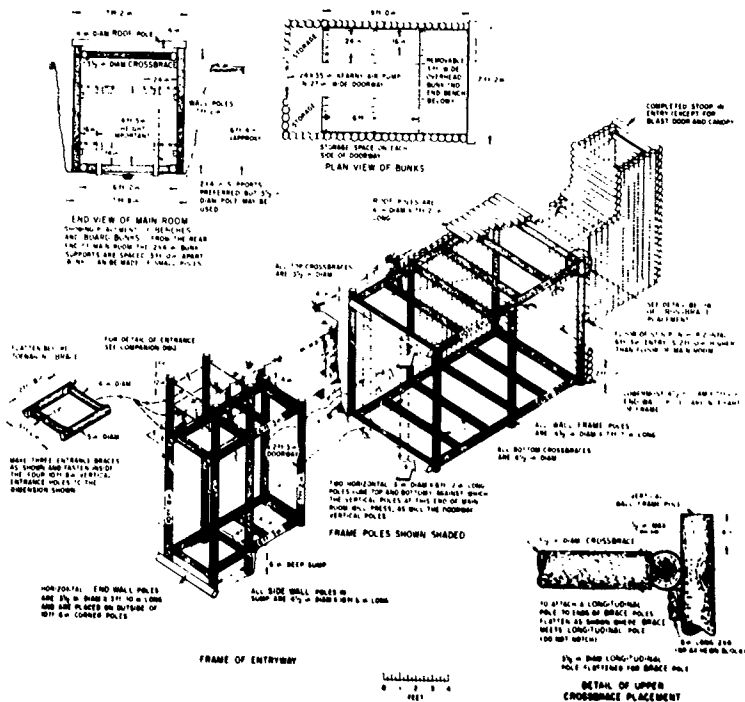


Fig. 4.2. Pictorial View of Small-Pole Shelter.

the hard caliche was made 2 ft deeper than the final level of the shelter floor. Then this bottom 2 ft was backfilled with dry, sandy earth. This soft earth under the wall poles permitted them to be pushed down sufficiently under blast loading to throw most of the load onto the resultant earth arching that blast overpressure sets up over a yielding structure.

A previous ORNL analysis⁸ of the survivability of this shelter indicated that without the protection of earth arching it would withstand an overpressure from a 200-kiloton weapon of about 15 psi with blast doors closed. This analysis assumed the use of green hardwood poles, the strengths of which were determined in the ORNL materials laboratory. The roof poles and wall poles of all the ORNL pole shelters in DICE THROW were ponderosa pine. In this shelter, the poles averaged about 5 in. in diameter including their bark. The 12-occupant shelter room was 10-1/2 ft long, as illustrated by Figs. 4.1 and 4.2.

The horizontal part of the entryway at the south end was only 4-1/2 ft in height, with its floor 2-1/2 ft above the floor of the main room and the east-end entryway.^{6,7} This height proved adequate, and this stoop-in entryway required significantly less material and labor to build than did the Russian-type horizontal entryway with 6 ft of headroom. (An unmodified Russian Small-Pole Shelter has only a small chimney-like air duct at one end; ORNL tests had proved that this small air duct would provide such inadequate ventilation that fatalities from excessive heat-humidity could result in warm or hot weather after a day of full occupancy.) The vertical entryways were of ORNL design,⁷ as shown in Figs. 4.1 and 4.2, except that they extended 5 ft above the ceilings of the horizontal entryways. (The Russian inclined stairway-entrance had been found to be weak and not suitable for the installation of a blast door.)

The roof poles of this box-like shelter were at ground level. The length of this shelter was perpendicular to the radius from GZ. To provide adequate shielding against the initial nuclear radiation to be

expected at the approximately 50-psi overpressure range from smaller nuclear weapons, the roofs of the shelter room and its entryways were covered with 5 ft of mounded earth. For adequate protection against initial radiation from a tactical weapon (through the entries), each entryway should have been at least 10 ft long. For protection against radiation from strategic weapons, the entries actually built would be satisfactory, and only 3 ft of earth cover would give a protection factor (PF) of over 500.

The need for blast doors on family shelters has long been recognized.^{9,10} ORNL blast tests¹ had demonstrated the effectiveness of expedient blast doors at overpressure ranges up to 29 psi, and since the present Soviet nuclear arsenal could subject over half of all Americans, if in their normal areas, to serious blast dangers, we included three new designs of expedient blast doors in our DICE THROW tests.

Both entrances of the Smali-Pole Shelter were protected by expedient blast doors (see Figs. 4.3 and 4.4). Each door measured 48 in. x 42 in.

PHOTO
6543-76



Fig. 4.3. Nailing Tire-Strip Hinges to Expedient Blast Door Tested at the 53-psi Overpressure Range.

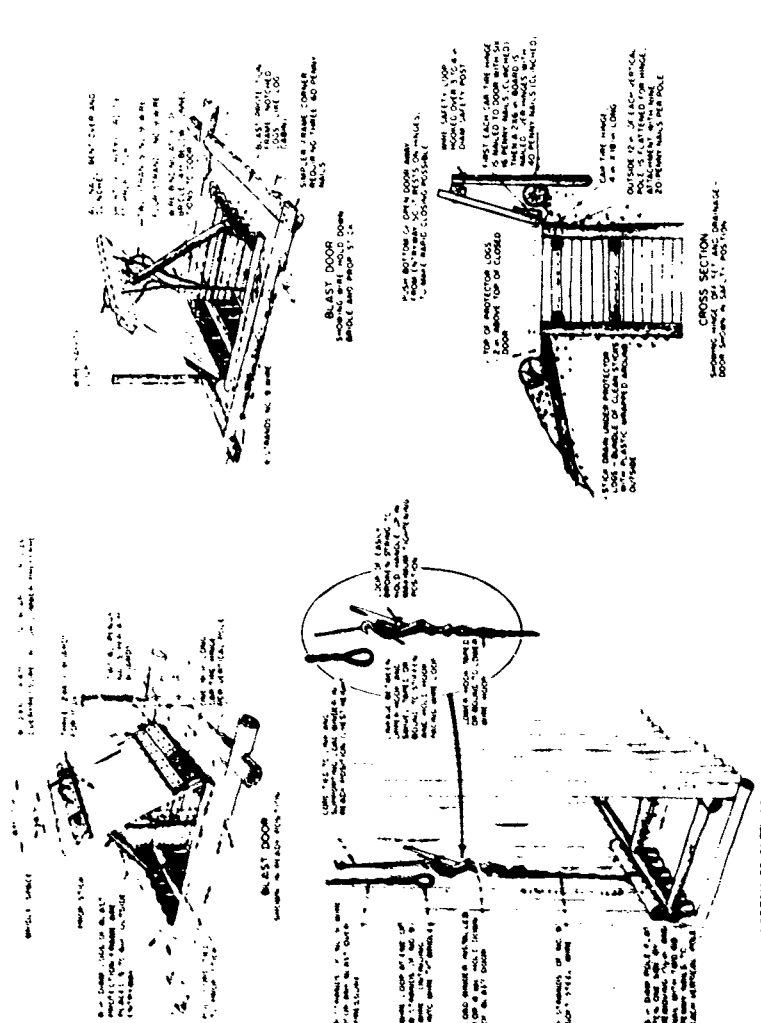


Fig. 4.4. Expedient Blast Door that Can Be Closed and Secured in Four Seconds. The expedient blast doors tested at DICE THROW were all of stronger construction than this door made of boards. This door was damaged but still intact after being subjected to about 17 psi in the main explosion of DNA's MIXED COMPANY EVENT.

and each was made of five thicknesses of 3/4-in. exterior plywood. The plywood sheets were glued together with waterproof resin and nailed together from both sides. Expedient hinges made of strips cut from the worn treads of automobile tires were nailed to the door and to vertical poles of the entry with No. 16 (4-in.) coated nails, on a rectangular spacing of 4 inches in each direction. A door was hinged on its side nearest ground zero with 5 hinges nailed to the 5 vertical poles of this side of its vertical entry. Each hinge was a 24-in.-long strip of worn, wide-tread automobile tire, 4 to 6-1/2 in. wide and 1/4- to 1/2-in. thick, measured in the grooves of the tread. Each strip was nailed to its door with twelve 5-in. nails, driven in about 3-1/2 in. with their heads bent away from the hinge line.

After seeing the bright light from a nuclear explosion, an alert shelter occupant can close and secure this type door within 4 seconds. This is fast enough to effect the closure of the door before the arrival of the airblast shock wave from an 8-MT or larger weapon at the 20-psi or less overpressure range, but not fast enough at the 53-psi range. (See Fig. 4.4.) Therefore, if this shelter is to afford protection against tactical weapons, it should be equipped with expedient blast valves of the tire-strip type, installed in separate intake and exhaust shafts. This type valve has been blasttested without being damaged at 65 psi.¹

Each blast door was surrounded with blast-protector logs which had been notched and spiked together and were evenly spaced around the door. These logs (about 8 in. in diameter and 8 ft long) had been placed with their upper sides about 2 in. higher than the top of the closed blast door.

4.3 Test Results

Figure 4.5 shows the four blast-protector logs around the north-end door after the blast. This explosion produced a measured peak overpressure



PHOTO
6545-76

Fig. 4.5. Blast-Protector Logs around Blast Door after Being Moved by Blast Effects at the 53-psi Overpressure Range.

of about 53-psi and a calculated peak blast-wind velocity of about 1,000 mph at this range (i.e., 540 ft from ground zero). The blast winds blew away up to 12 inches of the dry earth previously piled around the blast-protector logs. The shock wave and dynamic drag effects shifted these four logs from their original positions. In its final position, the log nearest ground zero was so close to the hinges that the door could be opened from the inside to an inclination of only about 60 degrees.

If this door and its protector logs had been subjected to the same overpressure from a large surface burst that would have produced dynamic drag and blast wind effects of much longer duration, the door might have been jammed in its closed position by the shifted logs. If long, strong stakes had been driven prior to the blast so as to secure the logs, their movement would have been reduced. However, for maximum blast protection against nuclear weapons this whole shelter should have been positioned deep enough in the earth so that its blast doors would have

been only a few inches above ground level, with the earth surrounding the blast-protector logs sloped up around them at an angle of less than 10 degrees. Or the earth mounded over the whole shelter should have all its slopes less than 10 degrees.

The pole frame and plywood blast doors of the Small-Pole Shelter were essentially undamaged by the blast effects at the 53-psi overpressure range (see Fig. 4.6). However, occupants would have been injured if they had been standing with their heads close to the ceiling,



PHOTO
0704-77

Fig. 4.6. Small-Pole Shelter after Being Tested with Blast Doors Closed at the 53-psi Overpressure Range. Note the slightly damaged expedient shelter-ventilating pump in the stoop-in entryway. Two men worked about 5 min. to replace the 4 blown-loose flaps, the only damage.

which was rapidly depressed when pressure on the roof poles caused the wall poles to be punched down into the soft, back-filled earth supporting them. This downward movement of the roof and walls varied from a minimum of 2 in. in the southwest corner to a maximum of 6-1/4 in. in the north-east corner. Figure 4.7 shows the movement at the center of the room, where



PHOTO
6453-76

Fig. 4.7. Movement of Upper Part of Small-Pole Shelter Away from Ground Zero due to Blast Effects at 53-psi Overpressure Range.

the upper part of the shelter was moved 4-1/4 in. away from ground zero and 4-3/16 in. downward, relative to the "fixed" vertical post to which the lower part of the damaged deflection gauge was attached. Furthermore, about 15% of the floor area "puffed up" from 2 to 8 in. above its original elevation.

Figure 4.8 shows how the floor "puffed up" about 6 in. in the northeast corner of the shelter in the east entryway; some pressurized earth caused some earth to "flow" up into the closed room, in which the measured peak overpressure was only 1.5 psi. About 85% of the floor area was undisturbed, as was the floor in front of the man's hand resting on the cross brace. Neither the blast gauge resting on the brace pole in the corner nor the small expedient fallout meter on top of it was moved.



PHOTO
6459-76

Fig. 4.8. "Puffed-Up" Part of the Floor of Small-Pole Shelter due to the Start of Earth Flow under Moderately Long-Duration Blast Overpressure at the 53-psf Overpressure Range.

If a person had been standing on the floor when it was "puffed up" suddenly, possibly his legs could have been injured. To prevent possible injuries due to an intact ceiling moving very rapidly downward and/or the floor moving upward, occupants could recline in expedient bedsheet hammocks¹¹ slung from the upper horizontal brace poles of the main shelter room, as shown in Fig. 4.9.



PHOTO
6458-76

Fig. 4.9. Expedient Bedsheet Hammock, Useful to Avoid Severe Shock Effects in a Shelter at High Overpressure Ranges. The man is operating an expedient shelter-ventilating pump via an expedient pulley-equivalent, a greased forked stick suspended on strings.

The whole roof, the upper horizontal braces, and the upper ends of the wall poles were all displaced about 4-1/4 in. to the west (away from GZ) by the blast effects on the 5-ft-high mound of shielding earth over the shelter. The sides of this mound sloped about 36 degrees; its width on top averaged about 10 ft. (If this dry mound had been subjected to the blast effects of a megaton or larger nuclear weapon at the same 53-pai overpressure range, the much greater impulse and longer-duration drag effects might have caused the earth mound to be displaced far enough to wreck the underlying pole shelter--especially since the long-duration blast-winds would have scoured away most of the earth cover. Even a mound of wet earth, which is much less vulnerable to long-duration blast-wind scouring, might have been displaced far enough to cause serious or disastrous structural damage.)

The maximum overpressure measured inside the shelter was 1.5 pai--not enough to be harmful. Less than half of this pressure increase was due to the sudden reduction in the volume of the shelter room which was described above. The rest was caused by blast wind that blew through cracks between the poles near the top of the vertical entryways. These

cracks appeared after the initial blast wind had scoured away several inches of the covering earth and torn away the polyethylene film that, with the essential help of small-scale earth arching, had kept earth from being forced between the cracks by the peak overpressure.

There was no damage to any of the life-support equipment in this shelter, except for quickly repairable damage to the expedient shelter-ventilating pump (KAP)¹² pictured in Fig. 4.6.

4.4 Conclusions and Recommendations

4.4.1 - A Small-Pole Shelter built in stable ground and equipped with blast doors can give reliable protection against the blast effects of small tactical weapons up to about the 50-psi overpressure range.

4.4.2 - A modification of this shelter with a continuous pole floor under the wall poles should not fail as a possible result of a large amount of pressurized and destabilized earth flowing up into it through its floor when subjected to the long-duration overpressures and large movements caused by a megaton explosion.

4.4.3 - In order to prevent the above modification from seriously reducing the capability of the shelter frame to yield under blast loading and thus promote protective earth arching, all parts of one of the shelters to be tested should first be covered with readily crushable material, such as small tree limbs. Then this material should be covered with fabric or plastic before placing earth around and over the protected shelter.

4.4.4 - Small-Pole Shelters modified in these ways should be subjected to the effects of blast simulating at least a 100-KT explosion at the 25-psi and 50-psi overpressure ranges, when installed in a trench dug in unstable earth, deep enough so that its blast doors are only about a foot above the original ground level.

5. UNMODIFIED RUSSIAN POLE-COVERED TRENCH SHELTERS AT 20 AND 6.7 PSI

5.1 Purpose

Two identical unmodified Russian Pole-Covered Trench Shelters were tested at the 6.7-psi and 20-psi overpressure ranges, in order to make a more accurate estimate of the blast protection afforded occupants of this common type of Russian expedient shelter. This unshored "dugout" is recommended for construction in stable earth.

5.2 Construction

The two unmodified Russian Pole-Covered Trench Shelters were of the design detailed in the 1969 Soviet civil defense handbook¹³ except that the entrance stairways were at right angles to their lengths, a modification recommended in both the 1972 and the 1976 Russian shelter-building manuals.^{14,15} Figure 5.1 shows most of the roof poles in position before the shelter was covered with 4-mil polyethylene and earth mounded 30 in. deep. A total of 62 lodgepole pine poles, each 7 ft long, were laid side by side across the 31-ft-long trench



PHOTO
6406-76

Fig. 5.1. Poles Covering Russian Pole-Covered Trench Shelter at 20-psi Overpressure Range, with Uncompleted Stairway Opening Facing Away from Ground Zero.

(not including the right-angle entry stairway that is shown in the foreground of Fig. 5.1). Figure 5.2 gives the details of this simple fallout shelter.

5.3 Location and Test Results

A Soviet civil defense handbook⁶ states that within "the zone of complete destruction" the overpressure exceeds 0.5 kg/cm^2 ($\sim 7 \text{ psi}$) and that all residential and industrial buildings and all fallout shelters will be destroyed. (This limitation obviously does not apply to the Russian "hasty shelters" built of prefabricated concrete or steel components. Typical Russian expedient fallout shelters are of light construction and are not designed to withstand blast effects.) Therefore, one unmodified Russian Pole-Covered Trench Shelter was built at the forecast 7-psi overpressure range (6.7 psi was measured). Because of the almost rock-like caliche earth, an identical shelter was built at the 20-psi range, to see if occupants might survive more severe blast effects than those at the 7-psi range. Neither shelter had a blast door.

In the shelter at 20 psi, two anthropomorphic dummies (supplied by the Lovelace Foundation) were seated side by side just inside the inner curtain (see Figs. 5.2 and 5.3). A movie camera was installed by Denver Research Institute for the U.S. Army's Ballistic Research Laboratory. This camera was farther inside the shelter, mounted on a concreted-in-the-ground post. This camera took 400 frames per second; the four photographs of Fig. 5.3 were taken in 1/100 second. The first photograph shows only a slight movement of the innermost blanket-curtain. The second shows the earth walls beginning to crumble under the forces of a ground shock wave, induced by the airwave slap overhead before the airborne shock wave reached these walls or the dummies. The third and fourth photographs show the innermost blanket-curtain being torn, revealing the torn outermost curtain, that was darker colored, being blown behind and against it. The collapsing walls trapped the two dummies before





PHOTO 6632-76 (No. 1)



PHOTO 6629-76 (No. 3)



PHOTO 6636-76 (No. 2)



PHOTO 6634-76 (No. 4)

Fig. 5.3. Dummies Being Struck by Airblast and Curtains Traveling about 180 mph. Note the walls collapsing under ground-shock stresses before the arrival of the airborne shock wave.

the entering blast wind, which was shown by the four movie frames to have a velocity of about 180 mph, could blow them over. (The blast wind peaked at about 470 mph outside this shelter.)

Figure 5.4 shows the dummies trapped by the collapsing walls. Because their strong steel joints did not permit these dummies to bend forward, the collapsing walls did not bend them forward, knock them down, and bury them, as would have been the fate of two men. Note the unbroken roof poles.



PHOTO
0705-77

Fig. 5.4. Dummies at 20-psi Range after Ground Shock Collapsed the Earth Walls of Shelter. Their steel "bones" and joints prevented them from being knocked down and buried.

The measured overpressure inside this shelter was 7 psi--high enough to break some persons' eardrums. (If this shelter had been subjected to the blast effects of a megaton weapon at the 20-psi range, the maximum overpressure inside the shelter would have been almost 20 psi.)

The entry was wrecked and much of its covering earth was blown away, as illustrated by Fig. 5.5. The ventilation duct was broken off.



PHOTO
6460-76

Fig. 5.5. Wrecked Entry of Russian Pole-Covered Trench Shelter at 20 psi.

At the 6.7-psi range, an identical shelter suffered serious damage. Chunks of hard caliche weighing up to about 400 lb were broken off the very stable earth walls and would have injured shelter occupants. A dummy seated on a fixed bench next to the blanket-curtains was knocked off the bench by the shock wave and the entering blast winds (see Fig. 5.6).



PHOTO
6462-76

Fig. 5.6. Dummy Knocked Off Bench in Russian Pole Covered Trench Shelter at the 6.7-psi Overpressure Range.

5.4 Conclusions

5.4.1 - In soils typical of most inhabited areas, if a shelter of this design were subjected to the blast effects of a much larger explosion at the 7-psi overpressure range, the Russian estimate of "total destruction" would probably prove to be realistic. (The author believes that "total destruction" in this sense means the shelter would be so badly damaged as to be uninhabitable--not that all occupants would be promptly killed.)

5.4.2 - Earth arching in adequately thick earth cover over pole roofs prevents the poles from being broken by overpressures far in excess of the pressures such roofs could withstand if uncovered.

5.4.3 - Stresses due to ground shocks and earth waves would be the predominant causes of failure of unshored trench shelters subjected to the blast effects of large explosions.

6. LOG-COVERED TRENCH SHELTER AT 53 PSI

6.1 Purpose

We constructed an unshored trench shelter with its roof poles positioned in two different ways and located at the predicted 50-psi overpressure range because:

a. We anticipated that the extremely stable, rock-like caliche earth at the test site would result in unshored trench walls being so strong that they would not collapse under the ground shock stresses produced at the 50-psi range by mere 1-KT blast effects.

b. We were confident that effective earth arching in the thick earth would prevent the breaking of roof poles.

c. We were interested in comparing the effectiveness of the Russian and the Chinese way of roofing a trench with poles or logs.

6.2 Construction

This shelter was built with half of its 12-ft-long room having its roof poles positioned in the Russian manner at ground level (see Figs. 5.1, 5.2, and 6.1). The other half of the room had its roof poles positioned

in a recommended Chinese manner¹⁶ (i.e., about 28 in. below ground level). Figure 6.1 shows the vertical cross sections of these two halves as modified from the original designs in order to permit a better comparison between the merits of the two different ways of positioning roof poles. (The room of the Russian half was made 16 in. less in height than in the original Russian design, and the Chinese half was made 4 in. less in width than specified in the Chinese handbook.¹⁶)

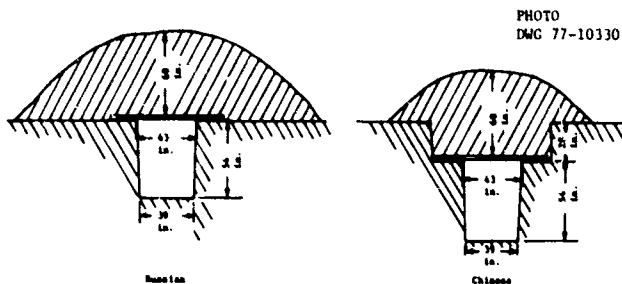


Fig. 6.1. Comparison of Russian Way and Chinese Way of Positioning Poles to Roof a Trench Shelter. Note that the Chinese way requires about 35% less earth to be moved in order to make a 5-ft-thick covering--about the thickness specified in a Chinese handbook for shielding against initial nuclear radiation.

As shown in Fig. 6.1, the Chinese half was built with its roof poles resting on earth shelves 28 in. below ground level, cut into the hard caliche. All roof poles (logs) were ponderosa pine. The poles averaged about 5 in. in diameter, not including their bark. All were cut 7 ft long. Earth was mounded about 5 ft above ground level over this whole shelter. This resulted in about 4-1/2 ft of earth covering the roof logs of the Russian half and about 6 ft covering the roof logs of the Chinese half. Blast-wind scouring removed a foot of this mounded earth.

The vertical parts of the two entries to the shelter were of a newly developed design with triangular cross sections. The expedient blast doors were of a new triangular type. This design (see Figs. 6.2 and 6.3) was developed in order to: (a) use green poles cut from ordinary trees to make a tight-closing expedient blast door that takes advantage of the fact that three intersecting straight lines determine a plane, (b) require only widely available hand tools and common materials (e.g., auto tires, nails, and some wire or rope, in addition to poles), and (c) make practical the use of a triangular vertical shelter entry, which has a smaller cross-sectional area than does a rectangular vertical entry big enough for the same sized person to use, and shows promise of requiring less materials to meet a given level of blast protection.



PHOTO
0700-77

Fig. 6.2. Expedient Triangular Blast Door Made of Pine Poles. The auto-tire flap valves over the 1-1/2-in.-wide spaces between the poles were undamaged by the blast effects at the 53-pai over-pressure range. Ground zero was to the left. Blast effects had moved the three connected blast-protector logs, preventing the door from being opened fully.



PHOTO
6442-76

Fig. 6.3. View of the Same Triangular Blast Door, Looking Toward Ground Zero. The hinge pole, originally 7-in. in diameter after peeling, had been flattened on its top and back side. The two other poles, 8-in.-diameter, had been flattened on their bottom, top, and inner sides. All three poles were notched and nailed together. Note the slots between the door-covering poles.

6.3 Test Results

Figures 6.2 and 6.3 show the triangular blast door on the south end of the shelter, undamaged after the blast. Note that one of the 3 blast-protector logs (the log in the lower left corner of the photograph) has been pushed by the blast up against the hinge-pole of the blast door. The door was undamaged. However, the movement of the earth mound had broken the door-seat pole on which the man's foot is shown resting in Fig. 6.3. Figure 6.4 shows the break more clearly.

Both of the triangular blast doors were undamaged. The expedient blast valves on the blast doors were closed by the blast, and about 75% opened after the blast, permitting adequate ventilation with an expedient pump, a KAP. The overpressure inside the Chinese half was 1.5 psi, and the overpressure directly under the north door was 3 psi. The results of this test indicate that the use of expedient blast valves over the



PHOTO
6443-76

Fig. 6.4. Broken Pole of Triangular Door-Seat. This pole was broken by differential earth movements of the earth mounded over the shelter. The man's hand rested on the unbroken hinge-pole.

1-1/2-in.-wide cracks of this blast door is impractical. Most of the flap valves opened before the strong blast afterwinds subsided. These winds plus the natural desert winds blew so much dirt and sand through the valves and into the shelter that a serious fallout entry problem could exist after a nuclear blast. Figure 6.5 shows the blast door at the north end of the shelter before it was opened after the blast. Much earth and sand had been deposited on it by the subsiding blast winds.



PHOTO
6441-76

Fig. 6.5. Posttest Condition of Expedient Triangular Blast Door. Some flap valves had been jammed shut, and much earth and sand had been deposited.

Although not one roof pole of any part of this shelter or any other shelter was broken or cracked, the ground-shock effects collapsed the walls of the Russian half of this shelter so badly (see Fig. 6.6) that all occupants would have been killed. Damage to the Chinese half was



PHOTO
6445-76

Fig. 6.6. Postshot View of the Caved-In Caliche Walls of the "Russian" Half of the Log-Covered Trench Shelter at 53 psi.

much less serious, although hundreds of pounds of caliche, some chunks weighing up to 20 lbs, were broken off the edges of the shelves supporting the roof logs. The roof-deflection gauge in the Chinese half recorded a maximum transient downward deflection of 1-1/2 in. and a permanent deflection of 7/8 in.

6.4 Conclusions and Recommendations

6.4.1 - Under the longer-duration blast effects of a large nuclear explosion, mounded entries extending several feet above original grade level would probably be wrecked by the combined effects of blast-wind scouring and dynamic drag.

6.4.2 - Blast doors should be positioned only about a foot above ground level, and earth should be mounded with slopes of 10 degrees or less. (Unfortunately, such deeper excavation, even in softer earth, might make construction within 48 hrs impractical for builders having only hand tools.)

6.4.3 - Triangular blast doors made of poles can readily be built to withstand 50-psi blast effects, but should be made solid and as nearly dust-tight as practical. Separate ventilation shafts with blast valves should be provided, with the blast valves positioned about 2 ft from the bottom of each shaft.

6.4.4 - Persons building expedient shelters to provide protection against nuclear blast effects should build well-shored shelters with blast doors whenever practical.

7. LOG-COVERED TRENCH SHELTER AT 31 PSI

7.1 Purpose

A near-counterpart of the Log-Covered Trench Shelter that was tested at 53 psi was tested at 31 psi, in order to determine at what overpressure range this type shelter, if built in extremely stable earth, will survive. Also we wished to test a semiexpedient design of steel blast door on a shelter entrance at approximately 30 psi.

7.2 Construction

This shelter was constructed the same as the Log-Covered Trench Shelter at 53 psi, except that protecting its single entry it had a semiexpedient blast door made of about 65% of a 30-gal. steel oil drum. Rubber-tire hinges and rubber-tire seals made a snug closure between the door and the upper part of the vertical entry. The upper 2 ft of the vertical entry was made of two thicknesses of 2-in. boards nailed together (see Fig. 7.1).

7.3 Test Results

Although the blast effects loosened some of the bolts of the steel blast door, tore the metal in several places, and produced other damage indicating that it was on the verge of failure, it did not fail.



PHOTO
6493-76

Fig. 7.1. Semiexpedient Blast Door Made of a 30-gal Steel Drum, Badly Damaged at 31 psi but Still Blast-Tight. Blast-wind scouring had removed up to 17 in. of the dry earth mounded around this entrance and blown away its single blast-protector log.

Figure 7.2 pictures the interior of the Chinese half of the shelter after the blast had broken hundreds of pounds of caliche off the very stable walls and lowered the roof but did not cause it to collapse. No poles were cracked in any part of this shelter. The walls of the Russian half collapsed so badly that all occupants would have been buried.

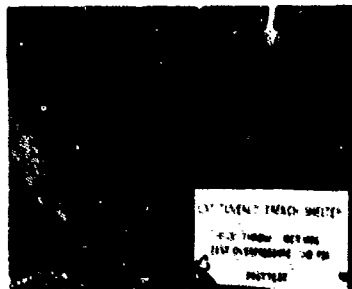


PHOTO
6446-76

Fig. 7.2. Serious Wall Caving at 31 psi (Predicted 30 psi). The beam deflection gauge on top of the post showed a 2-1/2 in. lowering of the center roof log.

7.4 Conclusion and Recommendations

7.4.1 - Even in extremely stable earth, an unshored trench shelter at 31 psi would give inadequate blast protection against even a small tactical nuclear weapon.

7.4.2 - The steel-drum blast door is not as blast resistant as pole or plywood blast doors that require materials much less difficult to find and that require less skill, tools, and time to build.

8. DOOR-COVERED EARTH-ROLL SHELTERS AT 15 AND 5.8 PSI

8.1 Purpose

Two of these aboveground small fallout shelters,⁷ made of interior hollow-core doors, bed sheets, and other materials available in tens of millions of American homes, were tested at the 15- and 5.8-psi overpressure ranges in order to determine if the shelters would afford better blast protection than would typical homes.

8.2 Construction

Each shelter was built with its long axis on a radius from ground zero. Figure 8.1 shows the interior of the shelter at the 15-psi range

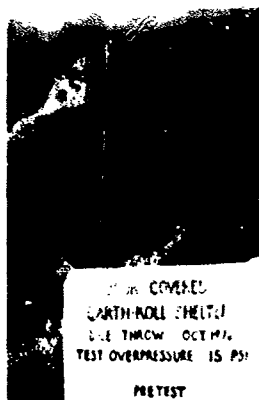


PHOTO
6497-76

Fig. 8.1. The Bedsheet "Earth-Roll" Walls Were 36 Inches Apart before Test.

before the explosion. The vertical stick touching a roofing door is a roof-deflection gauge, with its upper end consisting of nothing but a thin cylinder of household aluminum foil, an unsatisfactory device if exposed to blast wind. Figure 8.2 gives details of the construction of these shelters (see p. 33).

8.3 Test Results

Figure 8.3 is a posttest picture of the northward-facing entry of the shelter at the 15-psi overpressure range. This photograph also shows part of the northward-facing side of this shelter. The blast winds scoured only about 1 in. of earth from the top of this shelter, apparently because its long, flat top extended in the same direction that the blast winds blew. Note the proof of the toughness of polyester-cotton pillowcases used to make 100-lb sandbags. The sandbag in the foreground was blown about 7 ft by the approximately 370 mph blast wind without being broken.



PHOTO
6483-76

Fig. 8.3. Northward-Facing Entry (at Right Angle to the Direction to Ground Zero) of Door-Covered Earth-Roll Shelter at the 15-psi Overpressure Range. This is a post-test photograph.

To the surprise of most observers, earth arching above the roof doors prevented any of them from being broken in by the blast effects. The doors

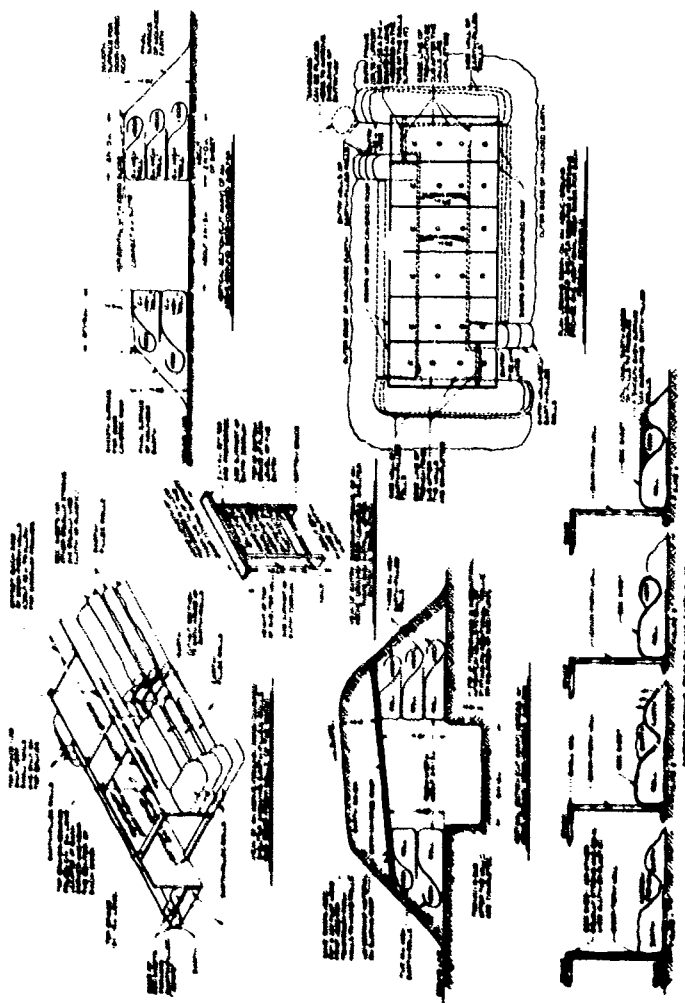


Fig. 8.2. Door-Covered Earth-Roll Shelter, Tested at 15 and 5.8 psi.

were not broken in, even though the lower 1/8-in.-plywood veneer of three of the six doors was broken. Figure 8.4 pictures the interior of the shelter at the 15-psi overpressure range after the blast effects outside had caused the sandy soil inside the bedsheet "earth-rolls" to "flow" inward rapidly. The width of the shelter was reduced from 36 in. to a minimum of 14 in. No additional earth movements were observed during the two weeks following this test. This unanticipated earth within the "earth rolls" did not tear any of the pieces of bedsheet cloth.



PHOTO
6484-76

Fig. 8.4. Interior of Door-Covered Earth-Roll Shelter after 15-psi Blast Effects had Reduced Width of Shelter from 36 Inches to a Minimum of 14 Inches Near Its Center.

Pressure-time measurements on the adjacent DNA Gauge Line No. 1 showed that only about 40 msec elapsed between the peak overpressure of 14.9 psi recorded at the same distance (820 ft) from ground zero, and its reduction to 6 psi, the maximum overpressure recorded inside

this shelter by the ORNL pressure gauge shown in the foreground of Fig. 8.4. The gauge that had been installed to measure the roof deflection was blown away by the entering shockwave and blast wind. The reduction in ceiling height appeared to be less than 1 in. in this part of the shelter, but up to about 4 in. in other parts.

At the 5.8-psi overpressure range, the Door-Covered Earth-Roll Shelter was still habitable for weeks after the test. Figure 8.5 shows that at 5.8 psi the walls were not forced inward by the blast effects. The unbroken upper 1/8-in. veneer plies of the doors held as flexible membranes, and earth arching was set up in time to prevent this shelter's roof from being collapsed either as a result of initial mechanized earth loading or due to the 5.8-psi blast effects.



PHOTO
6485-76

Fig. 8.5. Posttest Interior of the Door-Covered Earth-Roll Shelter at 5.8-psi Overpressure Range. The lower 1/8-in. veneer of the doors had been badly broken by impact before the test, due to a front-end loader having dumped tons of earth onto this yielding roof.

The peak overpressure measured inside this shelter was 3 psi, about half the 5.8 psi measured outside on DNA's adjacent Gauge Line No. 1. The blast winds, that peaked outside at about 175 mph, scoured away only a fraction of an inch of the shielding earth.

8.4 Conclusions and Recommendations

8.4.1 - A Door-Covered Earth-Roll Shelter obviously is impractical for use as a blast-protective shelter against blast effects considerably less than those at the 15-psi overpressure range from even a very small nuclear weapon.

8.4.2 - If this fallout shelter with a protection factor of at least 200 had been built in a typical suburb and had been subjected to the blast winds from a megaton weapon at the same 5.8-psi overpressure range, it might have been damaged or destroyed by blast-hurled pieces of houses and/or trees.

8.4.3 - Notwithstanding the hazards inherent in the use of this or any other lightly constructed aboveground shelter in a blast area, occupants of this simple shelter would have a decidedly better chance of surviving than would people inside typical suburban homes, which would be demolished by the blast effects at 5.8 psi.

9. RIDGE-POLE SHELTERS AT 15 AND 5.8 PSI

9.1 Purpose

In wooded areas having the water table or rock too close to the surface for belowground expedient shelters to be practical, untrained families with few tools have been able to build Ridge-Pole Shelters in less than 48 hours. No prior blast testing of this type shelter, that has its side poles merely leaning against its ridge pole, had been carried out anywhere (see Fig. 9.1).



PHOTO
6405-76

Fig. 9.1. Almost Completed Frame of Ridge-Pole Shelter at 15 psi. Only the outermost roof pole of the entry has been placed on its wall poles.

9.2 Construction

Two identical Ridge-Pole Shelters were built, each having the dimensions shown in Fig. 9.2. One was tested at the measured 15-psi overpressure range, and the other at the 5.8-psi overpressure range. Each was positioned with its ridge pole perpendicular to a radius from GZ, with one of its two crawl-in entries facing GZ and the other entry facing in the opposite direction. Figure 9.1 shows the almost completed pole frame, plus a temporary brace pole steadying the entrance. The pole frame was next covered with small, leafy limbs (Fig. 9.3), which in turn were covered with 4-mil polyethylene. Then a covering of dry, sandy earth 2 ft thick was placed over the whole shelter, with earth-filled potato bags retaining the earth over the entrances.

9.3 Test Results

9.3.1 - At 15 psi.--Contrary to our expectations that the blast effects would collapse the main room, the main room was undamaged (see Fig. 9.4). The ridge-pole was moved only one-half inch away from GZ. However, up to 9 in. of earth was scoured off the top of the shelter.

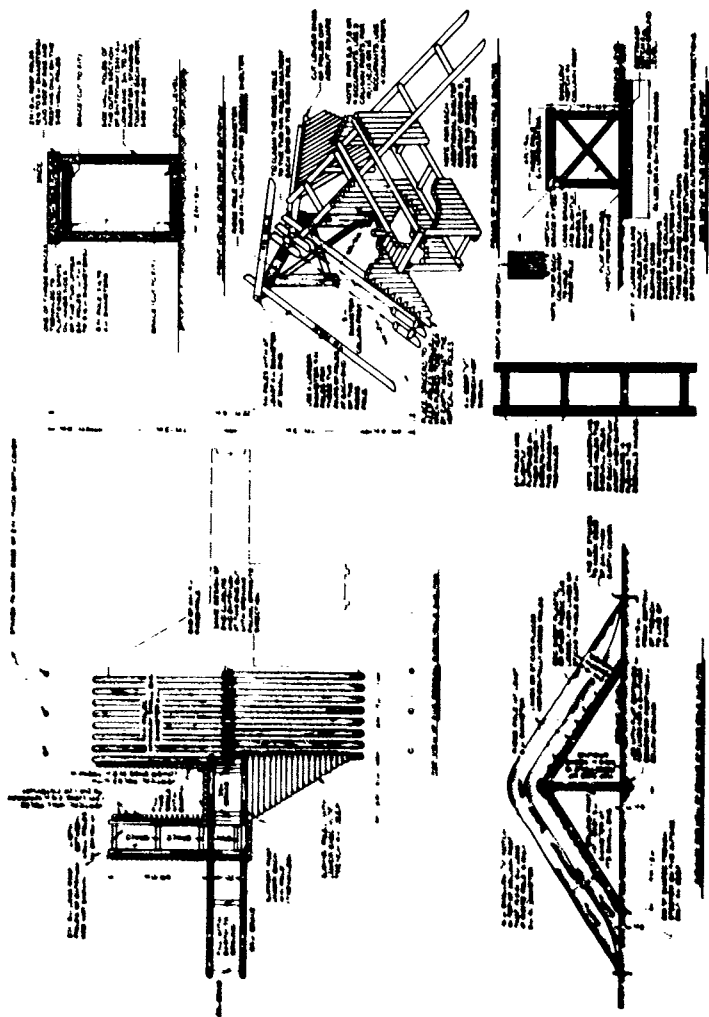


Fig. 9.2. Ridge-Pole Shelter Tested at 15 and 5.8 psi.



PHOTO
6476-76

Fig. 9.3. Covering the Frame of a Ridge-Pole Shelter with Salt Cedar Limbs.



PHOTO
6498-76

Fig. 9.4. Post-tension Interior of Ridge-Pole Shelter at 15 psi. The main room was undamaged; the ridge pole had been moved only 3/4 in. away from GZ.

In three places the underlying plastic over the ridge was broken; as a result, dry, sandy earth fell through the roof pole in these places, producing holes several inches across, open to the sky.

The seriousness of what would be the amount of blast-wind scouring by a 1-MT explosion (which at a given overpressure range would produce blast winds lasting 10 times as long as the 1-kiloton blast winds at DICE THROW) is indicated by the removal of all shielding earth from the GZ side of a 1/10-scale model of this Ridge-Pole Shelter, also tested at 15 psi (see Fig. 9.5).



PHOTO
6392-76

Fig. 9.5. Posttest Exterior of 1/10-Scale Ridge-Pole Shelter at 15 psi. Scouring by the blast winds had removed practically all the earth, plastic and twigs on the side facing GZ and over the two entries--indicative of blast-wind scouring of earth cover over a full-scale shelter by a megaton explosion.

The most surprising damage is shown by Figs. 9.6 and 9.7. Obviously, the dry earth "blow" away from the middle of the shelter and toward the two ends of the shelter. Apparently the pressures on the ends of the shelter were decreased as compared to the pressures on the center, both by the lack of reflected overpressures at the ends and the lowering of pressures at the ends caused by Bernoulli effects where the velocities of the blast winds were increased as the winds passed around the ends of the obstructing shelter.



PHOTO
6478-76

Fig. 9.6. Collapsed Entrance Facing Away from GZ. The blast winds had scoured away most of the covering earth, and the earth had "flowed" away from the center of the shelter, pushing the upper part of the entry in a direction perpendicular to the radius from GZ.



PHOTO
6477-76

Fig. 9.7. Postblast View of the Entry of the Ridge-Pole Shelter Facing GZ, at 15 psi. Note the scattered potato-sack sandbags, that had been placed to retain the earth over the entry. Earth "flow" had pushed all but the base of the entry away from the middle of the shelter, leaving none of the entry walls perpendicular.

The three fireplace-size logs (see Fig. 9.7) in front of the entrance facing GZ, and also the two poles pictured resting on the side of the shelter, had been carried by the blast winds from where they had been stacked before the test at the 70-psi range, 315 ft from where they came to rest. Note the identifying spot of paint on the end of the log on the right.

The overpressure inside only reached 3 psi, due to the small size of the semicollapsed entryways, the relatively large volume of the main room, and the relatively short time (about 80 ms) that the overpressure outside remained about 3 psi.

9.3.2 - At 5.8 psi,--As anticipated, this Ridge-Pole Shelter was undamaged as regards its pole frame. Measurements showed the ridge pole to be unmoved. However, 6 to 12 in. of dry, sandy earth was removed from the ridge, partly due to blast-wind scouring and partly due to shock effects having broken 5 holes in the 4-mil polyethylene where the thin plastic covered the rough ends of the wall poles. Some dry, sandy earth had fallen through these holes, but no part of the roof was wholly uncovered.

The overpressure measured inside was 2 psi.

9.4 Conclusions and Recommendations

9.4.1 - Due to the amount of dry shielding earth that would be removed by the blast winds that would be produced by the sizes of nuclear weapons that menace the United States, and also due to the damage that aboveground shelters built in wooded areas would suffer from blast-buried trees, the practicality of Ridge-Pole Shelters for protection against both blast effects and fallout is severely limited. (If the earth is wet, however, blast-wind scouring by 1-kiloton blast winds at the 10-psi overpressure range removes a negligible thickness of sandy earth from a shelter with the same slope and orientation of roof.¹)

9.4.2 - Before covering this type shelter with thin plastic preparatory to covering with earth, the ends of its poles should be covered with cloth, rugs, or other stronger material.

10. DOOR-COVERED TRENCH SHELTERS AT 31 AND 15 PSI

10.1 Purpose

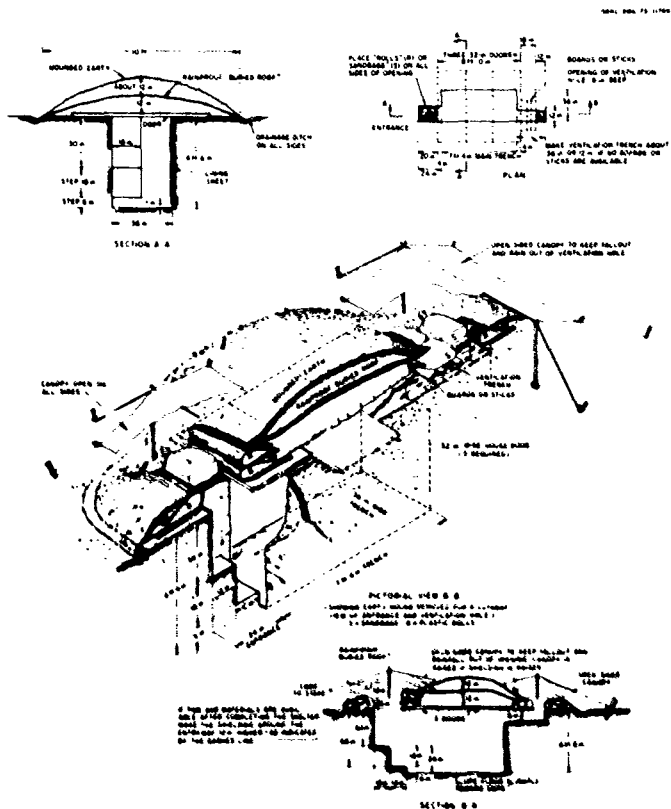
Most separate American homes have enough interior doors to roof a trench shelter for the occupants and thus provide them with much better protection against fallout radiation and fire than do the great majority of homes. In a prior DNA blast test, a Door-Covered Trench Shelter was essentially undamaged at 5 psi. Therefore, we tested this simple fallout shelter at the predicted 30- and 15-psi overpressure ranges. The test at 30 psi was carried out to learn whether or not earth arching would prevent the collapse of the hollow-core interior doors roofing a trench dug in almost rock-like earth--not to estimate the ultimate survivability of persons exposed to 30-psi blast effects in a very small open shelter.

10.2 Construction

The Door-Covered Trench Shelters at 31 and 15 psi were of identical construction, as shown by Fig. 10.1. However, a greater thickness of earth was mounded over these shelters, about 2-1/2 ft, than shown in this drawing. We had found that a hollow-core interior door can withstand being covered with earth many feet thick, since it yields under loading and protective earth arching develops in earth mounded over it.

10.3 Test Results

10.3.1 - The shelter at 31 psi was a total failure. Earth arching over the door did not prevent it from being broken in at this high overpressure. Figure 10.2 shows the depression resulting from this collapsed shelter, photographed eight days after the blast. Note the large amount of sand that had been blown into this depression during these



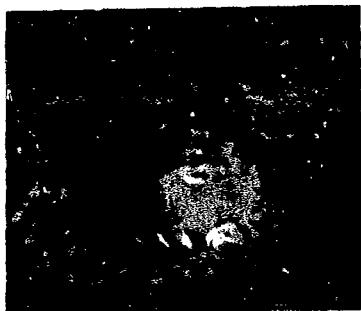


PHOTO
0703-77

Fig. 10.2. Photo of Door-Covered Trench Shelter Taken Eight Days After the Blast. The doors were smashed in. Note the sand accumulation in the right side of the hole indicative of the probability of dangerous amounts of fallout being blown into entries used as ventilation openings in blast-devastated areas.

postblast eight days. In the desert outside the blast-devastated area, the grass and desert shrubs prevented any consequential blowing of sand and dust during these same eight days. Open entries serving as ventilation openings had large amounts of sand blown into them, indicating a potential fallout-entry problem in blast devastated areas.

10.3.2 - At 15 psi the roofing doors were cracked but not broken in. (See Fig. 10.3.) However, much hard caliche was broken off the walls. The overpressure measured was 5 psi, high enough to break some occupants' eardrums.

10.4 Conclusions and Recommendations

10.4.1 - If subjected to the longer-duration overpressures and greater amplitudes of ground motions caused by strategic weapons,



PHOTO
6489-76

Fig. 10.3. Postblast Interior of Door-Covered Trench Shelter at 15 psi. Large chunks of earth were knocked off the walls. Between 16 and 24 days after the blast, the partly broken doors broke completely.

Door-Covered Trench Shelters would afford obviously inadequate blast protection at overpressure ranges considerably less than 15 psi.

10.4.2 - In blast-devastated areas, the problem of fallout particles being blown into shelters dependent for their air supply on ground-level openings could be serious.

11. CHINESE "MAN" SHELTER AT 20 PSI

11.1 Purpose

In the first Chinese handbook¹⁶ on nuclear defense that came into our hands, we saw the shelter illustrated by Fig. 11.1. Previously, we had never seen or conceived a blast shelter of this design or one built of such thin poles. If such thin poles could safely be used, it would

reduce the labor of obtaining the poles for an expedient blast shelter-- one of the chief constraints on the practicality of such shelters. Therefore, we decided to blast test this Chinese design.

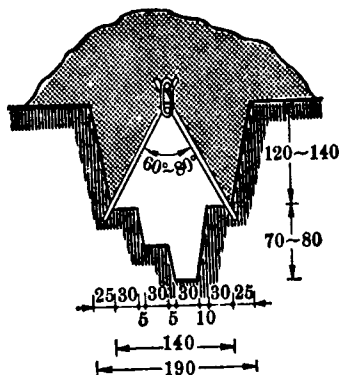


PHOTO
77-12599

图 3-107 人字形骨架避弹所

Fig. 11.1. Chinese "Man" Shelter Tested at 20 psi. This shelter is called "Man" Shelter in a Chinese civil defense handbook¹⁶ because a cross section of its frame resembles the Chinese character "人" for "man."

11.2 Construction

The main room was 10 ft long. It was made in a trench with two shelves, a bench and a 1-ft-wide foot-trench dug into the hard caliche. The sloping wall poles were first cut 6 ft 6 in. long, but later had to be reduced about 6 in. in length because their lower ends could not have been dug into the rock-like earth without breaking off large chunks of the two shelves on which the wall poles rested. The two small poles,

one below and one above where the wall poles crossed at the top of the frame, were encircled tightly with a single strand of No. 9 wire between each adjacent wall pole.

The 10-ft-long main room (see Figs. 11.2 and 11.3) plus a 5-ft-long horizontal entryway required 28 poles on each side, averaging about 3 in. in diameter, including bark. The tops of these poles averaged about 2-1/2 in., excluding bark. The horizontal entryway was of the same design as the main room, except that its entire floor was at the same level as the shelves and the bottoms of the wall poles of the main room. It led to the vertical south-end entry that, for lack of a Chinese drawing, we designed and built using the triangular construction pictured in Figs. 11.2 and 11.4. The poles of the vertical entry averaged a little over 3 in. in diameter, including bark. Above the 30-in. x 30-in. opening at the outer end of the horizontal entryway, the inside of the vertical entry was an equilateral triangle 39 in. on a side--big enough for a big man. (See Figs. 11.2 and 11.4.) The five uppermost poles averaged 4 in. in diameter, and the top three were notched and nailed together so as to make a plane on which the blast door could be closed snugly.

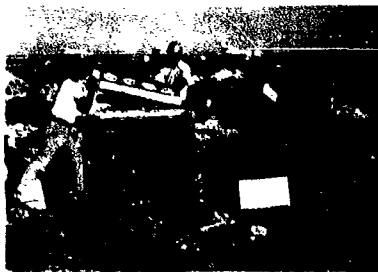


PHOTO
6464-76

Fig. 11.2. Completed Frame of Chinese "Man" Shelter Tested at 20 psi. In accord with the Chinese drawing, the poles of the main room averaged only about 3 in. in diameter. The triangular entries and triangular blast doors were of ORNL designs.

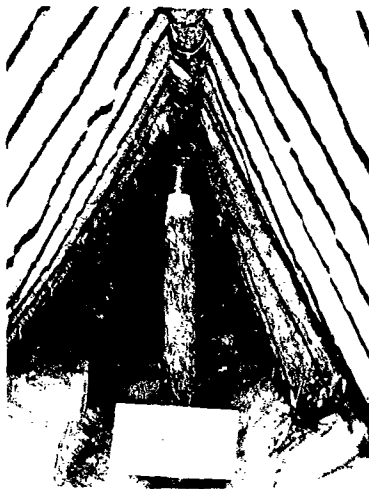


PHOTO
0698-77

Fig. 11.3. Undamaged Interior, Showing Earth Bench on One Side and Roof-Deflection Gauge on Post.

The blast door was very similar to the triangular blast doors on the Log-Covered Trench Shelters described in Section 6, except that the three frame poles of the door were smaller in diameter, and the door had six open slots and six flap valves, as shown in Figs. 11.5 and 11.6. To prevent the door and the uppermost poles of the triangular entry from being pulled up and blown away during the negative pressure phase of an explosion, the uppermost poles were wired securely to poles about 3 ft lower down the entry.

Fig. 11.7 shows the covering of the shelter frame, except for the mounding of the shielding earth. Due to a construction error, the earth was mounded 4 ft deep above the tops of the wall poles, rather than the approximate 3 ft shown by the Chinese drawing.



PHOTO
2954-77

Fig. 11.4. The Lower Part of the Vertical Triangular Entry is Pressed Horizontally Against Two Pairs of Vertical Posts. Each pair is wired together. The two pairs are held apart by two horizontal spacer poles toenailed in place to frame the rectangular opening between the horizontal and vertical parts of the entry. The pairs of vertical posts are pressed against two horizontal poles (the uppermost is shown) that in turn press against both the outermost two poles of the horizontal part of the entry and the earth in two slots dug in the sidewalls of the excavation.

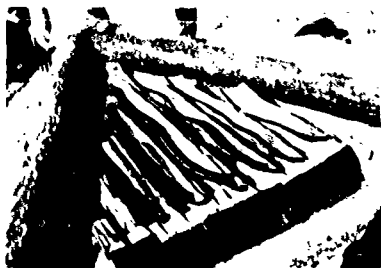


PHOTO
6467-76

Fig. 11.5. Posttest Undamaged Triangular Blast Door, Made of Three 5-in.-Diameter Peeled Poles Covered with Seven 4-in.-Diameter Peeled Poles. Between these covering poles were six 2-in.-wide ventilation slots, protected by six flap valves made of strips cut from worn tire treads.



PHOTO
6469-76

Fig. 11.6. Undamaged Triangular Blast Door, Partly Open and Viewed Looking Up the Side of the Triangular Entry to Which the Door was Hinged.



PHOTO
6466-76

Fig. 11.7. Covering the Limb-Covered Pole Frame with Bedsheets. Salt cedar limbs had first been placed crosswise over the lightly constructed pole frame.

The other (north) entry was ruggedly constructed of 6-in.-diameter vertical poles, with interior triangular braces. Its blast door was practically identical to the door on the ORNL-designed "Chinese" entry to the south end of the shelter. A rectangular expedient shelter-ventilating pump (a 20-in. x 24-in. KAP) was installed in a makeshift frame placed in the horizontal crawlway leading to the north entry.

11.3 Test Results

Contrary to our predictions, this lightly constructed shelter, tested closed, was undamaged by blast effects. The undamaged interior is pictured in Figs. 11.3, 11.8 and 11.9.



PHOTO
0701-77

Fig. 11.8. Posttest View of Opening at Bottom of Triangular Vertical Entry, Undamaged by 20-psi Blast Effects.



PHOTO
6470-76

Fig. 11.9. Postshot Condition of the Lightly Constructed Triangular Vertical Entry. The hammer rests on a step-pole. Earth arching prevented the yielding bedsheet outside from being torn.

The triangular blast-protector logs around the doors, each 8 ft long and 7 to 8 in. in diameter, were moved away from ground zero, so that a log pressed against the blast door hinges of each door. See Fig. 11.5. Both doors, however, could be opened. The blast winds scoured away about 8 to 10 in. of dry earth from around the six logs.

The blast valves on both doors obviously closed properly; a pressure rise of only 1 psi was recorded in the center of the shelter. The subsequently open valves permitted enough sand and dust to fall into the entries to have constituted a health hazard if heavy fallout had been on the ground outside. The ventilating pump and its flimsy frame were damaged slightly, but required only about 10 minutes to repair before postshot testing.

The undamaged shelter frame was moved only slightly. The top of the roof was permanently depressed 1-5/8 in. and pushed 3/4 in. away from GZ.

11.4 Conclusions and Recommendations

11.4.1 - The Chinese "Man" Shelter, if built with the ORNL-designed triangular vertical entry and expedient blast doors, is a good example of the blast protection attainable by properly building a lightly constructed shelter that yields under blast loading so as to attain effective earth arching in an adequately thick earth covering.

11.4.2 - We lack information concerning the magnitude and duration of the earth pressures produced by the blast on the wall poles--pressures that tend to collapse this A-frame structure. Therefore, we are unable even to hazard a prediction as to whether or not this closed shelter would survive the blast effects of a megaton weapon at the same 20 psi overpressure range, producing greater and much longer-lasting overpressures at depth, and ground waves of much greater amplitude.

11.4.3 - During a rapidly escalating crisis, in many wooded areas the most difficult poles to supply in adequate numbers at shelter-building sites would be the long, straight, stout poles required to make rectangular entries of blast shelters. Therefore, triangular blast entries made of short, light poles and triangular expedient blast doors should be tested at higher overpressure and longer duration.

12. RUG-COVERED TRENCH SHELTERS AT 15 AND 5.8 PSI

12.1 Purpose

Tarp-Covered Trench Shelters had been undamaged by heavy static and moving loads, including a 6-ton backhoe driven over the earth

covering a shelter of this type roofed by a cotton tarp.¹¹ Since a cotton tarp is not as strong as a piece of typical wall-to-wall carpeting made largely of strong synthetic fibers, we anticipated this shelter would withstand the blast at the 15 psi overpressure range, by facilitating earth arching.

12.2 Construction

Fig. 12.1 shows the principal design elements of a Rug-Covered Trench Shelter. The two models tested at DICE THROW had main-room trenches 40 in. wide, 6 ft deep, and 11 ft long. The roofing rugs were each 12 ft wide by 11 ft long. These rugs had a double laminated jute backing over nylon--typical low-cost wall-to-wall carpeting. No difficulties were experienced in covering the rugs with earth to a depth of 48 in. over the mid-line of the trench, nor in completing the 20-in.-wide entrances at each end. See Figs. 12.2 and 12.3.

12.3 Test Results

12.3.1 - At 15 psi, the rug was torn lengthwise on one side from end to end, and the mass of overlying earth fell into the trench. This complete failure is shown clearly by Fig. 12.4.

12.3.2 - At 5 psi, the rug was not torn, but the ground shock loosened it from the earth holding one of its edges in a side trench. As a result, the whole untorn rug and the mass of earth above it fell into the trench, to within about 18 in. of the trench floor. At this point, earth arching and the strength of the rug stopped the downward fall.

Occupants sitting in the trench would have been crushed.

12.4 Conclusions and Recommendations

12.4.1 - A Rug-Covered Trench Shelter definitely should not be built in areas likely to be subjected to blast effects.

12.4.2 - A Rug-Covered (or Tarp-Covered) Trench Shelter should only be built for fallout protection, in an area where the earth is very stable, by persons lacking other materials with which to roof an expedient trench shelter.

ORNL DRG 75-606

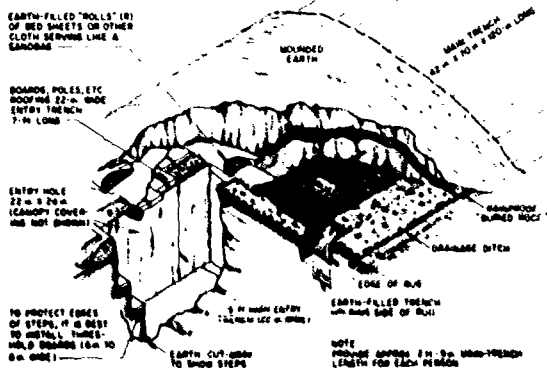
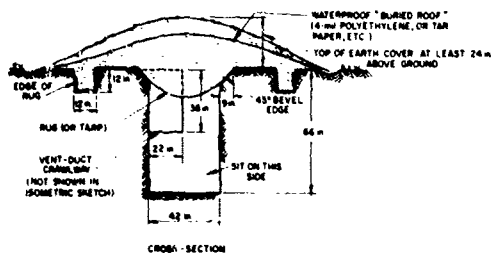


Fig. 12.1. Construction of Rug-Covered (or Tarp-Covered) Trench Shelter.



PHOTO
6490-76

Fig. 12.2. Tamping Earth over Edge of a Side-Trench of Rug-Covered Trench Shelter at 15 psi.



PHOTO
6491-76

Fig. 12.3. Dumping Earth on Side of Rug before Mounding Earth 4-ft Deep along Centerline. An earth-filled bedsheet "roll" and a pillowcase "sandbag" retained earth at each entry, pictured prior to completion.



PHOTO
6492-76

Fig. 12.4. Demolished Rug-Covered Trench Shelter at 15 psi. The edges of the rug were not pulled loose by blast effects; it was torn lengthwise.

13. SCALE MODELS OF SHELTERS

13.1 Purpose and Construction

In order to save money and to compare the resistance to blast effects of full-scale and reduced-scale shelters, the scale models listed below were tested. All scale models were built of materials as similar as practical to those of their full-scale counterparts, and linear scaling of all dimensions was used in all cases.

13.2 Test Results

13.2.1 One-Half-Scale Rug-Covered Trench Shelters at 15 psi and 5 psi.--Both were undamaged by the blast effects, whereas their full-scale counterparts failed at the same overpressure ranges. The canvas used to roof the one-half-scale models was approximately one-half as strong as the wall-to-wall carpeting used to roof the full-scale shelters. For the one-half-scale models, a fabric only one-fourth as strong should have been used, since the weight of earth supported by a 1-ft-wide

segment of the roofing fabric (measured along the edge of the trench) of the one-half-scale model is one-fourth as great as the weight of earth supported by a 1-ft-wide segment of the roofing fabric of the full-scale shelter ($1 \times 1/2 \times 1/2$ vs $1 \times 1 \times 1$). But even if we had selected roofing fabric only one-fourth as strong for the one-half-scale model, scaling would not have been satisfactory because the strength of the earth of the unsupported walls would have remained the same in both models, whereas the full-scale model to be equally strong would require earth having twice the resistance to shearing and tensile stresses.

13.2.2 - Unshored Earth Walls of Trench Shelters.--In all cases, at the same overpressure ranges the unsupported earth walls of small-scale trench shelters and of small-scale open trenches were less damaged by blast effects than were the corresponding walls of large-scale trench shelters and of large-scale open trenches. This was due to the fact that the volume of earth tending to be sheared off a trench wall by gravity and ground-shock forces increases as the cube of the increase in scale, whereas the area of the surface of the potential shearing-off of this volume increases as the square of the increase in scale. As a result of this difference, if we double all linear dimensions of a half-scale trench, then in the case of the full-scale earth wall a unit-area of the surface of potential shearing is subjected to twice the unit stresses to which a corresponding unit-area of the half-scale earth wall is subjected. Therefore, the full-scale trench wall fails first.

13.2.3 - One-Half-Scale Chinese "Man" Shelter at 31 psi.--This closed shelter (Fig. 13.1) was a one-half-scale counterpart of the Chinese "Man" Shelter tested at 20 psi, except that it had only one entry and had only one blast-protector log, which was 10 in. in diameter and secured by stakes.



PHOTO
6472-76

Fig. 13.1. One-Half-Scale Chinese Δ ("Man") Shelter Tested at 31 psi with Its Triangular Blast Door Closed. Before being covered with earth mounded as high as the blast door, the whole shelter was covered with 4-mil polyethylene.

The blast tore loose the blast-protector log. The blast winds, theoretically peaking at about 670 mph, hurled this log 180 ft, where it struck the side of the Ridge-Pole Shelter. About 10 in. of dry earth were scoured from around its entry. The earth shelves on which the lower ends of its side-poles rested were cracked, but not broken off. About 2 in. of powdery caliche earth accumulated on the floor. The height of the shelter roof was reduced only $7/8$ in.

13.2.4 - One-Tenth-Scale Chinese Δ ("Man") Shelter at 31 psi.--
This 1/10-scale model consisted only of a main room, closed at both ends with "poies," with its top at ground level. The frame was undamaged, but had been pushed into the sandy earth 2 in., reducing the ceiling height of the room from 4-1/4 in. to 2-1/4 in. (see Fig. 13.2). If a full-scale shelter built in soft earth had its poles proportionally pushed down into the earth by the 31-psi blast overpressure from a 1-MT explosion, with its duration of overpressure ten times as long as from

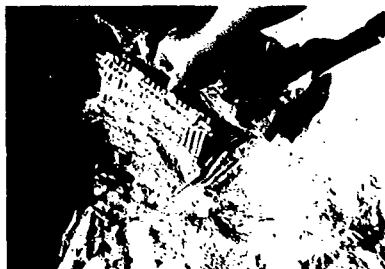


PHOTO
6473-76

Fig. 13.2. One-Tenth-Scale Room of Chinese "Man" Shelter at 31 psi, photographed Posttest. The frame had remained adequately covered, was undamaged, but had been pushed about halfway into the ground.

a 1-kiloton explosion, the intact survival of the shelter frame would be unimportant to occupants of this shelter.

13.2.5 - One-Half-Scale Log-Covered Trench Shelter at 53 psi.—This closed shelter consisted solely of a two-level room and a horizontal entry trench, counterparts of the adjacent full-scale Log-Covered Trench Shelter. Both of these shelters were built to compare the effectiveness of roofing a trench with poles laid on the surface of the ground as illustrated in Russian civil defense handbooks, as compared to the recommended Chinese procedure of placing the roofing poles on shelves well below ground level. See Fig. 13.3.

The blast damage suffered by both parts of this closed shelter indicated that occupants probably would have been injured, but was less serious than the damage suffered by its full-scale counterparts tested at 53 and 31 psi. In the Russian half, the upper parts of the earth walls were broken off, and the unbroken roof poles came to rest sloping, with a reduction of 3-3/4 in. in mid-ceiling height. In the Chinese half, the roof poles remained horizontal, although they were lowered 2-1/4 in. in the center.



PHOTO
6487-76

Fig. 13.3. Construction of 1/2-Scale Log-Covered Trench Shelter at 53 psi. The Chinese way of placing roofing poles below ground level is shown in front; the Russian way, to the rear.

13.2.6 - One-Tenth-Scale Ridge-Pole Shelter at 15 psi.--Unlike its adjacent full-scale counterpart, its entryways were undamaged. However, as shown by Fig. 9.5 of Section 9, the earth covering the side of its frame facing GZ and the tops of its entryways were completely uncovered.

13.2.7 - One-Tenth-Scale Small-Pole Shelters at 53, 106 and Approximately 180 psi.--The shelter at 53 psi was undamaged, as was its full-scale counterpart at 53 psi. The shelter at 106 psi failed; one of its two vertical entries was wrecked, and lethal overpressures apparently entered through its smashed entry (see Figs. 13.4 and 13.5). Neither of the 6-in.-deep earth covers of these 1/10-scale shelters was seriously wind-scoured. By contrast, their full-scale counterpart at 53 psi, shielded by an earth mound with slopes of 36°, lost over 8 to 12 in. of cover due to blast-wind scouring. However, the shielding earth over the 1/10-scale models was mounded with slopes of only about 10°, and the



PHOTO
6456-76

Fig. 13.4. One-Tenth-Scale Small-Pole Shelter, Pre-test at 106 psi. Earth was mounded over this shelter at slopes of about 10° to minimize blast-wind scouring. Only the plywood blast doors are visible.



PHOTO
6455-76

Fig. 13.5. One-Tenth-Scale Small-Pole Shelter, Posttest at 106 psi, Shown after Being Carefully Uncovered.

wind velocities a few inches above the quite rough ground were not as high as those striking the 5-ft-high mound over the full-scale shelter.

At the approximately 180-psi overpressure range, a 1/10-scale model of only the main room of a Small-Pole Shelter, tested closed and covered with 6 in. of unbounded sandy soil, failed. The wall poles were pushed down about one-third their heights, and the lower cross-bracing "ladder" broke, with poles left sticking upward into the living space.

13.3 Conclusions

13.3.1 - The successful testing of a reduced-scale shelter does not justify an assumption that its full-scale counterpart will survive as well in the same blast environment, especially under the dynamic loadings produced by large explosions.

13.3.2 - When the critical stresses in the test structures (including stresses in earth banks subject to failure by shear) are induced by gravity and/or the acceleration or deceleration of masses, these stresses in the model are reduced by the scale factor.

14. BLAST-HURLED DEBRIS

14.1 Purpose

Blast tests have very rarely involved simulating the conditions of urban, suburban, or wooded areas as regards the damage likely to be caused by blast-hurled debris. Structures that could easily be damaged by heavy projectiles have frequently survived shock waves and blast winds because no materials to simulate houses and trees were placed between them and GZ. See Ref. 3 for examples. Small expedient shelters, especially aboveground types and shelters with small, steeply-sloped earth coverings, could be damaged or destroyed by blast-hurled heavy projectiles such as tree trunks or the parts of houses.

Therefore, to get at least a feeling for the magnitude of this neglected problem, we secured permission to expose to the blast some fireplace-sized logs, left-over lumber, a 14-ft-high complete tree "planted" securely in the hard caliche, and three 16-ft 2 x 4's also "planted" securely. Most of the logs were stacked in a woodpile at the approximately 70-psi range, with the logs pointing toward GZ. Six logs averaging 8 in. in diameter were placed on top of the 5-ft-high mound of earth over shelters at 53 psi. The logs and boards were marked with paint of different colors, for posttest identification.

14.2 Test Results

The shock wave and blast winds hurled this debris farther than the standard blast wind velocities and theoretical calculations would lead one to believe. Most of the fireplace-sized logs came to rest 240 to 360 ft from their starting positions and seven were airborne between 360 and 640 ft. The farthest airborne, a 5-in.-diameter, 18-in.-long stick, came to rest 640 ft from the woodpile. Fourteen logs struck the 5-ft-high mound over the Log-Covered Trench Shelter at 53 psi and were imbedded in the soft earth, as pictured in Fig. 14.1. Of the 73 pieces of blast-hurled debris that were found, 33 pieces were hurled between 240 and 360 ft and came to rest between approximately the 19- and 13-psi overpressure ranges.

The 14-ft-high tamarisk (salt cedar) tree, cut and "planted" two days before and still in full leaf, was broken off at the ground. Apparently, it was broken into very small pieces, and the pieces carried far away, since we were unable to find any part of this tree. The three vertical 2 x 4's were each broken into two or more pieces, some as short as 2 ft long.

Two of the small logs were hurled end-on into the earth bank over the shelters at 53 psi and punched into the bank. See Fig. 14.2. Most of the logs apparently bounced upward on hitting this bank sloping toward



PHOTO
2653-77

Fig. 14.1. Some of the Fireplace-Sized Logs Hurlled from a Woodpile and Imbedded in the 5-ft-High Mound at 53 psi. Apparently, the blast winds of the negative phase had uncovered the two small logs in the foreground and moved them toward (Z).



PHOTO
6262-78

Fig. 14.2. Posttest Condition of the Side Facing GZ of the 5-ft-High Mound of Earth over Log-Covered Trench Shelter at 53 psi. The log sticking out of the mound had been hurled by the blast winds. The canvas had been covered with about 4 in. of earth, in a marginally successful attempt to reduce blast-wind scouring.

GZ at about 36° and were swept higher upward by the turbulent blast winds. Some came to rest when they struck shelter mounds farther from GZ, as is shown in Fig. 9.7 of Section 9.

14.3 Conclusions and Recommendations

14.3.1 - Blast-hurled debris would constitute a serious hazard to most expedient shelters built in areas of the types where most Americans live or would evacuate into during a nuclear crisis, if these areas were subjected to severe blast effects.

14.3.2 - For reasons explained in Section 17, "Limitations of the DICE THROW Tests," it is extremely difficult to estimate from this evidence (based on a 1-kiloton air blast) the much greater hazards from blast-hurled debris likely to result at the same overpressure ranges from strategic nuclear weapons.

15. EXPEDIENT WATER STORAGE

15.1 Purpose

For a shelter to be occupied for weeks in an area of severe fallout hazards, adequate drinking water must be available close at hand. The survivors in areas likely to be subjected to both blast effects and heavy fallout should not depend on normal sources of drinking water or on water stored in containers likely to leak as a result of blast effects. Therefore, we conducted the first blast tests of simple, inexpensive expedient means for storing many gallons of water per shelter occupant.

15.2 Construction and Test Results

15.2.1 - Water Stored in Plastic Bags Lining Cylindrical Pits in the Earth.¹¹ --As anticipated, lined cylindrical pits proved to be the most blast-resistant way to store water outside of blast shelters. See Fig. 15.1. Ordinary 30-gal polyethylene trash bags were used for water-proof liners. One bag was placed inside of another, since a very small

ORNL - DWG 77-10423

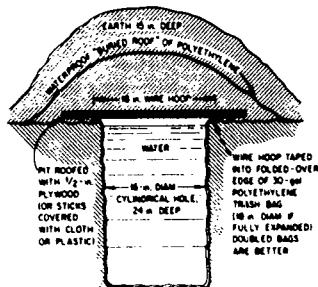
PHOTO
77-10423

Fig. 15.1. Vertical Section of Cylindrical Water-Storage Pit Lined with Waterproof Plastic Bag, or Two Bags.

fraction of polyethylene bags that are not made for water storage have pinhole leaks. Each cylindrical pit was dug so as to have a diameter about 2 in. smaller than the diameter of its waterproof liner-bag, when its liner-bag was inflated.

The best way to keep the upper edges of the pit-lining bag from slipping into a pit is illustrated by Fig. 15.2: Make a circular wire hoop the size of the mouth of the bag, and tape it into the mouth. This method was used in the water-storage pits at the 20-psi and 6.7-psi overpressure ranges. At the 53-psi range, the upper edges of doubled bags were satisfactorily held in place merely by sticking six 4-in. nails through the turned-under edges of the bags and into the very firm earth.

Before the test, the lined pits, each approximately 2 ft deep, were filled almost full, and then roofed and covered as illustrated by



PHOTO
6474-76

Fig. 15.2. Cylindrical Water-Storage Pit Lined with Two Polyethylene Trash Bags. After exposure to blast effects at 20 psi, this pit was undamaged and still full of water.

Fig. 15.1. Each lined pit contained about 20 gal of water. The earth cover was sufficiently thick to result in very effective earth arching under the blast loadings; both plywood pit-roofs were cracked but not broken. None of the three storage pits developed leaks. Even at the 53-psi range, the blast effects resulted in no caving of the pit wall.

The storage pit at 53 psi, that after the blast was left partly open to the dry desert winds, showed only 4% loss of water after 8 days. At the 20-psi range, after 24 days during which the pit was left completely open to the dry desert winds, it was about 70% full, and at 6.7 psi, the covered pit had only lost about 4% of its water after 24 days.

15.2.2 - Water Stored in One or Two Plastic Bags Used to Line a Smaller Fabric Bag or an Ordinary Pillowcase.--This method can be used to transport and store quite large volumes of water.¹¹ Two burlap potato bags, each lined with two 20-gal polyethylene trash bags, were each filled with about 10 gal of water.

One of these expedient containers was tested inside the Small-Pole Shelter at the 53-psi overpressure range. Its mouth was tied shut with a 1/4-in. cord, one end of which was then tied to a nail driven into a wall pole of the shelter, about a foot above the top of the water bag. This cord kept the mouths of the burlap bag and its double lining bags above the level of the water inside.

This water storage was unaffected by the quite severe ground shock inside the closed shelter.

Inside the open Russian Pole-Covered Trench Shelter at 20 psi, an identical water storage container was undamaged by the shock wave and blast winds that entered through the open stairway.

15.2.3 - Water Stored in Plastic-Lined Trenches.--Figure 15.3 is a postshot photo showing a lined water-storage trench at 6.7 psi. This



PHOTO
6451-76

Fig. 15.3. Postshot View of Plastic-Lined Water-Storage Pit at the 6.7-psi Overpressure Range.

trench was dug 8 ft long, 27 in. wide, and 30 in. deep, and had been lined with a 10-ft-wide sheet of 4-mil polyethylene, with its edges secured in small, earth-filled ditches. About 200 gal had filled it to within about 6 in. of full. The pit had then been covered with the pictured 3/4-in. plywood sheets. Earth had next been mounded about

30 in. deep over the plywood, incorporating a waterproof "buried roof" to keep out fallout-contaminated rain water. The resulting cross-sectional profile was similar to that shown in Fig. 15.1.

Ground shock resulted in some earth caving off the edges of the long sides of the trench, but no puncturing of the plastic lining resulted. Eight days after the blast, this side-wall caving had increased, but the trough still held a calculated 190 gal of water.

At the 20-psi range, a similar lined water-storage pit was badly damaged by side-wall caving, although earth-arching saved its roof. Before it could be examined after the blast, almost all of its approximately 200 gal of water had leaked out.

15.3 Conclusions

15.3.1 - If blast is expected in a shelter area, plastic-lined cylindrical pits, filled almost full and protected from blast and contamination as illustrated in Fig. 15.1, would usually be the most practical method of expedient water storage.

15.3.2 - Inside blast shelters, sufficient water for several days should be stored in fabric bags lined with larger plastic bags.

16. EXPEDIENT VENTILATION OF BLAST SHELTERS

16.1 Purpose

Expedient shelters that afford good protection against both blast and fallout have small entries, usually vertical. Such entries result in inadequate natural ventilation when a wind is not blowing. In hot weather, especially if it is humid, even with a breeze outside, a fully-occupied shelter can become dangerously or lethally hot and humid. Furthermore, we recognized the fact that air-intake and air-exhaust openings at ground level, if used for air supply in a blast-devastated area contaminated with heavy fallout, might have dangerous amounts of fallout blown into them. See Fig. 10.1 in Section 10.

The problem of pumping sufficient air through expedient blast valves of the types described earlier in this report needed investigation.

16.2 Observations, Construction and Test Results

Intermittently during the three weeks following the main event, we observed the amount of sand and dust that was added to the amount that came through the poorly-positioned blast valves in blast doors. Although in an area of very heavy fallout the amount that entered through these valves could prove serious, much more fell into the open entries of the shelters not partially protected by blast doors and the blast-protector logs around them.

The Small-Pole Shelter at 53 psi, which had solid plywood doors that had to be left partly open to secure adequate ventilation, presented a special problem. In an attempt to keep sand particles out, we built an improvised one-foot-high "wall" of sticks covered with polyethylene around the vertical entry, inside the blast-protector logs, and over the whole entry we erected an expedient tent. These measures reduced by about 60% the amount of sand subsequently blown into the shelter. However, if the area had been covered with heavy fallout, it would have been clearly impractical to work outside to install this "wall" and tent, even if all parts of the "wall" and tent had been carefully made to fit the opening before the blast, and stored inside the shelter for postattack use.

Postblast ventilation tests, using expedient KAPs and making air velocity measurements with a Hastings anemometer, yielded the following results:

(a) In the Log-Covered Trench Shelter at 53 psi, using a 20-in.-wide x 36-in.-high KAP (see Fig. 16.1), 412 cubic feet per minute (cfm) were pumped through the shelter when its blast doors were open; 177 cfm were pumped through the shelter with its two blast doors closed, with the air flowing through the blast valves. In each case a deduction was

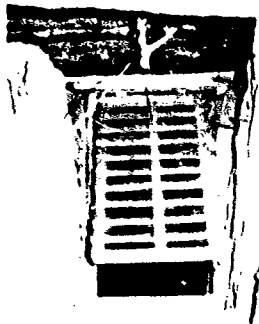


PHOTO
6182-76

Fig. 16.1. Expedient Shelter-Ventilating Pump (a 20-in. x 36-in. KAP) in an entry of the Log-Covered Trench Shelter at 53 psi. Tested preblast, it pumped 177 cfm through the valves of the two closed blast doors and 412 cfm with the doors open. This entry was demolished by blast effects.

made for the small measured volume of air that moved through the shelter during times when the wind was blowing outside. Each door had blast valves with openings totaling about 80 sq. in. in cross-sectional area.

(b) In the Chinese "Man" Shelter at 20 psi, using a 20-in.-wide x 24-in.-high KAP (see Fig. 16.2), with the two triangular blast doors open, 150 cfm were pumped through the shelter with the blast doors open; 240 cfm were pumped through the blast valves with the blast doors closed. Each door had valves with openings totaling about 115 sq. in. A gusty wind outside made these measurements less reliable, probably on the high side.

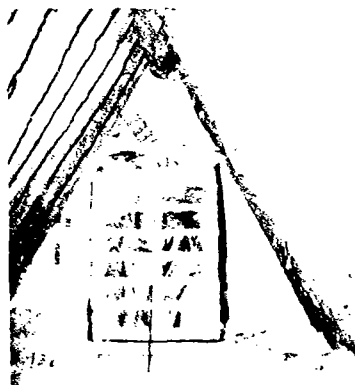


PHOTO
6142-76

Fig. 16.2. Expedient KAP (20 in. x 24 in.) Tested in the Chinese "Man" Shelter at 20 psi, After the Blast.

(c) In the Small-Pole Shelter at 53 psi, using a 29-in.-wide x 36-in.-high KAP when there was no wind outside, 861 cfm were pumped through the shelter while the two solid blast doors were each open about 1 ft, providing two openings each about 5 sq. ft in cross-sectional area. The fallout-protective "walls" and expedient tent were around and over the air-intake entry during this test. (A similar test conducted before the blast, but with the doors completely open, resulted in a measured airflow of 876 cfm.) See. Fig. 4.6.

16.3 Conclusions and Recommendations

16.3.1 - Blast valves in blast doors are impractical. If valves of the type tested are mounted in separate vertical ventilation shafts, as was done in the ORNL tests in DNA's MIXED COMPANY main event (see Ref. 1), the entry of fallout particles appears likely to be reduced

below dangerous levels. Ways to build expedient ventilation shafts that do not require heavy lumber should be developed and tested.

16.3.2 - Except in extremely hot and humid weather, an air supply of about 10 cfm per shelter occupant is enough to maintain tolerable conditions during continuous occupancy for several days. Therefore, even a KAP as small as 20 in. x 24 in. would usually prove adequate for a 15-man shelter protected by blast valves having total openings as large as those of the blast valves tested in DICE THROW (around 100 sq. in.) but installed in separate air-intake and air-exhaust ventilation shafts.

16.3.3 - Simple, expedient equipment to enable shelter occupants to raise ventilation air-intake and air-exhaust openings above ground level after the blast, and at the same time to quickly seal off the rest of the entries, should be developed and tested.

16.3.4 - For use in prefabricated blast shelters or in blast shelters that may be built in normal times or during slowly worsening crises, ventilation pipes that are installed with their upper ends safely below the earth until after the blast, and that can be raised by a jack above ground level after the blast, should be developed and blast tested. (Since DICE THROW, we have designed and built a prototype of such an extendable ventilation pipe, and also a manually operated, homemade suction pump capable of pumping around 60 cfm through a 3- or 4-in. pipe.)

17. LIMITATIONS OF THESE DICE THROW TESTS

Caution should be used in extrapolating from the results of these DICE THROW tests to estimate the survivability of expedient shelters--especially those built in typical urban, suburban or wooded areas--if subjected to the blast effects of a large nuclear weapon, for the following reasons:

a. This blast was small, with airblast effects roughly equivalent to a 1-kiloton nuclear explosion. At locations receiving the same peak overpressures from a multimegaton surface burst, much more severe blast effects would result, because:

(1) The duration of the overpressures and the dynamic overpressures would be much longer (20 times as long from an 8-MT explosion),³ and the energy transmitted to structures on and below the surface could be many times greater. At the same maximum overpressure ranges, the resulting destructive effects from an 8-MT explosion on deeply buried parts of shelters and the unshored earth walls of shelters would be greater. Also the earth-flow phenomena observed (to a relatively minor extent in some of these DICE THROW tests) would certainly increase in some areas.

(2) The damages due to ground shock would be more extensive due to the greater amplitude of the ground wave and (in the case of an 8-MT burst) to the 20-fold greater distances from ground zero to a given overpressure range. These greater distances usually would permit the ground shock to arrive at the ranges of interest up to hundreds of ms in advance of the air shock wave; this difference between arrival times would cause the shelter roof supports to be accelerated upward before any downward forces from the airborne shock wave could cause downward movement of the earth covering a shelter. The vertical amplitude of such initial ground-shock (ground-wave) effects can be several inches, and the inertial mass response of the earth covering a shelter roof would thus cause the roof members to be bowed downward, to an extent not observable in high-explosive tests of similar shelters at similar overpressure ranges.

(3) Earth scouring of above-grade mounds by the blast winds (that from an 8-MT explosion would blow for about 20 times as long as from this "1-kiloton" DICE THROW shot) could be much greater

depending on the contour of the mound. Especially if the shielding earth were dry, such long-duration blast winds could blow away much of the shielding earth mounded above ground level over a shelter, possibly reducing its usefulness as a fallout shelter.

(4) Blast-hurled heavy projectiles--including the trunks of large trees and parts of houses and other structures--can be accelerated by a 1-kiloton explosion to velocities only a small fraction of those to which the same objects, if at the same overpressure range, would be propelled by a multimegaton explosion. Persons estimating blast damage should remember that an object's kinetic energy varies as the square of its velocity. Furthermore, a hurled object 10 times as large as a small object having the same velocity, density, and relative proportions, and impacting in the same relative position on a fixed object, delivers 10 times the amount of energy per square inch of impact area. Therefore, the impact damage to be expected from large objects accelerated by a multimegaton blast cannot be accurately estimated from the results of experiments like those at DICE THROW nor from the damage caused by blast-displaced heavy objects at Hiroshima and Nagasaki.

b. Blast tests of scale models of shelters can give misleading results regarding the survivability of full-scale shelters subjected to the same blast effects. In the DICE THROW tests, all of the reduced-scale models of shelters withstood blast effects better than the corresponding full-scale shelters. For example, the half-scale Rug-Covered Trench Shelters tested at the 15- and 5.8-pai range both were undamaged, whereas the full-scale models both failed at the same overpressure ranges.

c. The earth was extremely stable in the DICE THROW test area. At almost all of the ORNL DICE THROW shelter sites, at depths of only a few inches the sandy desert soil changes to very stable caliche. At the 53- and 31-pai ranges, the hardness of this soil largely composed of sand grains cemented together with gypsum approached that of a very soft

limestone rock. Thus if shelters were built in typical habited areas--that have much less stable soils--and were subjected to blast effects similar in magnitude to those at DICE THROW, the collapse of the unshored walls of trench shelters, the pressures exerted on deeply buried parts of shelters, and the earth-flow effects would all have been more pronounced and damaging.

18. PRINCIPAL CONCLUSIONS AND RECOMMENDATIONS

18.1

Expedient shelters of the types tested--especially if the ones with shored walls are equipped with blast doors--would afford better protection against the blast and fire effects of nuclear weapons and much better fallout protection than do all but a small fraction of existing buildings.

18.2

Ground-shock effects--not overpressure effects--would cause the failure of most expedient shelters with sufficient earth covering to assure effective earth arching. (In order to assure effective earth arching, the earth covering should be at least one-half as thick as the free span of the shelter roof. Also the roof and/or the whole structure must yield when loaded--thus causing the resultant earth arching around the structure to bear most of the load.)

18.3

Even in very stable ground, unshored trench shelters would be unsafe if subjected to the blast effects of large nuclear explosions at overpressure ranges of more than about 7 psi.

18.4

When roof cover is adequate to assure earth arching, flexible poles considerably smaller in diameter than those used to roof the ORNL unshored shelters should prove adequately strong.

18.5

Shelters likely to be subjected to blast effects should be built, whenever practical, with their roofs far enough below ground so that the tops of their entrances are no more than a foot above ground level. This positioning would greatly reduce blast damage and the removal of shielding earth by blast winds.

18.6

Expedient blast doors--especially doors made of poles and of triangular design--can be readily built strong enough to withstand as severe blast effects as the strongest expedient shelters tested to date.

18.7

Since the ground shock and earth flow effects from large nuclear weapons were not well simulated by the DICE THROW blast, expedient shelters and their life-support equipment should be tested under conditions producing much more severe blast effects on below-ground structures. The Air Force Weapons Laboratory's 125-kiloton Dynamic Air Blast Simulation (DABS) test planned for April 1978 should provide a realistic blast environment.

18.8

Means for assuring adequate and safe ventilation-cooling of shelters after they have been subjected to severe blast effects is the most neglected essential component of shelter design. Simple air-intake and air-exhaust openings, that shelter occupants could raise above ground level after the blast and that would enable them to pump sufficient air through their shelter while excluding dangerous amounts of fallout, should be developed and blast tested.

REFERENCES

1. Cresson H. Kearny and Conrad V. Chester, Basic Tests of Expedient Shelters, ORNL-4905, (January 1974).
2. R. W. Manweiler, C. V. Chester, and C. H. Kearny, Measurement of Shock Overpressure in Air by a Yielding Foil Membrane Blast Gauge, ORNL-4868, (September 1973).
3. Samuel Glasstone, ed., The Effects of Nuclear Weapons, U.S. Atomic Energy Commission, U.S. Government Printing Office, Washington, D.C., (April 1962).
4. C. H. Kearny, "Hasty Shelter Construction Studies," Annual Progress Report, Civil Defense Research Project, March 1970-March 1971, ORNL-4679, (March 1972).
5. Exercise Laboratory Shelter: After Action Report, Headquarters XVIII Airborne Corps. and Ft. Bragg, Ft. Bragg, N.C., (December 1972).
6. P. T. Egorov, I. A. Shyakhov, and N. I. Alabin, Civil Defense, Moscow, 1979, ORNL-TR-2793, (December 1973).
7. G. A. Crilly and C. H. Kearny, Expedient Shelter Handbook, ORNL-4941 (August 1974).
8. C. V. Chester and R. O. Chester, "Analysis of Effects of Nuclear Weapon Overpressures on Hasty Pole Shelters," Annual Progress Report, Civil Defense Research Project, March 1971-March 1972, ORNL-4784, (December 1972).
9. Archie P. Flynn, Operation Buster, WT-359, Federal Civil Defense Administration, Washington, D.C., (March 1952).
10. Joseph B. Byrne, Effects of an Atomic Explosion on Underground and Basement Types of Home Shelters, WT-801, Federal Civil Defense Administration, Washington, D.C., (October 1953).

11. Cresson H. Kearny, Expedient Shelter Construction and Occupancy Experiments, ORNL-5039, (March 1976).
12. Cresson H. Kearny, How to Make and Use a Homemade, Large-Volume Efficient Shelter-Ventilating Pump, the Kearny Air Pump, ORNL-TM-3916, (August 1972).
13. N. I. Akimov et al., Civil Defense, Moscow 1969, ORNL-TR-2306, edited by J. S. Gailar and C. H. Kearny, (April 1971).
14. V. I. Molodykh et al., Antiradiation Shelters in Rural Areas, Moscow 1972, ORNL-TR-2745, edited by Cresson H. Kearny and Joanne S. Gailar, (October 1973).
15. G. K. Kotlukov et al., Civil Defense, Moscow 1976, translated by Defense Civil Preparedness Agency, Washington, D.C., (1977).
16. Chinese Civil Defense, ORNL/TR-4171, edited by C. V. Chester and C. H. Kearny (to be published).

**28. EXPERIMENTAL STUDY OF AIRCRAFT
STRUCTURAL RESPONSE TO BLAST -
DICE THROW PROJECT NO. 118**

by

**Rudolf Friedberg and Peter Hughes
Naval Weapons Evaluation Facility**

ABSTRACT

In a continuing effort to improve the survivability of aircraft to nuclear overpressure effects, the Naval Weapons Evaluation Facility (NWEF) fielded three parked A-4C aircraft in the Defense Agency (DNA) sponsored DICE THROW high-explosive event. This test shot, simulating a 4.2 TJ (1 KT) nuclear surface burst, was detonated 6 October 1976. The primary objectives of the NWEF experiment were to provide overpressure response data on parked aircraft structures and compare this test data with analytic predictions. These objectives were met through tape recorded pressure load and structural response data on a variety of structural elements.

Complete verification of the predictive techniques is necessarily a statistical problem; however, within the scope of this present effort, the specified accuracy of the analytic procedures have been verified.

This report points out some significant problems in the areas of computer modeling of a true-to-life structure and in the use of classical reflected blast loading for complex non-idealized shapes.

The three increasingly sophisticated analytic methods from the DNA-2048 Handbook, accordingly, give more accurate predictions; however, each is more time consuming and costly to implement. One method is not recommended over another because the analyst must make the trade-off of accuracy versus cost.

The test is assessed as an excellent means for observing various modes of structural response to overpressure. Considerable data has been compiled on (1) pressure loading, (2) structural response of panels, longerons and frames, (3) rigid body motion and tiedown restraining forces and (4) synergistic effects of overpressure and gust. This data is available, with DNA approval, for more detailed correlations and predictions of aircraft vulnerability.

THIS PAGE INTENTIONALLY LEFT BLANK

TABLE OF CONTENTS

	<u>Page</u>
Abstract	iii
Abbreviations and Acronyms	xv
Introduction	1
Objectives	3
Test Layout	5
Aircraft Configuration	9
Test Instrumentation	15
Instrumentation Description	15
Strain Gages	15
Pressure Gages	16
Deflection Gages	16
Stress Coat	17
Motion Picture Cameras	17
Load Cells	18
Selection of Structural Elements	18
Instrumentation Layout.	20
Strain Gages	20
Pressure Gages	32
Deflection Gages	32
Stress Coat	34

	<u>Page</u>
Motion Picture Cameras	34
Load Cells	35
Test Results	43
General	43
Damage Description	43
Aircraft BUNO 149558	43
Aircraft BUNO 145062	44
Aircraft BUNO 145074	52
Damage Assessment	52
Instrumentation Data	60
Analysis	63
Analytic Procedures	63
Method 1	63
Method 2	64
Method 3	68
Results Correlation	73
Method 1	73
Method 2	78
Method 3	84
Aircraft Rigid Body Motions	148
Nuclear Test Data Correlation	155
Conclusions	159
General Test Data	159

	<u>Page</u>
Method 1 - Assessment.	162
Method 2 - Assessment.	162
Method 3 - Assessment.	163

Appendices

A - Loading and Response Predictions for Testing an F-4 Trailing Edge Flap in PRE-DICE THROW II Event	167
B - Experimental Results of F-4 Trailing Edge Flap PRE-DICE THROW II Event.	185
References	199

FIGURES

1. Scenario Layouts	7
2. A-4C Aircraft Configuration - Side View . . .	10
3. Aircraft Support Platform	11
4. Tiedown Details	13
5. Tiedown Details	14
6. Load Cell - Exploded View	19
7. Instrumented Panel Location Diagram	21
8. Strain Gage Instrumentation Layout - Panel 1.	23
9. Strain Gage Instrumentation Layout - Panel 2.	24
10. Strain Gage Instrumentation Layout - Panel 3.	25
11. Strain Gage Instrumentation Layout - Panel 4.	26
12. Strain Gage Instrumentation Layout - Panel 5.	27
13. Strain Gage Instrumentation Layout - Panel 6.	28

14.	Strain Gage Instrumentation Layout - Panel 7.	29
15.	Strain Gage Instrumentation Layout - Panel 8.	30
16.	Strain Gage Instrumentation Layout - Fuselage Frame Station 277	31
17.	Deflection Gage Installation Diagram	33
18.	Catastrophic Failure of A/C BUNO 145074 Under 62.1-kPa Peak Free-Field Overpressure .	36
19.	Fuselage Damage - General View A/C BUNO 149558 Starboard Side.	37
20.	Rudder Hinge Failure - A/C BUNO 149558	38
21.	Engine Inlet Damage - A/C BUNO 149558 Starboard Side	39
22.	Aft Fuselage Damage - A/C BUNO 149558 Starboard Side	40
23.	Fuselage Damage Aft of F. STA 306 - A/C BUNO 149558 Starboard Side	41
24.	Mid-Fuselage Damage - A/C BUNO 149558 Starboard Side	42
25.	Frame Joint to Lower Longerons Failure - A/C BUNO 149558, Starboard Side	45
26.	Stiffener Damage - A/C BUNO 149558 Starboard Side	46
27.	Former Damage - A/C BUNO 149558 Starboard Site	47
28.	Aft Fuselage Damage - A/C BUNO 145062 Starboard Side	48
29.	Mid-Fuselage Damage - A/C BUNO 145062 Starboard Side	49
30.	Flange Failure, Frame STA 277 A/C BUNO 145062, Starboard Side	50

	<u>Page</u>
31. Aft Fuselage Damage - A/C BUNO 145062 Starboard Side	51
32. Canopy Failure - A/C BUNO 145074	53
33. Engine Inlet Damage - A/C BUNO 145074	54
34. Longeron No. 5 Rupture - A/C BUNO 145074	55
35. Lower Longeron Failure, Starboard Side A/C BUNO 145074	56
36. Lower Longeron Failure, Port Side - A/C BUNO 145074	57
37. Lower Longeron Section - Configuration Diagram	69
38. Sure-Safe Envelope, Method 1	75
39. Sure-Kill Envelope, Method 1	76
40. Strain Data Correlation for Panel 1 - Location A. NOVA 2 - DEPROP Solution	86
41. Strain Data Correlation for Panel 1 - Location B. NOVA 2 - DEPROP Solution	87
42. Strain Data Correlation for Panel 1 - Location C. NOVA 2 - DEPROP Solution	88
43. Strain Data Correlation for Panel 4 - Location A. NOVA 2 - DEPROP Solution	89
44. Strain Data Correlation for Panel 4 - Location B. NOVA 2 - DEPROP Solution	90
45. Strain Data Correlation for Panel 5 - Location A. NOVA 2 - DEPROP Solution	91
46. Strain Data Correlation for Panel 5 - Location B. NOVA 2 - DEPROP Solution	92
47. Strain Data Correlation for Panel 5 - Location C. NOVA 2 - DEPROP Solution	93

	<u>Page</u>
48. Strain Data Correlation for Panel 6 - Location A. NOVA 2 - DEPROP Solution	94
49. Strain Data Correlation for Panel 6 - Location B. NOVA 2 - DEPROP Solution	95
50. Strain Data Correlation for Panel 1 - Location A. NOVA 2 - KADBOP Solution	96
51. Strain Data Correlation for Panel 1 - Location B. NOVA 2 - KADBOP Solution	97
52. Strain Data Correlation for Panel 1 - Location C. NOVA 2 - KADBOP Solution	98
53. Strain Data Correlation for Panel 4 - Location A. NOVA 2 - KADBOP Solution	99
54. Strain Data Correlation for Panel 4 - Location B. NOVA 2 - KADBOP Solution	100
55. Strain Data Correlation for Panel 1 - Location A. NOVA 2 - KADBOB-A Solution (Ref. Table 7)	101
56. Strain Data Correlation for Panel 1 - Location B. NOVA 2 - KADBOB-A Solution (Ref. Table 7)	102
57. Strain Data Correlation for Panel 1 - Location A. NOVA 2 - KADBOB Solution	103
58. Strain Data Correlation for Panel 1 - Location B. NOVA 2 - KADBOB Solution	104
59. Strain Data Correlation for Panel 4 - Location A. NOVA 2 - KADBOB Solution	105
60. Strain Data Correlation for Panel 4 - Location B. NOVA 2 - KADBOB Solution	106
61. Strain Data Correlation for Panel 5 - Location A. NOVA 2 - KADBOB Solution	107
62. Strain Data Correlation for Panel 5 - Location B. NOVA 2 - KADBOB Solution	108

	<u>Page</u>
63. Strain Data Correlation for Panel 6 - Location A. NOVA 2 - KADBOB Solution	109
64. Strain Data Correlation for Panel 6 - Location B. NOVA 2 - KADBOB Solution	110
65. Strain Data Correlation for Panel 8 - Location A. NOVA 2 - KADBOB Solution - Simply Supported Edges	111
66. Strain Data Correlation for Panel 8 - Location A. NOVA 2 - KADBOB Solution - Clamped Edges	112
67. Strain Data Correlation for Panel 8 - Location B. NOVA 2 - KADBOB Solution - Clamped Edges	113
68. Analytic and Experimental Overpressure Profiles for Panel 1	114
69. Analytic and Experimental Overpressure Profiles for Panel 4	115
70. Analytic and Experimental Overpressure Profiles for Panel 5	116
71. Analytic and Experimental Overpressure Profiles for Panel 6	117
72. Analytic and Experimental overpressure Profiles for Panel 8	118
73. Strain Gage No. 5 Data - Panel 1	120
74. Strain Gage No. 9 Data - Panel 1	121
75. Strain Gage No. 27 Data - Panel 4	123
76. Strain Gage No. 28 Data - Panel 4	124
77. Strain Gage No. 31 Data - Panel 5	125
78. Strain Gage No. 43 Data - Panel 5	126
79. Strain Gage No. 1 Data - Panel 1	127

80.	Strain Gage No. 24 Data - Panel 4	128
81.	Strain Gage No. 22 Data - Panel 4	129
82.	Strain Gage No. 23 Data - Panel 4	131
83.	Strain Data Longeron 5, Support NOVA 2 - DEPROB Solution	137
84.	Strain Data Correlation - Longeron 5, Mid-Span, NOVA 2 - DEPROB Solution	138
85.	Strain Data Longeron 5, Support NOVA 2 - KADBOB Solution	139
86.	Strain Data Correlation - Longeron 5, Mid-Span, NOVA 2 - KADBOB Solution	140
87.	Fuselage Frame STA 277, Configuration.	141
88.	Predicted Strains at Frame STA 277 Support, Section RR (Fig. 87, Ref.).	144
89.	Strain Data Correlation Fuselage Frame STA 277, Section AA	145
90.	Strain Data Correlation Fuselage Frame STA 277, Section III	146
91.	Strain Data Correlation Fuselage Frame STA 277, Section MM	147
92.	Lateral Translation at Aircraft CG - BUNO 149558	149
93.	Roll of A/C BUNO 149558	150
94.	Yaw of A/C BUNO 149558	151
95.	Lateral Translation of Aircraft CG - BUNO 145074	152
96.	Roll of A/C BUNO 145074	153
97.	Yaw of A/C BUNO 145074	154

	<u>Page</u>
A-1. Trailing Edge Flap	168
A-2. Trailing Edge Flap Upper and Lower Torque Box Skin Diagram	169
A-3. Instrumentation Location Diagram	170
A-4. Rib Assembly x_p 72.750	171
A-5. Pressure Loading Normal to Panel Surface	173
A-6. Pressure Loading Assumed for Upper and Lower Rib Surfaces	176
A-7. Maximum Strain vs Reflected Overpressure for Skin Panel	178
A-8. Comparison of Skin Panel Edge Strains, Outer Surface.	179
A-9. Comparison of Skin Panel Center Strain, Inner Surface.	180
A-10. Comparison of Skin Panel Center Deflections	181
A-11. Maximum Strain vs Reflected Overpressure for Rib	183
B-1. F-4 Flap - Structure Configuration Diagram	186
B-2. Instrumentation Location Diagram - F-4 Flap Upper Skin Outer Surface.	187
B-3. Instrumentation Location Diagram - F-4 Flap Upper Skin Inner Surface.	188
B-4. Test Setup.	190
B-5. Local Pressure Data - Pressure Gage No. 1 (Gage location shown in Fig. B-2)	191
B-6. Rib Gages Response	195

	<u>Page</u>
TABLES	
1. Strain Gage Instrumented Panels Geometry Data	22
2. Predicted Free-Field Airblast Parameters. .	58
3. OVPR2 Solution for Panels 1, 5, and 6 Sure-Safe Condition Listing of Input and Output Data	66
4. OVPR2 Solution for Longerons 5 - Sure-Safe Condition Listing of Input and Output Data.	67
5. OVPR2 Solution for Lower Longerons - Sure-Kill Condition Listing of Input and Output Data	70
6. OVPR2 Solution for Fuselage Frame - Sure-Safe Condition, Listing of Input and Output Data	71
7. Chart of the NOVA 2 Solution Runs	74
8. Peak Experimental Strain Data Summary for Panels 1 through 8	79
9. Correlation of the Analytic Strains Obtained from NOVA-2 Solutions and the Experimental Strains: Skin Panels - Maximum Response Data Summary	133
10. Section Dimensions Data Fuselage Frame STA 277	142
11. Energy Absorption by the Tiedown Load Cells Following Blast Intercept	156
A-1. Instrumentation Plan	184
B-1. Experimental Strain Data, First Cycle Response	192
B-2. Experimental Strain Data, Maximum Response.	194
B-3. Strain Data Correlation	197

ABBREVIATIONS AND ACRONYMS

A/C	aircraft
ANFO	ammonium nitrate fuel oil (mixture)
BUNO	bureau number
C	Celcius (degrees)
dc	direct current
DEPROB	Dynamic Elastic Plastic Response of Beams (code)
DEPROP	Dynamic Elastic Plastic Response of Panels (code)
DNA	Defense Nuclear Agency
E	Young's Modulus of Elasticity
FM	frequency modulation
ft	foot
ft-lbs	foot-pound force
Fty, Fy	tensile yield stress
g	grams
G	shear modulus
GPa	gigapascal (10^9 Pa)
GZ	ground zero
Hz	hertz
in.	inch
J	joule
kHz	kilohertz (10^3 Hz)
kJ	kilojoules (10^3 J)
kN	kilonewton (10^3 N)

kPa	kilopascal (10^3 Pa)
KT	kiloton (10^3 metric tons (2208 lb))
lb	pound
lbf	pound-force
m	meter
mm	millimeter (10^{-3} m)
Mg	megagram (10^6 g)
MPa	megapascal (10^6 Pa)
ms	millisecond (10^{-3} s)
mV	millivolt (10^{-3} V)
N	newton
NOVA	Nuclear Overpressure Vulnerability Analysis (code)
NSWC/WOL	Naval Surface Weapons Center, White Oak Laboratory
NWEF	Naval Weapons Evaluation Facility
Pa	pascal
psi	pounds per square inch
s	second
t	time
TJ	terajoule (10^{12} J)
V	volt
WSMR	White Sands Missile Range
µin/in	microstrains (microinch per inch)
ε	strain
ν	Poisson's ratio

INTRODUCTION

The determination of aerospace structural response and vulnerability to nuclear blast effects under sure-safe and sure-kill criteria are the subjects of numerous analytic methods which have been developed for that purpose.

More recently, considerable effort has been spent on experimental studies which involved structural elements subjected to blast effects (Ref. 1). These studies, conducted on structural elements which were fabricated and tested under rigidly controlled conditions, provided useful results for correlating experimental and analytic data. This offered a measure of success in efforts to verify the validity of the analytic methods. The level of success varied, of course, with the accuracy of structural modeling, the blast representation, and the general sophistication of the analytic methods employed.

Despite these efforts, the pertinent questions which remain largely unanswered are:

1. How accurately does an idealized test structure represent a "true-to-life" airframe of an aerospace vehicle?
2. How does the response of a structural element incorporated within the aircraft structure compare to the response of an isolated, representative structural element when both are subjected to the same blast environment? - i.e., can an entire structure be modeled by a few representative elements?
3. Do current analytic techniques for airblast vulnerability accurately predict structural damage?

The Defense Nuclear Agency (DNA) sponsored DICE THROW program, which culminated in the detonation of a 564-metric-ton ammonium-nitrate-and-fuel-oil (ANFO) charge (4.2 TJ or 1 KT nuclear blast equivalent) on 6 October 1976, offered a unique opportunity for an experimental study of a complete aircraft structural response to a blast environment. Within the framework of that program, under DNA contract the Naval Weapons Evaluation Facility (NWEF) fielded three A-4C aircraft with the primary objective to obtain experimental data

of the structural response to overpressure for correlation with the analytic data derived from computer methods presented in the DNA-2048H-1 handbook (Ref. 2).

The description of the test program and the pertinent analyses and subsequent correlation of the experimental and analytic data are the subjects of this report.

OBJECTIVES

The primary objective of the DICE THROW Project No. 118 study was to experimentally verify the overpressure analysis techniques contained in the "Handbook for Analysis of Nuclear Weapon Effects on Aircraft," DNA-2048H-1 (Ref. 2). Subordinated to this broadly defined overall objective, several intermediate objectives were formulated as follows:

1. To collect experimental data from a suitably instrumented A-4C aircraft subjected to a blast environment generated by the detonation of the ANFO charge which closely simulated a 4.2-TJ (1 KT) nuclear detonation.
2. To conduct appropriate analyses of the aircraft structural response to overpressure using the three analytic methods described in the handbook.
3. To correlate of the experimental and analytic data in order to determine the degree of agreement between the predicted and the actual response of the aircraft structure to overpressure, i.e., the actual verification procedures.

In keeping with the scope of these methods, the instrumentation system for the experimental data collection was designed to provide pressure, strain, and deflection data which could be directly correlated with the analytic data.

An experimental program of this magnitude presented unique opportunities, and two secondary objectives were postulated:

1. To determine the actual aircraft motion during the positive phase of the blast.
2. To assess the resulting impulse absorbed by the aircraft.

These secondary objectives were realized through analyses of the motion picture records in conjunction with the data obtained from the calibrated load cells incorporated in the aircraft tiedown system.

In addition to these clearly defined objectives, the test was seen as a means of obtaining specimens for future studies on the effects of changes in the aerodynamic characteristic of the aircraft structure. It was envisioned that the aircraft components which sustained damage approaching a catastrophic failure, for example, extensive buckling of a skin panel, could be used in a test designed to determine the aerodynamic drag increase related to the sustained permanent deformation.

An extension of the data correlation objective to the relevant data which were obtained from past nuclear tests was also included among the objectives. It promised to provide an informative comparison survey of the available experimental data.

TEST LAYOUT

The definition of the test layout, i.e., positioning the aircraft with respect to ground zero (GZ), presented a singular problem arising from the lack of reliable data on the actual vulnerability of aircraft structures to overpressure. This was compounded by the fact that, in line with the objectives of this project, the desired structural response called for an overpressure level sufficient to produce permanent damage to the structural elements selected for instrumentation. Even more severe local damage, short of catastrophic failure, was considered necessary to provide adequate means for assessing the drag increase resulting from changes in the aerodynamic characteristics of the structure as a whole.

Earlier participation by NNEF in the PRE-DICE THROW II Event, described in Appendices A and B, consisted of a test on an instrumented F-4 wing trailing edge flap and was envisioned as the means for

1. An initial endeavor to correlate analytic and experimental overpressure induced structural response.
2. Shakedown and debugging of test instrumentation.

The NNEF test was only partly successful, even though it produced satisfactory experimental data. However, inasmuch as it failed to verify the presence of high strain levels predicted by the analysis, the problem of selecting locations for the aircraft for the main event remained unresolved. A certain amount of intuitive judgement based on related test programs had to be applied to arrive at suitable placements for aircraft within the blast field.

The final decision was predicated on information available from an experimental program conducted at the Naval Surface Weapon Center, White Oak Laboratory (NSWC/WOL), Maryland, which involved flat panels subjected to blast in a shock tube (Ref. 3). Also considered was the widely accepted notion that, according to the sure-safe criterion, skin panels should be regarded as the structural elements more vulnerable to the overpressure effects than the substructure elements such as stringers, longerons, or frames. With that in mind, 41.4 and 62.1 kPa (6.0 and 9.0 psi) were selected as the free-field overpressure levels which should produce the desired severity of damage in the fielded aircraft.

The general view of the aircraft emplacement is presented in Fig. 1. GZ marks the location where the 564-metric-ton ANFO explosive charge was assembled. The charge formed a cylinder of 4.27-m (14.0 ft) radius with a semispherical dome and a total combined height of 10.94 m (35.9 ft) and was designed to simulate the blast field from a 4.2-TJ (1 KT) nuclear ground burst.

The fielded aircraft were oriented side-on to the oncoming shock front. Two were placed 375 m (1230 ft) and one at 311 m (1020 ft) from GZ. These locations corresponded to the estimated ranges for free-field peak overpressures of 41.4 and 62.1 kPa (6 and 9 psi), respectively (Ref. 4).

THIS PAGE INTENTIONALLY LEFT BLANK

AIRCRAFT CONFIGURATION

The A-4C aircraft (Fig. 2) assigned for the DICE THROW project were bureau numbers (BUNO) 149558, 145062, and 145074. These aircraft, each with approximately 4000 in-service flying hours and designated for retirement from the Navy inventory, were flown to NNEF. Upon their arrival, engines, pilot seats, and all avionics components were removed in compliance with the salvage requirements. A general inspection of the airframes was subsequently performed and aircraft BUNO 149558 was selected for the test instrumentation.

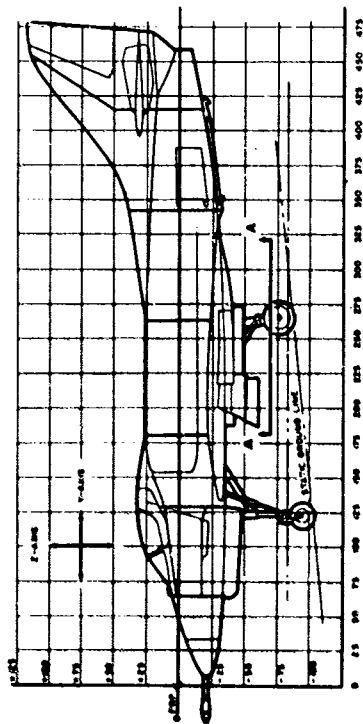
After the instrumentation was installed, the aircraft were transported by truck to the White Sands Missile Range (WSMR) test site and placed on 4.9 x 6.7 m (16 x 22 ft) pads (Fig. 3).

It was intended that aircraft BUNO 149558 and 145062, both 375 m (1230 ft) from the GZ, would demonstrate repeatability of damage for similar structures under practically identical blast environment. It was expected that the third aircraft BUNO 145074, 311 m (1020 ft) from the GZ, would sustain considerably more damage, bordering on catastrophic failure.

The desired test configuration for the aircraft was achieved through a series of operations which included:

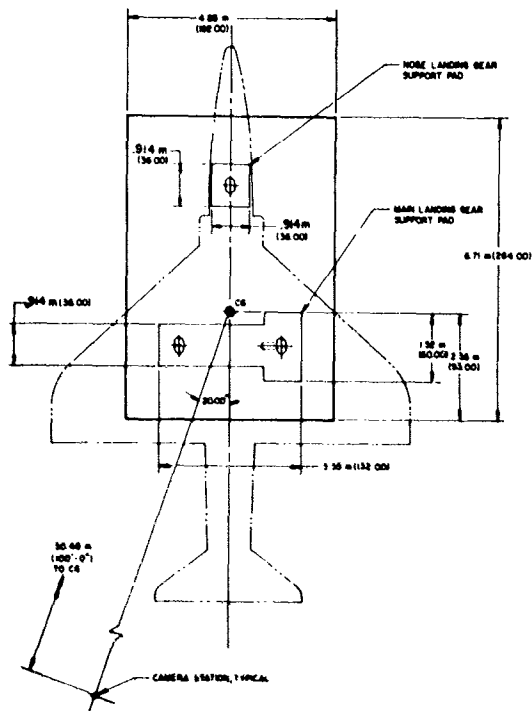
1. Pressurizing the landing gear struts with nitrogen gas to simulate the parked aircraft attitude.
2. Setting and locking all flying control surfaces in a neutral position.
3. Filling internal fuel tanks with water.
4. Installing tiedown system.

An external fuel tank filled with 1136 liters (300 gallons) of water was installed at the centerline store station of aircraft BUNO 145074, i.e., the aircraft closest to the GZ. This extra mass was added to observe the effect of blast on external stores.



NOTE: Numbers denote inches.

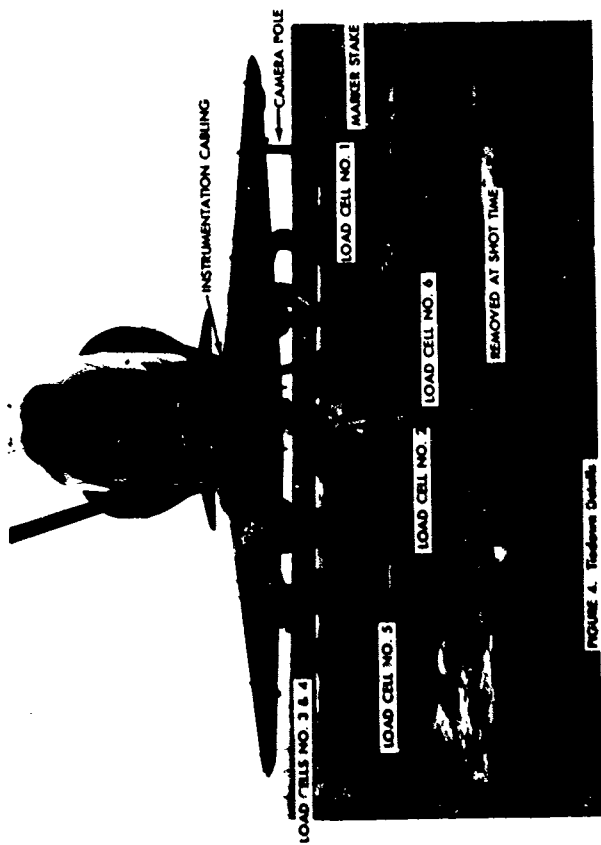
FIGURE 7. A-4C Aircraft Configuration - Side View

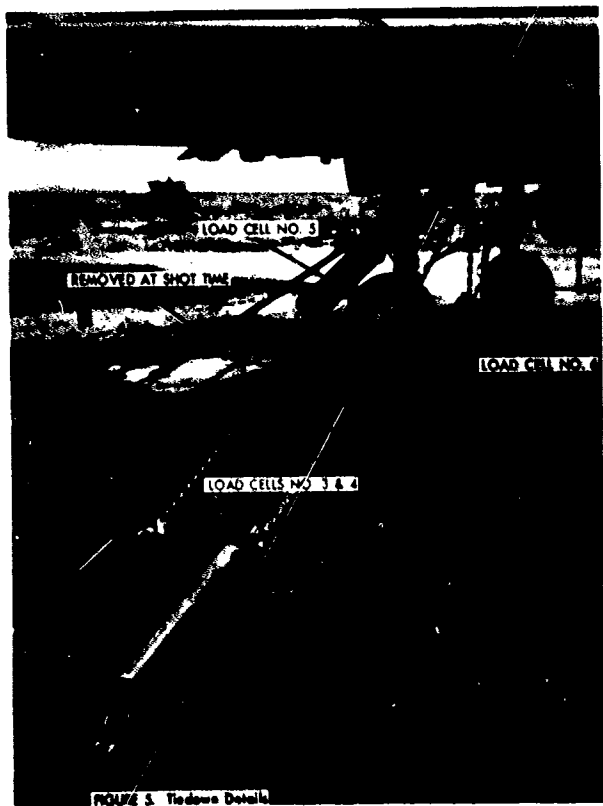


NOTE: Dimensions are in meters followed by inches in parenthesis.

FIGURE 3. Aircraft Support Platform

A temporary tiedown was initially applied to all aircraft as a precaution against excessive winds. However, on the eve of the test, a special tiedown system was installed (Figs. 4 and 5) on two aircraft to provide biased restraint against aircraft motion during the positive blast phase. The third aircraft (BUNO 145062) was not tied down during the blast in order to simulate a launch-ready condition and to allow comparison of rigid body motions of this aircraft with those of the secured aircraft.





TEST INSTRUMENTATION

The overall scope of this test program called for diversified instrumentation to provide adequate data to determine two kinds of the structural response to blast, i.e., local response and rigid body response. Consequently, the instrumentation selected may be divided into two categories according to the kind of response to be monitored.

For the local structural response to overpressure, strain and deflection gages were used. Pressure gages were required to monitor transient behavior of the external pressure loading in the vicinity of the structural elements under consideration. Stress coat was also used to augment strain gage data and provide qualitative rather than quantitative information on strain patterns developed in skin panels following the shock intercept.

In the case of the structural response to gust, where time related history of the entire aircraft motion had to be obtained, strategically located motion picture cameras were used to record the aircraft rigid body motion. Also calibrated load cells were installed within the tiedown system to measure the tiedown restraint forces.

In all cases of the electronic related instrumentation, i.e., strain, deflection, and pressure gages, the data was collected on FM magnetic tape recorders located in the instrumentation trailer using 1524 m (5000 ft) of instrument cable. Three cables of 50 twisted wire pairs with overall shield were required because telemetry of data to the trailer was prohibited as a policy of the DICE THROW test director.

Individual items of the instrumentation system, the selection of the structural elements to be instrumented, and the instrumentation layout are described in separate subsections which follow.

INSTRUMENTATION DESCRIPTION

STRAIN GAGES

Micro-Measurement strain gages type EA-13-250UW-120 were used to obtain strain data. These gages, with 120-ohm nominal resistance, are classed as general purpose strain gages suitable for static and dynamic stress analysis

and are capable of reliable operation within the temperature range of -75 to 250°C, over a range of $\pm 50,000$ microstrains. The self-temperature-compensation characteristics of these gages assured strain reading within ± 5 percent accuracy for 0 to 100°C temperature range.

A typical strain gage circuit used a conventional Wheatstone bridge arrangement with the active gage representing one arm of the bridge. The remaining three arms were made up of wire-wound resistors specially selected for low temperature drift. Only the Wheatstone bridge was located in the aircraft; all other elements of the strain gage system were installed in the instrumentation trailer.

The gage excitation was furnished by a 10 ± 0.5 V power supply. The gage signal, amplified by a fixed gain dc amplifier, was recorded on a magnetic tape recorder.

This system responded with a 6-kHz frequency bandwidth and its overall accuracy was assessed at ± 5 percent.

PRESSURE GAGES

Kulite pressure gages type XTH-1 190-10S were selected to obtain pressure data. This gage, specified for 0 to 138-kr (0 to 20 psi) pressure range with an operating temperature range from -20 to +80°C, provided pressure data with the accuracy rated at ± 5 percent.

A special excitation system was furnished by a 24-V battery regulated down to 20.1 V. The signal from the pressure gage was fed to a unity gain buffer amplifier located at the aircraft. This buffer amplifier was used to increase the frequency response capability. From the buffer amplifier, the signal was transmitted to the instrumentation trailer via the 50 pair cable. It was then amplified again through a dc amplifier and recorded on the magnetic tape.

This system assured overall pressure measurement accuracy to ± 10 percent.

DEFLECTION GAGES

Kaman Sciences Corporation deflection gages types KD-2300-6C and -8C were used as deflection sensors. The characteristic outputs of these gages, rated at 1 percent accuracy, were 2 mV per 0.0254-mm (0.001 in.) deflection for

-6C gage and 4 mV per 0.0254-mm deflection for -8C gage. Each gage consisted of a transducer and an oscillator package which had the operating temperature range limits of 0 to 75°C. These elements plus a ± 12 V battery power source were located in the aircraft. The processed output signal was then transmitted to the instrumentation trailer where it was amplified prior to being recorded on magnetic tape.

The overall accuracy of this system was approximately ± 4 percent.

STRESS COAT

As an instrumentation technique, stress coat can be successfully applied as an indicator of complex strain patterns developed in specimens under test. It is particularly useful in cases of structural components of intricate configuration for which reliable analytic methods are not available.

Stress coat, which can be easily applied to the specimen surface, cracks under load. These cracks form a pattern which can be correlated with the strains induced in the tested part, analogous to strain contours. Because of its high sensitivity to temperature changes, stress coat is best suited for tests conducted under strictly controlled environmental conditions.

For this test, stress coat was regarded strictly as a secondary instrumentation medium to augment dynamic strain gage data. Low temperature stress coat (Ref. 5) was selected because of low temperatures predicted for the test site at night.

MOTION PICTURE CAMERAS

Three 16mm Milliken model DBSS motion picture camera: were furnished to record aircraft rigid body motions following the shock wave intercept. Two cameras which had 25mm lenses were set at F-stop 2.8 and the third camera, with 13mm lens, was set at F-stop 4. The cameras were loaded with Kodak color film type EM, ASA 160, and the film speed was set at 400 frames per second.

LOAD CELLS

The exploded view of the load cell is presented in Fig. 6 which shows the assembly. The cylindrical tube serves as a housing for an aluminum honeycomb tube core element which is used as the energy measuring structure. With tension load applied through the end fittings, the core element is subjected to a compression load. When this load exceeds a predetermined value, crushing of the core takes place and motion results. The energy absorbed in this process can be determined from the known characteristics of the core and the amount of deformation stroke produced during crushing.

SELECTION OF STRUCTURAL ELEMENTS

With the strain and deflection gages assigned as the primary instrumentation to generate the experimental data, a selection of structural elements was undertaken. From the standpoint of the experimental data quality, the criteria which governed the selection of structural elements included:

1. Structural response preferably into the plastic range.
2. Low probability of catastrophic failure.
3. Applicability to computer modeling.

A broad spectrum of structural skin panels was initially contemplated to study effects of such parameters as panel size and aspect ratio, thickness and curvature, boundary conditions, and skin material. However, practical considerations which limited the choice were dictated by:

1. Desirability for simple geometry, i.e., square or rectangular shape.
2. Ease of modeling.
3. Easy access to panels.
4. Keeping panel skin thickness within a relatively narrow band to ensure post-yield response but preclude rupture.
5. Instrumentation and recording system costs.



FIGURE 4. Load Cell - Exploded View

The structural elements selected for instrumentation included eight skin panels, two longerons, and one fuselage frame. The panels, all made from 7075-T6 aluminum alloy were approximately rectangular. The panel locations on the airframe are shown in Fig. 7 and panel geometry data are summarized in Table 1. Panels 1 through 7 represented clamped-edge boundary conditions and an access door, panel 8, represented simply supported edge boundary conditions.

The longerons which formed the top and bottom boundaries of panel 5 together with the frame of fuselage station 277 completed the set of structural elements selected for instrumentation.

The longerons represented "L"-shape beams of uniform cross section supported at each end by adjacent fuselage frames.

The "C"-shape frame at fuselage station 277 was selected for its relatively simple cross section, basically a web with a flange on either side, forming a curved beam. Admittedly, this was a beam with cross section varying along its span, but it represented a continuous arch, symmetric about the vertical reference plane and supported by the lower longeron at either end.

INSTRUMENTATION LAYOUT

STRAIN GAGES

The strain gage instrumentation comprising 58 recording channels covered eight skin panels, two longerons, and one fuselage frame (Figs. 8 through 16). For skin panels, the gages were installed at principal locations such as the panel center, gages 1 through 4 (Fig. 8), or mid-points of panel edges, gages 27 or 47 (Fig. 11). For these locations, analytic data could be readily obtained from computer code solutions.

Clusters of strain gages were installed staggered-fashion at mid-panel locations close to the longer edge, gages 5 through 9 (Fig. 8). This arrangement was intended to provide strain gradient data in the area of the expected maximum strain variation.

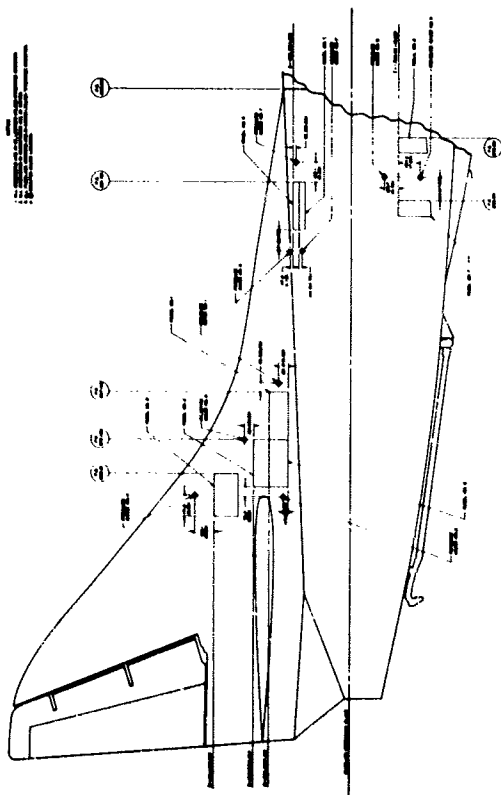
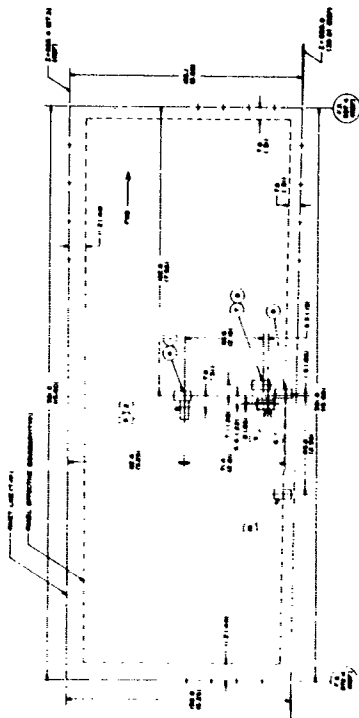


FIGURE 7. Instrumented Panels Location Diagram

TABLE 1. Strain Gage Instrumented Panels Geometry Data.

PANEL NUMBER	RIVET LINE (REF)		EFFECTIVE SIZE		THICKNESS mm (in.)	RADIUS OF CURVATURE mm (in.)	ASPECT RATIO (a/b) (in.)
	LENGTH mm (in.)	WIDTH mm (in.)	LENGTH (a) mm (in.)	WIDTH (b) mm (in.)			
1	381 (15)	162 (6.375)	362 (14.25)	143 (5.625)	1.02 (.040)	00	2.53
2	381 (15)	156 (6.125)	362 (14.25)	137 (5.375)	1.02 (.040)	00	2.65
3	381 (15)	133 (5.25)	362 (14.25)	114 (4.5)	1.02 (.040)	00	3.17
4	388 (15.29)	92 (3.609)	367 (14.44)	73 (2.859)	0.81 (.032)	782 (30.8)	5.05
5	386 (15.19)	106 (4.172)	363 (14.28)	87 (3.422)	0.81 (.032)	782 (30.8)	4.17
6	225 (8.844)	120 (4.719)	200 (7.87)	98 (3.87)	0.81 (.032)	00	2.03
7	242 (9.547)	129 (5.094)	227 (8.922)	110 (4.34)	0.81 (0.32)	00	2.05
8	343 (13.5)	162 (6.375)	318 (12.5)	137 (5.375)	1.57 (.062)	00	2.32

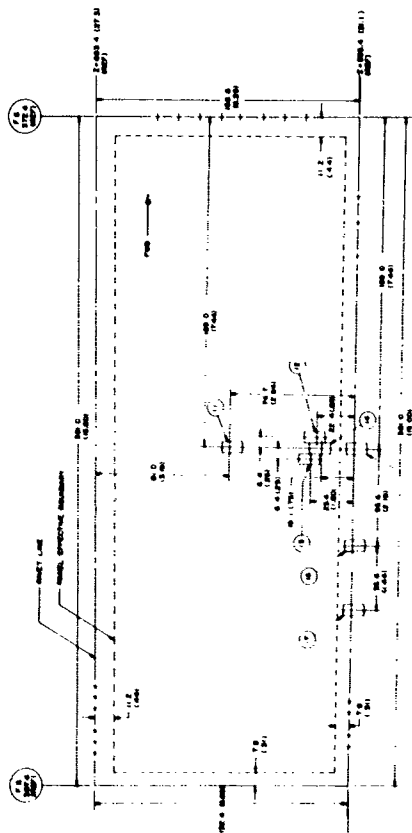
NOTE: Numbers in parentheses denote the dimension expressed in inches.



NOTE

1. All dimensions are in millimeters unless otherwise specified. Dimensions in parentheses are in inches.
2. All fuelage stations are in inches.
3. Strain gages Nos. 1, 2, 3, 4, 5, 6, 7, 8, 9 and 10 are installed on panel inside surface.
4. Strain gages Nos. 1, 2, 3, 4, 5, 6, 7, 8, 9 and 10 are installed on panel inside surface.

FIGURE 8. Strain Cage Instrumentation Layout - Panel 1

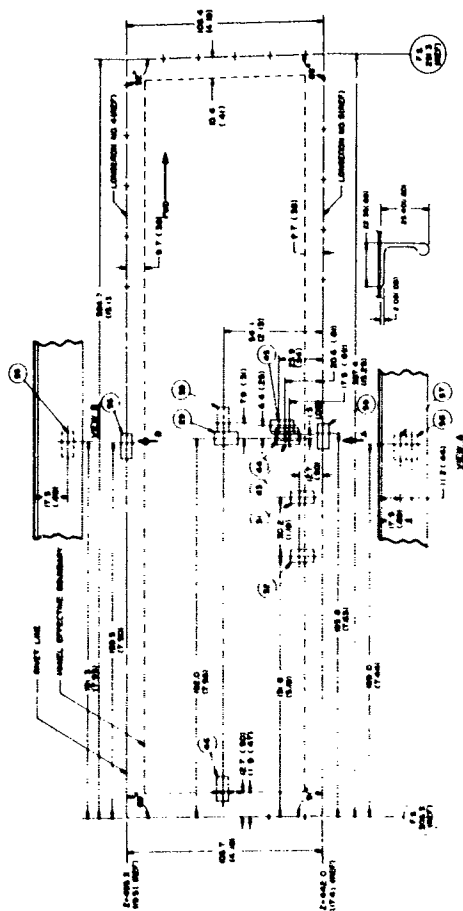


NOTE: Dimensions are in meters followed by inches in parenthesis.

FIGURE 9. Strain Gage Instrumentation Layout - Panel 2



FIGURE 11. Strain Gage Instrumentation Layout - Panel 4

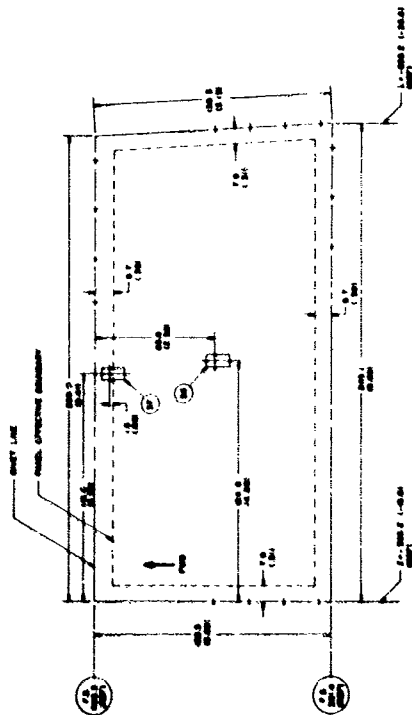


NOTE: Dimensions are in meters followed by inches in parenthesis.

FIGURE 12. Strain Gage Instrumentation Layout - Panel 5.

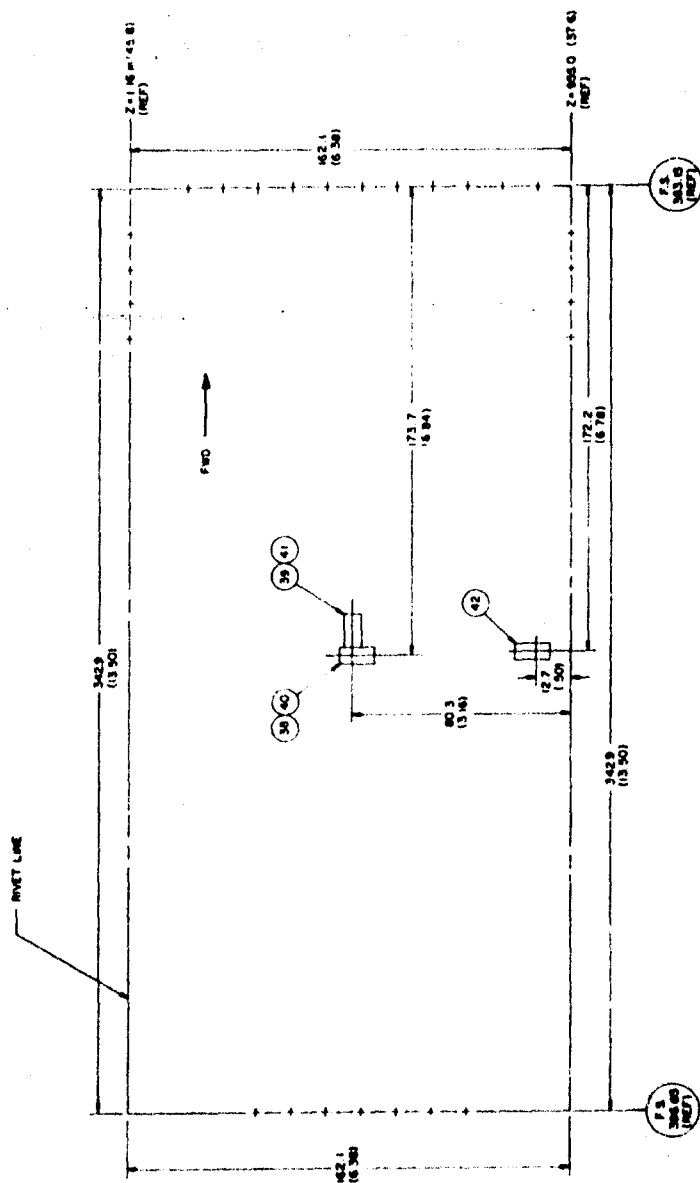


FIGURE 13. Strain Gage Instrumentation Layout - Panel 6



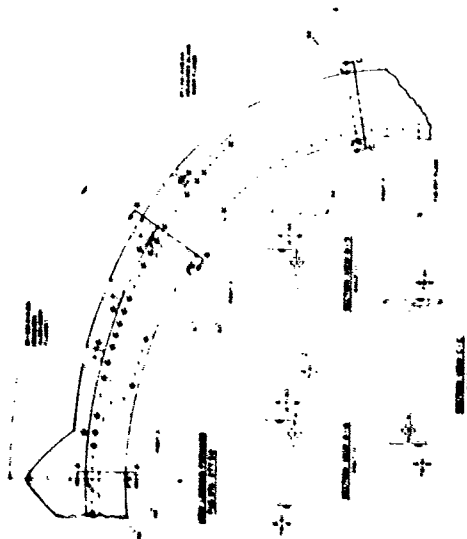
NOTE: Dimensions are in meters followed by inches in parenthesis.

FIGURE 14. Strain Cage Instrumentation Layout - Panel 3



NOTE: Dimensions are in meters followed by inches in parenthesis.

FIGURE 15. Strain Gage Instrumentation Layout - Panel 8



NOTE: Dimensions are in meters followed by inches in parenthesis.

FIGURE 16. Strain Cage Instrumentation Layout - Fuselage Frame Station 277.

Sets of several strain gages, such as gages 15, 16, and 17 (Fig. 9) installed along the panel longer edge, were designed to provide data on strain behavior between the mid-point and the corner. The strain for a panel with clamped-edge boundary condition was expected to vary between a maximum for the panel at the edge mid-point and zero at the corner.

The gage locations for number 4 and 5 longerons are shown in Fig. 12. Gages 55, 57, and 58 were installed on longeron webs at mid-span between fuselage frame stations 291.3 and 206.3. Gages 56 and 59 were bonded on the fuselage skin outer surface opposite longeron flanges where the skin and the flange were assumed to act as an integral unit.

Strain gages 48 through 53 were installed in pairs at three sections along the span of the fuselage frame station 277.312 (Fig. 16). With the exception of gage 53 which was bonded to the skin outer surface, all gages were installed on the frame flanges.

DEFLECTION GAGES

The displacement measuring system consisted of three deflection gages. A pair of these gages was installed on panel 5, one to measure the deflection at the center, the other to measure deflection of the supporting substructure. The third gage was installed to measure the central deflection of panel 7.

All deflection gages were mounted in specially designed brackets which were rigidly attached to the substructure members forming panel boundaries. A typical configuration of the deflection gage assembly is shown in Fig. 17.

PRESSURE GAGES

A system of ten pressure gages was provided to monitor overpressure in the areas of instrumented skin panels (Fig. 7). Gages 1 through 4 were installed on the vertical stabilizer and monitored the area of panels 1, 2, 3, and 8 to record the pressure variation in the lateral and vertical directions. Three gages, numbers 4, 5, and 6, were assigned to the fuselage area of panels 4 and 5. The curved profile of the fuselage at that location was expected to produce significant pressure variations in the reflected pressure because of its dependence on the incident angle of the shock wave.

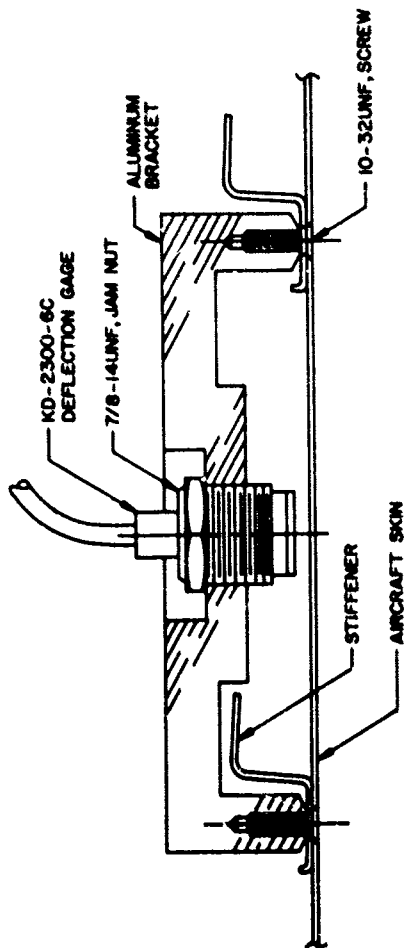


FIGURE 17. Deflection Cage Installation Diagram

Significant pressure gradient was also expected in the area of panels 6 and 7 where proximity of the wing root and fuselage intersection was likely to cause a local rise in the reflected pressure. Pressure gages 8 and 9 were located to record that pressure gradient.

Finally, gage 10 was installed inside the airframe, approximately in the middle of the fuselage, to monitor overpressure inside the structure during the diffraction

STRESS COAT

The weather forecast for the day of the test predicted the temperature drop to 5°C at the test site. Consequently, stress coat TL-500-50 (Ref. 5) was selected to minimize the hazard of crazing at low temperature because of thermal contraction. The stress coat was applied on the day preceding the test to allow the necessary curing time. This application was restricted to skin panels on aircraft BUNO 145062 and 145074 which corresponded to the strain gage instrumentation panels of aircraft BUNO 149558. Hopefully, this would allow comparison with the real-time strain gage results.

MOTION PICTURE CAMERAS

A typical camera layout given in Fig. 1 shows the camera station at 30.5 m (100 ft) from the aircraft CG with the line of sight at 20-degree angle to the aircraft longitudinal axis. Each camera was mounted on a 0.3-m (12 in.) diameter pole, 2.5 m (8.2 ft) above the ground. This approximated the height of the aircraft CG above the ground. The poles were anchored with four cables to minimize the camera motion during the shock front intercept.

The cameras equipped with 25-mm lenses were positioned to record the motion of the aircraft BUNO 149588 and 145074 and the 13-mm lens camera was used for aircraft BUNO 145062.

Scale reference was supplied by a pair of marker stakes at each aircraft. One stake was installed directly below the aft end of the engine exhaust shroud and the other was laterally displaced by approximately 1.52 m (60.0 in.) to the port side.

The measured distances between each set of marker stakes are listed below:

AIRCRAFT IDENT. BUNODISTANCE

149588	1.59 m (62.75 in.)
145062	1.53 m (60.3 in.)
145074	1.53 m (60.2 in.)

LOAD CELLS

The load cells were installed as extension links within the tiedown system. The tiedown setup for aircraft BUNO 149588 and 145074 (Figs. 4 and 5) consisted of six chains attached between the aircraft and buried anchors.

This tiedown pattern was devised as the restraint to the anticipated translatory and rotational motions of the aircraft as well as the means of measuring the impulse sustained by the structure over the blast positive-phase duration.

A tether system furnished for aircraft BUNO 145062 consisted of several lengths of tiedown chain arranged in such a manner as to permit approximately 6 m (19.7 ft) of free lateral displacement before the restraint would become effective. In view of rather conflicting predictions for aircraft rigid body behavior under blast effects, this setup was designed to check the conservativeness of predictions for overturning.



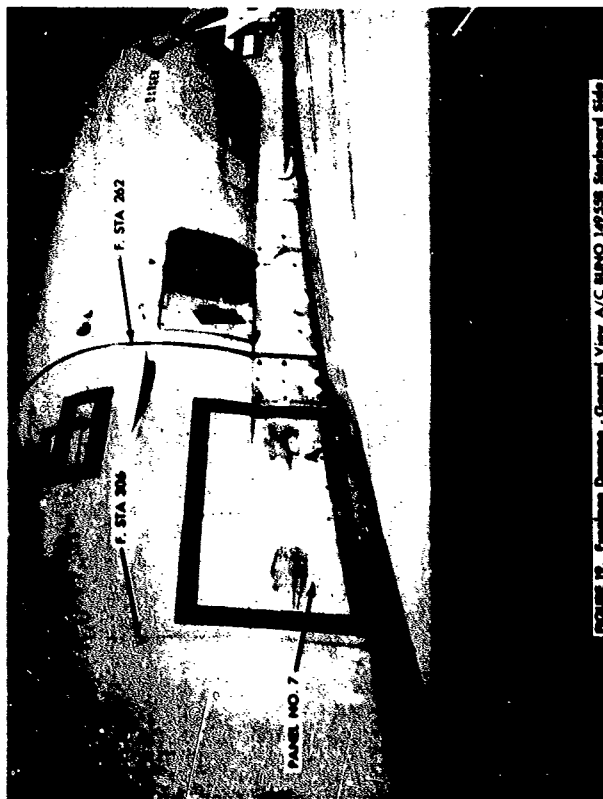


FIGURE 19. Fuelage Damage - General View A/C BUINO 14958 Starboard Side



FIGURE 20. Rudder Hinge Failure - A/C BUNO 149558

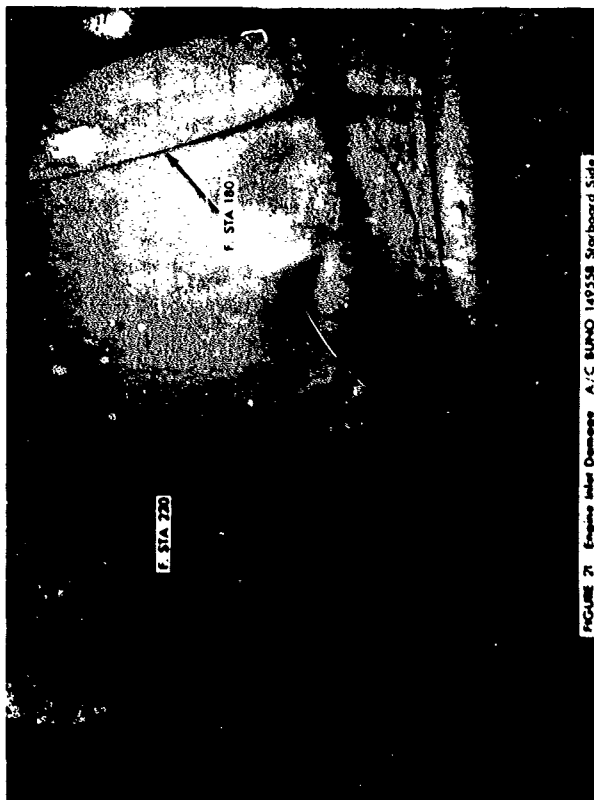


FIGURE 21 Engine Inlet Damage A/C BUINO 149558 Starboard Side

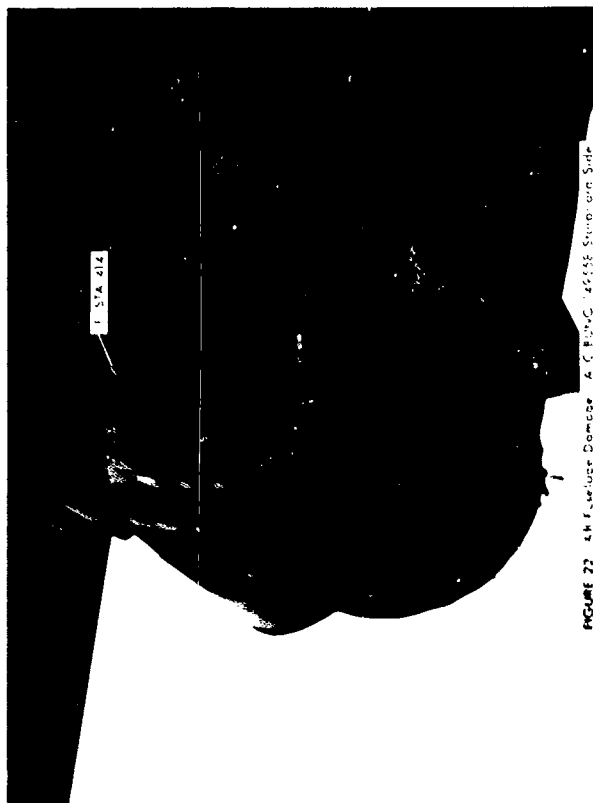


FIGURE 22 44 Fuel Use Damage A C Fuel C 4658 Side and Side

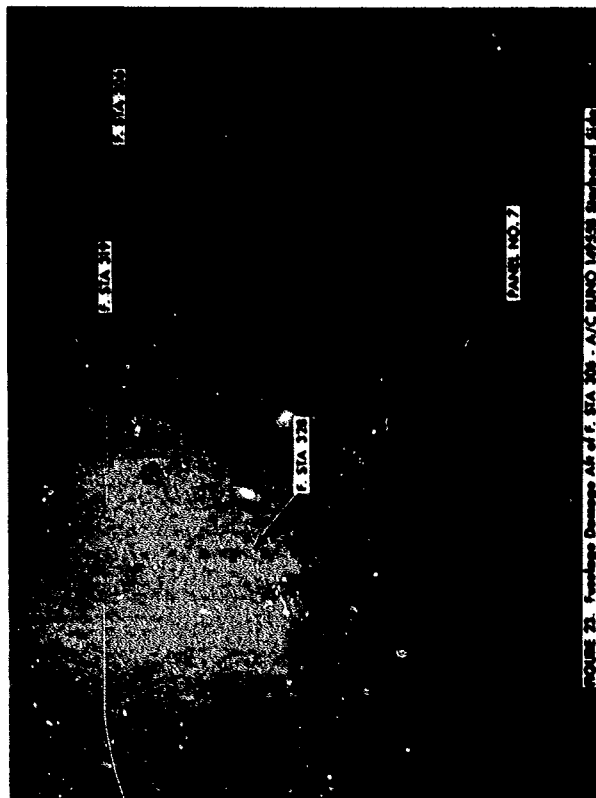


FIGURE 21. Footage Damage Air of P. SIA 308 - A/C RUINO 149558 Subboard S24.



TEST RESULTS

GENERAL

This section of the report is devoted to a detailed description of damage and a presentation of selected experimental data obtained from the instrumentation installed in aircraft BUNO 149558, which was exposed to 41.4-kPa (6 psi) peak free-field overpressure. A complete presentation of the experimental data is included in Volume II of NWEF Report 1145 (Ref. 6).

As mentioned previously, two aircraft were located 375 m (1230 ft) from the GZ. At this range, the peak free-field overpressure was approximately 41.4 kPa (6 psi). The third aircraft, located 311 m (1020 ft) from the GZ experienced approximately 62.1-kPa (9 psi) peak free-field overpressure. Accordingly, the degree of damage caused by the blast was expected to differ significantly in those two cases. An inspection following the test revealed relatively light damage sustained by the aircraft farther away from the GZ whereas the aircraft closer to the GZ ruptured in a catastrophic failure (Fig. 18). This leads to an immediate and rather significant observation that within very narrow limits of the distance from the GZ, approximately 61 m (200 ft) in this case, the damage sustained by the aircraft varied from slight to catastrophic.

DAMAGE DESCRIPTION

AIRCRAFT BUNO 149558

The posttest inspection of the exterior of this aircraft, which experienced 41.4-kPa (6 psi) peak free-field overpressure, revealed widely scattered local damage on the starboard side (i.e., the side exposed to blast), ranging from buckling of the skin panels to rupture of the skin (Fig. 19), failure of the landing gear doors, and loss of the rudder (Fig. 20). Details of skin buckling are illustrated in Figs. 21 and 22 which show the engine inlet at fuselage STA 175 and the fuselage region aft of STA 400, respectively, where the skin material was 0.81-mm (0.032 in.) thick. Figure 23 shows the fuselage in the region aft of Sta 306 where extensive rivet failures were observed.

More severe damage was sustained in the vicinity of the forward and aft fuselage joint, STA 262. Just aft of that station (Fig. 24), a skin rupture initiated at fuselage

STA 277, approximately 220 mm (8.5 in.) above the wing surface, and proceeded diagonally towards the wing and then along the lower longeron for about 355 mm (14 in.). From this area of panel rupture, a severe skin buckle radiated upwards crossing several panel boundaries. Also shown in Fig. 24, forward of STA 262, is the failure of a non-structural panel which ruptured at its lower boundary and was forced inward under the overpressure loading.

Regarding the landing gear door damage, it can be generally stated that the pretest arrangement of fastening these doors by means of cables and struts to compensate for the deactivated hydraulic system failed completely. In addition, failures of the door structure were incurred as exemplified by the rupture of the nose landing gear retraction fitting and the failure of the main landing gear port-side door hinge.

Slight buckles were observed on the port side (i.e., side not exposed to the blast) on the engine inlet duct and mid-fuselage STA 300.

Moderate damage of substructure was noted on the starboard side of the aircraft at the mid-fuselage region between Stations 236 and 342. The damage included sheared fasteners at the joint of such major components as a former and the lower longeron (Fig. 25), buckles and cracks in the stiffener or former flanges (Fig. 26), and a complete failure of a former cross section (Fig. 27). Significantly, fastener holes were invariably present at the crack or rupture locations which implies that considerable strength degradation associated with the presence of a fastener hole may lead to premature failure of the substructure element.

AIRCRAFT BUNO 145062

This aircraft, also subjected to 41.4-kPa (6 psi) peak free-field overpressure, sustained, in general, an identical type of damage as the first aircraft. However, a distinct evidence of greater severity of the damage was apparent. This is illustrated in Fig. 28, where the buckles of the aft fuselage region form a much more clearly defined pattern, in Fig. 29 which shows more extensive skin rupture in the fuselage frame Sta 277 area, and in Fig. 30 which shows flange failure in the frame itself. Similarly, Fig. 31 shows fuselage STA 320 area with the skin ruptured whereas only fastener failures were observed for the other aircraft. Also, more severe landing gear door failures were observed.



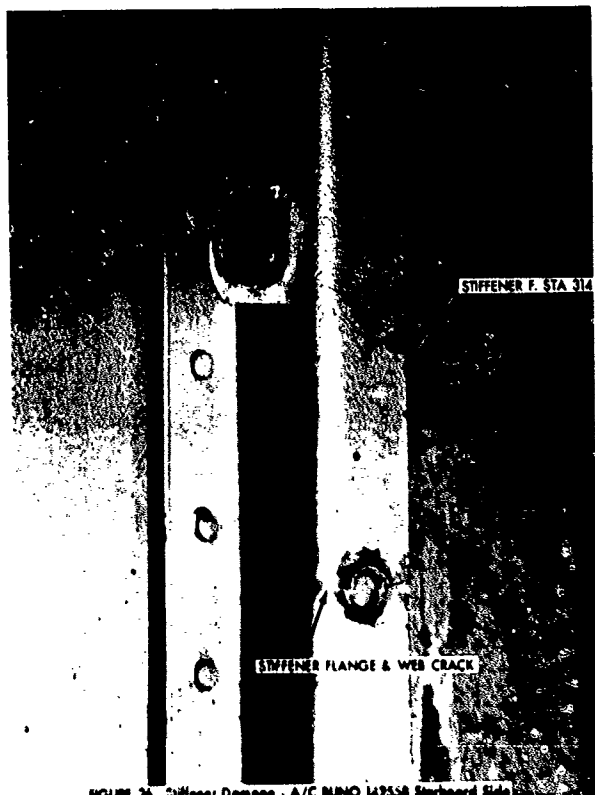
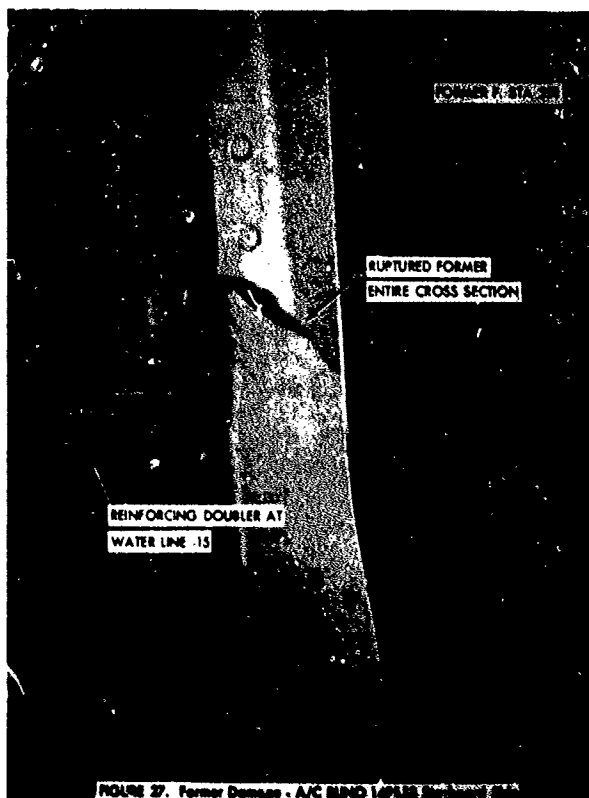


FIGURE 26 Stiffener Damage - A/C BUINO 147558 Starboard Side



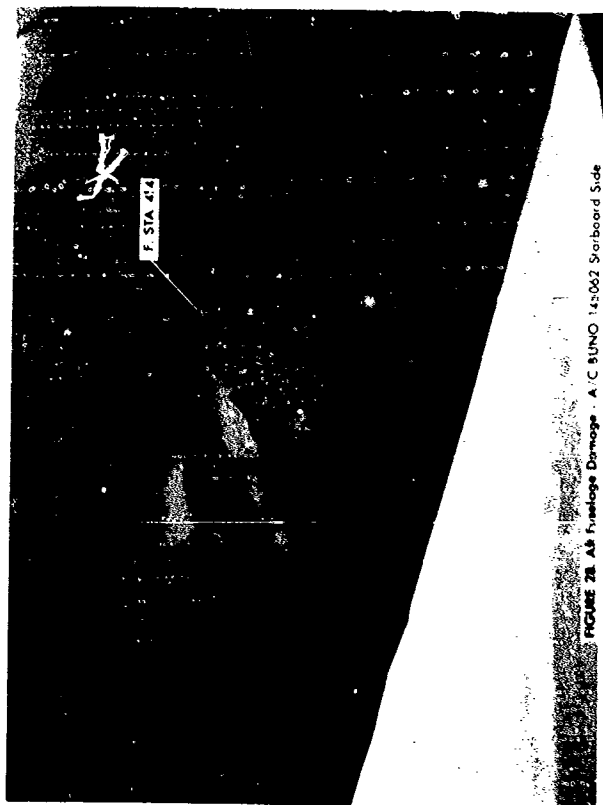


FIGURE 28. All Pre-Flight Damage - A/C 81NO 145062 Starboard Side

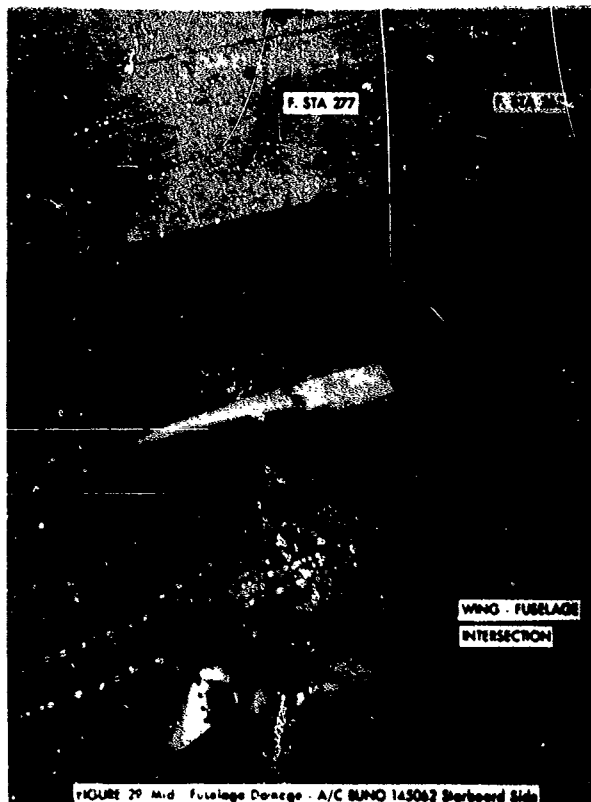






FIGURE 34. All Feedings Damage - A/C BUNO 145052 Starboard 24.

AIRCRAFT BUNO 145074

The devastating effects of the blast were clearly demonstrated (Fig. 18) for this aircraft which suffered catastrophic failure under 62.1-kPa (9 psi) peak free-field overpressure. The aft fuselage section between Stations 262 and 342 was virtually demolished, presumably under overpressure loads. The rupture of lower longerons, which constitute the primary structural members in the axial direction, resulted in the empennage section breaking away from the rest of the airframe.

The catastrophic nature of the damage was also apparent from complete disintegration of the canopy (Fig. 32) as well as from the extensive skin rupture and extreme severity of buckling patterns in the engine inlet duct structure (Fig. 33).

The failures of the primary substructure members are illustrated in Figs. 34 through 36. The appearance of ruptured cross sections suggests tensile failures for the starboard upper (Fig. 34) and lower (Fig. 35) longeron members. The port lower longeron (Fig. 36) exhibits a compressive failure characteristic.

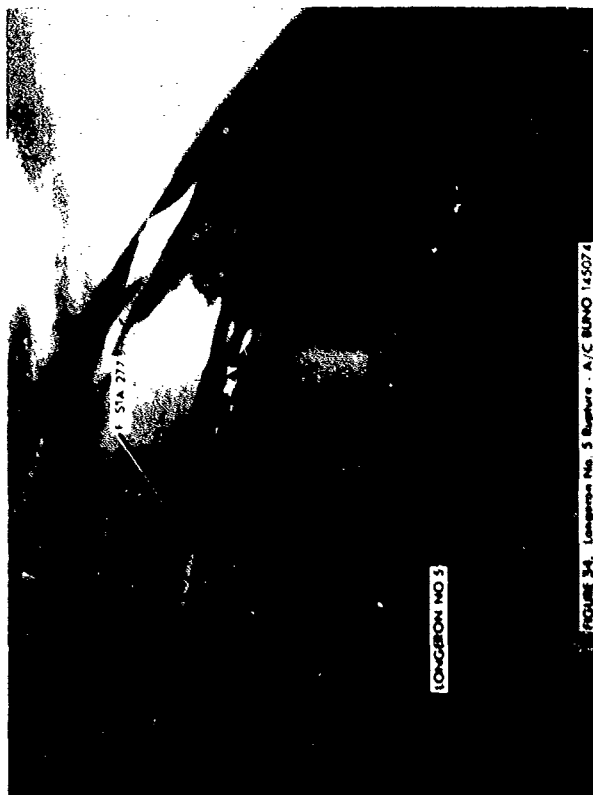
DAMAGE ASSESSMENT

Considering the blast characteristics at the two principal aircraft locations shown in Table 2, it is not surprising that the extent of damage sustained by the aircraft differed significantly in each case. However, based on the pretest predictions, it was assumed that the aircraft exposed to 41.4-kPa (6 psi) overpressure might sustain local, permanent-set type damage of the weakest panels or substructure elements, but no failures in the form of panel skin rupture or fracture of an entire former cross section were anticipated (Figs. 24 and 27). Similarly, for the aircraft exposed to 62.1-kPa (9 psi) overpressure, even though a possibility of failure was not completely ruled out, it was presumed that the damage, however extensive, would not precipitate the catastrophic failure which actually occurred (Fig. 18).



FIGURE 32 Canopy Failure A C BUNO 143074





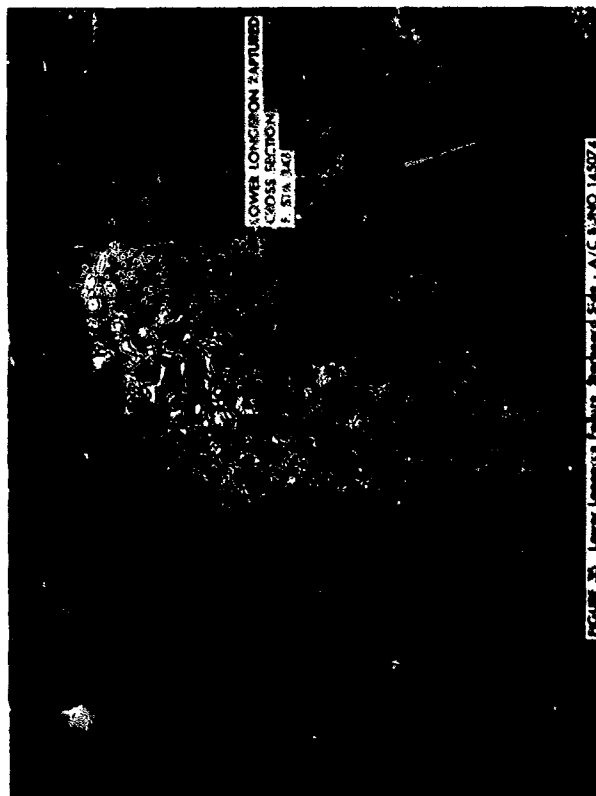


FIGURE 20. Lower Longicorn Failure, Seaboard 246 - A/C BUNO 145071



FIGURE 36 Lower Longeron Failure, Port Side - A/C BUNO 145074

TABLE 2. Predicted Free-Field Airblast Parameters.

DISTANCE FROM GZ m	OVERPRESSURE kPa	OVERPRESSURE IMPULSE kPa·ms	HORIZ. DYN. OVERPRESSURE kPa	HORIZ. DYN. OVERPRESSURE IMPULSE kPa·ms
311	62.1	4588	13.8	799
375	42.4	3792	6.8	455

The fact that structural failures did occur can be partially attributed to the strength degradation of the aircraft structure, resulting from extensive in-service use, as well as to the synergistic effect of the overpressure and gust interaction. These were not considered in the structural integrity assessment by analytic methods.

The overall damage sustained by the two aircraft located 375 m (1020 ft) from the GZ can be divided into three categories:

1. Loss of the rudder.
2. Buckling of the skin panels.
3. Failure of substructure elements and associated skin panel rupture.

The side-on intercept of the aircraft by the blast represented the most severe orientation for the vertical stabilizer including the rudder. The rudder structural integrity was not subjected to pretest analytic prediction. Therefore, comments regarding the loss of the rudder resulting from hinge failure (Fig. 20) are limited to stating that the loads associated with 41.4-kPa (6 psi) free-field peak overpressure exceeded the hinge strength at some point and resulted in failure.

The occurrence of moderate skin buckling was primarily restricted to the engine inlet (Fig. 21) and the fuselage section aft of STA 414 (Fig. 22) where panels with thinnest skin, 0.81 mm (0.032 in.), were located. Characteristically, these panels were susceptible to early buckling because they were long with an aspect ratio approaching 6.0. This type

of damage was associated with only a minor substructure deformation as suggested by the appearance of the engine inlet area, where several rivet failures were also observed.

The severity of the buckling pattern in the aft fuselage area differed noticeably for the two aircraft located 375 m (1230 ft) from the GZ. The more severe buckling in the case of aircraft BUNO 145062 (Fig. 28), as compared to aircraft EUNO 1459558, can be explained by potentially different strength characteristics of the individual aircraft. However, it is possible that a slight variation in the blast intensity had occurred locally and was sufficient to produce discernible difference in the damage level of those two aircraft. Also, variations in the tiedown arrangement for the two aircraft might have affected the gust response and produced differences in the aft area buckling patterns.

The most severe damage was obtained in the mid-fuselage area between bulkheads STA 262 and 306 (Fig. 19), immediately above the wing-fuselage intersection. The skin rupture in panel 6 (Fig. 13) was associated with failures of numerous substructure elements. Ignoring for a moment the substructure failures, it is difficult to explain the skin rupture on the basis of the panel geometry relative to other panels within the airframe. Admittedly, the ruptured panel skin (Fig. 24) was only 0.81 mm (0.032 in.) thick, but its length, 200 mm (7.87 in.), was considerably less than the 363-mm (14.28 in.) long panel 5 of identical skin thickness where no signs of damage were found.

It may be suggested that, at this location, where the wing and fuselage met, the local shock reflection produced higher overpressure, but that alone could not account for the skin rupture. A much more plausible explanation of the skin rupture in this area is that it occurred in conjunction with the substructure failure. The structural distortion produced by the former failure at STA 291 (Fig. 27) and the fastener failures at the joint of STA 277 former to the lower longeron (Fig. 25) had a compounding effect which led to the skin rupture.

This category of damage was also more severe in aircraft BUNO 145062 (Fig. 29) as compared to BUNO 1459558 (Fig. 24). The former shows the skin rupture extending upwards towards the top of the fuselage, while the latter failure is contained within the lower fuselage area. A similar situation

prevailed in the aft fuselage region of STA 319 and 328 where the fastener failure and slight damage of the substructure for aircraft BUNO 149558 (Fig. 23) were contrasted with a more extensive damage including the skin rupture for aircraft BUNO 145062 (Fig. 31). The explanation given earlier for the panel buckling patterns is considered equally applicable in this case.

The assessment of the catastrophic failure of aircraft BUNO 145074 can best be made in the context of the blast parameter data (Table 2) and the nature of damage sustained by the aircraft located farther away from the GZ. A comparison of the blast parameters shows 50 to 100 percent higher intensity in overpressure and dynamic pressure, respectively, for the 311-m (1020 ft) location over the 375-m (1230 ft) location from the GZ.

The failure sequence as reconstructed from the post-test examination of the aircraft was as follows. The failure initiated in the vicinity of STA 277 was produced by the overpressure loads just as in the case of the aircraft located 375 m (1270 ft) from the GZ. Naturally, with the 50 percent higher overpressure, this failure resulted in the skin rupture extending possibly from the lower longeron to the top of the fuselage. This was accompanied by extensive substructure failure over the entire fuselage segment between bulkheads STA 262 and 343 which was crushed into the fuselage body. The main skeletal members of the fuselage, the longerons, appeared to have remained intact to this point, but the progressive loss of skin strength was sufficient to complete the rupturing process of the entire fuselage cross section under the subsequent gust loads. This is substantiated by a tension fracture appearance of the starboard longerons, i.e., those towards the GZ (Figs. 34 and 35), and a compression fracture of the portside lower longeron (Fig. 36). It is interesting to note that the initial failure of the upper longeron occurred at STA 277 (Fig. 33) which coincides with the most severe substructure damage to the aircraft located 375 m (1230 ft) from the GZ. Both lower longerons (failure at STA 343) contained an apparent weakness in the form of cutout holes.

INSTRUMENTATION DATA

The experimental data in their entirety are compiled in Volume II of NWEF Report 1145 (Ref. 6). This includes the data obtained from NWEF Projects implemented in both PRE-DICE THROW II and DICE THROW Events.

However, for the purpose of correlation, pertinent experimental data are presented graphically in this volume in conjunction with the analytically predicted data for overpressure, strain, and deflection. In addition, selected strain gage data plots are included to illustrate relevant subject material covered in the discussions. References to these experimental data are made within the text as applicable.

THIS PAGE INTENTIONALLY LEFT BLANK

ANALYSIS

ANALYTIC PROCEDURES

The analytic treatment of the aircraft structural response to overpressure provided in this report is based on three overpressure analysis methods formulated in the "Handbook for Analysis of Nuclear Weapon Effects on Aircraft" (Ref. 2). The complexities of the structural modeling and the nuclear blast representation vary with each method. Presumably, the accuracy of the analytic predictions vary accordingly.

METHOD 1

The least complex technique, Method 1, is based on two major assumptions:

1. Overpressure damage to an aircraft is the same for all aircraft of a given generic type.
2. The preblast atmosphere is homogeneous, having characteristics associated with aircraft altitude.

The method employs predetermined, critical sure-safe or sure-kill overpressure levels depending on the type of aircraft under consideration. Then, given the weapon yield, this method can be readily used to determine critical ranges and obtain plots of sure-safe and/or sure-kill envelopes.

For A-4C aircraft, which is classed in the fighter or fighter-bomber category, the method prescribes the following critical pressures:

1. 17.24 kPa (2.5 psi) for sure-safe condition
2. 137.9 kPa (20.0 psi) for sure-kill condition

Sure-safe and sure-kill envelopes were constructed based on the scenario data:

Aircraft altitude HZ = 1.2 km (4000 ft)

Ground altitude HG = 1.2 km (4000 ft)

Equivalent yield W = 4.2 TJ (1 KT)

A step-by-step procedure was applied using furnished graphical and tabular data which included special provisions to account for the ground reflection effects.

METHOD 2

Method 2 is based on the premise that an aircraft subjected to an overpressure loading can experience structural damage in several ways. Skin panels may yield or rupture, while longerons, stringers and frames may fail by compressive yielding or local buckling. Since the fuselage is generally the most susceptible to these types of damage, it is explicitly considered for overpressure effects according to the analytic procedure defined by Method 2.

The method is governed by the following assumptions:

1. The skin panel is thin, flat, and rectangular with edges restrained against rotations and deflections, i.e., clamped.
2. The stringer or longeron supports one-half the pressure load acting on adjacent panels.
3. The ends of a stringer or longeron are fully restrained against deflection and rotation.
4. The frame is circular and has constant cross-section dimensions.
5. The frame supports one-half the pressure load acting on the fuselage between the frame preceding and the frame following the one being considered.
6. The pressure loading is transferred to the frame by the skin and stringers and local buckling of flanges or webs occurs before an overall instability of the frame develops.
7. Initial stresses due to preblast flight loads are negligible.
8. The preblast atmosphere is homogeneous, having characteristics associated with the aircraft altitude.

Regardless of the structural element under consideration, the analytic procedure consists of two basic phases. In the first phase, the static critical overpressure to produce the onset of damage is determined based on the material yield stress allowables. For the skin panels, the allowable stress corresponds to the tensile yield of the material. For the stringers, longerons and frames, the allowables are defined in terms of the elastic buckling (crippling) stress or the compressive yield stress, whichever is less.

In the second phase, a dynamic factor is computed based on the natural frequency of the structural element under consideration as well as on the time duration of the reflected blast wave and the reflection factor. The resultant critical overpressure value is then obtained as the critical static overpressure divided by the dynamic factor.

The sure-safe condition is defined according to the minimum critical overpressure computed for the weakest panel, stringer, longeron, or frame. The sure-kill condition is based on the critical overpressure determined for the strongest longeron with the cross-section characteristics and spacing corresponding to a fuselage station near the forward end of the tail cone.

The analysis of A-4C aircraft in accordance with Method 2 was accomplished using the OVPR2 code, which is structured to follow the iterative computational procedure developed for this method (Ref. 2). The required input data for OVPR2 solutions were chosen to ensure a basis for correlation between the analytic and the experimental data. The structural elements modeled correspond to those instrumented in the DICE THROW experiment. Skin panels 1, 5, and 6, in Figs. 8, 12, and 13, respectively, were represented in this manner to conform to the input format for an OVPR2 solution. Panel 1 was entered as the side panel, panel 5 as the top panel, and panel 6 as the bottom panel; see Table 3.

The analytic representation of the longeron element for the sure-safe condition was based on longeron 5 configuration, Fig. 12. As shown in Table 4, the critical overpressure is a function of the angle of incidence. This angle was assessed at 32 degrees at the longeron 5 location.

Following the Method 2 criteria, the analysis for the sure-kill condition was based on the section characteristics of the lower longeron, i.e., the strongest longeron, at

TABLE 3. OVPR 2 Solution for Panels 1, 5, and 6 - Sure-Safe Listing of Input and Output Data.

OVERPRESSURE ANALYSIS: METHOD 2: SECTION C1.2
 AIRCRAFT IDENTIFICATION - OVERPRESSURE ANALYSIS. A-4C AIRCRAFT. DICETHROOM
 THE CONDITION IS SURE-SAFE

SIMPLE LAYER PANELS			
THE AIRCRAFT ALTITUDE IS	4000.0 FEET		
THE WEAPON YIELD IS	1.00 KILTON		
THE HEIGHT OF THE GROUND ABOVE SEA LEVEL IS	4000.00 FEET		
THE AIRCRAFT IS PARIED			
	TOP PANEL	SIDE PANEL	BOTTOM PANEL
PANEL WIDTH BETWEEN SUPPORTING STRINGERS (IN)	3.4	5.6	3.9
PANEL LENGTH BETWEEN SUPPORTING FRAMES (IN)	14.4	14.3	7.9
PANEL THICKNESS (IN)	.032	.040	.032
RADIUS OF CURVATURE (IN)	2.6	3.0	2.6
MODULUS OF ELASTICITY (PSI)	-10E+08	-10E+08	-10E+08
TENSILE YIELD STRESS (PSI)	-030E+05	-030E+05	-030E+05
INTERNAL RAY PRESSURIZATION	0.000 PSI		
WEIGHT DENSITY (LBS/CU IN)	.100	.100	.100
CRITICAL VALUES OF LOCAL OVERPRESSURE FOR THE SKIN PANEL			
THETA (DEGREES)	TOP PANEL	SIDE PANEL	BOTTOM PANEL
0.0	10.54	7.83	9.15
10.0	8.71	6.57	7.60
20.0	7.56	5.75	6.62
30.0	6.77	5.15	5.92
40.0	6.24	4.73	5.44
50.0	5.85	4.42	5.09
60.0	5.55	4.18	4.83
70.0	5.42	4.02	4.72
80.0	5.29	3.82	4.62
90.0	5.17	3.74	4.52

BEST AVAILABLE COPY

TABLE 4. OVRP 2 Solution for Longeron 5 - Sure-Safe Condition
Listing of Input and Output Data.

	TOP ST-INCHES	MID ST-INCHES	BOTTOM ST-INCHES
DISTANCE TO ADJACENT STRINGER			
ON EITHER SIDE (IN)	3.0	3.0	3.0
STRINGER TO ADJACENT FRAMES (IN)	15.3	15.3	15.3
WIDTH OF LOWER FLANGE (IN)	.207	.207	.207
WIDTH OF UPPER FLANGE (IN)	.21	.21	.21
RADIUS OF CURVATURE (FT)	.2320	.2320	.2320
CROSS-SECTIONAL MOMENT OF INERTIA (IN ⁴)	.71	.71	.71
AREA MOMENT OF INERTIA (IN ⁴)	.630	.630	.630
MODULUS OF ELASTICITY (KSI)	106E+04	106E+04	106E+04
COEFFICIENT OF THERMAL EXPANSION (1/°F)	.000004	.000004	.000004
WEIGHT DENSITY (LBS/IN ³)	15.3	15.3	15.3
THE BUCKLING COEFFICIENT FOR LOWER FLANGE	15.3	15.3	15.3
THE BUCKLING COEFFICIENT FOR UPPER FLANGE	15.3	15.3	15.3
THE BUCKLING COEFFICIENT FOR LOWER FLANGE	15.3	15.3	15.3
THE BUCKLING COEFFICIENT FOR UPPER FLANGE	15.3	15.3	15.3
CRITICAL VALUES OF LOCAL BUCKLING STRESS FOR ST-INCHES			
TOP (KSI)	15.3	15.3	15.3
MID (KSI)	15.3	15.3	15.3
BOTTOM (KSI)	15.3	15.3	15.3
TOP (KSI)	15.3	15.3	15.3
MID (KSI)	15.3	15.3	15.3
BOTTOM (KSI)	15.3	15.3	15.3
TOP (KSI)	15.3	15.3	15.3
MID (KSI)	15.3	15.3	15.3
BOTTOM (KSI)	15.3	15.3	15.3

fuselage station 387, Fig. 37. OVPR2 input data for the lower longeron together with the analytic results are presented in Table 5.

The frame analysis restricted, as in the case of skin panels, to the sure-safe condition was based on the fuselage frame station data presented in Table 6 which also includes the analytic results.

METHOD 3

By far the most sophisticated of the three methods, Method 3, offers detailed and diversified modeling of aircraft structural elements. It also includes a comprehensive blast representation based on a state-of-the-art airblast model and permits completely arbitrary selection of the scenarios defining the spatial relation of the aircraft with respect to the detonation point. In its latest version, Method 3 contains a special provision for a point by point representation of the blast characteristics on the local level (i.e., pertaining directly to the structural element analyzed) which can be advantageously applied to simulate actual experimental data.

NOVA-2 (Nuclear Overpressure Vulnerability Analysis, Version 2), Ref. 7, the computer program for Method 3, provides a technique for predicting the elastic and elastic-plastic response of aircraft structural elements to transient pressure loads associated with the blast wave from a nuclear explosion.

The program consists of three distinct routines, NOVA, DEPROB (Dynamic Elastic Plastic Response of Beams), and DEPROP (Dynamic Elastic Plastic Response of Panels), written in FORTRAN IV language.

The NOVA routine is the master routine which controls the logic of the overall program. It contains the sub-routines for (1) predicting the aerodynamic flight loads and the blast pressure loads that are applied to the lifting surfaces and fuselage during subsonic and supersonic flight and (2) determining the slant range at which a structural element incurs damage which has been specified on a probabilistic basis.

The DEPROB routine provides the response of aircraft structure such as stringers, longerons, frames, ribs, and conical or cylindrical radomes which can be represented by

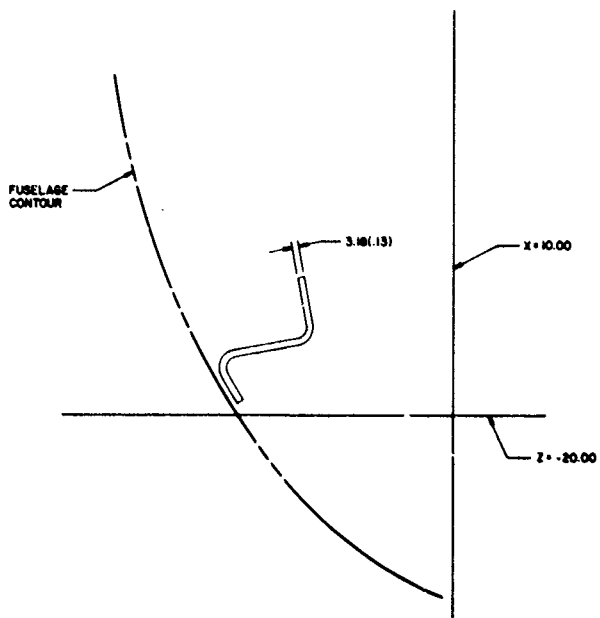


FIGURE 37. Lower Longeron Configuration Diagram.

BEST AVAILABLE COPY

TABLE 6. OVR 2 Solution for Fuselage Frame - Sure-Safe Condition
Listing of Input and Output Data.

CRITICAL FRAME		BOTTOM FRAME	
DISTANCE TO ADJACENT FRAMES	15.3		5.76
ON EITHER SIDE (IN)	14.3		5.04
THICKNESS OF INNER FLANGE (IN)	.050		4.52
WIDTH OF INNER FLANGE (IN)	.50		4.11
RADIUS OF FUSELAGE (FT)	2.5		3.80
CROSS-SECTIONAL AREA (SQ IN)	.3162		3.55
DISTANCE FROM INNERMOST EDGE TO CENTERLINE (IN)	2.33		3.35
AREA MOMENT OF INERTIA (IN ⁴)	.435		3.24
MODULUS OF ELASTICITY (PSI)	.104E+04		3.23
COMPRESSIVE YIELD STRESS (PSI)	.690E+05		3.14
WEIGHT DENSITY (LBS/CU IN)	.210		
THE BUCKLING COEFFICIENT FOR THE INNER FLANGE IS 1.25			
CRITICAL VALUES OF LOCAL COMPRESSURE FOR FRAMES		SIDE FRAME	
TORTA (DEGREES)		TOP FRAME	
0.0	5.74		5.76
10.0	5.84		5.04
20.0	4.57		4.52
30.0	3.81		4.11
40.0	3.56		3.80
50.0	3.35		3.55
60.0	3.24		3.35
70.0	3.23		3.24
80.0	3.14		3.23
90.0			3.14

an annular cross section. The method of analysis used in this routine applies to beams which can be modeled in one dimension by a series of discrete masses interconnected by weightless springs. It features the ability to analyze elements with variable cross section, both simply supported and free edge conditions, an improved elastic-plastic stress-strain model, and the inclusion of rib buckling as a failure mechanism.

The DEPROP routine provides the response of aircraft skin panels, canopies, and radomes that can be approximated by a cylindrical panel. The linear elastic option applies to single and multilayered panels of isotropic or orthotropic material; and the elastic-plastic option applies to single-layered panels of isotropic material. DEPROP includes (1) symmetric or nonsymmetric combinations of clamped or simply supported edge constraints, (2) a much improved elastic-plastic stress-strain model, and (3) improved overall accuracy.

Method 3 offers individual treatment for a variety of structural elements through specified input data which call for detailed modeling of an individual element under consideration and the surrounding structure. This enables the determination of the local overpressure conditions in conjunction with the blast model incorporated within the program.

When local overpressure data are available, e.g., experimental data, the program computes transient response of that individual element based on the supplied overpressure data.

A special provision of the program allows a panel response solution through a beam representation. This solution yields results of acceptable accuracy and offers a considerable saving in the computer time which may be one-tenth of that required for a corresponding regular panel solution.

The A-4C aircraft analysis using NOVA-2 code was directed towards:

1. Obtaining the maximum amount of data for direct correlation with the experimental test data.
2. Providing adequate comparisons between the various analytic solution modes.

Note that the distinction is made here between a solution based on the analytic blast model and a solution using arbitrary (may be experimental) local overpressure data.

The scope of the analysis is presented in Table 7 where DEPROP and DEPROB denote, respectively, the panel and beam solutions based on the analytic blast models. KADBOP and KADBOB denote the panel and beam solutions, respectively, using arbitrary overpressure data inputs.

Beam representation of a panel using the analytic overpressure model is denoted by KADBOB-A.

RESULTS CORRELATION

This part of the report is devoted to the presentation of the analytic results and their correlation with the experimental data obtained from the test conducted on the A-4C aircraft.

The analytic results obtained for each method are presented in separate paragraphs which include comprehensive discussions. For each case, the discussion describes the area and the degree of correlation between the analytic and experimental data.

METHOD 1

The sure-safe and sure-kill envelopes constructed according to the procedure for Method 1 are presented in Figs. 38 and 39, respectively. For a ground detonation and a parked aircraft, corresponding to the DICE THROW event configuration, the sure-safe and sure-kill ranges shown on these figures are 693 m (2275 ft) and 210 m (690 ft), respectively.

Only a generalized and largely qualitative correlation between these results and the experimental data is possible since Method 1 is limited in scope to the determination of the critical range values according to the specified sure-safe and sure-kill criteria. These range values which are based on predetermined allowable peak overpressures do not offer a suitable basis for correlation with the experimental data obtained for different overpressure conditions. However restrictive this situation, revealing observations can be made in assessing validity of this method.

TABLE 7. Chart of the NOVA-2 Solution Runs.

Structural Element	Panel Representation		Beam Representation		
	DEPROP	KADBOB	DEPROB	KADBOB	KADBOB-A*
Panel 1	X	X	-	X	X
Panel 4	X	X	-	X	-
Panel 5	X	-	-	X	-
Panel 8	-	-	-	X	-
Longeron 5	-	-	X	X	-
Frame 277	-	-	X	-	-

*KADBOB-A denotes the solution of a panel represented as a beam subjected to the analytic overpressure entered as a point by point input.

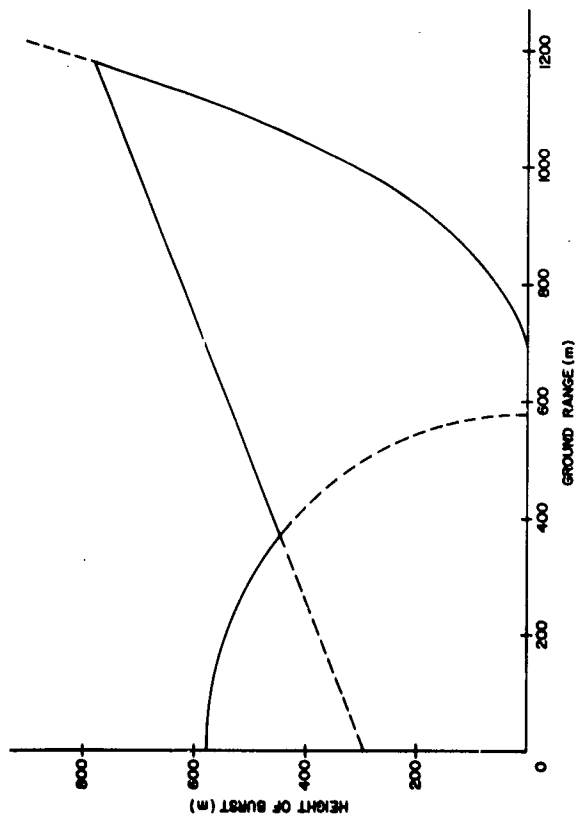


FIGURE 38. Sure-Safe Envelope, Method 1.

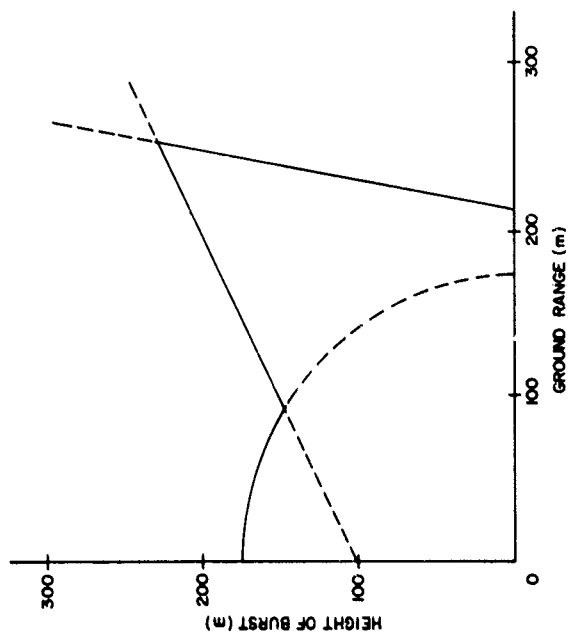


FIGURE 39. Sure-Kill Envelope, Method 1.

The assessment of damage sustained by the instrumented A-4C aircraft located at 375 m (1230 ft) from the GZ suggested that the sure-safe condition was exceeded at 41.4-kPa (6 psi) peak overpressure. This was indicated by localized damage particularly in the fuselage STA 277 region, Fig. 25, where the failure of the frame to lower longeron joint led to panel skin rupture.

The experimental results show that this joint was the critical structural element. Unfortunately, no strain records were obtained for that area because this was not previously predicted to be the weak element.

However, the localized nature of the failure implies that the loading was not grossly in excess of yield; otherwise, more widespread failure would have resulted. This, in turn, leads to the final observation that, for A-4C aircraft, the vulnerability prediction according to Method 1 for sure-safe condition is decidedly conservative.

The consideration of the sure-kill condition presents a directly opposite picture. Here, the analytic value of 210 m (690 ft) for the critical range corresponding to 137.9-kPa (20 psi) peak overpressure is well in excess of 62.1-kPa (9 psi) peak overpressure which was sufficient to produce the catastrophic failure of the aircraft located 311 m (1020 ft) from the GZ. This immediately suggests that the analysis is severely unconservative.

There is no accurate way to predict from the available experimental data the lowest overpressure level which would have produced a catastrophic failure. Assuming that 62.1 kPa (9 psi) represented a minimum overpressure value for a catastrophic failure to occur, this is equivalent to at least 120 percent error in the critical overpressure postulated by the analysis.

In the final assessment, the test has demonstrated that Method 1 applied to the aircraft in the fighter and fighter-bomber classes, as represented by A-4C aircraft, tends to be conservative in predicting the critical range for sure-safe condition, but unconservative in predicting the critical range for sure-kill condition. However, the extent of conservatism and unconservatism fall within the error limits specified in the method formulation.

The plots of the analytic solutions presented in Figs. 38 and 39 appear rather crude. The multiple ground range values obtained for a given height of burst are not realistic and tend to be confusing.

For an analyst familiar with Method 1, the analysis requires an estimated 20 minutes of engineering time to perform and less than one second computer time to execute on a large computer. The method provides a means for rapid determination of the vulnerability envelopes and can be satisfactorily used where a solution error factor of two is acceptable.

METHOD 2

Skin Panels

The analytic data obtained for three panels are presented in Table 8 and are applicable to the sure-safe condition only. They represent three sets, each consisting of ten critical overpressure values related to the angle of incidence, theta, which is defined as the angle subtended between the panel surface and the direction of shock propagation.

For panel 1, the critical overpressure of 27.2 kPa (3.94 psi) was indicated at 90-degree angle of incidence which corresponded to the actual panel orientation during the test.

With incidence angles of approximately 30 and 90 degrees for panels 5 and 6, respectively, the corresponding critical overpressure values of 46.9 kPa (6.8 psi) and 31.2 kPa (4.52 psi) were obtained.

The selection of panels 1, 5, and 6 for the skin panel representation in the analysis was made to provide the best possible correlation between the analytic and experimental data. These panels were suitably instrumented with strain gages and produced satisfactory strain data during the test.

However, the overall survey of the strain data indicated that the actual panel response falls somewhere between the idealized simply supported and clamped edge boundary conditions. This was particularly apparent for panels 1, 2, and 4. For these panels, strains of comparable magnitudes were obtained at the panel center and at mid-points along the longer edge.

TABLE 8. Peak Experimental Strain Data Summary
for Panels 1 through 8.

Panel No.	Panel Center Inside Surface		Panel Longer Edge Outside Surface	
	Microstrains	Gage No.	Microstrains	Gage No.
1	3400	1	2600 2880	9 10
2	-	-	2200 2180	15 17
3	3900	19	-	-
4	5000	24	6000	27
5	-	-	8000 8800	31 32
6	3200	34	7600	35
7	-	-	4600	37
8	3800	40	2400	42

NOTE: (a) Strain gage locations are shown in Figs. 8
through 15.
(b) Peak strains are tensile in every case.

It appears, therefore, that the assumption of clamped edge boundary conditions for the panels does not necessarily hold true in the actual true-to-life aircraft structure. The less than rigid quality of the panel boundary substructure comprising panel boundaries and the structural deterioration of the entire aircraft structure through the years of service should be considered among the factors likely to contribute to the departure from the idealized panel behavior.

The apparent inconsistency between the experimental data and the behavior of idealized panels with clamped edge boundary conditions can also be attributed to the fact that the exact locations of panel boundaries could not be determined. The location of the panel boundary depends on the configuration of substructure and its rigidity. Where the substructure is less than rigid, the effective boundary location also depends on the deformation which is a function of the loading. Consequently, the strain gages installed in the vicinity of the panel edge, where steep strain gradients prevailed, produced data which could be easily misinterpreted.

There are two alternatives. On one hand, there is a possibility that a skin panel, which constitutes an element of a larger structural component, does not necessarily respond according to idealized, clamped edge boundary conditions. On the other hand, the experimental data obtained from even slightly misplaced strain gages can easily lead to erroneous observations.

At this stage, no sufficient evidence is available to ascertain which of these possibilities should play the dominant role in the experimental data interpretation. This situation severely complicates any attempt to verify Method 2 on the basis of the experimental data.

However, closer examination of the strain gage data summarized in Table 8, in conjunction with Figs. 8 through 15, further implied that the actual panel response was somewhere in between the clamped edge and simply supported boundary conditions. Steep strain gradients in the vicinity of the panel edge did exist, but strains of comparable magnitude might have also been present at the center of the panel. The typical response for a panel with clamped edge boundary condition was not entirely evident in the experimental data for panels 5 and 6. The thinner skin of panel 5, as compared to panel 1, naturally developed higher strains (gages 31 and 32 as compared to gages 9 and 10). These high

strains might have been accompanied by comparably high strains at the panel center in a pattern similar to that of panels 1, 2, and 4. The local failure of panel 6 substrate no doubt affected the skin strains to the extent that the panel response cannot be represented by the clamped edge condition.

From the foregoing arguments emerges a postulate that the experimental data reflected with a fair degree of accuracy the actual strains developed in skin panels during the test. Based on that postulate, qualifying statements regarding Method 2 can now be made.

The sure-safe condition for Method 2 implies impending yield of material. For the biaxial stress field this can be defined by

$$F_y = \frac{E \epsilon_y}{1-\nu^2}$$

where F_y (63000 psi) is the yield stress,
 E_y (10.4×10^6 psi) denotes the Modulus of Elasticity,
and ν (0.33) is the Poisson's Ratio.

Then, the corresponding yield strain, ϵ_y , in the direction normal to the panel longer edge is approximately 5400 microstrains.

The yield condition for panel 1 indicated by the analysis was at 27.2-kPa (3.94 psi) peak overpressure. However, the experimental data showed no yield even at 41.4-kPa (6 psi) peak overpressure. In fact, only 60 percent of yield was reached.

A directly opposite picture is presented in the case of panel 5, for which the yield condition was obtained analytically as 46.9-kPa (6.8 psi) peak overpressure. According to the experimental data, at 41.4-kPa (6 psi) peak overpressure, the yield condition was already exceeded by 48 percent of the yield strain value.

Considerable discrepancies between the analytic and experimental data are in evidence for the panel structural elements. Within these discrepancies, the analytic values of critical peak overpressure may be higher or lower than the corresponding experimental data by an appreciable margin. However, since the degree of accuracy of the experimental data could not be adequately determined, there is insufficient evidence to verify or deny the validity of Method 2.

In any case, the observed discrepancies appear to fall within the error factor of 1.6 specified by the method for the vulnerability ranges determined in the sure-safe condition analysis.

Method 2 is distinctly superior to Method 1 as it provides for a selection and analysis of weakest structural elements which are individually modeled in some detail. The analytic solutions using OVPR2 code are readily obtained in less than 10 seconds of computer time on a large computer.

Longerons

For the sure-safe condition, the analysis modeled longeron 5. The analytic results are presented in Table 4. Shock incidence at that location was 32 degrees and the critical peak overpressure was assessed at 65.6 kPa (9.51 psi).

For the sure-kill condition, the lower longeron was used in the analysis and the resulting critical peak overpressure values are summarized in Table 5. For the actual lower longeron location, the shock incidence angle was approximately 90 degrees and the critical peak overpressure was 50.3 kPa (7.3 psi).

The most striking result of the longeron analysis is that a higher critical peak overpressure was indicated for the sure-safe condition than for the sure-kill condition. This apparently irrational result was not altogether unexpected when one considers the modeling process for longeron elements prescribed by the method.

The weakest longerons selected for the sure-safe condition analysis were closely spaced. Consequently, the effective pressure loads sustained by an individual longeron were relatively small and a large critical peak overpressure value was predicted by the analysis. For the sure-kill condition, the strongest longerons were modeled; however, they were spaced far apart. This was equivalent to a disproportionately higher pressure load being sustained by this longeron and produced a lower critical peak overpressure value.

It appears, therefore, that very careful consideration, based primarily on the analytic experience, must be exercised in the selection of longeron elements to assure compatible analytic results.

In the case of A-4 aircraft, the selection of longeron elements for modeling was difficult. The fuselage structure was made up of closely spaced frames and ring-like, stiffener members. Typical stringers were absent and the longitudinal structural members were limited to two types of longerons represented in the analysis.

Adequate strain gage instrumentation of the longerons was not available for the test because of limited recording channels, and other sources of relevant experimental data were totally absent. However, some insight into the overall structural integrity was gained from the extent of damage sustained by the aircraft exposed to different overpressure levels. At 41.4-kPa (6 psi) free-field peak overpressure, no damage of longerons was evident. At 62.1-kPa (9 psi) overpressure, the catastrophic failure of the fuselage, initiated in the vicinity of the frame STA 277, progressed through the weak longerons and led to a rupture of the strong longerons and the entire section of the fuselage.

For the specified test conditions, the longeron vulnerability between no damage and catastrophic failure are equivalent to a 64 m (210 ft) change in the range from the GZ, i.e., from 375 m (1230 ft) to 311 m (1020 ft).

The critical free-field peak overpressures predicted according to Method 2 are equivalent to the ranges between 305 m (1000 ft) and 335 m (1100 ft) from the GZ. This is well within the 1.6 error factor value specified for this method. Therefore, the analytic results obtained for longerons are reasonable.

Fuselage Frame

The frame analysis data based on fuselage frame STA 277 are presented in Table 6, and the indicated minimum critical peak overpressure value was 21.9 kPa (3.18 psi). According to the free-field overpressure data collected during the test, this pressure level was recorded approximately 610 m (2000 ft) from the GZ.

Considering that a damage of fuselage frame STA 277 was sustained by both aircraft fielded 375 m (1230 ft) from the GZ, the analytic prediction may be assessed outright as at least reasonable. It almost falls within the 1.6 error factor value specified for the method. However, noting the extent of damage, it is immediately suggested that yielding

of the material had to begin at substantially lower load level. This can be readily deduced by examining Fig. 25 which shows failure of the joint between frame STA 277 and the lower longeron in the instrumented aircraft BUNO 149588. There, sheared fasteners and the displacement of the attaching angle from its normal location are clearly visible. The displacements of that magnitude were associated with considerable plastic deformation preceded, of course, by yielding. In the second aircraft BUNO 145062, failure of frame STA 277 was more severe and more extensive. Besides the joint failure, the frame flanges buckled and ruptured higher up the span, approximately 0.61 m (2 ft) above the lower longeron joint, Fig. 30. It was interesting to note that the flange failure occurred at a cutout hole in the frame web, which was present in aircraft BUNO 145062 but absent in aircraft BUNO 149588.

With this demonstration that the frame yielded at an overpressure level distinctly below 41.4 kPa (6 psi) and therefore closer to the predicted value of 21.9 kPa (3.18 psi), experimental verification of Method 2 for the frame element analysis is satisfactorily accomplished.

METHOD 3

Results of the analysis, covering all options available in NOVA 2, are presented in a series of plots for strain data versus time, with zero-time corresponding to the instant of blast intercept. Wherever applicable, plots of pertinent experimental data are also included, superimposed on the analytic data.

Five skin panels, one longeron and one frame represent the three types of structural elements analyzed using the NOVA 2 code. Each element is covered in separate paragraphs which follow.

Skin Panels

The overriding objective of this study was to implement a correlation between the experimental and analytic data. Thus, considerable effort was initially made to provide a representation of various panel configuration parameters in order to assess their effect on panel response to blast. However, as mentioned earlier, restrictions imposed by practical considerations reduced the parametric aspect of this study to:

1. Flat and curved panels.
2. Clamped and simply supported edge boundary conditions.
3. Panels of different width.

A comparison between a flat and a curved panel was provided by panels 1 and 5 respectively. Panels 1 and 8 represented the clamped and simply supported edge boundary conditions, respectively. Panels 4 and 5 illustrated the effect of the width parameter variation on the panel response. Panel 6, which was also covered analytically, should be considered separately. Its slightly trapezoidal rather than rectangular shape renders it unsuitable for a direct correlation with other panels.

The data plots for these five panels are presented in three sets. Figures 40 through 49 represent strain and deflection data obtained from the solutions based on the analytic blast model.

The panel solutions based on the experimental overpressure data (KADBOP solutions) are illustrated by Figs. 50 through 54. The corresponding data for beam representation of panels (KADBOB solutions) are given in Figs. 55 through 67.

The analytic blast model and the experimental overpressure data are correlated in Figs. 68 through 72 for each panel analyzed.

The panel response observed during the test has been described in general terms in the assessment of Method 2. Additional and more detailed observations will follow as more pertinently applicable to the assessment of Method 3.

Several comments concerning the overpressure characteristics related to structural elements in general seem appropriate at this point. Examination of the pressure gage records revealed considerable variation of overpressure across structural elements, such as skin panels, during the blast diffraction phase. (See pressure gage data in Volume II. of NWEF Report 1145, Ref. 6.) The time of shock arrival was found generally to vary from point to point on the panel

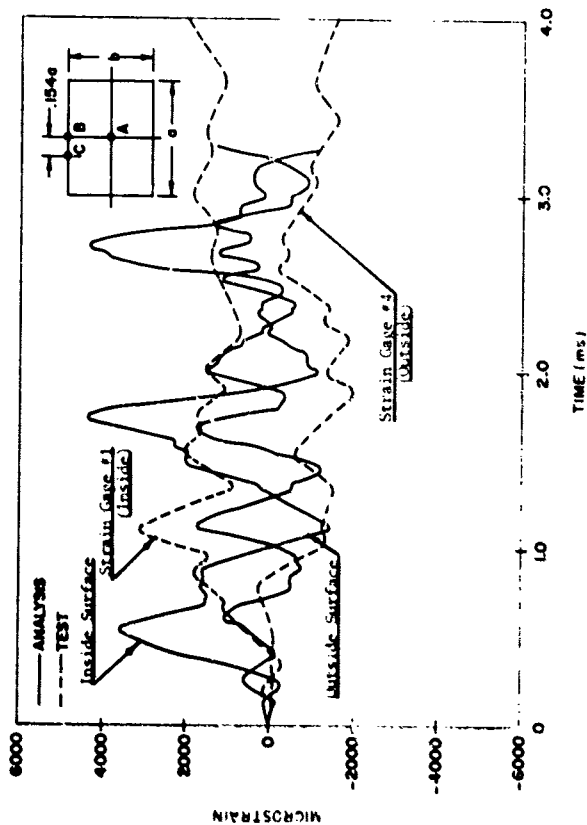


FIGURE 40. Strain Data Correlation for Panel 1 - Location A.
NOVA 2 - DEPROP Solution.

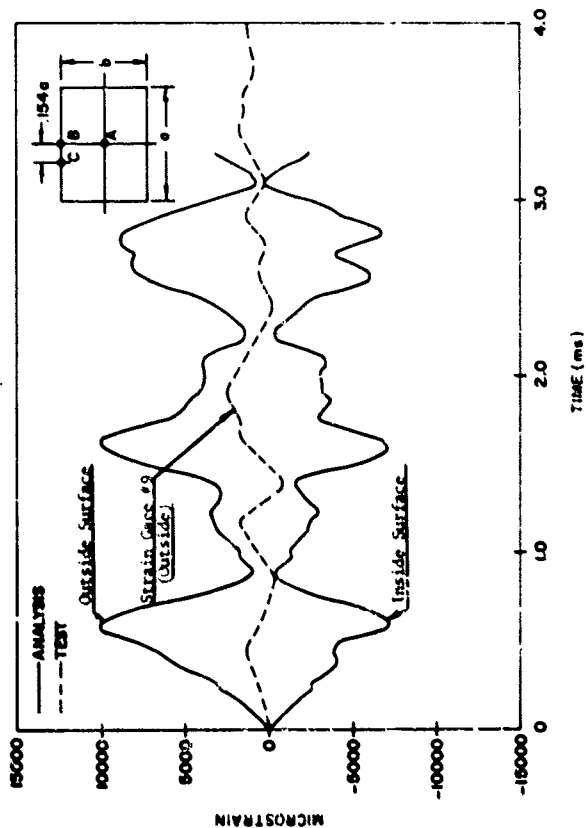


FIGURE 41. Strain Data Correlation for Panel 1 - Location B
NOVA 2 - DEPRCP Solution.

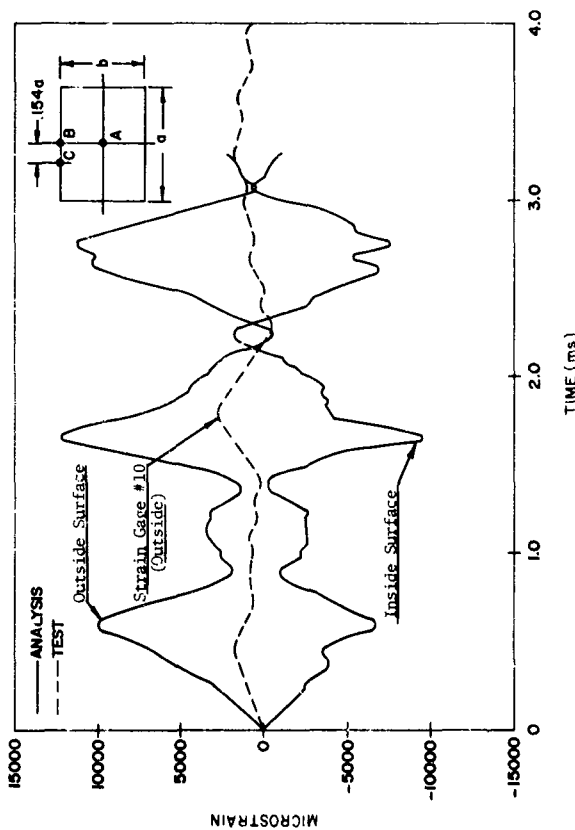


FIGURE 42. Strain Data Correlation for Panel 1 - Location C
NOVA 2 - DEPROP Solution.

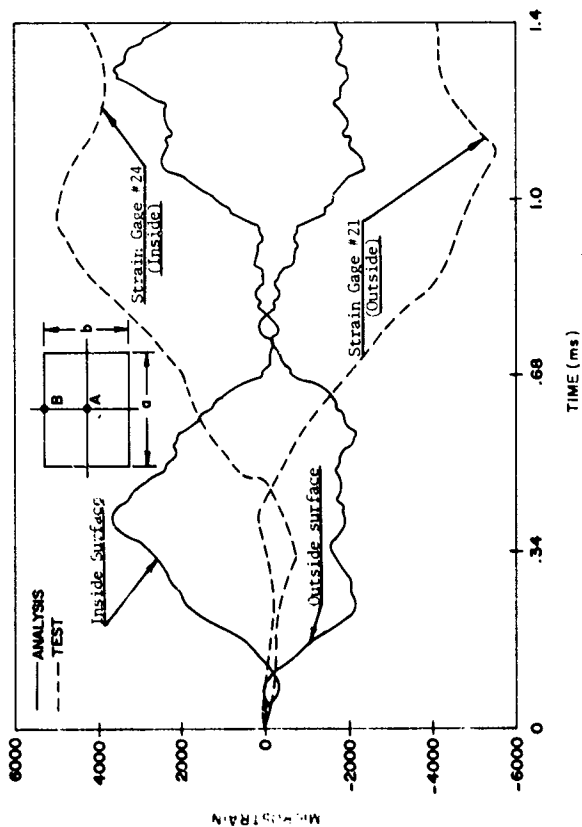


FIGURE 43. Strain Data Correlation for Panel 4 - Location A
NOVA 2 - DEPROP Solution.

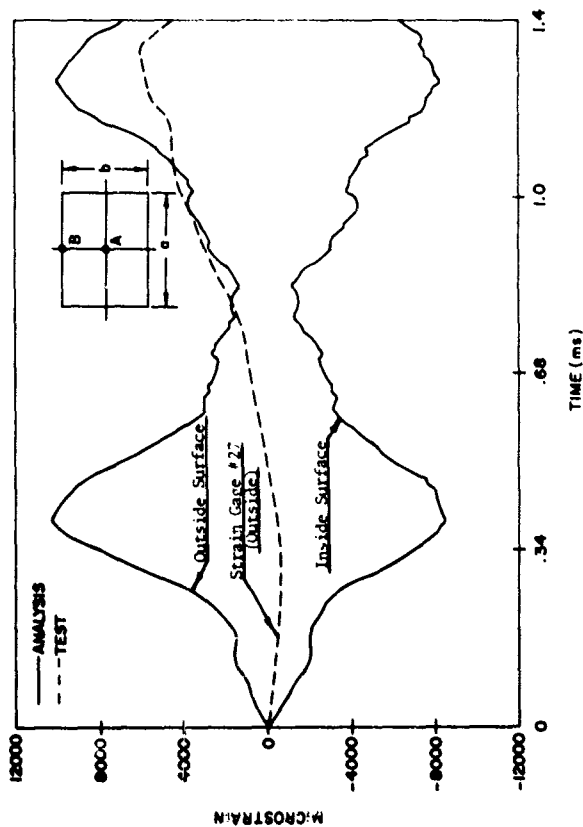


FIGURE 44. Strain Data Correlation for Panel 4 - Location B
NOVA 2 - DEPROP Solution.

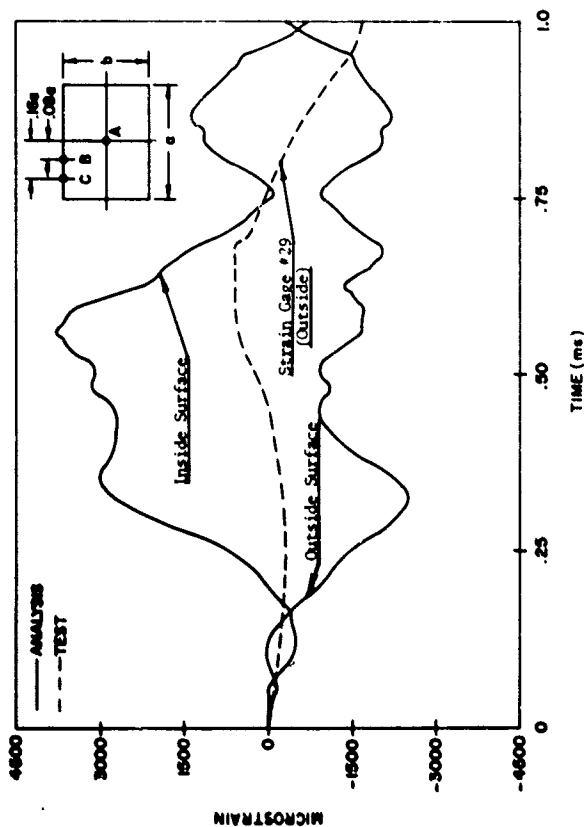


FIGURE 45. Strain Data Correlation for Panel 5 - Location A
NOVA 2 - DEPROP Solution.

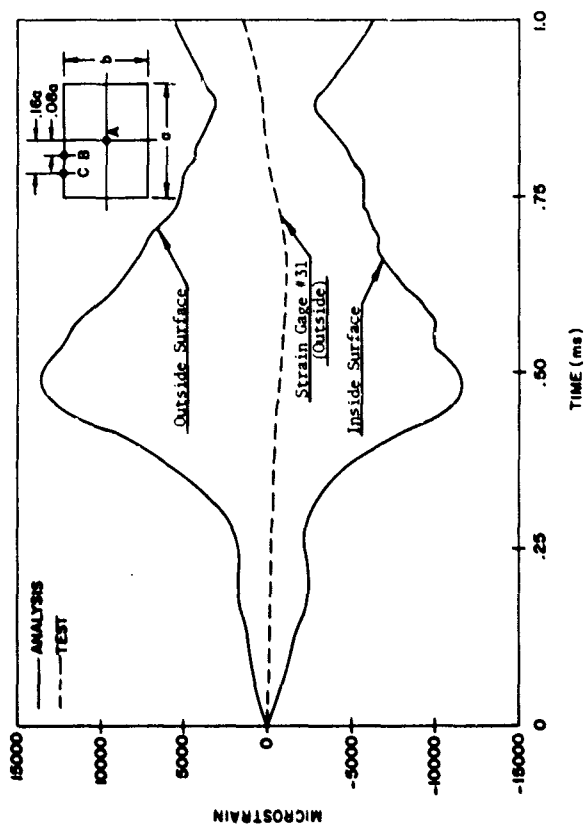


FIGURE 46. Strain Data Correlation for Panel 5 - Location B
NOVA 2 - DEPORP Solution.

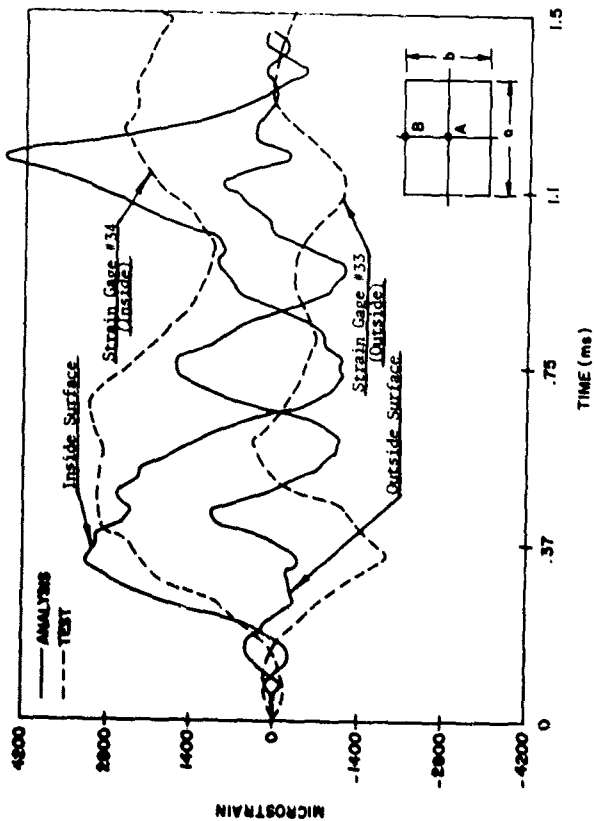


FIGURE 48. Strain Data Correlation for Panel 6 - Location A
NOVA 2 - DEPROP Solution.

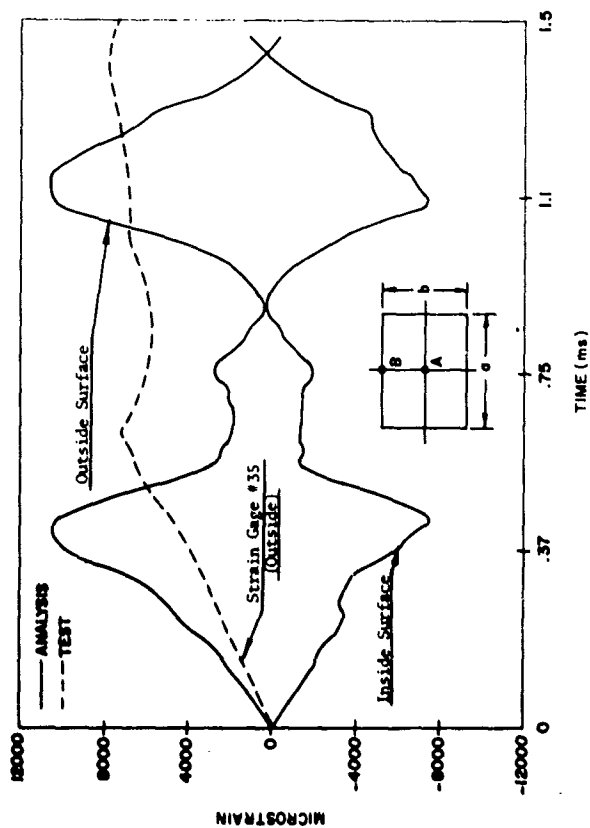


FIGURE 49. Strain Data Correlation for Panel 6 - Location B
NOVA 2 - DEPROP Solution.

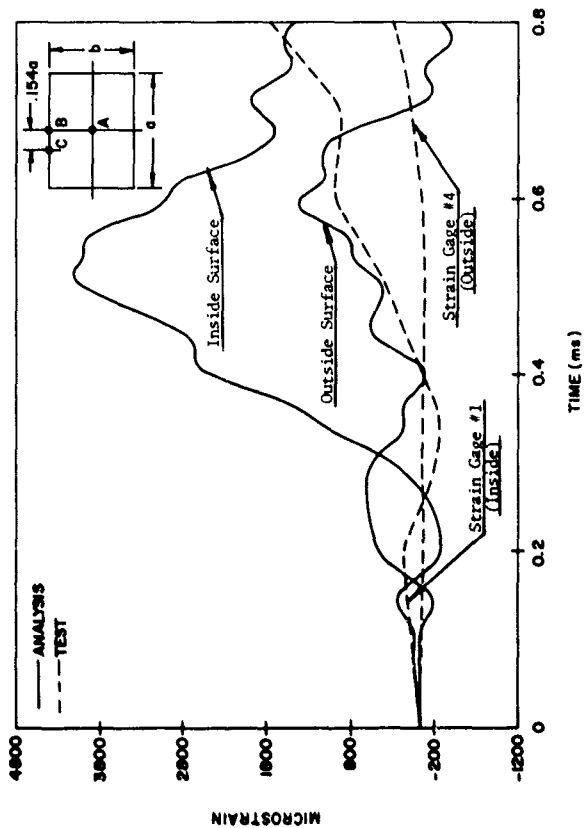


FIGURE 50. Strain Data Correlation for Panel 1 - Location A
NOVA 2 - KADBOP Solution.

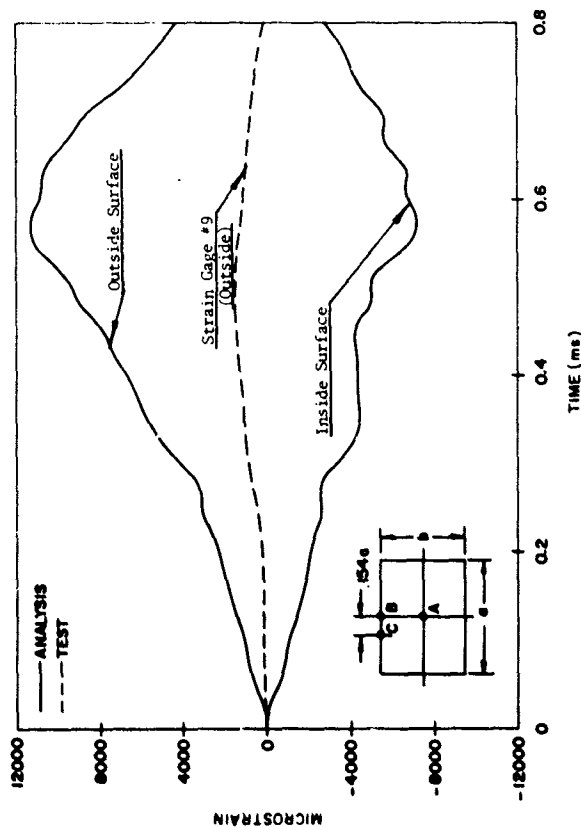


FIGURE 51. Strain Data Correlation for Panel 1 - Location B
NOVA 2 - KADBOP Solution.

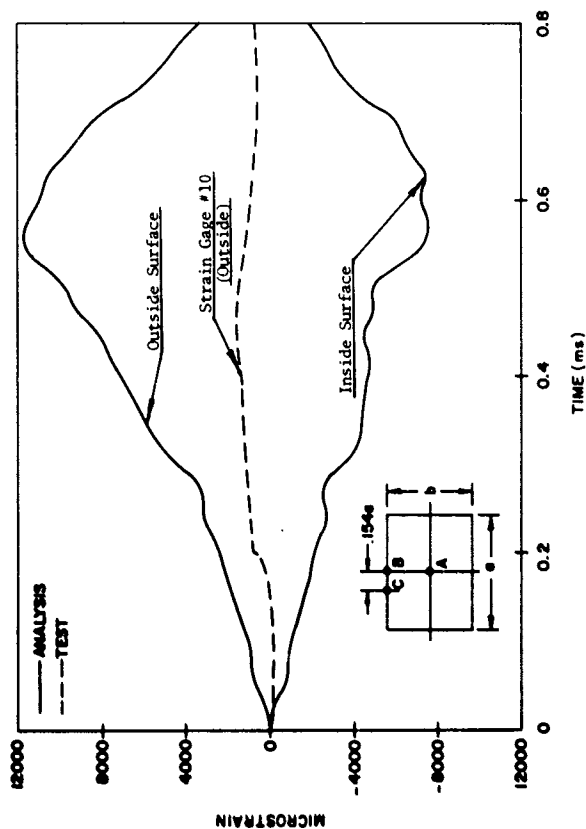


FIGURE 52. Strain Data Correlation for Panel 1 - Location C
NOVA 2 - KADBOP Solution.

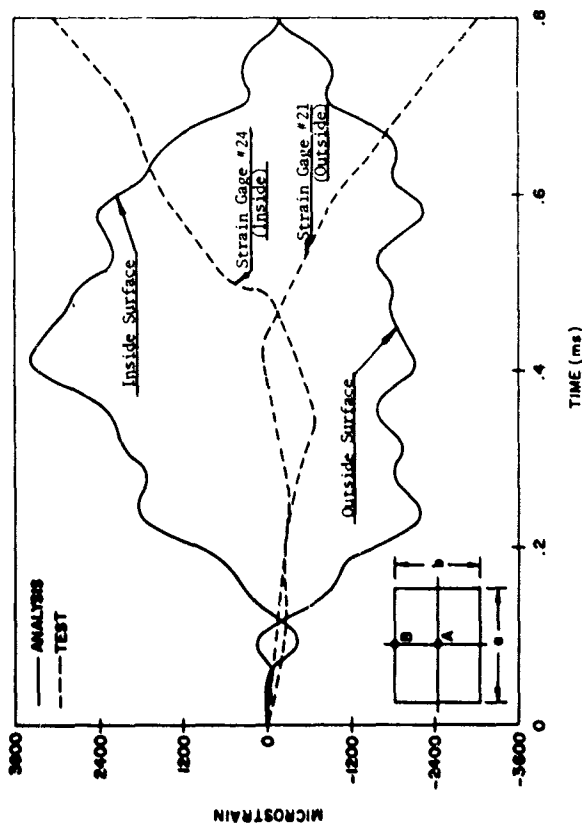


FIGURE 53. Strain Data Correlation for Panel 4 - Location A
NOVA 2 - KADBOP Solution.

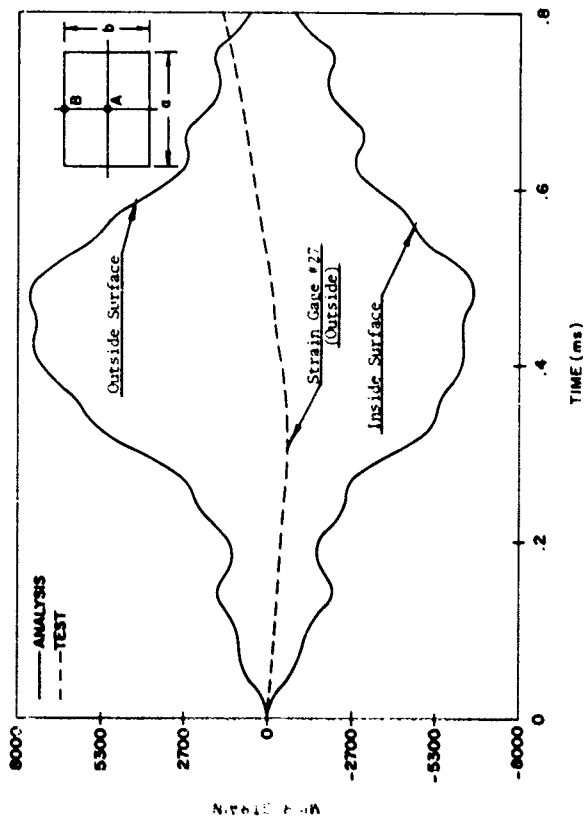


FIGURE 54. Strain Data Correlation for Panel 4 - Location B
NOVA 2 - KADBP Solution.

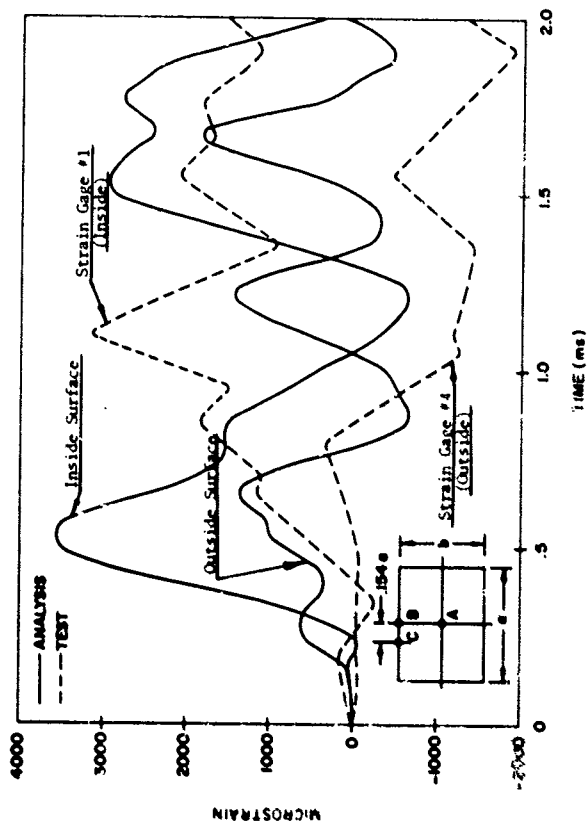


FIGURE 55. Strain Data Correlation for Panel 1 - Location A
NOVA 2 - KADROB-A Solution (Ref. TABLE 7).

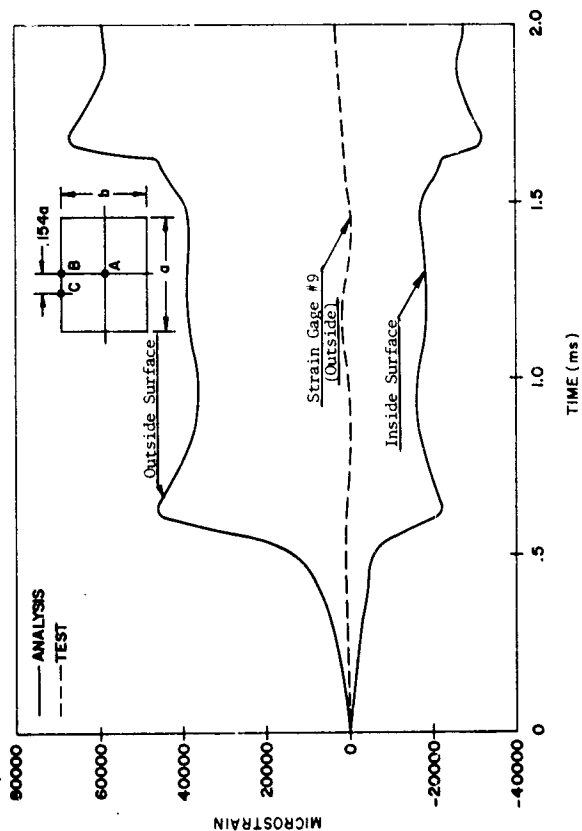


FIGURE 56. Strain Data Correlation for Panel 1 - Location B
NOVA 2 - KADBOB-A Solution (Ref. TABLE 7).

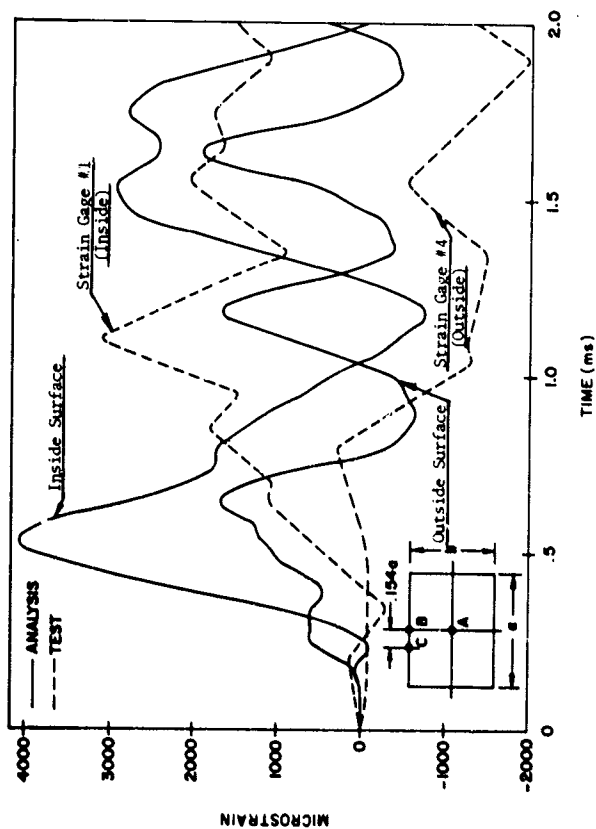


FIGURE 57. Strain Data Correlation for Panel 1 - Location A
NOVA 2 - KADBOB Solution.

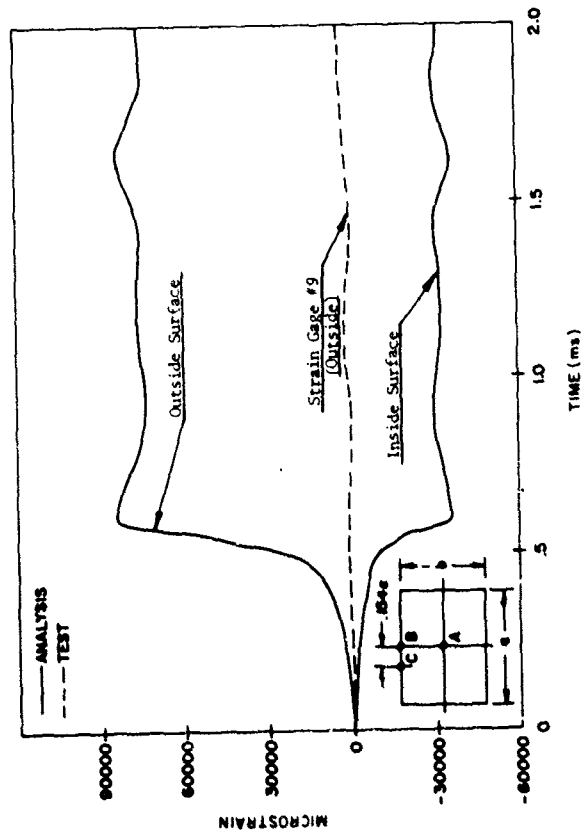


FIGURE 58. Strain Data Correlation for Panel 1 - Location R
NOVA 2 - KADBOB Solution.

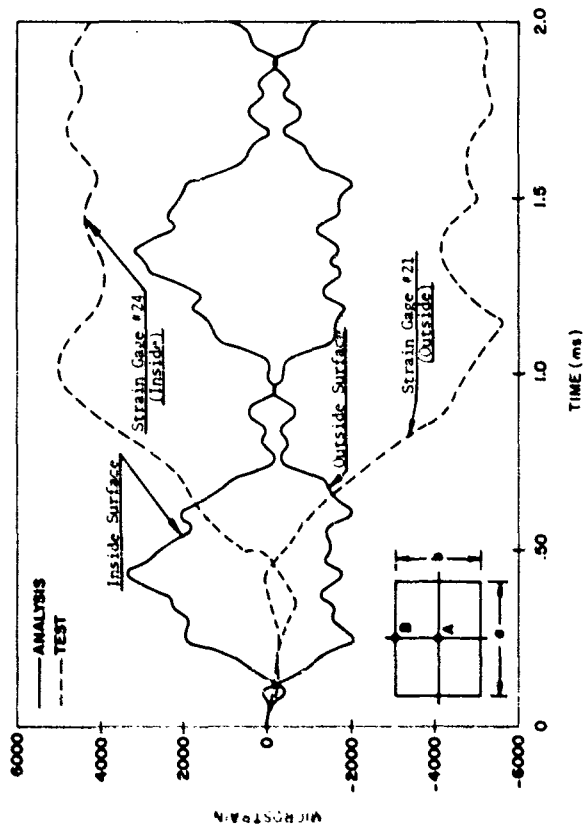


FIGURE 59. Strain Data Correlation for Panel 4 - Location A
NOVA 2 - KADBOB Solution.

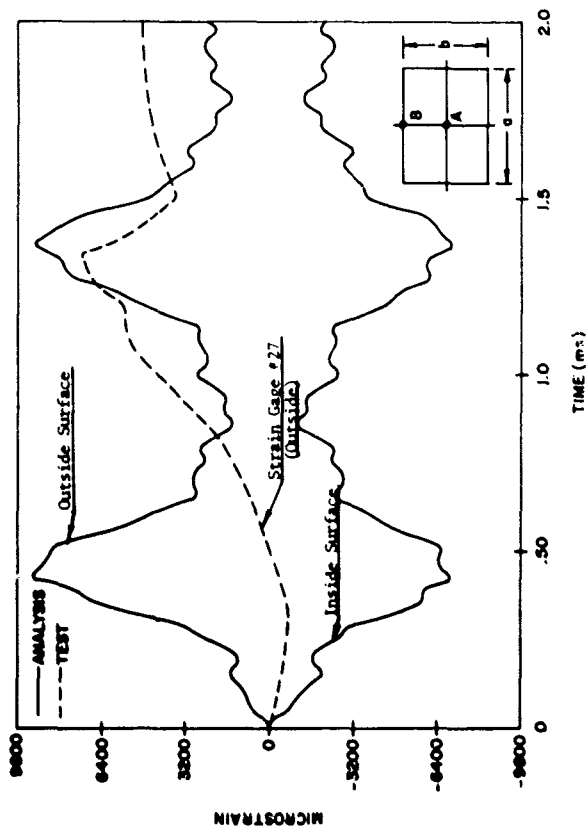


FIGURE 60. Strain Data Correlation for Panel 4 - Location B
NOVA 2 - MADBOB Solution.

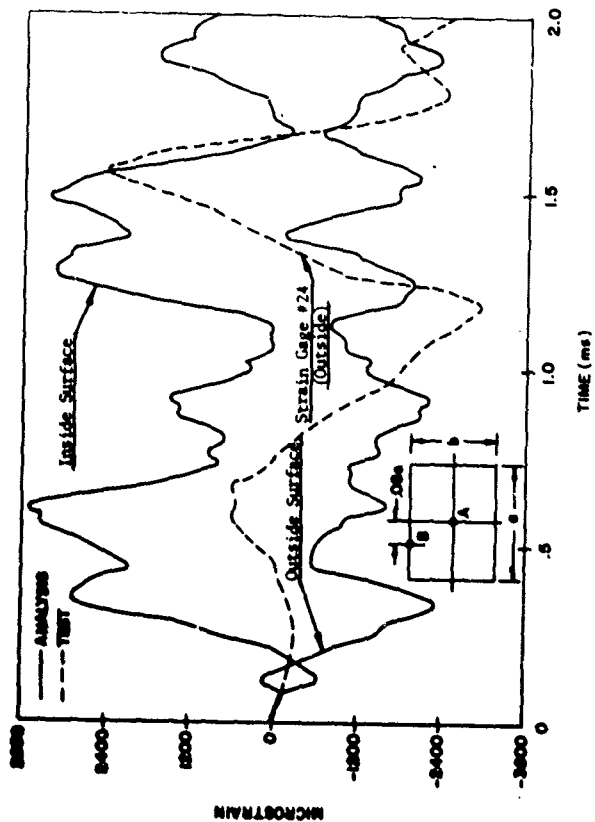


FIGURE 61. Strain Data Correlation for Panel 5 - Location A
NOVA 2 - KADBOB Solution.

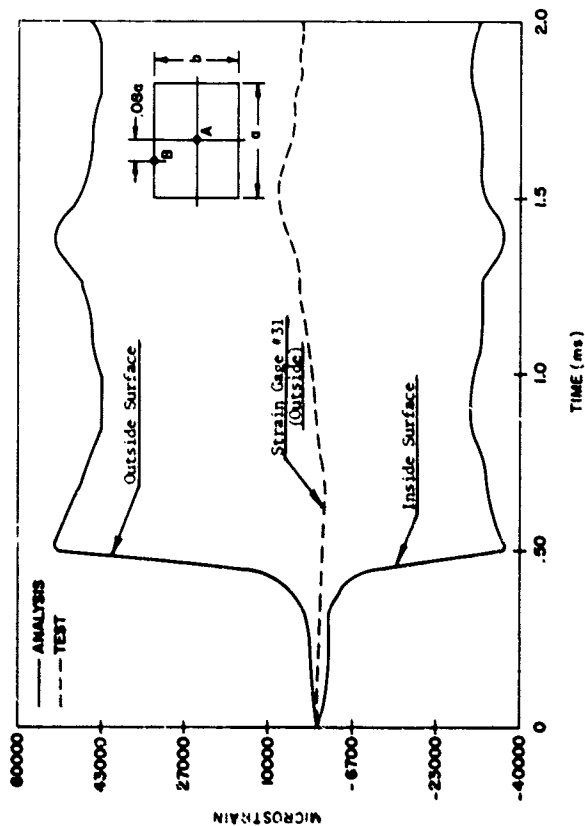


FIGURE 62. Strain Data Correlation for Panel 5 - Location B
NOVA 2 - KADBOB Solution.

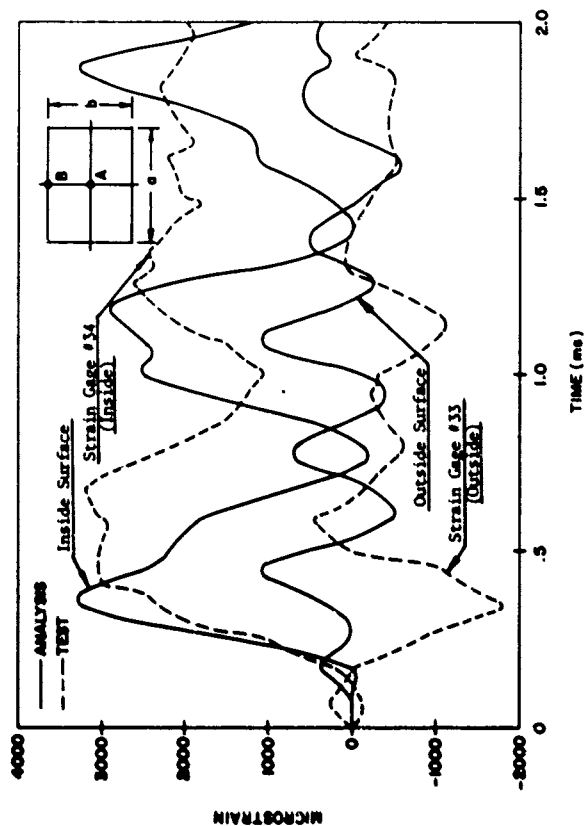


FIGURE 63. Strain Data Correlation for Panel 6 - Location A
 NOVA 2 - KADOB Solution.

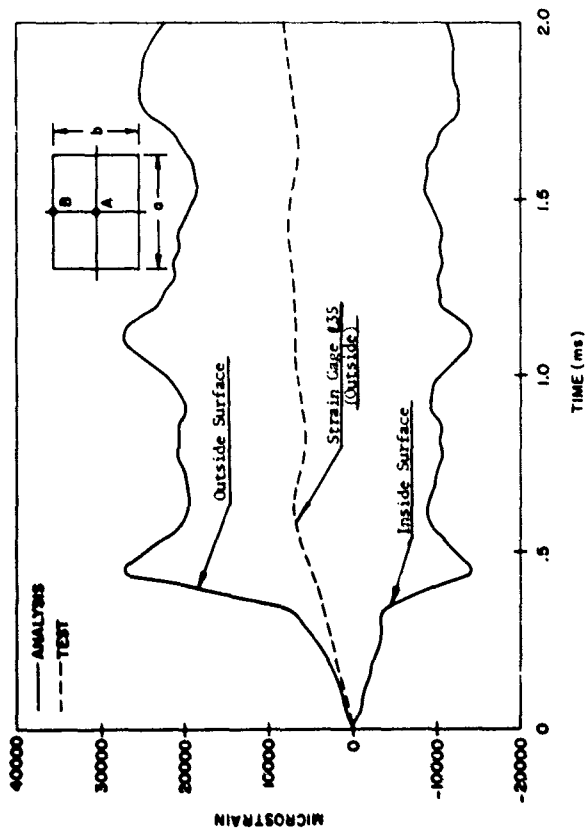


FIGURE 64. Strain Data Correlation for Panel 6 - Location B
NOVA 2 - KADROB Solution.

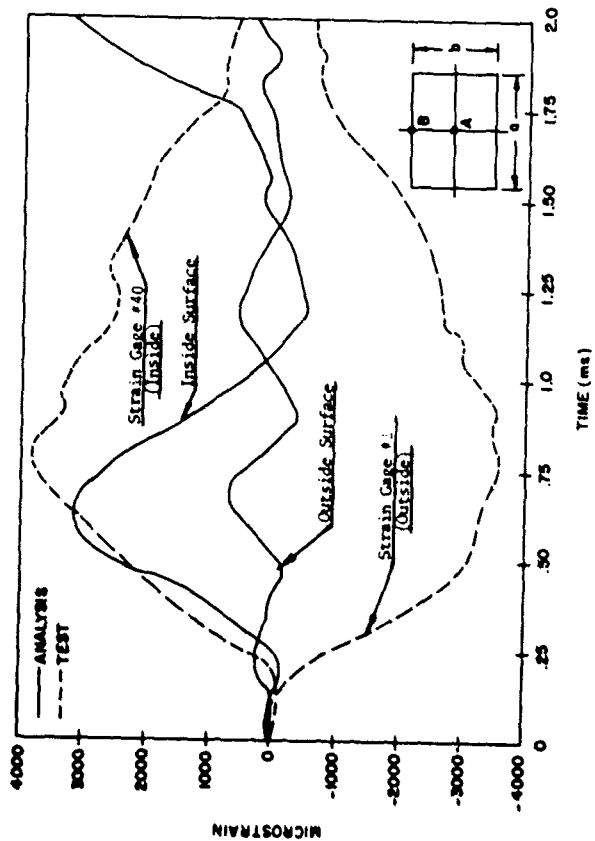


FIGURE 65. Strain Data Correlation for Panel 8 - Location A
NOVA 2 - KADBOB Solution - Simply Supported Edges.

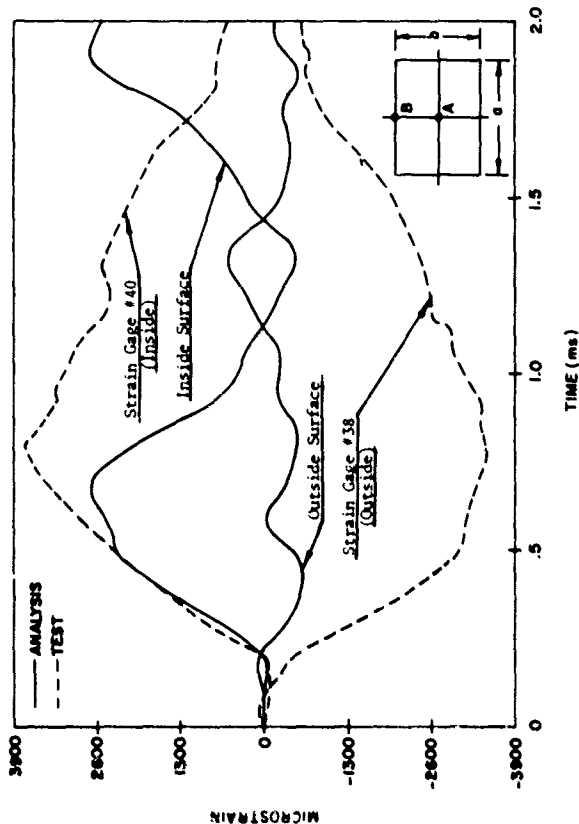


FIGURE 66. Strain Data Correlation for Panel 8 - Location A
NOVA 2 - KADROB Solution - Clamped Edges.

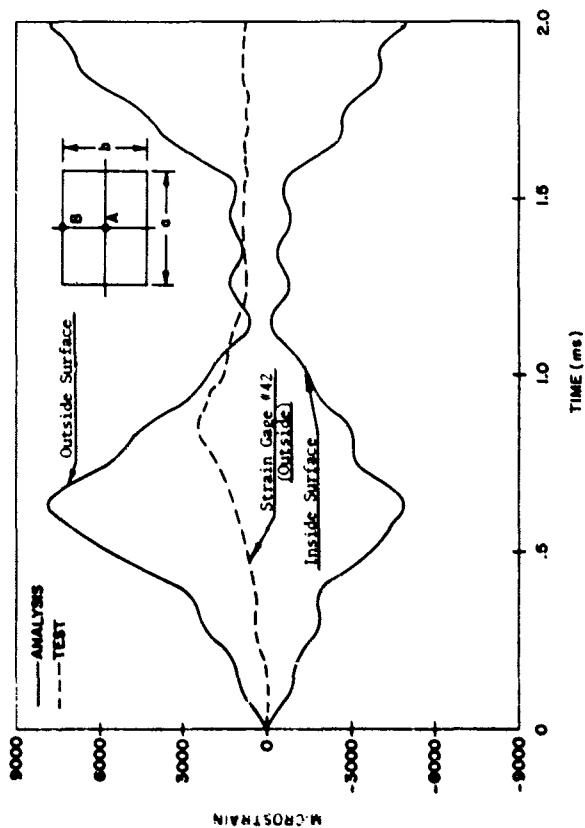


FIGURE 67. Strain Data Correlation for Panel 8 - Location B
NOVA 2 - KADBOB Solution - Clamped Edges.

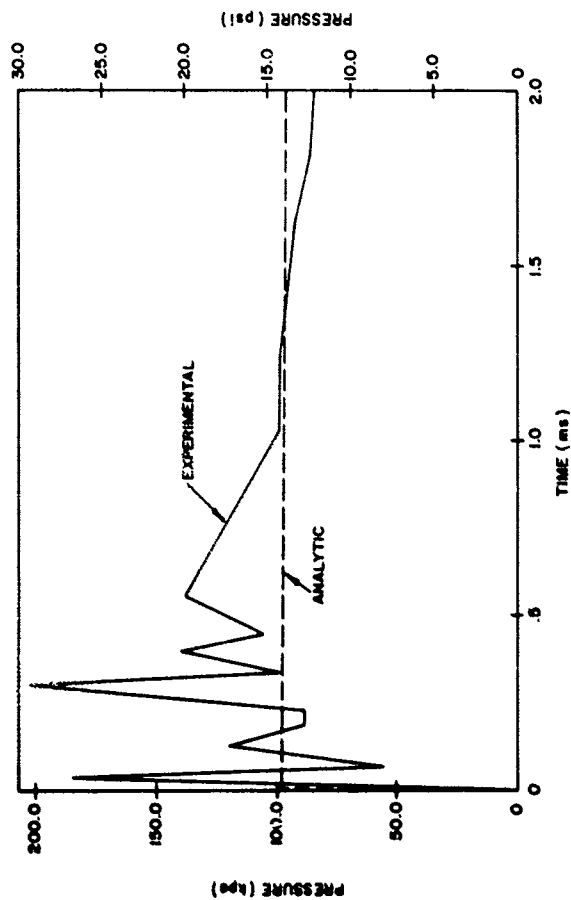


FIGURE 68. Analytic and Experimental Overpressure Profiles for Panel 1.

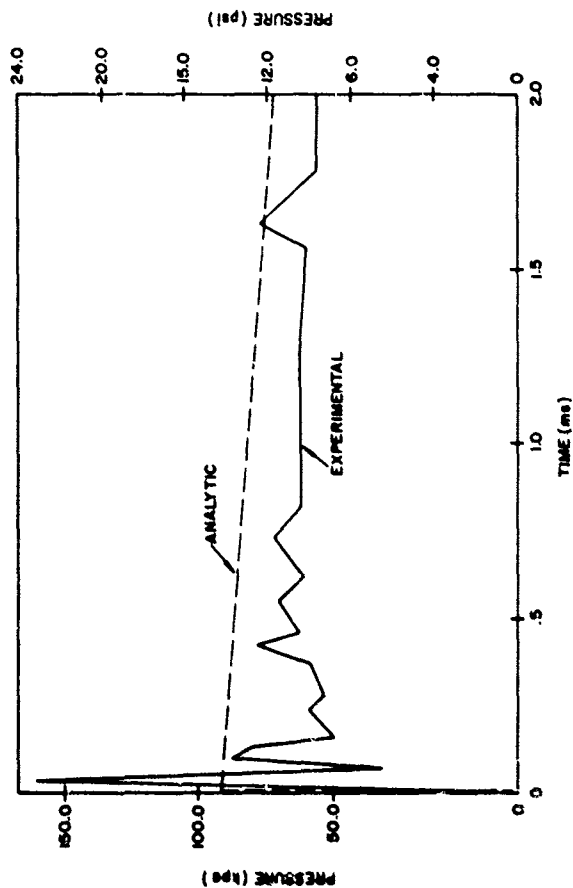


FIGURE 69. Analytic and Experimental Overpressure Profiles for Panel 4.

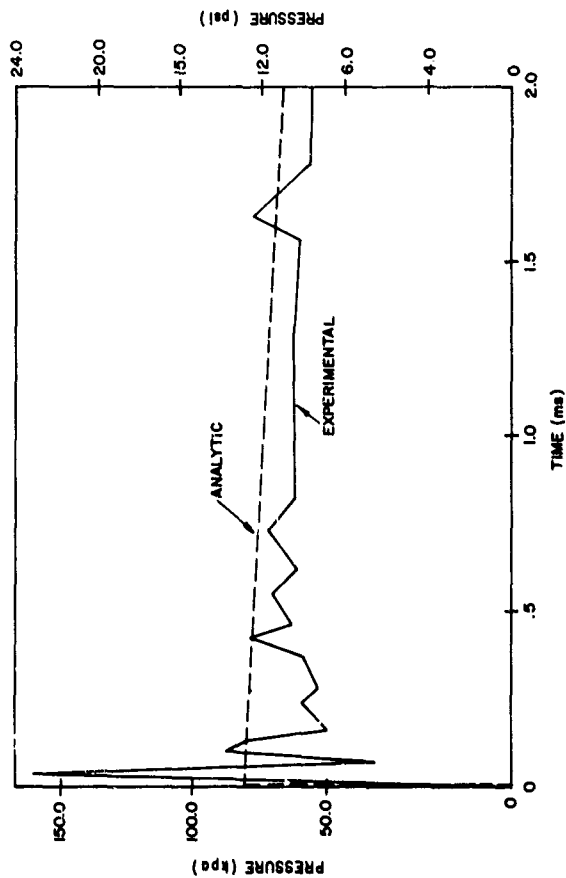


FIGURE 70. Analytic and Experimental Overpressure Profiles for Panel 5.

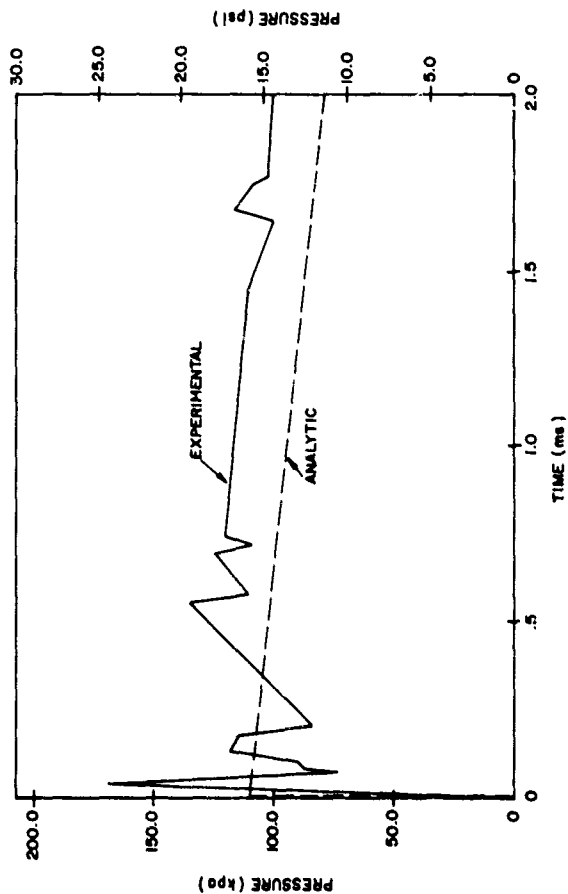


FIGURE 71. Analytic and Experimental Overpressure Profiles for Panel 6.

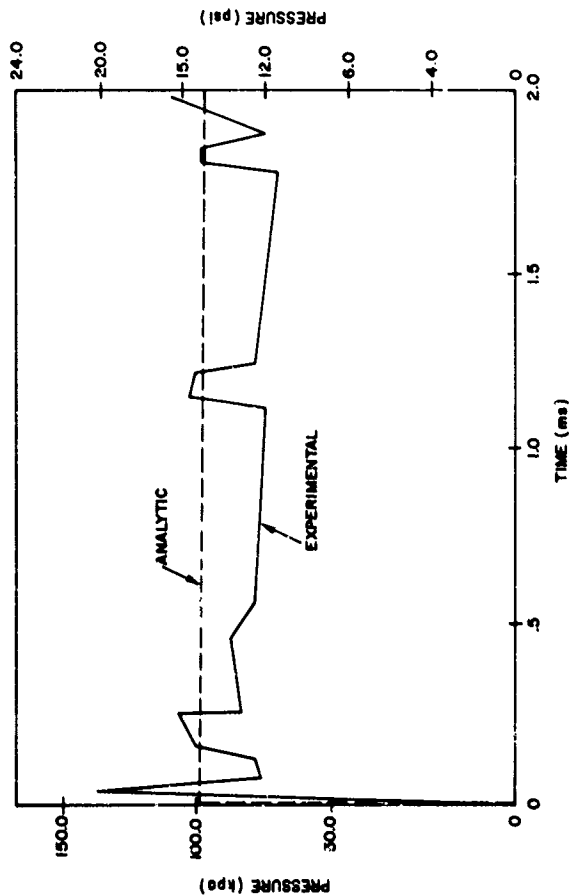


FIGURE 72. Analytic and Experimental Overpressure Profiles for Panel 8.

surface. This was dependent on the panel shape and its orientation to the direction of blast propagation.

As mentioned earlier, the panel response did not conform either to the classic clamped edge or simply supported edge boundary conditions. Rather, an intermediate response was generally evident from the experimental data which is summarized in Table 8. This gives peak strains recorded at the center of the panels and along the longer edge near the panel boundary.

At the center of panel 1, for instance, the strain was 3400 microstrains, as compared to 2880 microstrains at the panel boundary. This implied a response more characteristic for panels with simply supported rather than clamped edge boundary conditions. A similar response could be observed for all panels located in the vertical stabilizer area. In contrast, the response of panels located on the fuselage appeared to approach more closely that of clamped edge boundary conditions. There, strains along the longer side near the boundary are higher than at the center of the panel.

A comparison of the peak strain values suggests that, generally, the response of the panels located in the vertical stabilizer area resemble more closely that of panels with simply supported edge boundary condition. The fuselage panels, however, approximate more closely responses for the clamped edge boundary conditions. This behavior appears to be related to the rigidity of the substructure at the panel boundaries. The substructure of the vertical stabilizer was more flexible than the fuselage substructure.

The survey of the strain gage data for the strain gradients developed near the panel boundary along the longer edges provided further evidence that the response of the panels during the test was between those responses typically expected for panels with simply supported boundary conditions and those with clamped edge ones.

For panel 1, a strain gradient of only 59 microstrains/mm (1500 microstrains/in.) was indicated from the records of strain gages 5 and 9, Figs. 73 and 74. Much higher strain gradients were developed in panels 4 and 5. These were 640 and 970 microstrains/mm (16,200 and 24,700 microstrains/in.) respectively, as obtained from the data of strain



FIGURE 73. Strain Gage No. 5 Data - Panel 1.

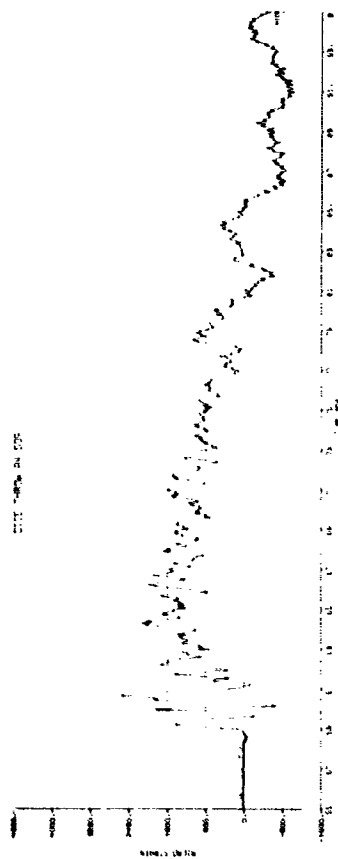


FIGURE 74. Strain Gage No. 9 Data - Panel 1.

gages 27 and 28 for panel 4 and gages 31 and 43 for panel 5 (Figs. 75 through 78).*

An interesting pattern in tensile strain histories was observed for the flat and curved panels. At the center of flat panels, a maximum strain level was generally reached during the first oscillation. This was followed by the strain attenuation during subsequent cycles. At the panel edge, this was contrasted by several cycles of increasing strain amplitudes with the peak value reached, generally, on the third cycle. This initial amplification trend is followed by strain attenuation. Illustrations of these strain histories are presented in Figs. 79 and 74 for the center and the edge of panel 1, respectively. For the curved panels, the peak strain values both at the center and at the edge of the panel invariably occurred on the first oscillation, Figs. 80 and 75.

The study of the effect of the width parameter on panel response was limited to a comparison of strain data for panels 4 and 5. These panels, located side by side on the fuselage had a curvature of approximately 782 m (30.8 in.) radius. Both had identical dimensions except the width which was 73 and 87 mm (2.86 and 3.42 in.), respectively, for panels 4 and 5. Both panels responded in a similar manner and, as expected, the peak strain in panel 5, the wider panel, was substantially higher (8000 microstrains) than in the narrower panel 4 (6000 microstrains), as shown in Table 8.

In accordance with the fairly high natural frequency of the instrumented panels, their maximum response usually occurred within one millisecond after the blast intercept. A departure from this behavior was reflected in the strain histories obtained for some fuselage panels. It consisted of both high and low frequency oscillations. The high frequency oscillation reached peak strain during the first cycle following the blast intercept, but, typically, an even higher peak was registered at a later time in conjunction with the low frequency oscillation. This mode of response was most clearly apparent from the record of gage 22, on panel 4, Fig. 81, and shows the overall maximum response

*NOTE: Typically, a strain gage covers a finite area and its record represents average strain over that area. The data are, therefore, approximate values of the actual strain gradients that were induced during the test.



FIGURE 75. Strain Gage No. 27 Data - Panel 4.

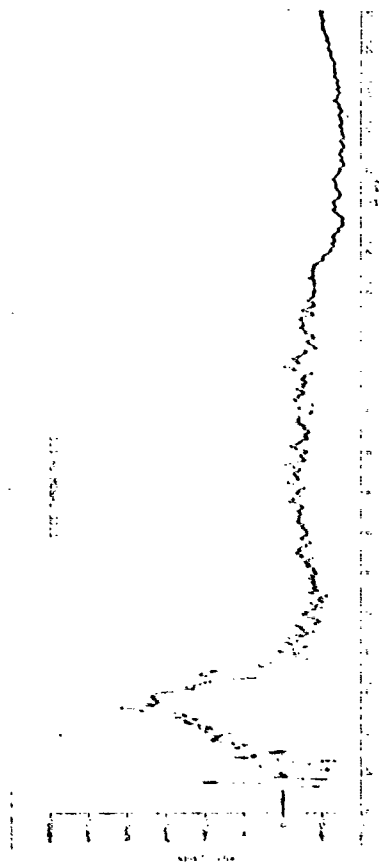


FIGURE 76. Strain Gage No. 28 Data - Panel 4.

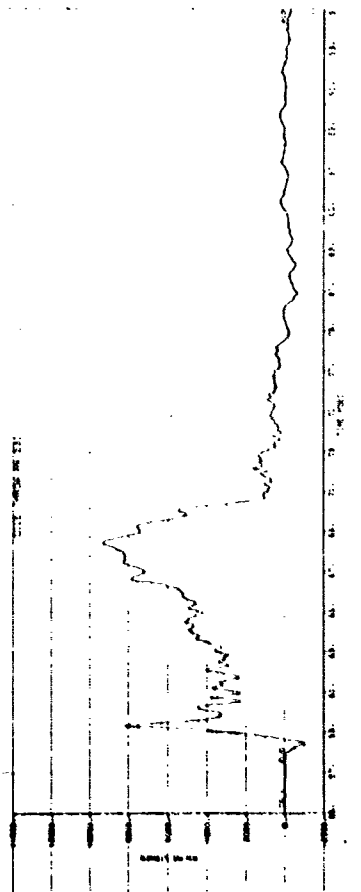


FIGURE 77. Strain Gage No. 31 Data - Panel 5.

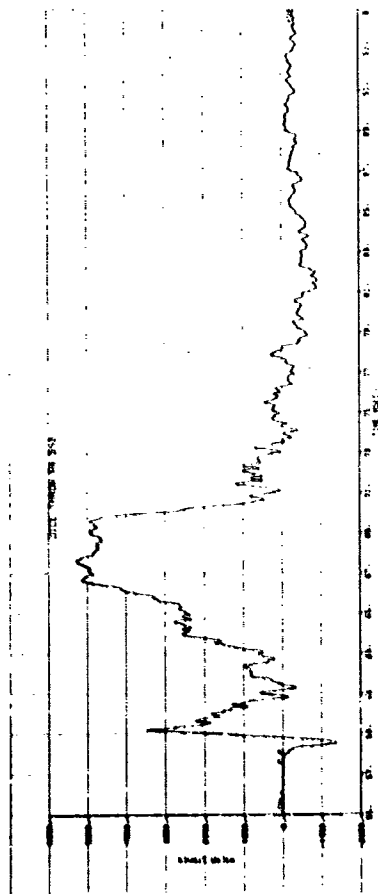


FIGURE 78. Strain Gage No. 43 Data - Panel 5.

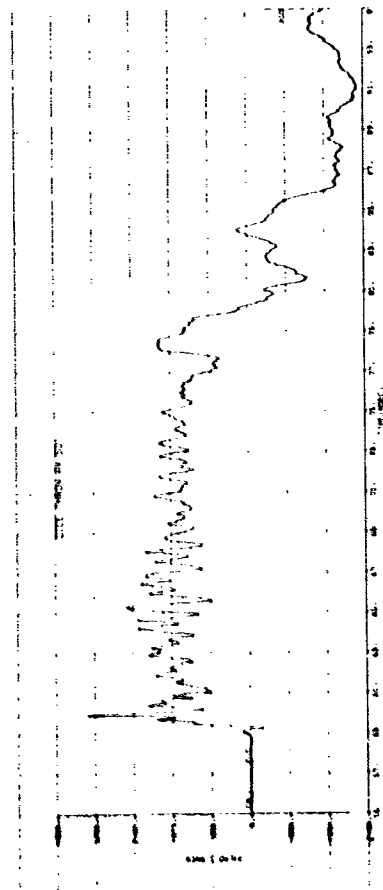


FIGURE 79. Strain Gage No. 1 Data - Panel 1.

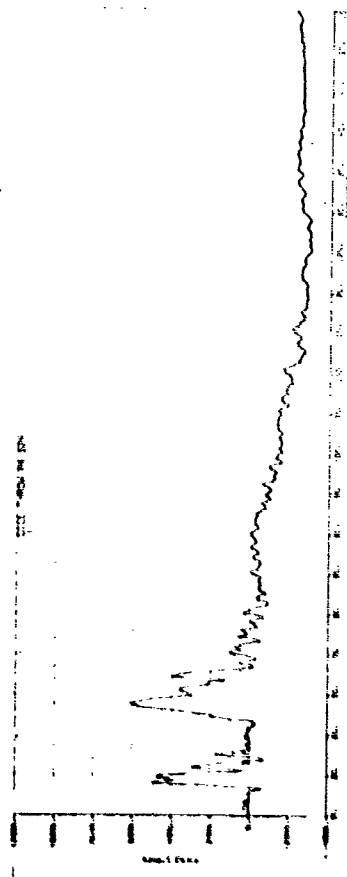


FIGURE 80. Strain Gage No. 24 Data - Panel 4.

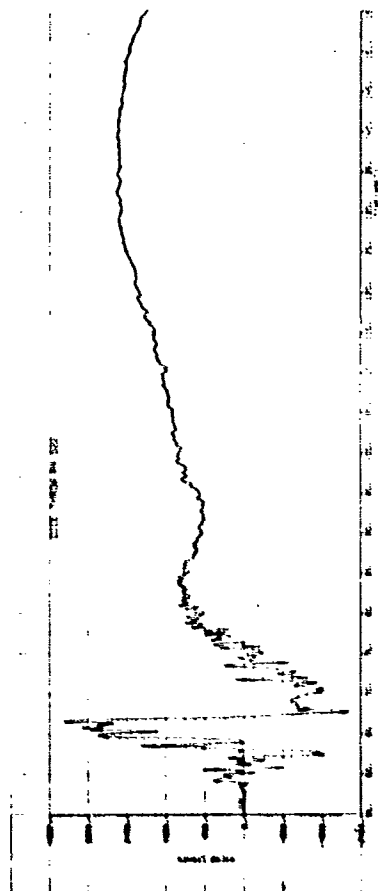


FIGURE 81. Strain Gage No. 22 Data - Panel 4.

at approximately 9-10 ms after the blast intercept. The pattern occurred for the majority of gages installed on the fuselage, and it is attributed to the synergistic effects of overpressure and gust. It was found to manifest itself as early as 7 ms after the blast intercept, which approximately corresponds to the fuselage natural frequency determined in the ground vibration tests conducted by the manufacturer, Ref. 8.

The gust effect may, as in the case of gage 23, Fig. 1, become increasingly pronounced so as to reach the maximum tensile strain value after the high frequency response has virtually died out. There, the gradual build up of tensile strains peaked between 70 to 80 ms after the shock arrival.

The correlation of the experimental data and the analytical predictions obtained from the NOVA 2 solutions was approached with the understanding that the idealized modeling of panel elements can, at best, represent a reasonable approximation of the aircraft structure response. Certain limitations of the NOVA 2 modeling are generally recognized and this test offered a unique opportunity to put these limitations in proper perspective.

The panel boundary condition representation in NOVA 2 forces a choice between either the simply supported or clamped edge boundary conditions. This immediately suggests a potential source of error. Similarly, the lack of provisions for adequate modeling of a structural element in conjunction with the adjoining structure constitutes a departure from the true-to-life structure representation.

The NOVA 2 code was designed to predict the structural response restricted to the overpressure effects. Therefore, in the situations where the synergistic effects of overpressure and gust are present, the gust effects have to be assessed separately and suitably combined with the overpressure effect predictions.

The NOVA 2 assumptions of a single instant for the time of shock arrival and of the overpressure uniform across the entire panel surface (overpressure changing with time, of course) are found to be inconsistent with the actual events. Furthermore, the overpressure histories obtained during the test differed significantly from the analytic blast model incorporated within the NOVA 2 program. This

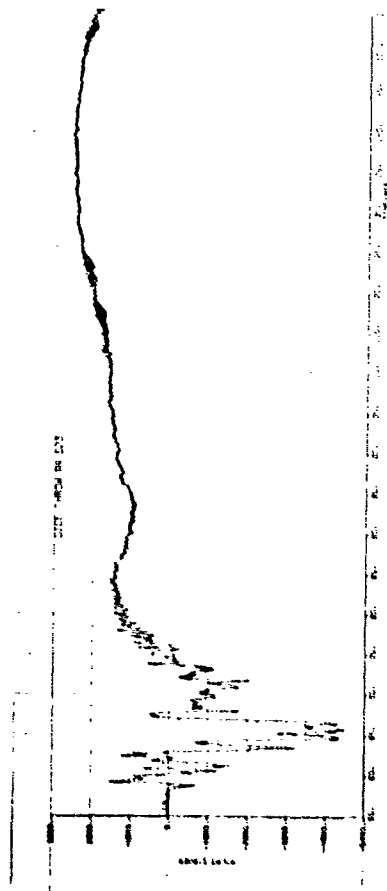


FIGURE 82. Strain Gage No. 23 Data - Panel 4.

is illustrated in Figs. 68 through 72 which show superimposed overpressure versus time plots for the analytic and experimental data. All these factors are bound to affect the accuracy of the analytic predictions.

Nevertheless, for all these limitations, NOVA 2 offers the panel response predictions which compare quite favorably with the experimental data. In some cases, these predictions may be remarkably accurate. In other cases, appropriate interpretation must be applied to the analytic data in order to define the sources of discrepancies and assess the significance of the analytic solution in relation to the true-to-life structural response.

These cases are graphically illustrated in the analytic and experimental strain data plots for panels 1, 4, 5, 6, and 8 presented in Figs. 40 through 67 and in Table 9 which summarizes the peak values.

For the center of Panel 1, the maximum strain values obtained from the NOVA 2 DEPROP, KADBOP, and KADBOB solutions varied between 3500 and 4100 microstrains and were comparable with the experimental strain value of 3400 microinches. However, the analytic strain histories, shown in Fig. 40, differ significantly from the experimental strain histories inasmuch as the dominant membrane strains indicated by the analysis contrast the test data which showed very significant bending strains.

Even greater discrepancies can be observed for the strains near the longer side boundary of the panel. The analytic strains of 10,100 and 11,100 microstrains were obtained from the NOVA 2 DEPROP and KADBOP solutions, respectively. The higher strains obtained from the KADBOP solution illustrate the effect of the more severe experimental overpressure as compared to the analytic blast used in the DEPROP solution, Fig. 68. These strain levels, which signify considerable yielding of the panel skin material, appear to be much greater than the corresponding experimental strains which peaked at 2880 microstrains, well within the elastic range. This discrepancy between the analytic and experimental values is further accutuated by the KADBOB solutions which use a beam representation of panels in the analysis. This representation was advertised as an acceptable approximation which offers considerable saving in the computer time without significant sacrifice of the solution accuracy. The colossal strain values of 45,600 and 70,900 microstrains obtained from the KADBOB-A

TABLE 9. Correlation of the Analytic Strains Obtained from NOVA 2 Solutions and the Experimental Strains: Skin Panels - Maximum Response Data Summary.

Skin Panel		Maximum Strain (Microstrains) at Time (milliseconds) After Shock Arrival				
No.	Location	Experimental Data	DEPROP Solution	KADBP Solution	KADBP Solution	KADBP-A Solution
1	Center	3400 @ 1.1 ms	3600 @ .5 ms	4100 @ .5 ms	4000 @ .5 ms	3500 @ .5 ms
	Longside	2880 @ 1.8 ms	10,100 @ .6 ms	11,100 @ .5 ms	70,900 @ .6 ms	45,600 @ .6 ms
4	Center	5000 @ 1.0 ms	3700 @ .4 ms	3300 @ .4 ms	3300 @ .4 ms	-
	Longside	6000 @ 1.3 ms	10,300 @ .4 ms	7500 @ .4 ms	9000 @ .4 ms	-
5	Center	-	3800 @ .5 ms	-	3600 @ .6 ms	-
	Longside	8800 @ 1.5 ms	13,600 @ .5 ms	-	51,600 @ .7 ms	-
6	Center	3200 @ 0.6 ms	3100 @ .3 ms	-	3200 @ .4 ms	-
	Longside	7600 @ 0.6 ms	10,500 @ .4 ms	-	27,200 @ .5 ms	-
8	Center	3800 @ .8 ms	-	-	2800 @ 0.7 ms (clamped edge model) 3200 @ 0.6 ms (SS edge model)	-
	Longside	2400 @ .9 ms	-	-	7900 @ 0.6 ms	-

NOTE: Unless stated otherwise, panels are modeled for clamped edge boundary conditions.

and KADBOB solutions, respectively, (Figs. 56 and 57, and Table 9) clearly indicate that for strain levels beyond the elastic limit, the beam representation of panels produces increasingly unrealistic results. This was consistently demonstrated in the KADBOB solutions for panels 5 and 6, Figs. 62 and 64, respectively, with the corresponding strain maxima of 51,600 and 27,200 microstrains. As expected, for the larger of the two panels, panel 5, farther excursion into the plastic range was predicted.

The selection of panel 8 was based on the premise that this panel was most likely to demonstrate a typical response for the simply supported edges boundary condition. This access door panel was characterized by skin discontinuities at all edges. This was largely verified by the experimental data, Table 9, which indicated 3800 microstrains maximum at the center of the panel and lower strain, 2400 microstrains, near the panel edge.

Two analytic solutions were obtained for this panel. For one solution, the panel was modeled as simply supported, and for the other solution as clamped-edge boundary conditions. The resulting analytic strain data and the corresponding experimental strain data plots are presented in Figs. 65 through 67. The experimental strains obtained for the inside surface at the center of the panel corresponded rather closely to the analytic strains for the simply supported edge model, Fig. 65. A disparity can be observed between the outside surface strains for the experimental and analytic data. This mode of behavior, mentioned earlier in the discussion of panel 1, implied that, in the analysis, panels are treated as membranes rather than plates. The experimental data indicated the panel response more closely resembles that of a plate. It should be noted that the membrane behavior is related to the panel width-to-thickness ratio and to the load level. Thus, thin panels tend to respond as membranes and, at higher load levels approaching the yield point and beyond, the membrane action becomes increasingly dominant.

The clamped-edge solution for panel 8, Figs. 66 and 67, showed considerably greater discrepancy between the analytic and experimental data, particularly near the panel edge. The analytic strain value at that location, 7900 microstrains, implied a response in the plastic range whereas the experimental strain maximum of 2400 microstrains clearly denoted a response within the elastic range.

Overall, Method 3 does an acceptable job of approximating complex real-world panel structures. However, considerable judgement is required on the part of the analyst. The engineering time required to obtain a first-case solution is approximately 40 man-hours and the computer time may exceed 2 hours on a large-scale computer (CDC-6600 was used in this analysis).

Longerons

Because of recording channel limitations allowed for longerons 4 and 5, the instrumentation was clearly inadequate for a comprehensive definition of the longeron response during the overpressure phase of the blast. This inadequacy was further compounded by erratic behavior of the deflection gages and the crucial strain gages Nos. 56 and 59, (Fig. 12) which were located on the outside surface of the skin directly opposite the longeron flanges. Strain gages 55, 57, and 58 (Fig. 12), located on the longeron legs, were too close to the neutral axis to provide data relevant for correlation with the analytic data. The longeron leg which terminated in a bulb-type flange was unsuitable for strain gage installation.

The only strain gage which appeared to provide reasonable data was gage 59. Unfortunately, the tensile strain indicated by this gage could not be readily accepted as valid for the location where compressive strain was expected, based on the load configuration and structure geometry.

A plausible, though possibly conjectural, explanation for the tensile strains actually developed at the gage 59 location is postulated as the overall response of the fuselage curved panel sector bounded fore and aft by two rigid bulkheads at Stations 262 and 306, respectively, and, top to bottom, by longeron 6 and the lower longeron. In the vicinity of STA 306, at the outside surface location, this large fuselage sector might well be subjected to the initially tensile stresses as indicated by strain gage 59. This line of reasoning leads to an observation that a structural member which constitutes one element of a multi-element integral structure should be modeled in conjunction with the entire structure to enhance adequate correlation between the experimental and analytic data.

The longeron 5 analysis was accomplished using DEPROB and KADBOB solutions. The former was based on the analytic blast model and, for the latter, the experimental overpressure data of the closest pressure gage was used as the input. In both solutions, the longeron was assumed clamped at either end.

From the DEPROB solution (Fig. 83) the overall maximum compressive strain of 4800 microstrains was obtained at the longeron inner flange at the support point and the corresponding outside flange strain was 2200 microstrains in tension. At the longeron mid-span (Fig. 84), lower strains of 2700 and 1200 microstrains were indicated for the inner and outer flanges, respectively.

Slightly lower strains were consistently obtained from the KADBOB solution (Figs. 85 and 86), because the experimental overpressure profile less severe than the analytic blast model, Fig. 70.

The strain gage 59 data plot was included in Figs. 84 and 86 for reference only. The lack of adequate experimental data precluded a correlation with the analytic predictions. However, the available experimental and analytic data support the observation that only moderate strains were developed in the longerons during the overpressure phase of the blast.

Fuselage Frame

The fuselage frame STA 277, Fig. 87, is a complex, partial ring structure which consists of several composite elements with discontinuities along the perimeter. Presence of elastic supports such as longerons and cantilever segments increases the complexity and makes the structural modeling for the NOVA 2 solution difficult and requires a series of approximations. In addition, the overpressure representation which, in the case of a frame analysis, was required to account for pressure variation around the frame at any given time during the diffraction phase, involved approximations inherent in the NOVA 2 blast model. Each approximation carried with it a potential source of error which was bound to affect the solution accuracy.

The frame analysis was restricted to a DEPROB solution. The KADBOB solution which, at present, lacks the capability for a multi-point representation of pressure variation

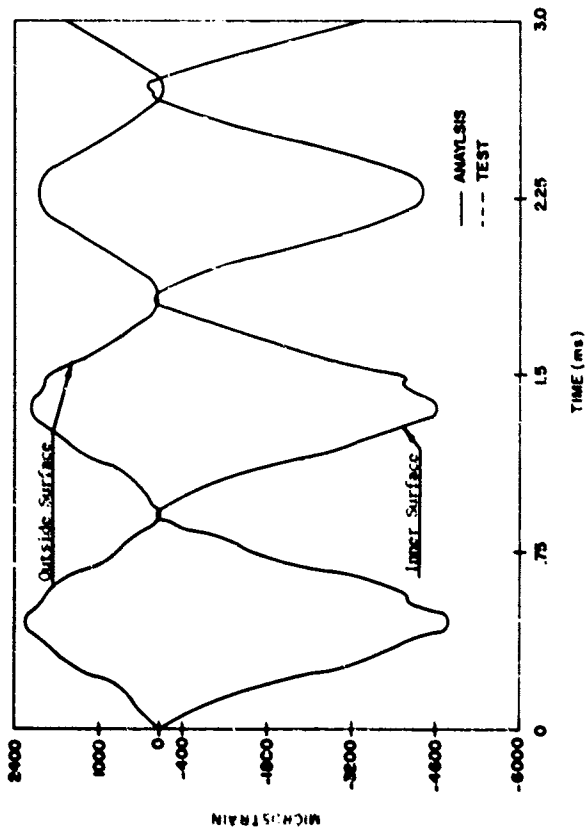


FIGURE 83. Strain Data Longeron 5, Support NOVA 2 - DEPROB Solution.

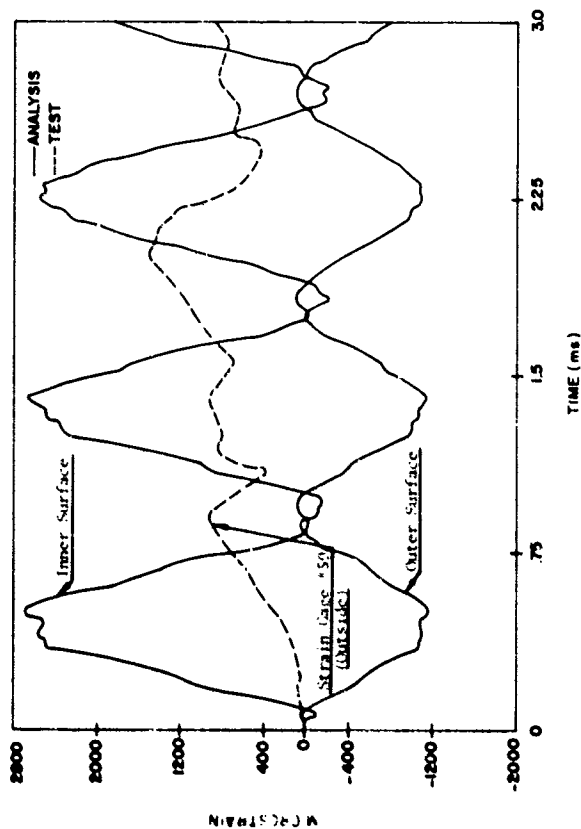


FIGURE 84. Strain Data Correlation - Longcron 5, Mid-Span, NOVA 2 - DEPROB Solution.

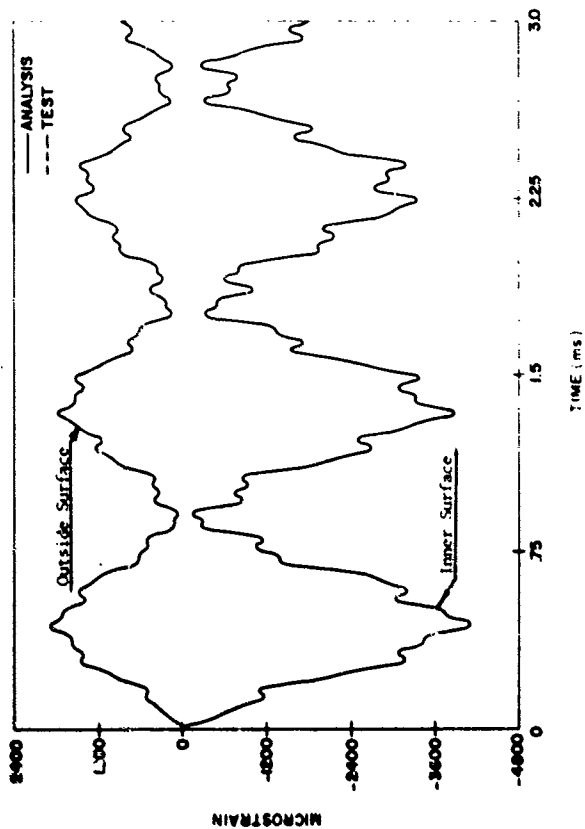


FIGURE 85. Strain Data Longeron 5, Support
NOVA 2 - KAUBOB Solution.

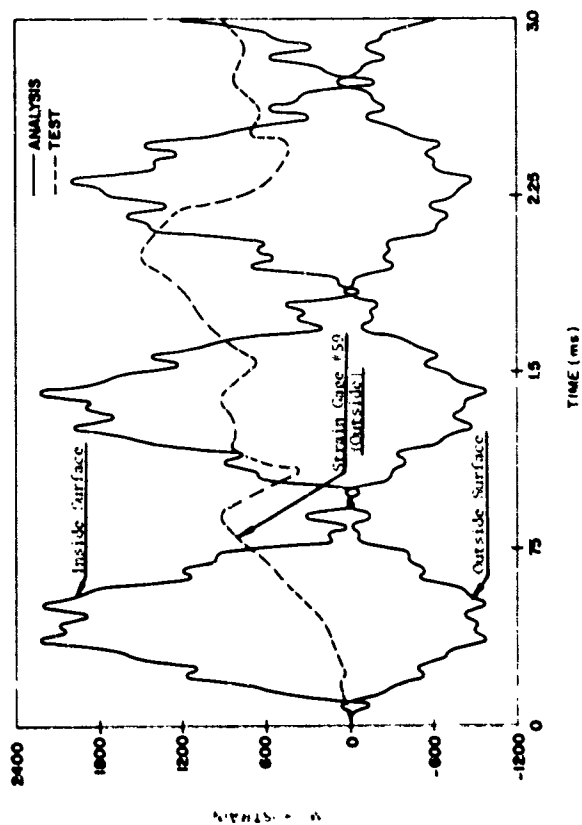
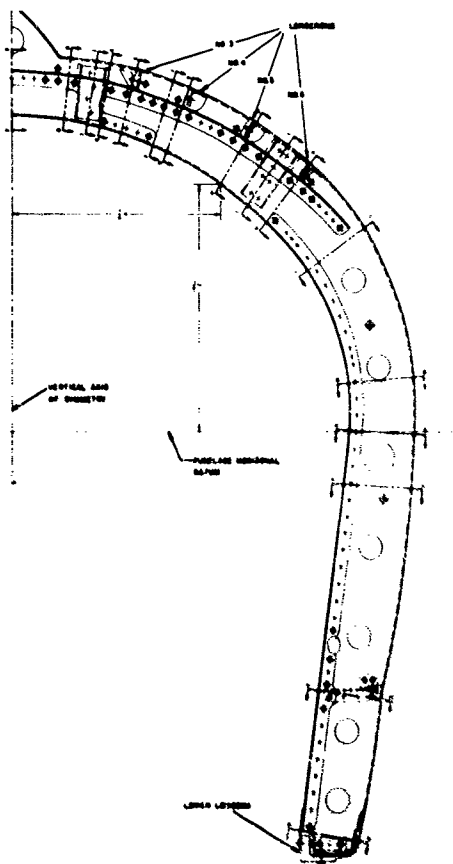


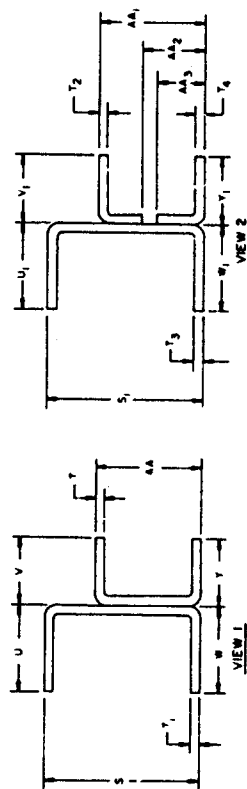
FIGURE 56. Strain Data Correlation - Longeron 5, Mid-Span, NOVA 2 - KANBON Solution.



NOTE: Dimensions Listed in TABLE 10.

FIGURE 87. Fuselage Frame STA 277, Configuration.

TABLE 10. Section Dimensions Data Fuselage Frame STA 277.

[illegible]

around the frame, was not attempted. (The code designers at Kaman Avidyne are currently working at improving NOVA 2 code to include that capability.)

The predicted strain data, together with relevant experimental data, are presented in Figs. 88 through 91. For the frame support at the lower longeron location, i.e., section RR in Fig. 87, high strains in excess of 14,000 microstrains were predicted, Fig. 88. It is difficult to assess the validity of this prediction because a realistic representation of this frame-to-lower longeron joint poses an intricate modeling problem. In view of the failure at this joint during the test, Fig. 25, close correlation between the analytic prediction and the test results is quite remarkable and may be a coincidence.

For the plane of geometric symmetry at section AA, Fig. 87, moderate strains, below 2800 microstrains, were predicted. A low peak strain (650 microstrains) was obtained experimentally by gage 48, Fig. 89. Modeling of the section AA was also complicated, particularly by a discontinuity in the main element of the frame and by the presence of an intersection with the vertical stabilizer structure. Representation of that configuration required a great deal of judgement which apparently produced fair correspondence between the predicted and experimental data.

For the curved segment of the frame, bounded by sections HH and MM, Fig. 87, the maximum predicted strains approached 4500 microstrains at the frame inner flange. The corresponding experimental strain maxima were 5500 microstrains for section HH, Fig. 90, and 2000 microstrains for section MM, Fig. 91. Since all these strains were compressive, a possibility of buckling failure could not be ruled out. In fact, an inner flange buckling in that region occurred in the free-standing aircraft BUNO 145062, Fig. 30. Detailed examination of the failure area revealed a lightening hole in the frame web of BUNO 145062 at that location. In the instrumented aircraft, BUNO 149558, the lightening hole was absent. It appears that this segment of the frame was critical and a relatively small strength reduction in this area precipitated a failure.

Considering the approximation procedures involved in modeling the frame structure, the remarkably close correlation between the predicted data and test results is regarded as highly satisfactory.

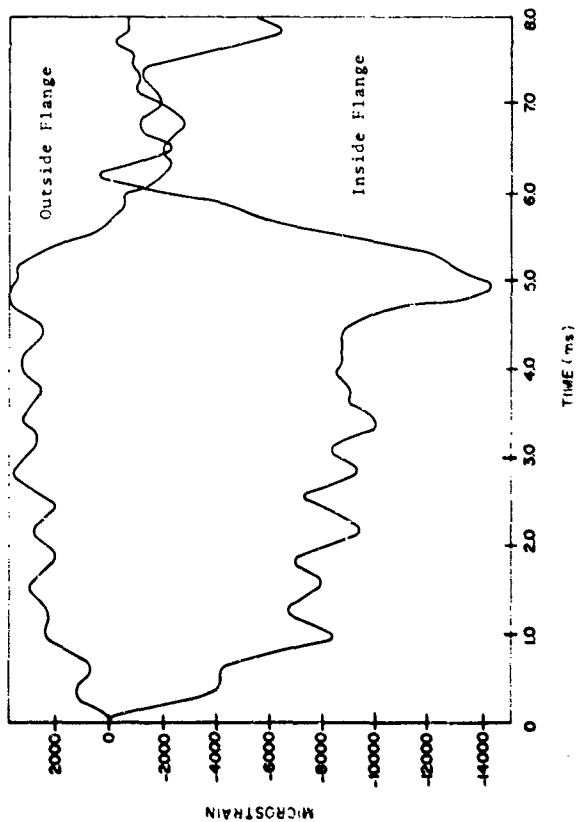


FIGURE 88. Predicted Strains at Frame STA 277 Support, Section RR (Fig. 87, Ref.).

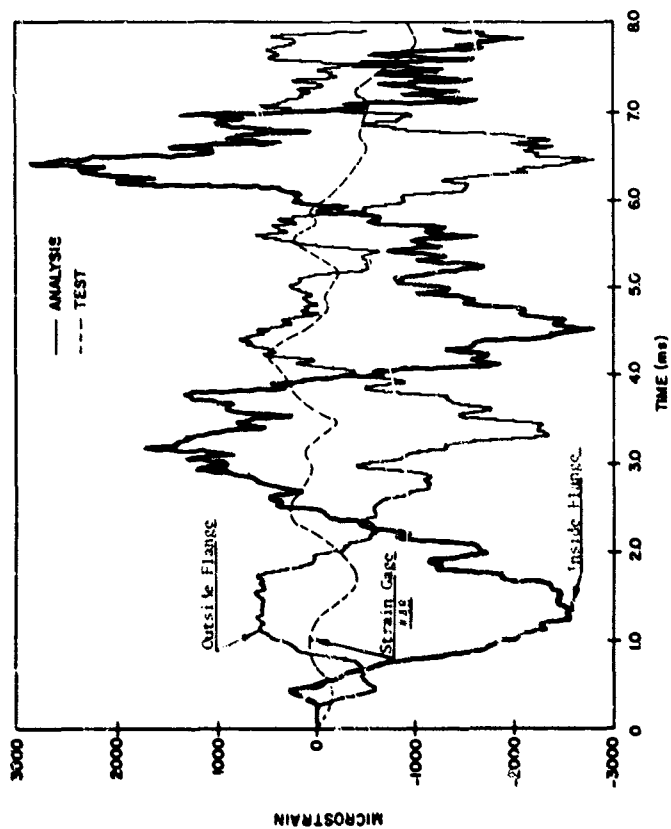


FIGURE 89. Strain Data Correlation Fuselage Frame STA 277, Section AA.

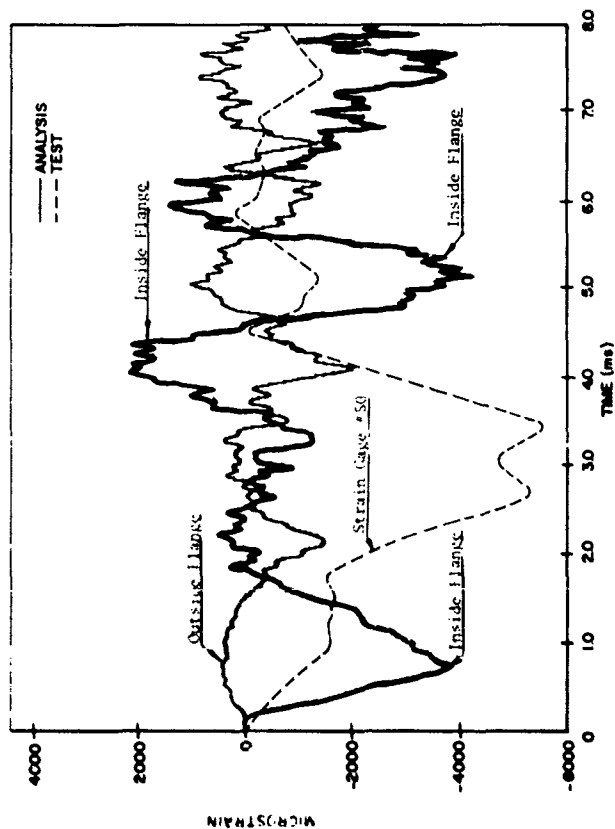


FIGURE 90. Strain Data Correlation Fuselage Frame
STA 2-- Section HH.

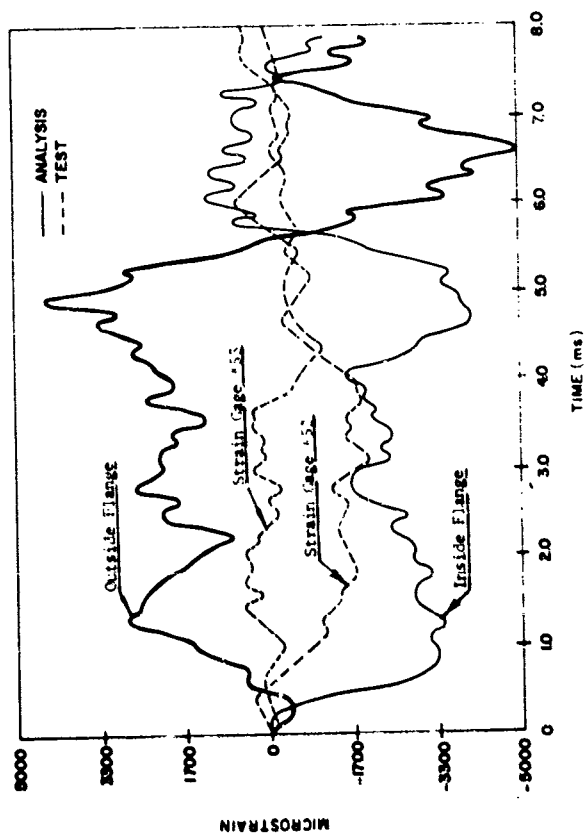


FIGURE 91. Strain Data Correlation Fuselage Frame
STA 277, Section MN.

AIRCRAFT RIGID BODY MOTIONS

All three aircraft had motion picture cameras located as shown in Fig. 1. The film record obtained for the free-standing aircraft BUNO 145062 was of poor quality and inadequate for analysis.

Mapping of rigid body motions during the positive and negative phases of the blast was, therefore, limited to BUNO 149558 and 145074. Since only one camera was installed for each aircraft, the rigid body motions which could be determined with a reasonable degree of confidence were restricted to:

1. Lateral translation.
2. Roll.
3. Yaw.

The analysis of the film records, Ref. 9, extended to the point in time when the field of vision became obscured by the cloud of dust raised by the blast. For aircraft BUNO 149558 and 145074, this corresponded to, respectively, 0.8 and 0.55 s after the shock front arrival.

Results of this analysis are presented in Figs. 92 through 97. Because of the tiedown restraints (primarily against the translation away from GZ), Fig. 4, the aircraft motions during the positive blast phase were relatively small (translation) to virtually nonexistent (roll). Sizeable motions occurred during the negative blast phase. BUNO 149558 experienced, approximately, 0.9 m (2.9 ft) maximum translatable motion of the aircraft CG, Fig. 92 towards the GZ. The corresponding rotational motions in roll and yaw peaked at 6 and 18 degrees, respectively, Figs. 93 and 94.

Generally smaller motions were obtained for BUNO 145074 with 0.5 m (1.6 ft), 4.5 degrees, and 16 degrees indicated for the translation, roll and yaw, respectively, Figs. 95 through 97. The smaller motions for this aircraft which was exposed to 62.1 kPa (9 psi) overpressure as compared to BUNO 149558 which experienced 41.4 kPa (6 psi) overpressure can be explained by the fact that, following the catastrophic fuselage failure, Fig. 18, the aircraft area exposed to the effect of the negative drag phase was greatly reduced.

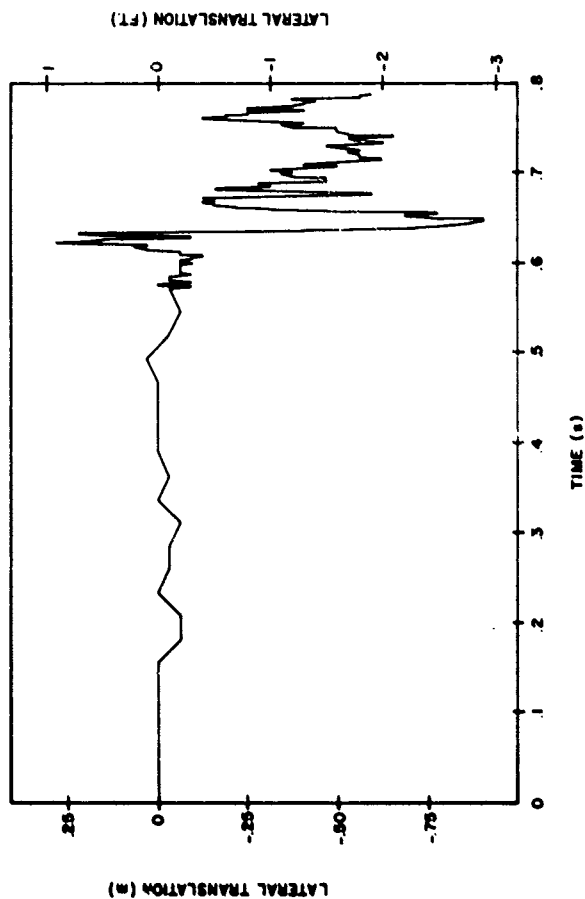


FIGURE 92. Lateral Translation at Aircraft CG -
BUNO 149558.

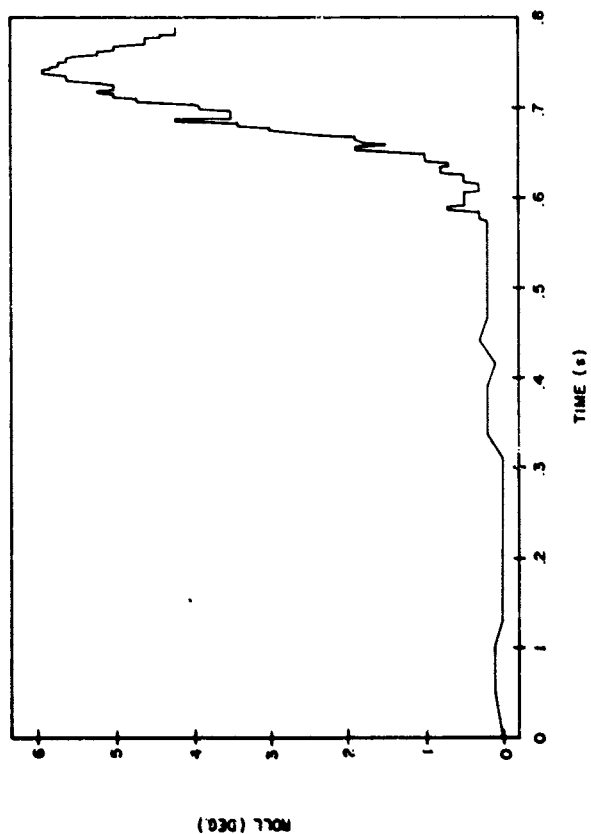


FIGURE 93. Roll of A/C BUNO 149558.

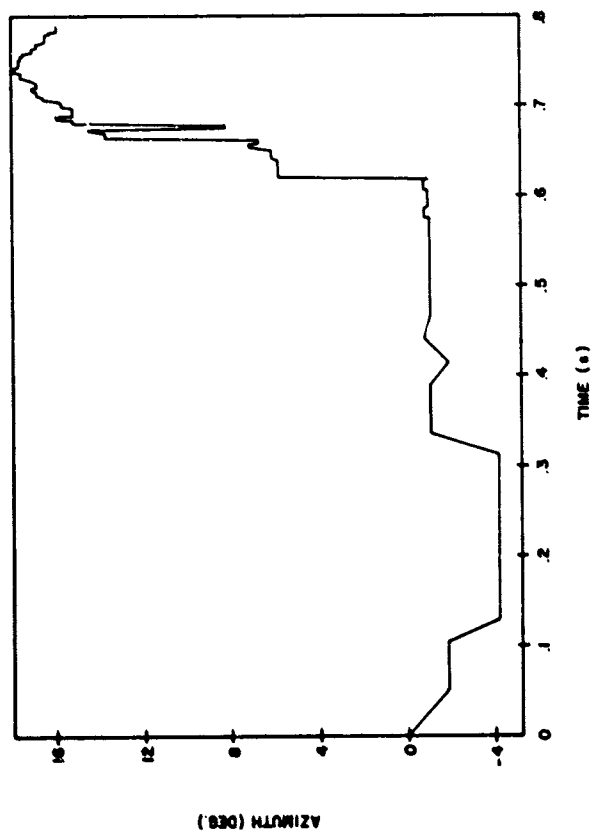


FIGURE 94. Yaw of A/C BUNO 149558.

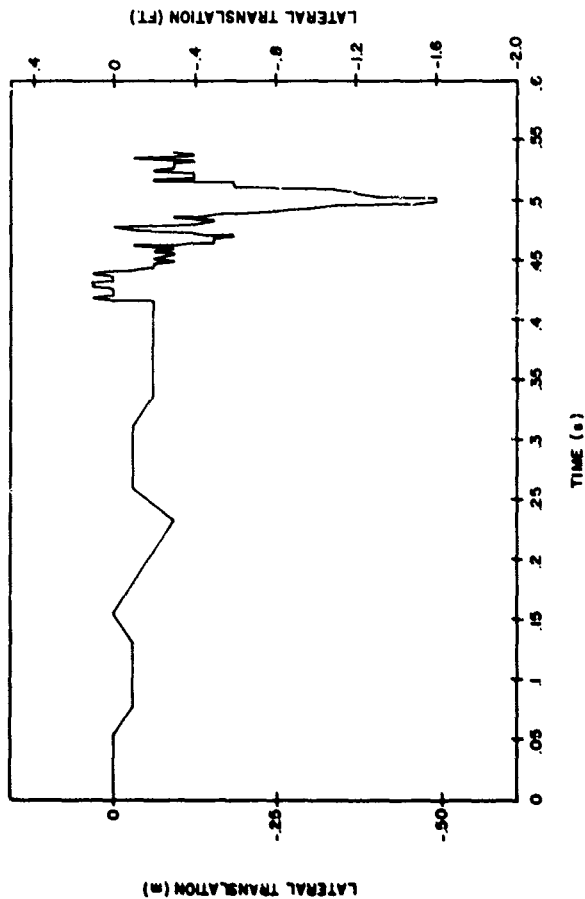


FIGURE 95. Lateral Translation at Aircraft CG -
BUNO 145074

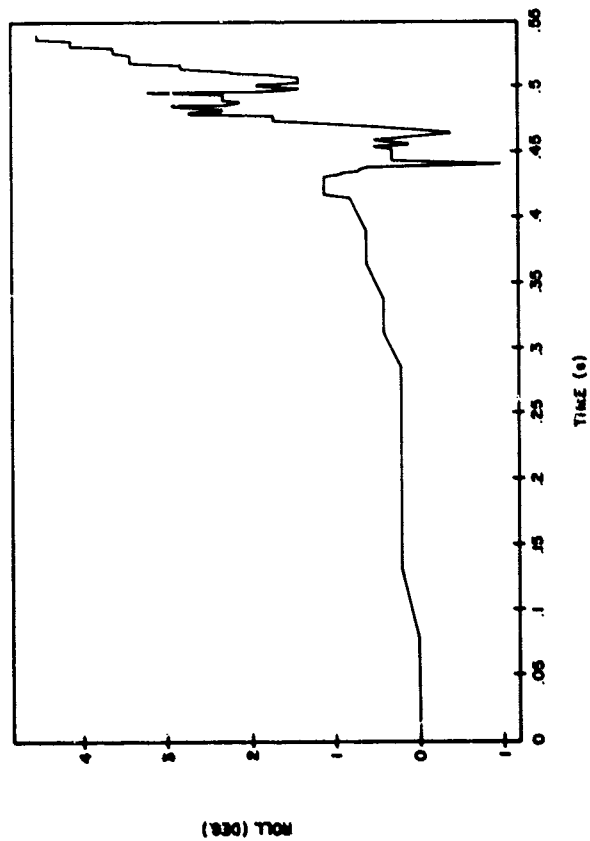


FIGURE 96. Roll of A/C BUNO 145374.

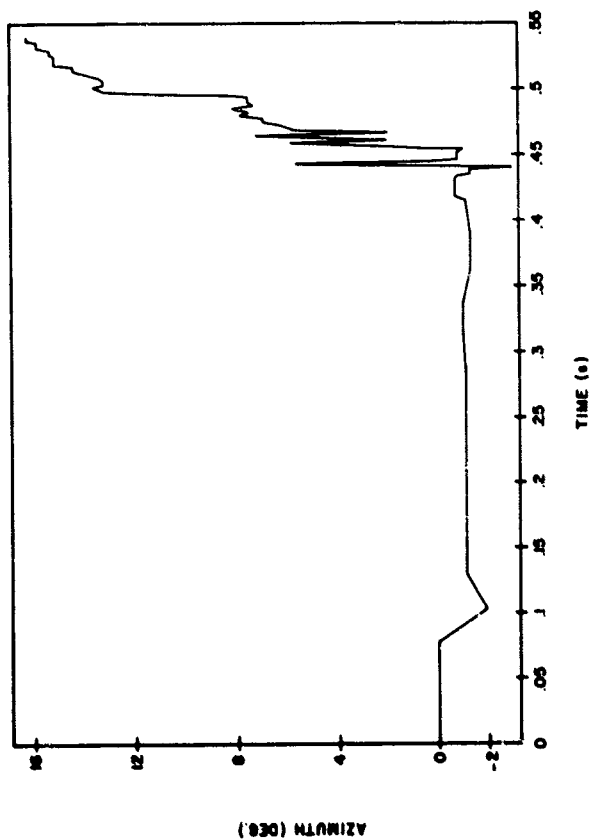


FIGURE 97. Yaw of A/C RUNO 145074.

in absence of the quantitative data for the free-standing aircraft, BUNO 145062, qualitative observations will have to suffice. This aircraft did not exhibit any tendency to overturn during the positive drag phase but the tire skid marks provided valid evidence that translatory and yaw motions did take place. The sequence of events was difficult to reconstruct from the postblast location of the aircraft which showed:

1. The main landing gear wheels were found displaced approximately 30 cm (12 in.) downstream (away from the GZ). Tire marks extending 30 cm (12 in.) forward were also observed.

2. The nose landing gear wheel was found displaced 38 cm (15 in.) upstream (towards the GZ) with no indication of forward or aft motion.

As mentioned earlier, the tiedown system used for the two secured aircraft provided an effective restraint against aircraft motions during the positive blast phase. The extent of that effectiveness is illustrated by the data on energy absorbed immediately following the shock intercept by the load cells incorporated in the tiedown system, Table 11.

As an initial attempt at defining aircraft rigid body motion during blast phase, this test provided basic data for follow-on studies in the verification of overturning predictions.

NUCLEAR TEST DATA CORRELATION

A review of old nuclear test data reveals that project 3.1 in OPERATION SNAPPER in the spring of 1952 involved extensive testing of parked aircraft. Test films and photographic records were reviewed to check correlation with the recent DICE THROM results. Numerous aircraft were exposed to combined blast and thermal effects at different intensities and from different orientations. The aircraft of interest were the F-47, the XF-90 and the F-86.

The damage to these aircraft exposed to increasing pressure levels was observed as follows:

Onset of damage pressure - slight buckling of control surfaces, access doors blown off, and occasional panel ruptured.

TABLE 11. Energy Absorption by the Tiedown Load Cells Following Blast Intercept.

Air- craft No.	Load Cell No.	FORCE		STROKE		ENERGY ABSORBED	
		kN	lbf	m	ft	kJ	ft-lbf
BUNO 149558	1	46.7	10,500	.0190	.063	0.896	661
	2	46.7	10,500	.0016	.001	0.0149	11
	3	46.3	10,400	.0538	.177	2.496	1841
	4	46.7	10,500	.0635	.208	2.967	2188
	5	47.8	10,750	.0286	.094	1.367	1008
	6	49.8	11,200	0	0	0	0
BUNO 145074	1	47.8	10,750	.0079	.026	0.377	278
	2	47.8	10,750	.0064	.021	0.317	234
	3	46.3	10,400	.1286	.422	5.951	4389
	4	45.1	10,150	.1492	.490	6.737	4969
	5	46.7	10,500	.0778	.255	3.635	2681
	6	45.1	10,150	.0540	.177	2.436	1797

NOTE: Details of the tiedown system geometry are available at WEF AT Department.

Intermediate pressure - moderate buckling of control surfaces and fuselage panels between substructure supports, broken canopies (on F-47 only). Damage appears much like that occurring on the two A-4C aircraft subjected to 6 psi in the DICE THROW test.

Severe damage pressure - large rigid body motions causing major substructure damage, vertical stabilizers broken, canopies broken, XF-90 and F-47 fuselages broken completely at aft section joint - - damage similar to A-4C damage at 9 psi location in DICE THROW.

Admittedly, thermal radiation effects played a big part in the total picture of damage; i.e., many aircraft had scorched paint, wrinkled skins and extensive damage to the very vulnerable control surfaces. However, the damage described above was, for the most part, attributed to blast effects. A conscious effort was made, in the present assessment, to consider only blast induced damage; nevertheless, some synergistic effects are necessarily present.

Overall, this data correlated well with the results on the A-4Cs in DICE THROW. The presence of skin panel dishing-in or buckling was similar and tail cone buckling was quite similar. Both sets of test data confirm that the weak point in the fuselage is at the aft section or tail joint. However, even though the SNAPPER data shows bent rudders, they were not torn off the tails as was uniformly the case in DICE THROW. The rudder hinges must be extremely weak on the A-4C aircraft.

THIS PAGE INTENTIONALLY LEFT BLANK

CONCLUSIONS

The conclusions, presented below, are based on the experimental and analytic data for the Navy A-4C aircraft. It should be noted that the structural response to over-pressure is directly related to the aircraft design characteristics. An extension of these conclusions to aircraft of difference class, configuration, etc. can only be made with proper regard to the design and configuration similarities.

The conclusions are listed grouped into four separate categories:

1. General - Test Data
2. Method 1 - Assessment
3. Method 2 - Assessment
4. Method 3 - Assessment

GENERAL - TEST DATA

1. The response of panels in the actual aircraft structure does not conform to the classic, clamped edge boundary condition. An intermediate response between the simply supported and clamped edge boundary conditions is implied by the test data. The analytic representation (NOVA 2) allows only one or the other.
2. Location of the panel boundary could not be determined precisely because it depended on substructure configuration and rigidity. With a finite rigidity of the true-to-life substructure, the effective panel boundary location was a function of load intensity. None of the analytic methods allows for boundary flexibility.
3. Because of the physical size of strain gages, their strain averaging characteristic makes the determination of maximum strain subject to significant errors in the regions of steep strain gradients.

4. Rigidity of panel boundaries is shown to be a dominant factor in panel response characteristic. This was evidenced by the response of panels 1 and 8 whose behavior approached that of panels with a simply supported edge boundary condition. This is contrasted with the behavior of panels 4, 5, and 6 which behaved more like panels with a clamped edge boundary condition. The former panels were located on vertical stabilizer characterized by more flexible substructure. The latter were located on the fuselage with more rigid substructure.
5. The likely effect of finite rigidity of the substructure at panel boundaries is that, at lower stress levels, the panel response resembles more closely the response for a clamped edge boundary condition. At higher stress levels, the panel response tends to approach the response for simply supported edge boundary condition.
6. Only narrow limits separate slight damage from catastrophic failure of the aircraft structure exposed to the blast test conditions. In terms of the range for the parked and tied down aircraft, this amounts to approximately 60 m (200 ft).
7. Local substructure failure may lead to a premature skin panel failure.
8. Holes in the substructure members act as fracture initiation points and are likely causes of premature failure.
9. Substantial pressure variations across structural elements such as skin panels are experienced during the blast diffraction phase.
10. Time of shock arrival for panel elements varies from point to point and is dependent on the panel shape and its orientation with respect to blast.
11. The strain history for flat panels varies across the panel area. Strains at the center of the panel peak to a maximum value during the first oscillation which is followed by attenuation of strain amplitudes during subsequent cycles. At the panel edge, several cycles with increasing amplitudes precede the attenuation trend.

12. The strain history for curved panels is more uniform across the panel area. Maximum response during the first oscillation, followed by an attenuation, is generally observed at the center as well as at the edge of the panel.

13. Strain histories for fuselage locations were characterized by initial high frequency oscillations, followed by low frequency oscillations, which resulted in an even higher, delayed, secondary peak.

14. For gages on panels 4 and 5 (curved panels located at approximately mid-fuselage), the maximum strain values are indicated at approximately 10 ms after the shock intercept. This implies a synergistic effect of overpressure and gust and constitutes a convincing evidence that these two effects can not be divorced from one another in considering the overall vulnerability of aircraft structure to blast.

15. The maximum response of panels to overpressure alone was generally observed to occur within 1 ms after the blast intercept.

16. The synergistic effects of overpressure and gust first appear approximately 7 ms after the shock intercept. This corresponds approximately to the fuselage natural frequency, demonstrated in ground vibration tests conducted by the manufacturer.

17. Gust effects were observed to become increasingly more prominent and reached their maximum at 70 to 80 ms after the shock intercept. For strain gages installed on the fuselage in the direction parallel to aircraft axis, the overall maximum response was obtained at that time.

18. The strain gage data survey for the strain gradients developed in the vicinity of the panel boundary along the longer edge further reinforce the conclusion that the actual panel response falls between the clamped and simply supported edge boundary conditions. For the simply supported edge boundary condition, a low strain gradient is expected with membrane strains dominating. For the clamped edge boundary condition, a very high strain gradient is predicted with bending strains dominating. The experimental data also show high strain gradients and significant bending strains in the vicinity of the panel boundary. However, the differences between strains at panel center and at the edge are not as great as expected for the theoretical clamped edge boundary condition.

METHOD 1 - ASSESSMENT

1. Critical overpressure calculated at 17.2 kPa (2.5 psi) for the sure-safe condition according to Method 1 is slightly conservative for fighter and fighter-bomber class aircraft represented by the A-4C.
2. Critical overpressure calculated at 137.9 kPa (20 psi) for the sure-kill condition according to Method 1 grossly exceeds the limit of the attack-class aircraft survivability. An A-4C sustained catastrophic failure at a 62.1 kPa (9 psi) peak free-field overpressure.
3. Vulnerability envelopes constructed according to Method 1 appear rather crude. The multiple ground range values obtained for a given height of burst are unrealistic and tend to be confusing.
4. Method 1 provides means for rapid determination of the vulnerability envelopes and can be satisfactorily used where the range error factor of two is acceptable.
5. The engineering time required to obtain a solution according to Method 1 is assessed at 20 minutes.

METHOD 2 - ASSESSMENT

1. The panel analyses according to Method 2 yield results which may differ significantly from the experimental data. However, the discrepancies are found to be within the error limits specified for this method.
2. The results of frame analysis according to Method 2 were found to be compatible with the test results.
3. The longeron analysis according to Method 2 for sure-safe and sure-kill conditions may lead to contradictory results, i.e., indicated critical overpressure value calculated for the sure-safe condition may be higher than the overpressure value for the sure-kill condition.
4. Considerable familiarity with aircraft structural response to blast and experience in structural modeling are required to ensure rational results from the analysis using Method 2.

5. The aircraft vulnerability data obtained according to Method 2 are well within the 1.6 error factor limits specified in terms of the equivalent critical range values.

6. Method 2 is distinctly superior to Method 1. Selection of weakest structural elements for analysis and their modeling in some detail assures results of greater accuracy.

7. Analytic solutions based on Method 2 can be obtained in less than ten seconds of computer time using OVPR2 code. The engineering time required to obtain a solution is assessed at five hours for the first case and approximately two hours for each subsequent case for the same aircraft.

METHOD 3 - ASSESSMENT

1. The NOVA 2 computer code represents by far the most sophisticated analytic tool of the three methods considered.

2. NOVA 2 offers a capability for modeling structural elements in considerable detail. This ensures a high degree of accuracy for predicting the overpressure response of an idealized, isolated structural element.

3. There are no provisions in NOVA 2 for adequate modeling of structural elements in conjunction with the adjacent structure. This tends to reduce the accuracy of NOVA 2 predictions.

4. NOVA 2 is limited to the analysis of overpressure effects on aircraft structure. Consideration of synergistic effects of overpressure and gust are beyond its scope.

5. The assumption in NOVA 2 that a given time of the shock arrival applies to the entire area of the element analyzed holds true only in specific cases. A finite time is required for the shock to sweep across the structure in the majority of situations. This introduces some error to the analytic solution.

6. Complex shock reflection patterns are evident from the experimental data but are not duplicated in the analytic (NOVA 2) blast representation.

7. For the structural elements of considerable size, particularly the curved elements such as fuselage frames, NOVA 2 contains no provisions to adequately model the

overpressure distribution during the diffraction phase. The assumption of constant pressure across the element analyzed by NOVA 2 does not necessarily represent the actual condition and constitutes a source of error in the analytic prediction. In actuality, pressure gradients do exist across the structure.

8. By providing data for idealized structural elements analyzed under selected boundary condition, NOVA 2 is capable of approximating the response of a true-to-life structural element.

9. Weighing all the evidence, boundary condition modeling is most critical for panel response prediction.

10. Panel 8 modeling with the simply supported edge boundary condition provided results closely comparable with the experimental data--at the panel center 3180 versus 3800 microstrains and at the edge 2300 versus 2400 microstrains were indicated for the analytic (NOVA 2) and experimental values, respectively.

11. Panel 8 modeling with the clamped edge boundary condition representation (NOVA 2) predicted considerable yielding of the material at the panel boundary. This was not verified by the experimental data where the corresponding strains were well within the elastic limit.

12. Lack of adequate correlation between the analytic (NOVA 2) and experimental data is evidenced by predominantly membrane strains indicated at panel center in the analysis while the experimental data show bending strains as dominant.

13. In some cases, strain values obtained from the NOVA 2 (KADBOB) solution are extremely sensitive to the relationship between the numerical integration time step, DELTIM and the segment length parameters. For short segment lengths, small DELTIM values are required. If DELTIM value is insufficiently small, unrealistically high strain values are obtained. This was apparent in panel 8 analysis for the simply supported edge condition, but was not indicated in the solutions for panels 1 and 5 with the clamped edge boundary condition representation.

14. Analytic predictions based on beam representation of panels (NOVA 2 - KADBOB) give increasingly poor predictions of peak strain for increasing excursions in the plastic range. For conditions beyond the material yield, KADBOB solutions indicate colossal strains at the panel boundary, completely unrelated to the experimental data. For panel 1, the analytic strains were 45 times higher than the corresponding experimental strains. This trend is not indicated by the panel, NOVA 2 - DEPROP, representation.

15. Applicability of beam representation for panels is not clearly specified in the Method 3 (NOVA 2) handbook, and its accuracy is not defined as related to the stress range. It appears that the stress level is the factor governing the solution accuracy.

16. Taking a holistic view, NOVA 2 does an acceptable job of approximating true-to-life structural response. However, this requires considerable engineering time and expert judgement on the part of the analyst. The engineering time required to obtain a solution is assessed at 40 man-hours for the first case, and the required computer time may exceed two hours on the CDC 6600 computer system.

17. This experimental study, exclusively devoted to the primary airframe structural response to overpressure loads, was not concerned with the nonstructural damage. Loss of rudders, damage to landing gear doors, and rupture of access doors in the engine area were all sustained during the test. This damage was in itself serious because of potential flight impairment and/or fire hazard and should be considered in the overall assessment of aircraft vulnerability/survivability.

18. A brief review of the nuclear test data obtained during OPERATION SNAPPER in 1952 indicated that, for the attack class aircraft, the damage at corresponding overpressure levels was comparable to that sustained by A-4C aircraft during the nonnuclear DICE THROW event.

THIS PAGE INTENTIONALLY LEFT BLANK

APPENDIX A

LOADING AND RESPONSE PREDICTIONS FOR TESTING AN F-4 TRAILING EDGE FLAP IN PRE-DICE THROW II EVENT

Abstracted from report prepared by John M. Calligeros
and William N. Lee of Kaman Avidyne, Burlington, Massachusetts
01803 under DNA Contact No. DNA001-75-C0080
August 1975

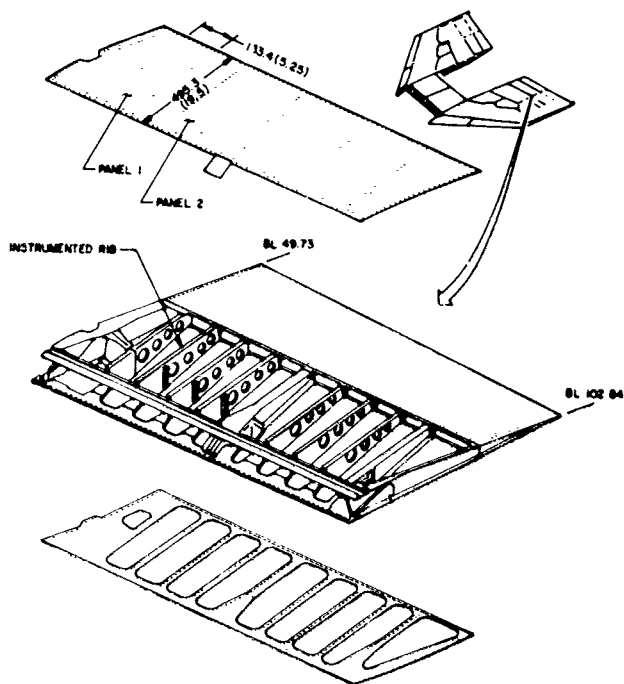
OBJECTIVES

The purpose of this technical memorandum is to provide pretest support to the Naval Weapons Evaluation Facility (NWEF) for testing a F-4 trailing edge flap in the PRE-DICE THROW II project. This support includes the following items:

1. Calculation of the flap panel response and the likelihood of rib buckling to blast using the latest revision of the NOVA code.
2. Review of the strain gage and pressure gage instrumentation scheme formulated at NWEF and making recommendations for setting instrumentation gains.
3. Definition of the test data-reduction requirements.

DESCRIPTION OF STRUCTURE

The flap assembly is illustrated in Figs. A-1 through A-3. Figure A-3 also shows strain gage locations. The structural items of interest in this analysis are a typical skin panel 1.02 mm (0.040 in.) thick, measuring 492 x 133 mm (19.5 x 5.25 in.) between rivet lines, as shown in Fig. A-3, and a rib (Fig. A-1). A detail of the rib, taken from McDonnell-Douglas drawing 32-18509, is shown in Fig. A-4. As indicated in Fig. A-2, the extremities of the panel are represented by fastener lands 1.60 mm (0.063 in.) thick and 19.1 mm (0.75 in.) wide. The pertinent dimensional and material characteristics of these two structural items are summarized as follows:



The length is in millimeters
with inches in parenthesis.

FIGURE A-1. Trailing Edge Flap.

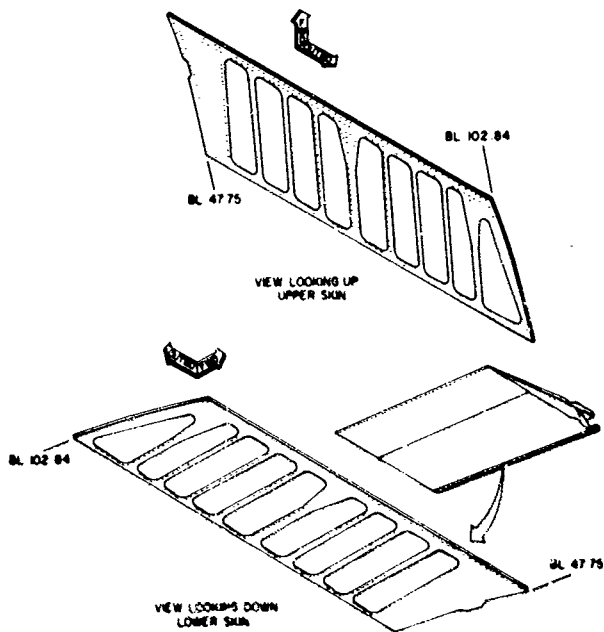
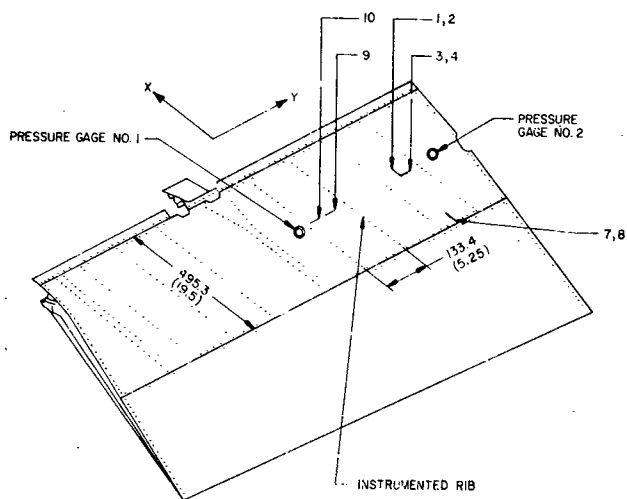


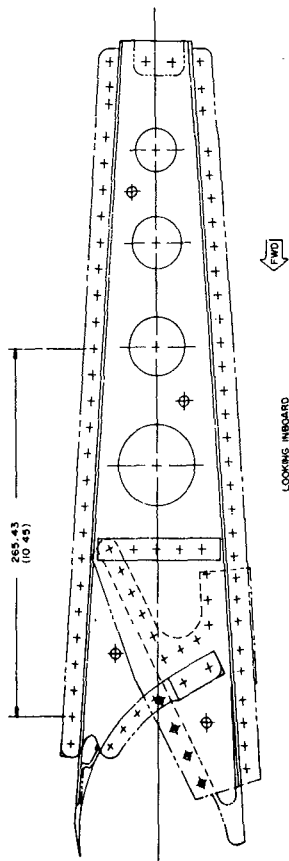
FIGURE A-2. Trailing Edge Flap Upper and Lower Torque Box Skin Diagram.



LEGEND
 - STRAIN GAGE
 ○ PRESSURE GAGE

The length is in millimeters
 with inches in parenthesis.

FIGURE A-3. Instrumentation Location Diagram.



The length is in millimeters
with inches in parenthesis.

FIGURE A-4. Rib Assembly x_B 72.750.

Skin Panel

length = 495 mm (19.5 in.) between rivets
width = 133 mm (5.25 in.) between rivets
thickness = 1.02 mm (0.040 in.)
fastener lands thickness = 1.60 mm (0.063 in.)
fastener lands width = 19.1 mm (0.75 in.)
material 7075-T6 Aluminum
 E (Young's modulus of elasticity) = 71.0 GPa
(10.3×10^6 psi)
 f_{ty} (tensile yield stress) = 476 MPa
(69,000 psi)
 ν (Poisson's ratio) = 0.33
 G (shear modulus) = 26.9 GPa (3.9×10^6 psi)
 ρ (density) = 2.77 Mg/m³ (0.10 lb/in.³)

Rib

thickness = 0.81 mm (0.032 in.)
 r_1 = radius of 1st lightening hole
= 29.2 mm (1.15 in.)
 r_2 = radius of 2nd lightening hole
= 21.3 mm (0.84 in.)
 z = distance between lightening hole centers
= 88.6 mm (3.49 in.)
 d = rib depth between lightening holes
= 93.7 mm (3.69 in.)
material 7178-T6 Aluminum
 E = 71.0 GPa (10.3×10^6 psi)
 f_{ty} = 503 MPa (73,000 psi)
 ρ = 2.77 Mg/m³ (0.10 lb/in.³)

The dimensions r_1 , r_2 , t , and d were scaled from the rib blueprint.

LOADING

The flap is subjected to a shock wave impinging side-on to the skin surface. The shock wave results from a ground explosion of 109 Mg (120 tons) of ANFO at White Sands Missile Range testing grounds at 1220 m (4000 ft) elevation. The flap is located approximately 305 m (1000 ft) from the burst center, and the resulting free-field incident overpressure, p_{so} , is 25.5 kPa (3.7 psi). The pressure loading normal to the panel surface is calculated with the standard method given in Ref. 10 and the pressure-time profile is shown in Fig. A-5. The peak reflected overpressure, Δp_r , is calculated to be 57.2 kPa (8.29 psi) and the diffraction time, t_c , is 2.06 ms. Since the peak structural panel responses occur in less than 1.0 ms, the drag loading is of no consequence in the panel response and the imposed loading could be taken as a step function if desired. The linear decay shown in Fig. A-5 was used in the NOVA program for the panel response calculations.

The rib experiences loading on its upper and lower surfaces due to the enveloping shock front (the upper surface of the rib faces GZ). For the upper rib surface, the overpressure loading, Δp_p^u , is

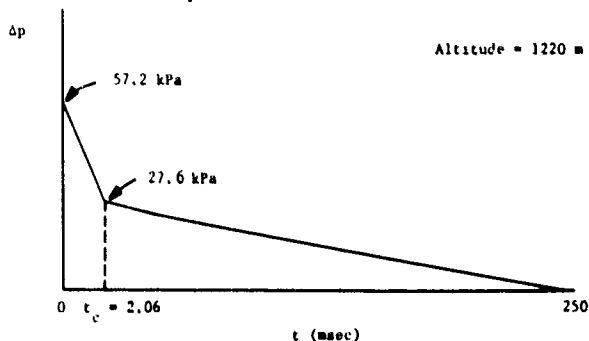


FIGURE A-5. Pressure Loading Normal to Panel Surface.

$$\begin{array}{lll} p_{so} = 25.5 \text{ kPa} & \text{Incident} & C_o = 335 \text{ m/sec} \\ p_{so} = 87.6 \text{ kPa} & \text{Ambient} & \end{array}$$

$$\Delta p_r = 2 p_{so} \left[\frac{7 p_o + 4 p_{so}}{7 p_o + p_{so}} \right] = 57.2 \text{ kPa}$$

$$t_c = \frac{3h}{C_{ref}} = 2.06 \text{ msec where}$$

$$C_{ref} = \frac{C_o}{\sqrt{7}} \sqrt{\frac{16(p_{so}/p_o)^2 + 70(p_{so}/p_o) + 49}{6(p_{so}/p_o) + 7}} = 360 \text{ m/sec}$$

$$h = 495/2 = 247.5 \text{ mm}$$

$$\Delta p^u = [\Delta p_r - \Delta p(t_c)] \left(1 - \frac{t}{t_c} \right) + \Delta p^u(t_c) \quad 0 \leq t \leq t_c$$

$$\Delta p^u = p_s(t) + C_D^u q(t) \quad t \geq t_c$$

where

$$\Delta p^u(t_c) = p_s(t_c) + C_D^u q(t_c)$$

and

C_D is the drag coefficient

q is the dynamic pressure

For the lower rib surface, the overpressure loading, Δp^l , is

$$\Delta p^l = \Delta p^l(t_c) \frac{t}{t_c} \quad 0 \leq t \leq t_c$$

$$\Delta p^l(t_c) = p_s(t_c) + C_D^l q(t_c) \quad t \geq t_c$$

where

$$\Delta p^l(t_c) = p_s(t_c) + c_D^l q(t_c)$$

For the present application with the NOVA code, the average of the upper and lower pressure loadings was applied equally to the upper and lower surfaces of the rib. Thus, for each surface, the applied (compressive) pressure loading on the rib was taken to be

$$\frac{\Delta p^u + \Delta p^l}{2} = \frac{1}{2} \left\{ [\Delta p_r - \Delta p^u(t_c)] \left(1 - \frac{t}{t_c} \right) + \Delta p^l(t_c) \frac{t}{t_c} + \Delta p^u(t_c) \right\} \quad 0 \leq t \leq t_c$$

$$\frac{\Delta p^u + \Delta p^l}{2} = p_s(t) + 0.3q(t) \quad t \geq t_c$$

where, for $p_{s0} = 25.5$ kPa (3.7 psi) (see Fig. A-5),

$$\Delta p_r = 57.2 \text{ kPa (8.29 psi)}$$

$$t_c = 2.06 \text{ ms}$$

$$t_0 = 250 \text{ ms}$$

and

$$p_s(t) = p_{s0} \left(1 - \frac{t}{t_0} \right)^2 e^{-\frac{t}{t_0}}$$

$$q(t) = q_0 \left(1 - \frac{t}{t_0} \right)^2 e^{-3.5 \frac{t}{t_0}}$$

$$q_0 = p_0 \left[\frac{5/14 (p_{s0}/p_0)^2}{1 + \frac{1}{7} (p_{s0}/p_0)} \right]$$

$$c_D^u = 1.0$$

$$c_D^l = -0.40$$

Figure A-6 presents a plot of the pressure loading assumed for each surface of the rib.

STRUCTURAL RESPONSE

Two structural response subroutines in the NOVA code may be used for obtaining the nonlinear blast response of the flap skin panel (Ref. 7). One subroutine is DEPROP, which treats the panel as a plate structure and is based on a modal solution. The other is DEPROB, which is a beam solution and uses a lumped-mass representation. If the aspect ratio of the panel is sufficiently high, as it is in the present case, the beam solution will give results which are comparable to the panel solution at a considerable saving in computer time. In addition, the beam solution (DEPROB) is expected to calculate the edge strain more accurately than the panel solution (DEPROP). The beam solution uses a unit strip of the panel of length equal to the panel width to represent the panel response.

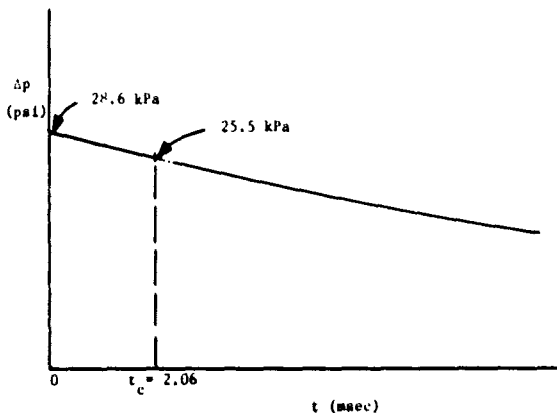


FIGURE A-6. Pressure Loading Assumed for Upper and Lower Rib Surfaces.

Both codes are exercised for the present problem, DEPROB for three loading conditions and DEPROP for one loading condition (i.e., the 25.5-kPa (3.7 psi) incident overpressure case). Clamped boundary conditions are used in both codes. The fastener lands introduce an uncertainty regarding the panel dimensions to be used in the codes. Because of this, it was decided to run two cases, one in which the rivet line dimensions are employed and the other in which the rivet line dimensions are reduced by the lands width of 19.1 mm (0.75 in.), in anticipation that the correct model would fall in between.

Figure A-7 summarizes the maximum edge strain and the strain at the panel center as a function of reflected overpressure, Δp_r . The maximum edge strain occurs in the outer panel surface and the maximum center strain occurs in the inner panel surface. It is seen that at Δp_r equal to 57.2 kPa (8.29 psi) (which corresponds to the 25.5-kPa (3.7 psi) incident level), the maximum edge strain is very close to the yield strain whereas the maximum center strain is considerably lower than yield strain. At the higher pressure levels in Fig. A-7, which extend to 300 percent of Δp_r equal to 57.2-kPa (8.29 psi), the edge strain exceeds 10 percent whereas the center panel strain remains below yield strain. The beam results shown in Fig. A-8 are based on an elastic-plastic solution using 10 masses for a half-beam length, which is allowed by symmetry. The single panel result shown in the figure is based on an elastic solution using a 7 x 7 modal formulation, of which 25 modal combinations are selected.

Some typical strain histories are shown in Figs. A-8 to A-10, in which comparisons are made between the beam and panel solutions for p_{so} of 25.5 kPa (3.7 psi). The two solutions are in very close agreement with respect to peak values and the shape of the response curves. The peak strains and deflections, incidentally, occur at about 0.5 - 0.6 ms, well within the blast diffraction phase.

The rib response is obtained with the beam code DEPROB by selecting a unit strip of the web between the first two lightening holes. The length of the beam strip is 93.7 mm (3.69 in.) and its thickness is 0.81 mm (0.032 in.). Sliding, clamped boundary conditions, characterized by zero slope and only axial motion at the edge, are used. In DEPROB, a

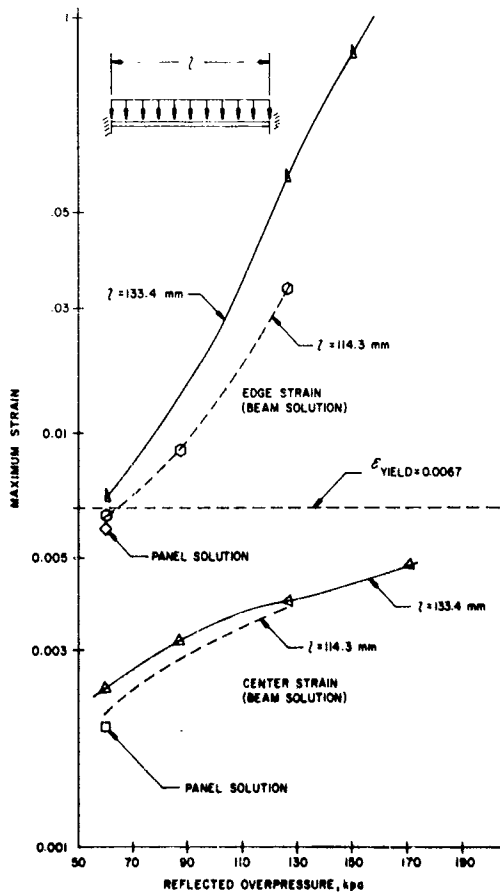


FIGURE A-7. Maximum Strain vs. Reflected Overpressure for Skin Panel.

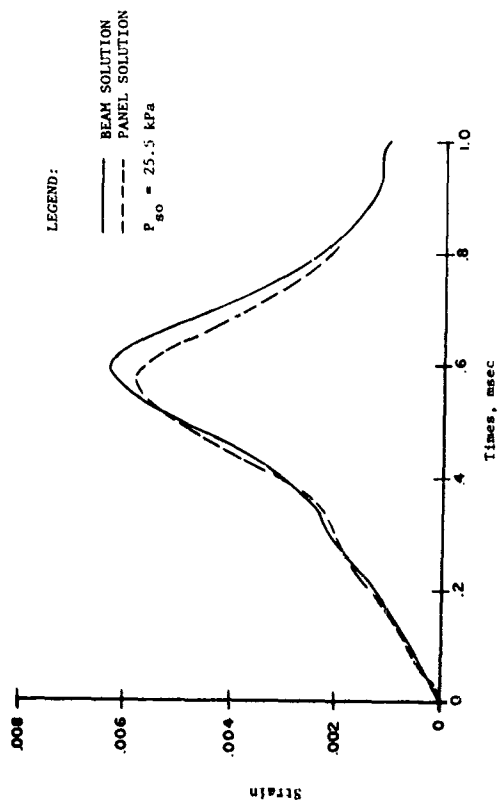


FIGURE A-8. Comparison of Skin Panel Edge Strains, Outer Surface.

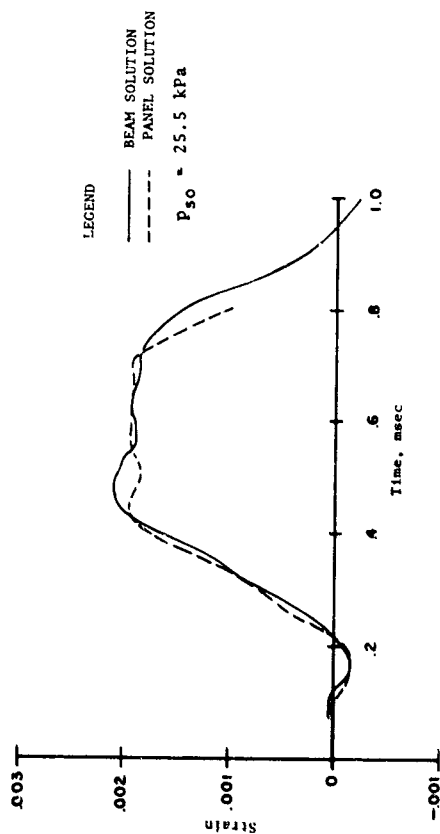


FIGURE A-9. Comparison of Skin Panel Center Strain, Inner Surface.

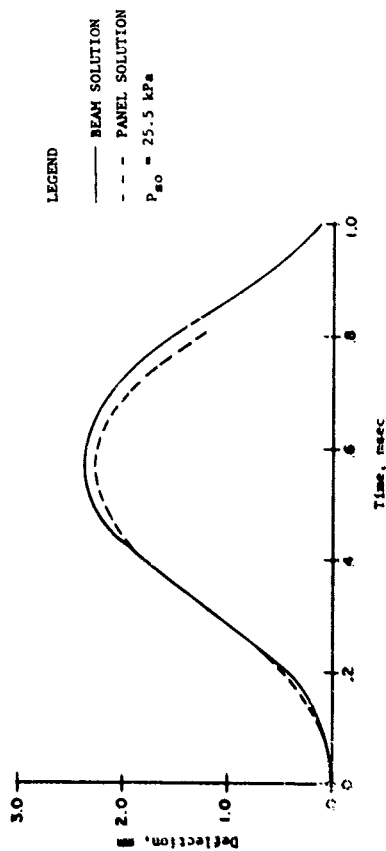


FIGURE A-10. Comparison of Skin Panel Center Deflections.

$\frac{\delta}{2} \left\{ 1 - \cos \frac{(2\pi x)}{t} \right\}$ variation is assumed for the shape of the initial imperfection, where δ is the peak amplitude of the imperfection. Two values of δ are investigated, as δ of 0.254 mm (0.01 in.) and 0.508 mm (0.02 in.). The beam strip is subjected to compressive end loads based on the pressure loading discussed earlier, the panel width, and the dimensions relating to the lightening hole radii and the spacing between lightening holes. Thus, for the pressure loading shown in Fig. A-7, for example, the pressure curve is multiplied by

$$133.4 \frac{t}{t-r_1-r_2} = 310.19 \text{ mm (12.22 in.)}$$

to obtain the compressive end loads acting on the strip.

Figure A-11 presents the maximum edge strain and center strains of the rib as a function of the reflected overpressure. At the reflected overpressure corresponding to the 25.5 kPa (3.7 psi) incident shock, the rib strains are considerably lower than the yield strain. Yield is not experienced until the reflected overpressure is increased by 60 percent (for $\delta = 0.508$ mm (0.02 in.)). It may also be noted that the maximum edge strain and center strain at the outer surface are fairly close for both imperfection values. The peak rib strains occurred between 1 and 2 ms for the 25.5 kPa (3.7 psi) shock and between 3 and 4 ms for the higher pressure levels. As expected, these times are considerably higher than those for the peak skin panel strains.

In summary, the results of Figs. A-7 and A-11 indicate that at incident overpressure of 25.5 kPa (3.7 psi), the skin panel will experience strains comparable to the yield strain along its long edge. Strains will be lower than yield at other points on the panel, even at reflected overpressures considerably greater than the reflected overpressure corresponding to an incident shock of 25.5 kPa (3.7 psi). The rib, on the other hand, will experience strains considerably below yield at the 25.5 kPa (3.7 psi) level, and therefore will not buckle at this load level. At pressure levels approximately 60 percent higher, a possibility of rib buckling exists. The predicted strain data are summarized in Table A-1.

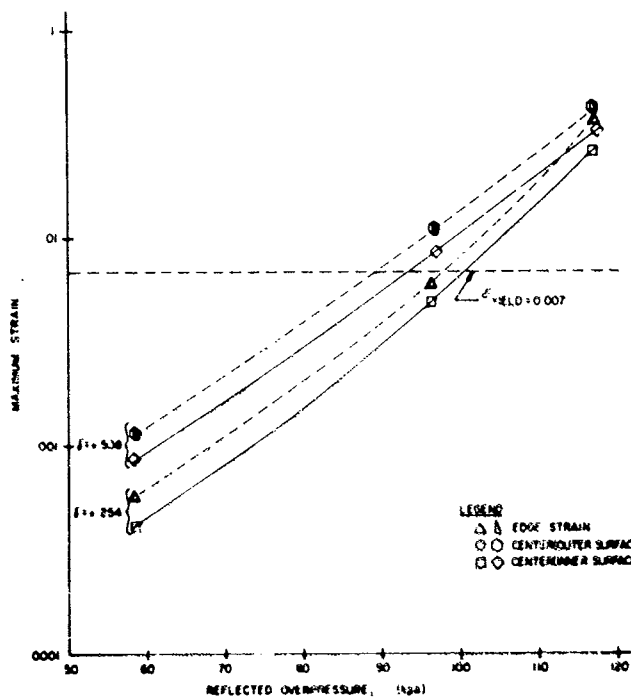


FIGURE A-11. Maximum Strain vs Reflected Overpressure for Rib.

TABLE A-1. Instrumentation Plan.

Gage Number	Panel Number	Gage Location	Surface	Orientation On Centerline	ϵ_{\max} Microstrains
1	1	C	OUT	X	-93
2	1	C	IN	X	-85
3	1	C	OUT	Y	-715
4	1	C	IN	Y	1950
5	1	LS	OUT	Y	6500
6	1	LS	IN	Y	-4200
7	1	SS	OUT	X	1709
8	1	SS	IN	X	-2248
9	2	C	OUT	Y	-715
10	2	LS	OUT	Y	6500
11	-	RIB	-	-	1000
12	-	RIB	-	-	1000
Location: Center (C), Long Side (LS), or Shortside (SS) Surface: Outside (OUT) or Inside (IN) Orientation: Parallel to Long Side (X) or to Short Side (Y)					

APPENDIX B

EXPERIMENTAL RESULTS OF F-4 TRAILING EDGE FLAP IN PRE-DICE THROW II EVENT

TEST OBJECTIVE

The NWEF test, conducted as one project in the PRE-DICE THROW II Event, involved an instrumented F-4 wing trailing edge flap.

The test objective was to obtain preliminary information on structural response to blast. The data from this test was used in planning the configuration and the instrumentation requirements for the A-4C aircraft test specimens which were subsequently exposed to blast during the main DICE THROW Event.

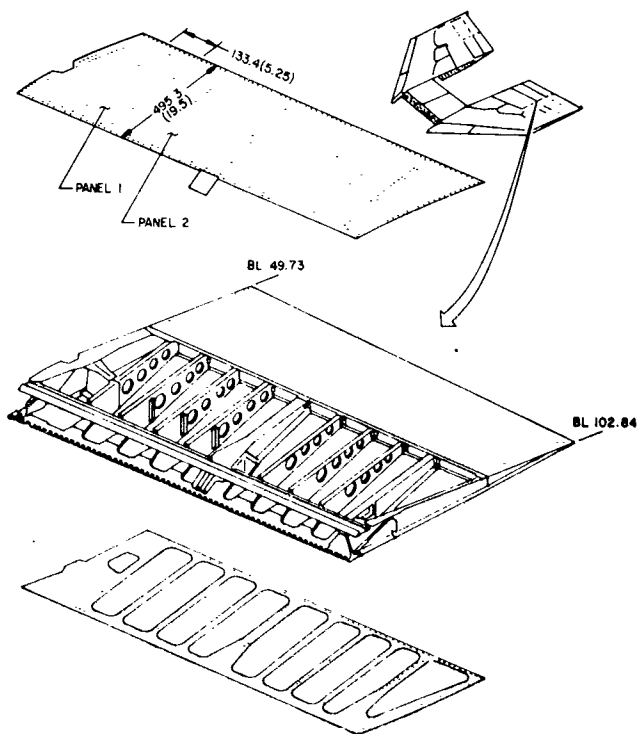
TEST SPECIMEN

An F-4 trailing edge flap, shown in Fig. B-1, represents a structural panel with relatively rigid boundary members. The aft section was made of honeycomb structure and the forward section consisted of top and bottom skins riveted to a substructure made up of a series of light ribs. The skins, made of 7075 Aluminum alloy were chem-milled to 1.02 mm (0.4 in.) basic thickness with 1.6 mm (0.063 in.) thick lands.

TEST INSTRUMENTATION

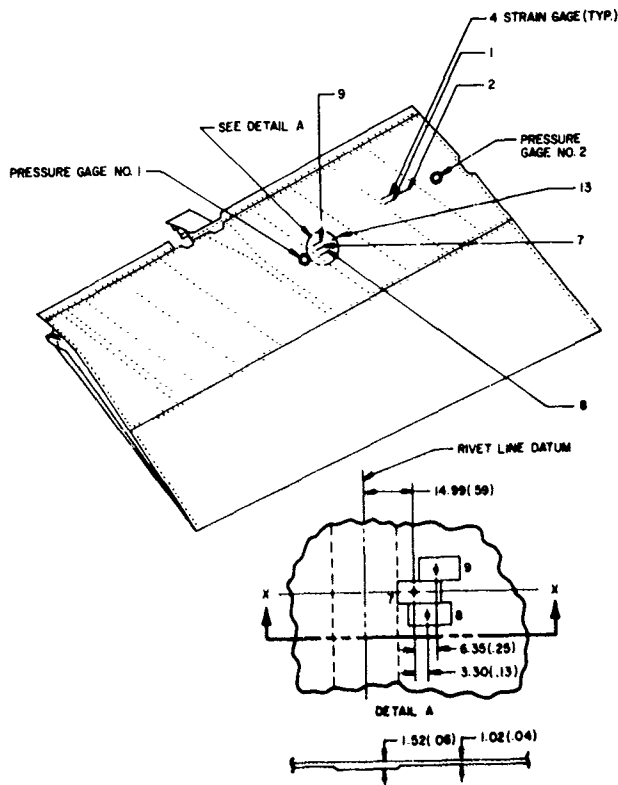
The basic instrumentation consisted of pressure gages and strain gages. For the purpose of correlating analysis and equipment, Panel No. 1 and Panel No. 2 (Fig. B-1), measuring 495 x 133 mm (19.5 x 5.25 in.) between rivet lines, were the areas selected for the instrumentation.

Strain gages were installed on the upper skin outside and inside surface as well as on the web of the rib which made up the outboard boundary of Panel No. 1. Detailed disposition of the instrumentation is shown in Figs. B-2 and B-3 for the outer and inner skin surfaces, respectively.



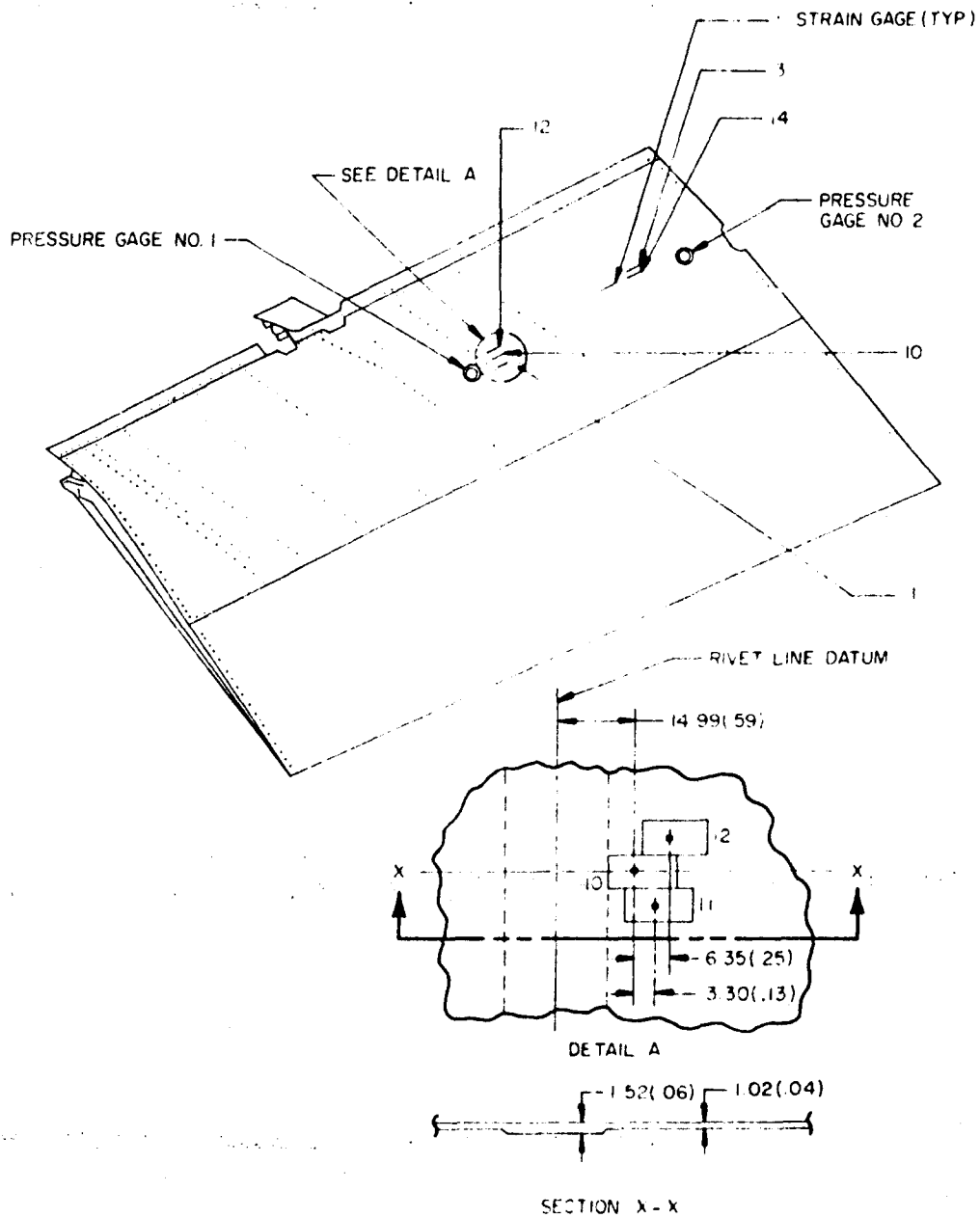
The length is in millimeters
with inches in parenthesis.

FIGURE B-1. F-4 Flap - Structure Configuration Diagram.



The length is in millimeters
with inches in parenthesis.

FIGURE B-2. Instrumentation Location Diagram - F-4 Flap
Upper Skin Outer Surface.



The length is in millimeters
with inches in parenthesis.

LEGEND

- STRAIN GAGE
- PRESSURE GAGE

FIGURE B-3. Instrumentation Location Diagram - F-4 Flap
Upper Skin Inner Surface.

TEST SETUP

The flap panel was mounted vertically on two poles located at a distance of 305 m (1000 ft) from the GZ. See Fig. B-4. Approximately 25.5-kPa (3.7 psi) overpressure was expected at that location. To minimize edge effects which produce local pressure variation, plywood panels extended the flap boundaries in the vicinity of the instrumented areas.

TEST RESULTS

The pressure data obtained from pressure gage No. 1, Fig. B-5, indicated peak overpressure of 57.2 kPa (8.3 psi). The Ballistic Research Laboratory data taken on the master gage line showed a free-field overpressure of approximately 27.6 kPa (4 psi) at the 305 m (1000 ft) radial distance. This yields a reflection factor of 2.1.

The strain gage maximum response data during the first cycle immediately following the blast intercept are summarized in Table B-1. Generally higher strain values of up to 2100 microstrains were obtained at the panel center inside surface as compared to 1680 microstrains maximum indicated for the midpoint of outside surface of the panel longer side. Since the highest strains for a clamped panel were expected at the midpoint of the boundary of the panel longer side, this might suggest that the effective fixity of the panel boundaries was less than rigid. However, it must be noted that, because of the rivet line and substructure support the exact location of the panel boundary is debatable. Consequently, the area along the panel edges where strain gages were installed may only be defined as the vicinity of the panel boundary. Existence of a steep strain gradient at these locations implied some measure of fixity even though the actual strain level at the effective panel boundary remained undetermined.

The presence of steep strain gradients in the vicinity of the panel boundary was convincingly demonstrated by the strain record of gages 7, 8 and 9 as one set and gages 10, 11 and 12 as the second set. These sets of gages indicated strain gradients in excess of 300 microstrains per millimeter.

An interesting observation is implied in the comparison of the strain data obtained from the gages installed along the longer side edges of panels 1 and 2. Panel 1 was bounded



FIGURE B-4. Test Setup.

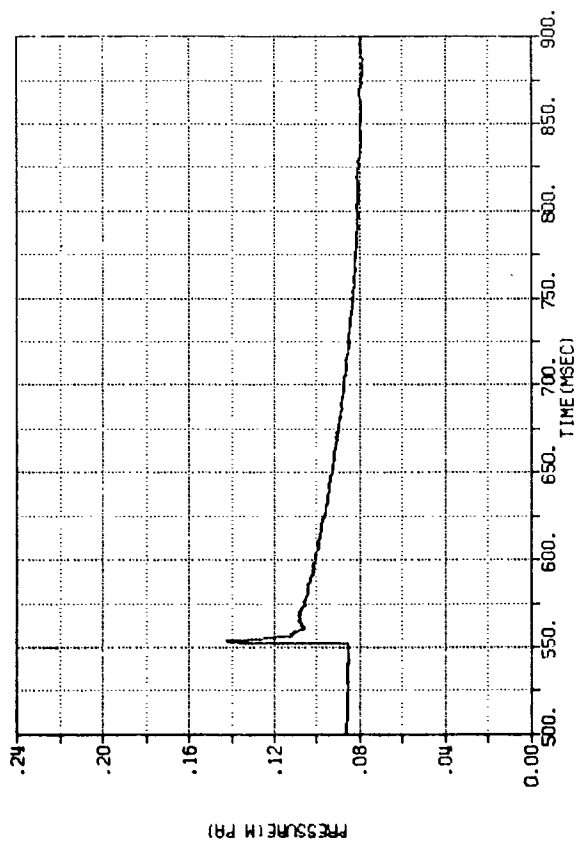


FIGURE B-5. Local Pressure Data - Pressure Gage No. 1
(Gage location shown in Fig. B-2)

TABLE B-1. Experimental Strain Data,
First Cycle Response.

GAGE LOCATION DATA			GAGE NO.	MAX STRAIN MICROSTRAINS	TIME AFTER SHOCK ARR. ms
REGION	PANEL NO.	SURFACE			
CENTER	1	OUTER	2	-1160	0.68
CENTER	2	OUTER	13	-1180	0.63
CENTER	1	INNER	3	2060	0.68
CENTER	1	INNER	14	2100	0.68
MID LONG SIDE	1	OUTER	1	1280	0.63
"	1	OUTER	4	1300	0.59
"	2	OUTER	7	1680	0.73
"	2	OUTER	8	1220	0.68
"	2	OUTER	9	1150	0.68
MID LONG SIDE	1	INNER	5	-500	0.63
"	2	INNER	10	-570	0.73
"	2	INNER	11	-400	0.68
"	2	INNER	12	-40	0.68
RIB	1	INNER	16	-400	1.19
RIB	1	OUTER	15	2720	1.19

by a rib of single thickness. There, a strain of 1300 microstrains was obtained. The flanges and the web of the panel 2 boundary rib were twice as thick as the panel 1 rib elements and the corresponding strain exceeded 1900 microstrains. This appears to indicate greater degree of fixity associated with stiffer substructure member at the panel boundary.

The maximum response data presented in Table B-2 in correlation with the first cycle data of Table B-1 show generally higher strain values obtained during subsequent oscillations. This implies a definite relationship between the responses of the individual elemental panels and the flap as a whole. It appears that the maximum response occurred when the elemental panel and the flap bending oscillations were momentarily in phase.

Along the lines of this reasoning, one might anticipate that the differences between the maximum and the first cycle responses should also be dependent on the panel location with respect to the flap boundary. Thus, greater differences in the strain values are expected for panel 2 than panel 1, since the former was farther away from the flap boundary than the latter. This, in fact, was the case as illustrated by the strain data of gages 2 and 13. For the gage 2 located on panel 1 the indicated strain difference was 640 microstrains and for gage 13 on panel 2 that difference was 780 microstrains. This situation is consistently apparent from the panel 1 data (gages 1 and 4) on one hand and the panel 2 data (gages 7, 8 and 9) on the other hand. There, the strain differences averaging to 35 microstrains for panel 1 were contrasted with the average difference of 270 microstrains for panel 2. This behavior pattern focuses on the interdependence of the response of a structural element comprising a part of a larger assembly.

The strain data of gages installed on the panel 1 rib (see Fig. B-6) indicates a maximum strain of 2720 microstrains for gage 15 which was located on the outer face of the rib. The corresponding strain on the rib inner face, obtained from gage 16 was -400 microstrains. These data show the presence of considerable spanwise bending, as illustrated by the differences in the instantaneous strain values. The graph also shows the trace of the direct strain profile. The response cycle of just over 2-ms duration is indicated with the direct strain initially compressive changing to tensile with a maximum value of 2720 microstrains at approximately 1.19 ms after shock arrival.

TABLE B-2. Experimental Strain Data,
Maximum Response.

GAGE LOCATION DATA			GAGE NO.	MAX STRAIN MICROSTRAINS	TIME AFTER SHOCK ARR. ms
REGION	PANEL NO.	SURFACE			
CENTER	1	OUTER	2	-1800	3.5
CENTER	2	OUTER	13	-1960	4.0
CENTER	1	INNER	3	2150	3.5
CENTER	1	INNER	14	2220	3.6
MID LONG SIDE	1	OUTER	1	1350	1.8
"	1	OUTER	4	1300	0.59
"	2	OUTER	7	1940	2.9
"	2	OUTER	8	1500	4.5
"	2	OUTER	9	1420	4.5
MID LONG SIDE	1	INNER	5	-1050	2.2
"	2	INNER	10	-1730	4.5
"	2	INNER	11	-1690	4.3
"	2	INNER	12	-1330	4.3
RIB	1	INNER	16	-400	1.19
RIB	1	OUTER	15	2720	1.19

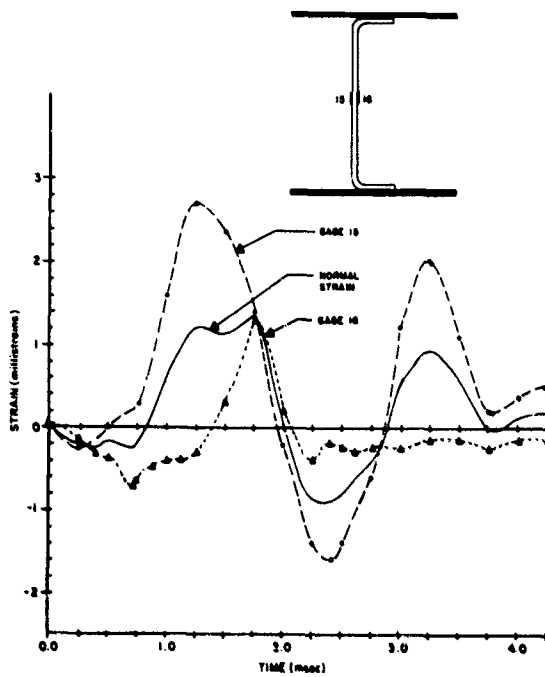


FIGURE B-6. Rib Gages Response.

DATA CORRELATION

The analytic prediction of the panel response to blast was provided by Kaman AviDyne of Burlington, MA. (See Appendix A.) The data was obtained from a NOVA 2 code solution.

As shown in Table B-3 a reasonable agreement exists between the analytic and the experimental data. At the center of the panel inside surface, the analytic strain of 1950 microstrains is only slightly smaller than the corresponding experimental strain of 2100 microstrains. The discrepancy between the strain data for the outside surface (-715 for the analysis was opposed to -1180 and -1160 microstrains for the experiment) may be attributed to somewhat higher membrane stresses predicted in the analysis, whereas a higher degree of bending was indicated by the experimental data (gages 2 and 3).

Considerable discrepancy exists between the analytic and experimental strains at the midpoint of the panel longer edges. The analysis predicts strain level approaching yield condition (6500 microstrains) whereas the experimental strains were less than 1700 microstrains.

As already mentioned, the panel boundary could not be precisely defined. Nevertheless, the high strain gradient indicated for this region tends to support the analytic prediction of high strain level, possibly approaching yield at the panel boundary.

A significant difference between the predicted and the actual strain data is also indicated for the rib response: 1000 as opposed to 2720 microstrains, respectively. However, closer examination of the experimental data shows considerable bending of the rib web, which was not predicted in the analysis. The maximum direct strain obtained for the rib was assessed at 1380 microstrains, which was reasonably close to the predicted value.

A survey of the strain gage data presented in Table B-1 to determine the time after the shock arrival for maximum response during the first cycle indicated a range of 0.59 to 0.73 ms for the panels. This compares very favorably with the analytic prediction of 0.5 to 0.6 ms. Close correlation between the experimental and analytic data for the maximum first-cycle response time was also indicated for the rib with 1.19 ms and 1.0 to 2.0 ms obtained from the test and analysis, respectively.

TABLE B-3. Strain Data Correlation.

LOCATION		STRAINS MICROSTRAINS		
Element	Surface	Analysis	Test	Gage No. Ref
Panel Center	INSIDE	1950	2100 2060	14 3
	OUTSIDE	-715	-1180 -1160	13 2
Panel No. 1	INSIDE	-4200	-500	5
Mid Long Side	OUTSIDE	6500	1300 1280	4 1
Panel No. 2	INSIDE	-4200	-570	10
Mid Long Side	OUTSIDE	6500	1680	7
Rib	INSIDE	1000	-400	16
Web Center	OUTSIDE	1000	2720	15

It should be noted that, for the analysis, each instrumented panel was assumed as a separate structure. In actual fact, however, these panels constituted elements of the multi-panel flap structure. The consequence of this limitation in the analytic modeling is reflected in the overall maximum response data presented in Table B-2 which shows consistently higher strain values than the corresponding data of Table B-1. These strain maxima reached, on the average, at 5 ms after the shock arrival imply a resultant, composite response of the elemental panels and the entire flap structure.

In the overall assessment, this test was considered extremely valuable. It generated some valid data on structure response to blast and furnished information required to specify disposition of the A-4C aircraft specimens within the blast field for the DICE THROW event. The correlation of the experimental and analytic data provided an initial insight regarding the effects of structural modeling and accuracy of the analytic solutions. The discrepancies between the analytic and experimental data could be attributed either to the sensitivity of the analytic solution to given parameters or to the inherent differences between a "true-to-life" structure and its idealized representation in the analysis.

REFERENCES

1. R. P. Syring and W. D. Pierson, "Structural Response to Simulated Nuclear Overpressure (STRESNO): A Test Program Establishing a Data Base for Evaluating Present and Future Analytic Techniques." The Boeing Company, Wichita Division, Wichita, KA. March 1977.
2. Staff of Kaman AviDyne, "Handbook for Analysis of Nuclear Weapon Effects on Aircraft." Kaman AviDyne, Burlington, MA. DNA 2048H-1. March 1976.
3. Personal conversations with Neil Griff, Naval Surface Weapons Center, White Oak Laboratory, Silver Spring, MD. February 1976.
4. CAPT T. Y. Edwards, "Airblast Predictions for DICE THROW". Field Command, Defense Nuclear Agency, Kirtland AFB, NM. Letter dated 9 March 1976.
5. "Instructions for the Selection and Use of TENS-LAC Brittle Lacquers and Undercoatings." Photoelastic Inc. A subsidiary of Vishay Intertechnology Inc., Malvern, PA. Bulletin TL-201.
6. R. Friedberg and P. S. Hughes, "Experimental Study of Aircraft Structural Response to Blast." Naval Weapons Evaluation Facility, Albuquerque, NM. NWEF Report 1145, VOL. I and II, (to be published).
7. W. N. Lee and L. J. Mente, "NOVA2 - A Digital Computer Program for Analyzing Nuclear Overpressure Effects on Aircraft." Kaman AviDyne, Burlington, MA. AFWL-TR-75-262. August 1976.
8. C. J. Kolar, "Ground Vibration Tests of the Model A4D-5 Airplane." Douglas Aircraft Company, McDonnell Douglas Corporation, El Segundo, CA. E.S. 29917. August 1961.
9. "Fixed Camera Data. DICE THROW" Report No. 35524, prepared by New Mexico State University, Physical Science Laboratory, Las Cruces, NM, 15 Mar 1977.
10. Norris, Hensen, Halley, Biggs, Namyet, Ninanis, "Structural Design for Dynamic Loads. McGraw-Hill. 1959.

29. BLAST DISPLACEMENT IN FIELD FORTIFICATIONS

by

E.R. Fletcher, D.R. Richmond,

R.O. Clark, and J.T. Yelverton

Lovelace Biomedical and

Environmental Research Institute, Inc.

E. R. Fletcher
D. R. Richmond
R. O. Clark
J. T. Yelverton

BLAST DISPLACEMENT IN FIELD FORTIFICATIONS

FOREWORD

This report presents information on blast-displacement effects on personnel inside field fortifications. This project was supported by the Defense Nuclear Agency under Contract DNA 001-75-C-0237. The DNA project officer was COL E. T. Still (USAF, VC), Armed Forces Radiobiology Research Institute, Bethesda, Md. A portion of the funding was provided by the Defence Research Establishment, Ottawa, Canada. Dr. G. A. Grant was the Canadian Project Officer.

The outstanding support rendered to this project by the test group staff of the DNA Field Command is acknowledged. The authors also wish to acknowledge A. Trujillo, W. Hicks, and K. Saunders for technical assistance during the test phase and B. Martinez and T. Minagawa for report preparation.

INTRODUCTION

Objectives

The objectives of this project were (1) to determine the displacement-time histories of dummies inside 3- x 6-ft fighting bunkers and inside a 14- x 14-ft underground personnel shelter and (2) to use these data to confirm a method for predicting whole-body translation of personnel in open structures.

Background

Airblast-displacement effects on personnel inside field fortifications have received little attention. Because of the lack of information in this area, blast-casualty criteria have been based solely on damage to the structure,

and safety and risk criteria have been linked to damage to the fortification or to direct-overpressure effects (Reference 1). Results from a previous field test (Reference 2) have suggested that impact injury associated with whole-body displacement induced by the entering jet flow can occur at overpressures well below those required for injury from direct-overpressure effects or structural collapse.

Laboratory studies of jet phenomena in scale models of field fortifications in a shock tube have resulted in the development of a method for predicting whole-body translation of personnel in open structures. It was desirable to confirm this method using full scale structures on the Dice-Throw field test.

PROCEDURES

Layout

Three 3- x 6-ft fighting bunkers and one 14- x 14-ft underground personnel shelter were located on the test site. Two of the fighting bunkers were face-on to the charge, one each at the 680- and 820-ft ground ranges, and one bunker was side-on at 820-ft (Figure 1). The predicted peak overpressures at these ranges were 25 and 15 psi, respectively. The personnel shelter was located at the 740-ft range at a predicted overpressure level of 20 psi.

Fighting Bunkers

The geometry and dimensions of the bunkers are given in Figure 2 along with the locations of the dummies, pressure gages, and camera. These bunkers were a modification of the fighting bunker with overhead cover described in Reference 3. They were constructed of 1/8-inch sheet steel welded inside a frame of 2-inch angle iron. The bunkers were placed in excavations and covered with earth and sandbags. An asphalt pad extended 70 ft toward ground zero in order to reduce the amount of dust carried by the blast wave.

The volume of the bunker was 140 ft³ and the areas of the firing port and rear entrance were 4.5 and 5.4 ft², respectively. Two dummies were placed in each bunker; the one nearer to the camera was kneeling on the firing step and the other was standing on the floor. The heads of the

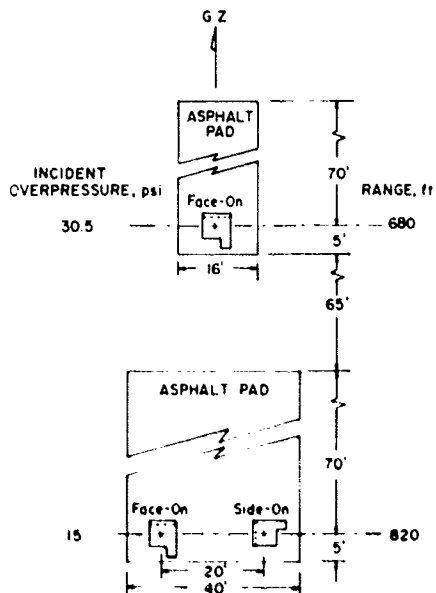


Figure 1. Field Layout of Fighting Bunkers.

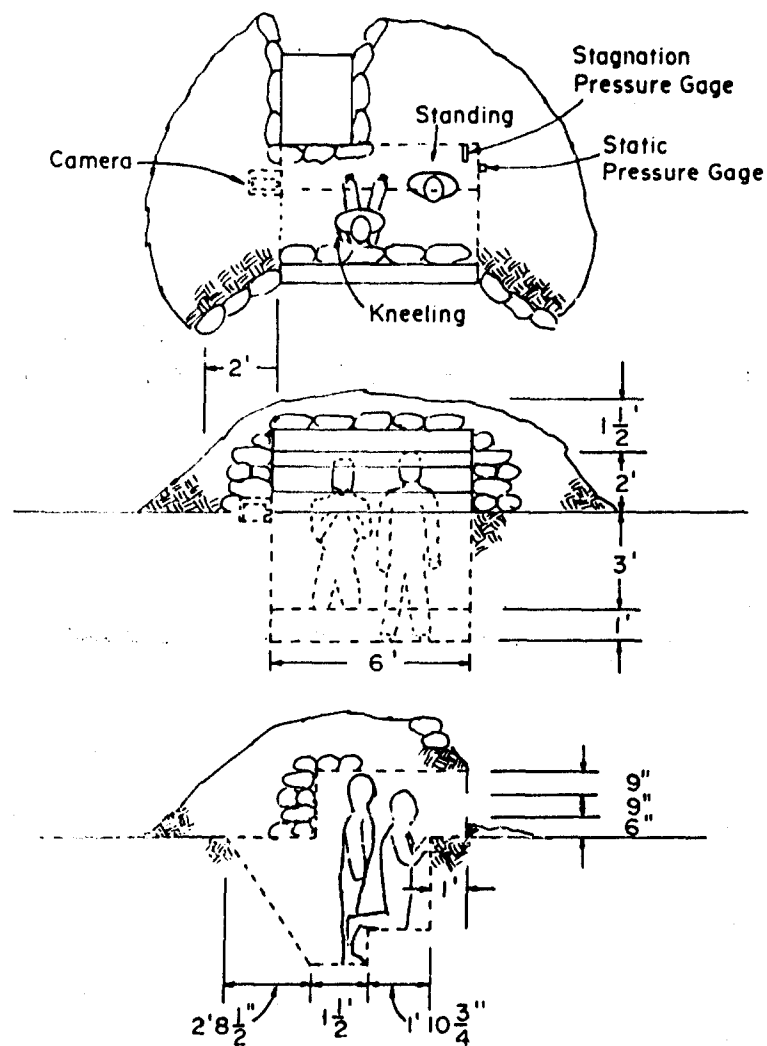


Figure 2. Diagram of Fighting Bunker Showing Locations of Dummies, Camera, and Gages.

kneeling and standing dummies were 29 and 12 inches, respectively, from the rear wall. The dummies wore green fatigues, white helmets, and G.I. boots. In Figure 3, the dummies can be seen through the firing port of one bunker. The other two bunkers can be seen in the background.

Personnel Shelter

The geometry and dimensions of the personnel shelter appear in Figure 4. This 14- x 14- x 6.5-ft shelter was identical to the one on the Mixed Company Event (Reference 2) except that the roof was made of steel instead of the 18-inch-diameter pine logs that were used before. An 18-inch I-beam served as the main roof support, and 7-inch I-beams on 2-ft centers spanned between the girder and the side walls. The walls, ceiling, and floor of the shelter were made of 1/8-inch steel plate that was spot welded to the frame. The surface entrance was a 2- x 4-ft opening that was flush with the ground on the upstream side of the shelter. An 8.5-ft-deep vertical shaft and a 6-ft-long tunnel led from the surface entrance to the chamber. The ratio of the chamber volume to the entrance area was 160 ft.

The locations of the dummies, pressure gages, and camera in the personnel shelter are shown in Figure 4. In order to provide photographic reference points, the floor was painted a black and white checkerboard pattern of 1-ft squares and the wall opposite the camera was covered with checkerboard wallpaper. Golden Bear® was applied to the ground surface around and upstream of the entrance in order to reduce the amount of dust carried into the shelter by the blast wave.

Figure 5 is a preshot view of the three dummies which were standing and facing the front wall inside the personnel shelter. Dummy No. 14 was 3 ft from and directly in line with the entryway tunnel. The other two dummies, Nos. 12 and 13, were 3 ft to the side of the centerline extending from the tunnel (Figure 4). The dummies were stabilized in an upright position by leaning them forward at a slight angle against supports made of 1/4-inch pipe anchored to the ceiling.

Photography

The motion-picture photography in the bunkers and shelter was the responsibility of the Denver Research



Figure 3. Preshot View of the Dummies in the Fighting Bunker at the 680-Ft Range. The two bunkers at the 820-ft range can be seen in the background.

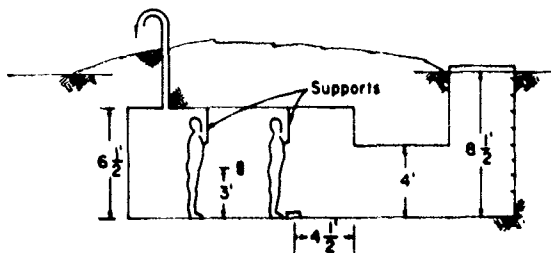
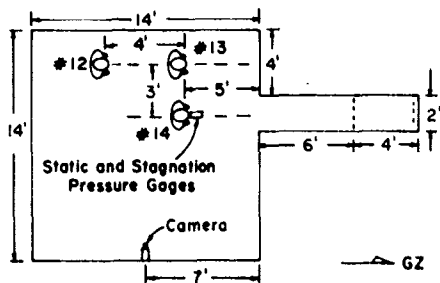


Figure 4. Diagram of Underground Personnel Shelter Showing Locations of Dummies, Camera, and Gages. The surface entrance was at a ground range of 740 ft, 21-pai incident overpressure.

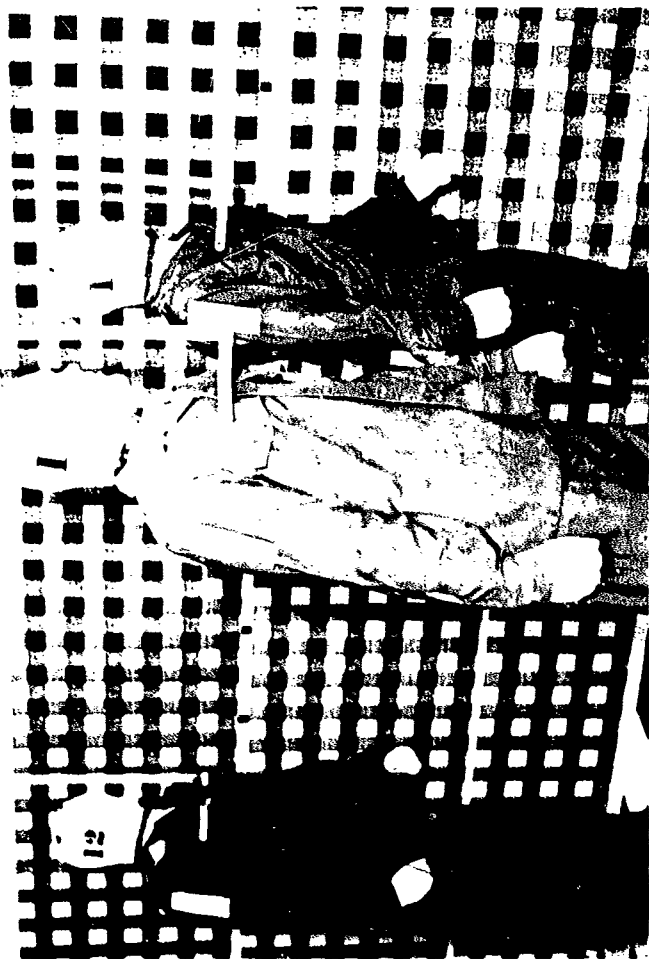


Figure 5. Preshot View Inside Underground Personnel Shelter.

Institute. Each of the four cameras operated at approximately 400 fps.

The pre- and postshot still photography was accomplished by White Sands Missile Range photographers.

Accelerometers

Four omnidirectional, peak-g, mechanical accelerometers were mounted in the chest cavity of each dummy. Each of these Impact-O-Graphs® contained four small spheres which were pressed into pairs of oppositely facing seats by two interposed springs. The four accelerometers used in each dummy were designed such that the spheres would unload at a peak acceleration of 10, 40, 200, or 800 g's, respectively.

In preshot calibrations, dummies in a prone, supine, or lateral orientation were dropped from various heights onto a concrete pad. For each of these three orientations, the 10-g units unloaded at an impact velocity of approximately 5 ft/sec, the 40-g units at 8 ft/sec, the 200-g units at 17 ft/sec, and the 800-g units at 28 ft/sec. The probabilities of injury for these four impact velocities have been estimated to be 0, 5, 50, and 95 percent, respectively (Reference 4). It should be noted that considerably higher velocities were required to unload the various Impact-O-Graphs® when the dummies were dropped at an angle onto the concrete pad.

Pressure-Time Gages

A static pressure gage was located in each of the three fighting bunkers (Figure 2). In addition, a stagnation pressure gage was located in each of the face-on bunkers in order to measure the jet flow entering through the firing port. The incident free-field pressures were measured by gages on the surface. The gages associated with the bunkers were installed and operated by the Ballistic Research Laboratories.

One static and one stagnation pressure gage were located inside the underground personnel shelter (Figure 4). These gages and one on the surface adjacent to the entrance to the shelter were the responsibility of the Nuclear Weapons Effects Branch of the White Sands Missile Range.

RESULTS

Fighting Bunkers

Dummy Displacements

The postshot locations and conditions of the dummies in the fighting bunkers are summarized in Table 1. The four dummies in the face-on bunkers impacted head-first against the rear wall. This was evident from the postshot positions and was observed in the motion pictures of the kneeling dummies. The two dummies in the bunker that was side-on to the blast had moved approximately 6 inches in the downstream direction.

Only the 10-g Impact-O-Graph[®] was unloaded in each of the four dummies in the face-on bunkers. No Impact-O-Graphs[®] unloaded in the two dummies in the side-on bunker.

Only the heads of the kneeling dummies were visible in the motion-picture films taken in the face-on bunkers. Figure 6 shows the measured head displacements vs time. In both cases, dust obscured the initial phase of the motion. Therefore, those portions of the translation curves (dashed in Figure 6) were estimated from the initial head positions and the predicted durations of acceleration.

The peak horizontal component of the head velocity was 9 ft/sec for the dummy kneeling in the face-on bunker at an incident overpressure of 15 psi and 24 ft/sec for the corresponding dummy at 30.5 psi. In each case, the impact velocity was smaller than the peak velocity. The deceleration of the dummy's head prior to impact was probably related to the fact that the body was rotating. Had the subject rotated 90 degrees, the horizontal component of the head velocity would have decreased to the center-of-mass velocity, which was approximately equal to one-half of the peak head velocity.

The heads of both dummies could be seen in the film taken in the side-on bunker. The maximum horizontal component of the head velocity was less than 1 and 2 ft/sec for the standing and kneeling dummies, respectively (Table 1).

TABLE 1
EFFECTS OF VIBRATION ON FIGHTING NUMBERS

Section	Survey No.	Preventive Location	Dummy Description	Condition of Dummy	File Analysis
Section No. 1 - Post-20	1st	Swinging	Dummy moved 3 in. to right above name, body tilted 30 deg. backward	Midst strap released, lightly around neck. Helmet off and broken. Shirt blown off and broken. Collar torn. Dummy shows shadow of debris impact on rear wall and face of dummy above.	Dummy rotated backward, head-first, minimum horizontal component 47 ft/sec. Motion observed at 7 ft/sec. velocity decreased to 3 ft/sec prior to impact.
	2nd	Swinging	Left supporting arm swung down to side below original position. Lower leg, extended forward until it contacted rear wall at 45 deg. to his right.	Helmet could not be found. Shirt collar torn. Both arms broken. Collar torn. Dummy shows shadow of debris impact on rear wall and face of dummy above.	Obscured by dust.
Section No. 2 - Post-20	1st	Swinging	Ball in kneeling position. Above name tilted 45 deg. backward. Head to his right. Collar torn and lower leg.	Midst torn from head and broken. Collar torn around neck. Motion observed at 7 ft/sec. Debris impact marks on face.	Dummy rotated backward, head-first, minimum horizontal component of head velocity was 9 ft/sec. Motion observed at 7 ft/sec. Debris impact marks on face. At which point the velocity had decreased to 7 ft/sec.
	2nd	Swinging	Supporting left arm below original position. Upper body tilted 60 to 70 deg. to his right.	Helmet scratched at back and tilted down. Collar torn. Debris impact marks on face.	Obscured by dust.

TABLE 1 - CONTINUED
EFFECTS ON DUMMIES IN FIGHTING BUNKERS

Station	Dummy No.	Prestab Location	Dummy Postshot Location	Condition of Dummy	Film Analysis
Bunker No. 3 - Sig-Op: 430-ft range 15.0-pel Overpressure	24C	Kneeling	Entire body moved 6 in. to left, toward rear stream to outside flow.	None in original position over eyes. Right side collar torn on side seam. No debris impact.	Dummy rotated backwards 180 degrees. Horizontal component of head velocity was 0.9 ft/sec. Obscured by dust after a 6 in. displacement.
	25C	Standing	Entire body moved 6 in. to left, toward rear stream to outside flow. Body tilted forward.	Right side collar torn on side. No debris impact.	Dummy rotated backwards 180 degrees. Horizontal component of head velocity was 0.9 ft/sec. Obscured by dust after a 2-in. displacement.

Impact-O-Graph® Unloaded

- a Both 10g.
- b One 10g.
- c None.

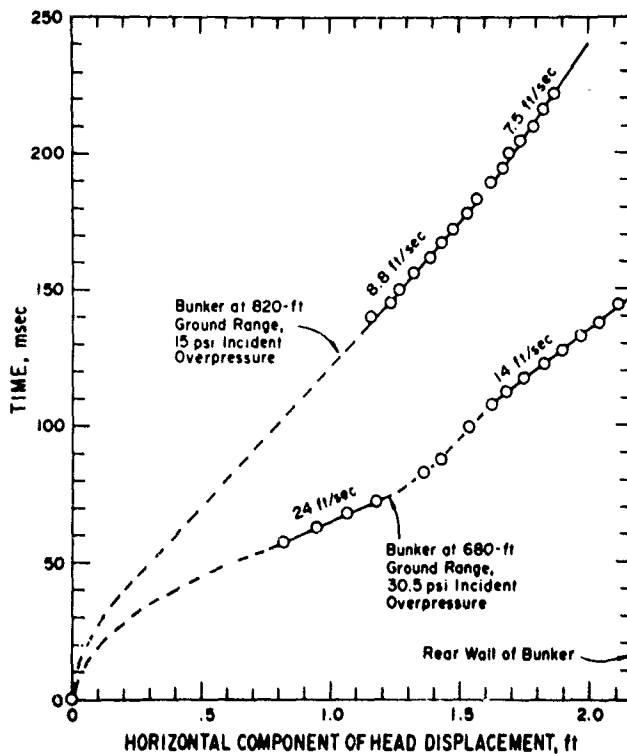


Figure 6. Measured Horizontal Components of the Head Displacements of the Dummies Kneeling in the Face-On Bunkers vs Time.

Pressure-Time Records

Figures 7 and 8 illustrate the smoothed static and Pitot pressures measured in the face-on bunkers, and Figure 9 shows the static pressure measured in the side-on bunker. The prominent pressure fluctuations in these records are believed to be primarily due to compression and rarefaction waves reflecting back and forth within the interior, and therefore do not represent the average pressures throughout the interior or in the jet until the waves are damped out after about 12 msec.

Figures 10 and 11 give the first 15 msec of the free-field pressure-time measurements at the 680- and 820-ft ranges. The peak incident overpressure was 30.5 psi at the 680-ft range and 15 psi at the 820-ft range. Also shown in the figures are the calculated free-field total pressures and the calculated static pressures inside the bunkers, the determination of which will be derived in a following section.

Personnel Shelter

Dummy Displacements

The postshot locations and conditions of the dummies in the underground personnel shelter are summarized in Table 2. Dummy No. 14 (initially in line with the entry-way tunnel) was found against the rear wall of the shelter. Shoe marks on the wall (Figure 12) started 39 inches above the floor, suggesting that the dummy was airborne when its feet first struck the wall. The support pipe broke loose from the ceiling, and Dummy No. 13 fell forward onto the floor with no apparent additional displacement. Dummy No. 12 remained standing, although its shoes had slid backwards about 6 inches. It was not determined if the movements of Dummies Nos. 13 and 12 resulted from airflow or ground shock.

None of the Impact-O-Graphs[®] unloaded in the three dummies in the personnel shelter.

Because of dust, only the displacement of the head of Dummy No. 14 could be accurately measured from the motion-picture film taken in the personnel shelter. Figure 13 presents the displacement-time measurements of the head of the dummy and the path of its center-of-mass estimated from the predicted acceleration period, the dummy's rotation rate, and its initial and final positions (see Table 2).

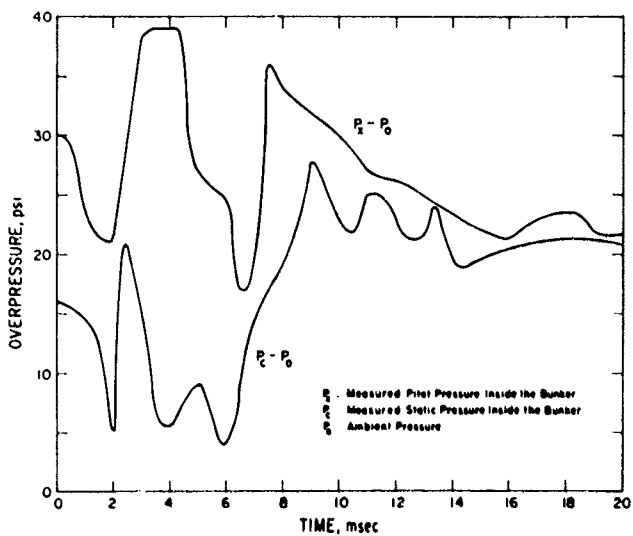


Figure 7. Smoothed Overpressures Measured in the Jet in the Face-On Fighting Bunker at 680 Ft.

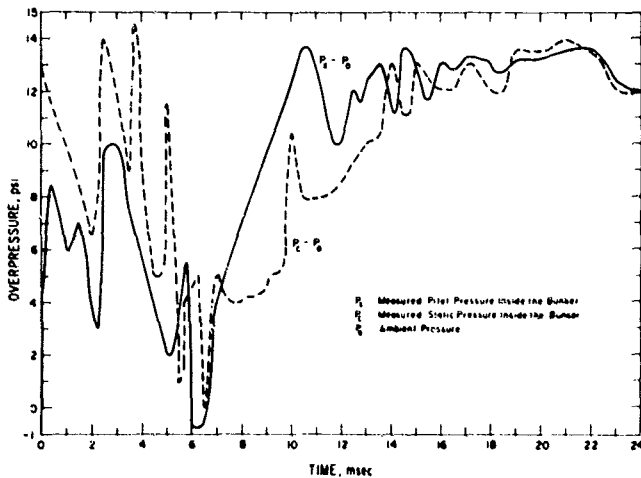


Figure 8. Smoothed Overpressures Measured in the Jet in the Face-On Fighting Bunker at 820 Ft.

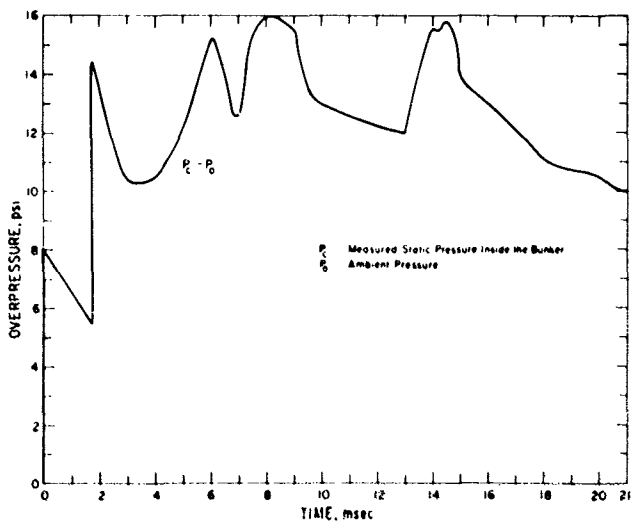


Figure 9. Smoothed Static Overpressure Measured in the Jet in the Side-On Fighting Bunker at 820 Ft.

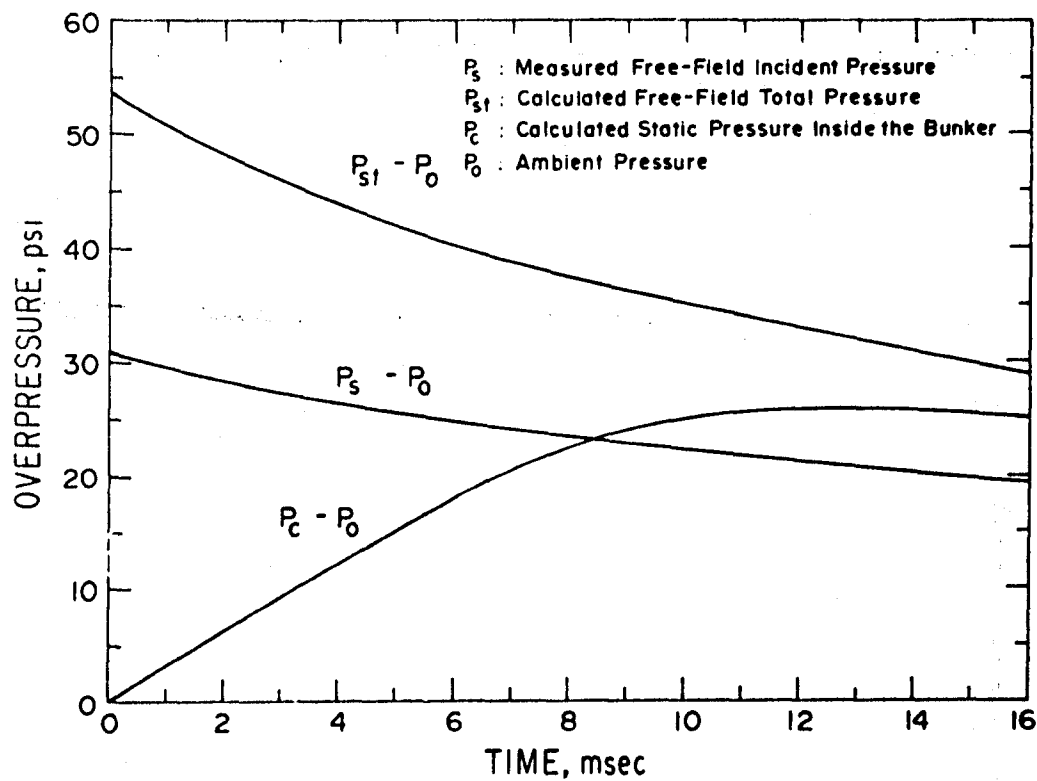


Figure 10. Measured and Calculated Overpressures for the Face-On Fighting Bunker at the 680-Ft Range.

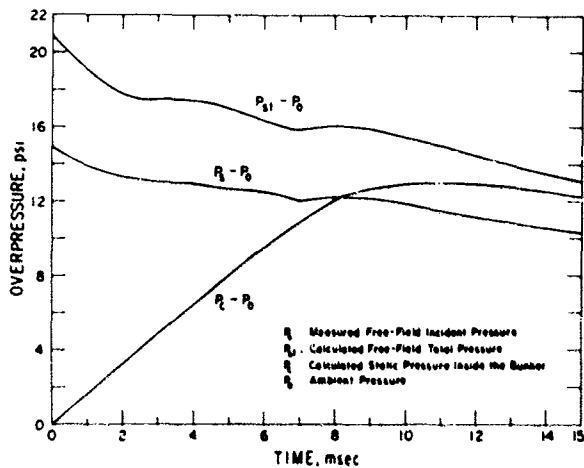


Figure 11. Measured and Calculated Overpressures for the Face-On Fighting Bunker at the 820-Ft Range.

TABLE 2
EFFECTS ON DUMMIES IN PERSONNEL SHELTER

Range, ft	Overpressure, psi	Dummy No.	Dummy Preshot Location	Dummy Postshot Location	Condition of Dummy	Film Analysis
710	21	11*	Standing 5 ft inside and in line with entryway of personnel chamber.	Against rear wall on floor.	Two-in.-long, 1-in.-deep laceration under chin	Dummy moved backward, rotated feet-first, then revolved, impacted with feet-first, then head-first, then impacted floor head-first, 9 ft.
		13*	Standing 5 ft inside and to the left of entryway.	Fell forward, face down.	No damage.	Obscured by dust.
		12*	Standing 10 ft inside and to the left of entryway.	Dummy still standing but shoes had slid backwards 6 in.	No damage.	Obscured by dust.

* Impact-O-Graphs® not unloaded.

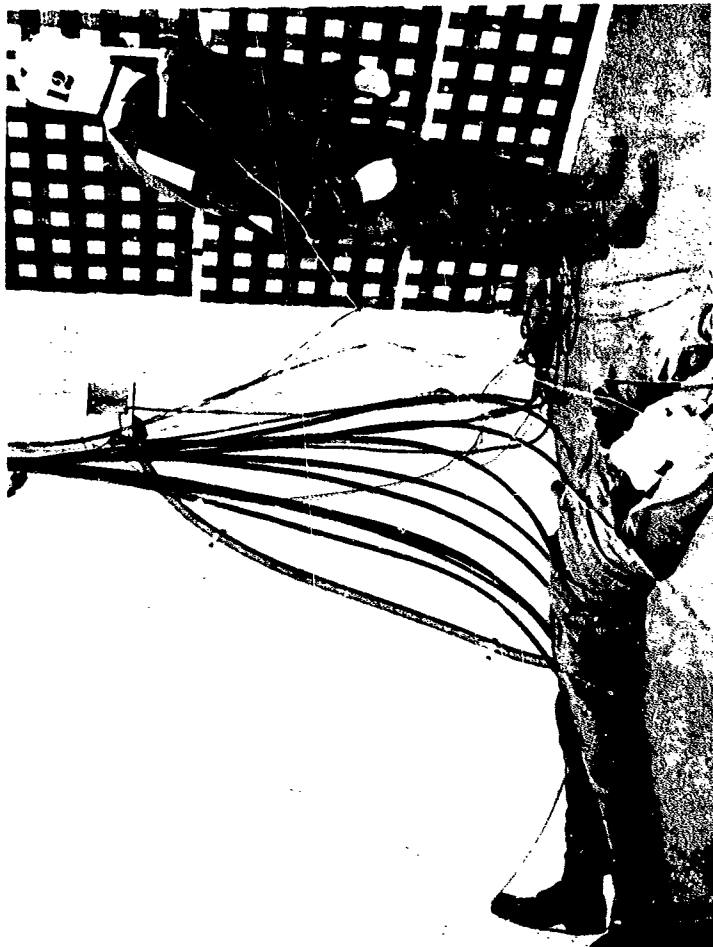


Figure 1: Postshot View of Dummies Nos. 14 (Supine) and 12 (Standing) in the Underground Personnel Shelter. Note the shoe marks on the rear wall.

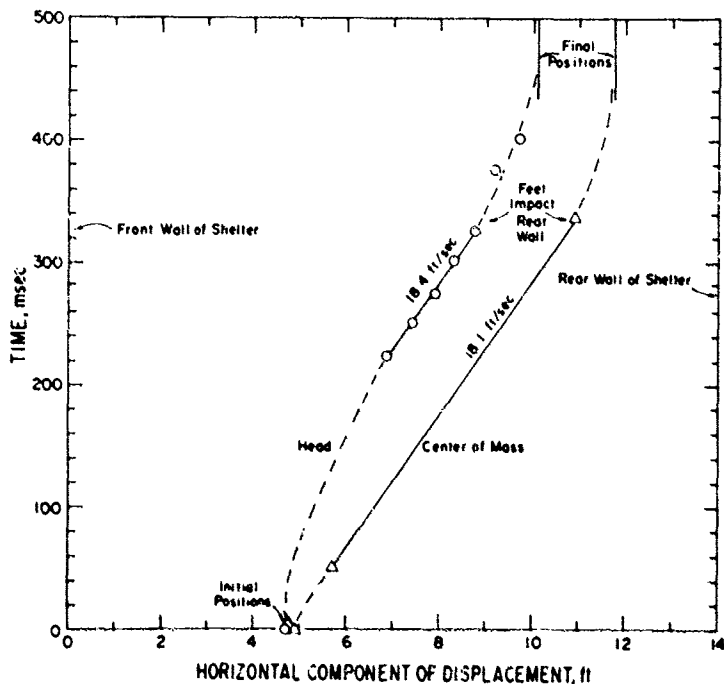


Figure 13. Measured Horizontal Components of the Head and Center-of-Mass Displacements of Dummy No. 14 vs Time. The dummy was standing in the jet entering the underground personnel shelter (see Figure 4).

The horizontal component of the head or center-of-mass velocity at impact was 18 ft/sec. Prior to impacting the rear wall, the dummy rotated slightly more than 90 degrees at a rate of approximately 0.8 rev/sec. It was also determined from the analysis that, shortly after the feet of Dummy No. 14 struck the rear wall, the head struck the floor at a vertical component of impact velocity of 9 ft/sec.

Pressure-Time Records

The static and stagnation pressure gages in the shelter produced poor quality records. Figure 14 shows the first 60 msec of the free-field pressure-time measurement at the 740-ft range. The measured peak incident overpressure was 21 psi. Also shown in the figure is the calculated static pressure inside the shelter.

PREDICTIONS

A method has been developed for predicting whole-body translation induced by jet flow entering an open structure subjected to airblast. The procedure involves the sequential calculation of (1) the external pressures on the openings, (2) the static pressure inside the structure, (3) the indicated dynamic pressure in the jet, and (4) the resultant acceleration of the dummy exposed to the jet, all of which vary with time.

External Pressure on an Opening

The external pressure on an opening into a structure is the driver pressure for the jet entering through that opening. The external pressure on an opening that is side- or face-on to the incident shock wave may be assumed to be the free-field incident or total pressure (i.e., the pressure that arises when the free-field flow is brought to rest isentropically and adiabatically), respectively. Assuming that classical conditions describe the free-field shock wave, the incident and total pressures and the corresponding speeds of sound are given by the following

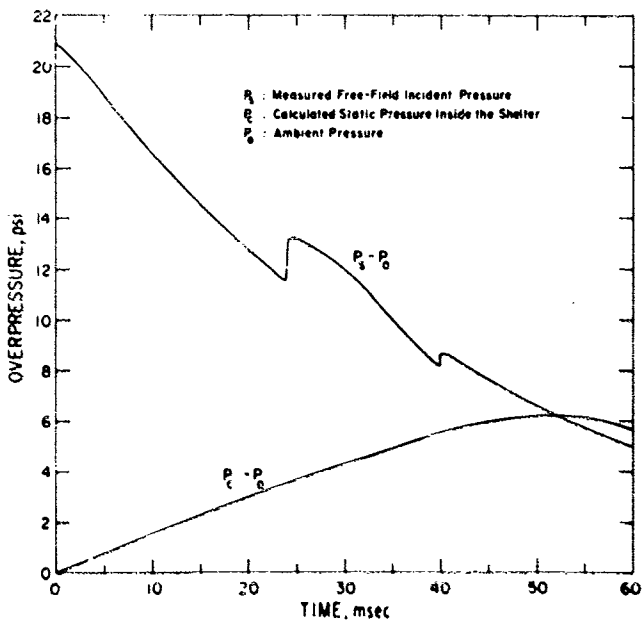


Figure 14. Measured and Calculated Overpressures for the Underground Personnel Shelter at the 740-Ft Range.

Incident pressure ratio

$$P_d/P_o = P_s/P_o$$

Incident sound speed ratio

$$A_d/A_o = A_s/A_o = \left((P_s/P_o) \frac{P_s/P_o + 6}{6 P_s/P_o + 1} \right)^{1/2}$$

Total pressure ratio

$$P_d/P_o = P_{st}/P_o = (P_s/P_o) \left[1 + \frac{5 (P_s/P_o - 1)^2}{7 (P_s/P_o) (P_s/P_o + 6)} \right]^{1/2}$$

Total sound speed ratio

$$A_d/A_o = A_{st}/A_o = (A_s/A_o) (P_{st}/P_s)^{1/2}$$

where P is pressure and A is the speed of sound, and the subscript o indicates ambient conditions, d indicates external conditions at the opening, s indicates free-field shock conditions, and st indicates the conditions that arise when the free-field flow is brought to rest isentropically and adiabatically.

In the case of the fighting bunkers facing the charge, the free-field total pressure, Equation 2, was applied to the firing port and the incident pressure, Equation 1, was applied to the rear entrance. In the case of the personnel shelter and the side-on bunker, the incident pressure was applied to all openings.

Static Pressure Inside a Structure

The jet flow into a structure with one or more openings causes the static pressure in the interior

to increase. The incremental change in the static pressure in the structure is given by

$$\Delta P_c = \Delta t \sum_n (B_n R_n / W) \quad (3)$$

where ΔP_c is the change in the internal static pressure (P_c) during the time interval Δt , W is the volume of the structure, B_n is the area of the n th opening, and R_n is a flow factor for the n th opening. The R 's are defined as follows:

For supersonic inflow $P_d > 1.893 P_c$

$$R = (175/216) A_d P_d (P_c/P_d)^{2/7} \quad (4)$$

For subsonic inflow $P_c < P_d < 1.893 P_c$

$$R = (7/\sqrt{5}) A_d P_c \left[1 - (P_c/P_d)^{2/7} \right]^{1/2} \quad (5)$$

For supersonic outflow $P_c > 1.893 P_d$

$$R = -(175/216) A_c P_c \quad (6)$$

For subsonic outflow $P_d < P_c < 1.893 P_d$

$$R = - (7/\sqrt{5}) A_c P_d (P_c/P_d)^{2/7} \left[1 - (P_d/P_c)^{2/7} \right]^{1/2} \quad (7)$$

where A_c is the speed of sound in the structure. Equations 1 through 7 were used to calculate the internal static pressure vs time for the face-on fighting bunkers and the personnel shelter (Figures 10, 11, and 14).

Indicated Dynamic Pressure in a Jet

For a jet flowing into a structure through an opening, the indicated dynamic pressure is the difference between the Pitot pressure, P_x , and the internal static pressure, P_c . The Pitot pressure has a maximum value of P_{xm} at the opening and decreases approximately linearly with distance, X , from the opening. The indicated dynamic pressure as a function of distance can be calculated from the following formulas:

$$\frac{P_x}{P_c} - 1 = (P_{xm}/P_c - 1) \left(1 - \frac{X/R}{X_m/R} \right) \quad (8)$$

$$\left. \begin{aligned} &\text{where } P_{xm}/P_c - 1 = P_d/P_c - 1 \quad \text{for } P_d < 1.893 P_c \\ &\text{or } P_{xm}/P_c - 1 = 6 \left[(P_d/P_c)^{1/3} - 1 \right] \left[\frac{(P_d/P_c)^{1/3} - 1}{(35/36)(P_d/P_c)^{1/3} - 1} \right]^{1/2} - 1 \quad (9) \\ &\quad \text{for } P_d > 1.893 P_c \end{aligned} \right\}$$

$$\text{and } X_m/R = \left[0.02905 + 0.02121 (P_d/P_c - 1)^{0.4} \right]^{-1} \quad (10)$$

where X_m is the distance from the opening at which the indicated dynamic pressure is zero, and R is the radius of a circular opening. For a noncircular opening with an aspect ratio of less than 3:1, an effective radius $R = (B/\pi)^{1/2}$ can be used without introducing significant error.

Acceleration of a Dummy

In order to calculate the acceleration of a dummy, it is necessary to estimate the projected area and drag coefficient of the portion of the dummy engaged by the jet. It was determined that a standing, face-on, clothed dummy has a height of 68 inches, a projected area of 6.8 ft², and a drag coefficient of 1.12, the latter measurement having been obtained in a 6-ft-diameter shock

tube. In the fighting bunkers, the jet entering the firing port was approximately the same height as the port, i.e., 9 inches. It was therefore estimated that the jet intercepted 9/68 of the dummy's height and projected area. In the shelter, it was estimated that one-half of the projected area of Dummy No. 14 was intercepted by the jet. For want of a better approach, the drag coefficient measured for the entire dummy was assumed to apply to the portions of the dummies engaged by the jets in the bunkers and shelter.

If the velocity of an accelerated object remains small compared to the flow velocity in the jet, the indicated dynamic pressure, $P_x - P_c$, may be used to calculate the motion from

$$\Delta V / \Delta t = (S C_D / M) (P_x - P_c) \quad (11)$$

$$\Delta X / \Delta t = V_i + (S C_D / 2M) (P_x - P_c) \Delta t \quad (12)$$

where S is the projected area of the object engaged by the jet, M is the mass of the object, C_D is the drag coefficient, V_i is the velocity of the object at the beginning of time interval Δt , and ΔX and ΔV are the change in the object's position and velocity, respectively, during Δt .

Fighting Bunkers

Time-displacement histories for the centers-of-mass of the dummies in the face-on fighting bunkers were predicted using the methods described above. In each case, the predicted horizontal component of the center-of-mass velocity reached its maximum value within the first 2 inches of displacement, and there was no significant deceleration prior to impact. The measured maximum horizontal components of the head velocities of the dummies kneeling in the face-on fighting bunkers, the corresponding velocities from 1/7-scale shock-tube experiments, and double the calculated peak velocities are given in Table 3. The calculated center-of-mass velocities were doubled in order to make them comparable to the measured head velocities; i.e., initially, the upper portion of each dummy was rotating head-first such that the head velocity was approximately equal to two times the center-of-mass velocity. The predicted and measured

TABLE 3
MEASURED AND PREDICTED MAXIMUM HORIZONTAL
COMPONENTS OF HEAD VELOCITIES FOR DUMMIES KNEELING
IN FACE-ON FIGHTING BURNERS

Incident Overpressure, psi	Maximum Horizontal Component of Head Velocity, ft/sec		
	Dice Throw Measurements	Shock-Tube Model Measurements	Predicted Values
12		9	6
15	9		8
20		13	14
30.5	24		24
53			37

maximum horizontal components of the head velocities (excluding the shock-tube data) are shown in Figure 15,

For the dummy kneeling in the face-on fighting bunker at 30.5 psi on Dice Throw, the ratio of the horizontal component of impact head velocity to the maximum horizontal component of head velocity was 0.58. In the shock-tube experiments, corresponding ratios of 0.66 and 0.71 were obtained at incident overpressures of 12 and 20 psi, respectively. Because the three measured ratios were reasonably close together, a constant ratio of 0.6 was assumed for making predictions of impact head velocity for a dummy kneeling in a fighting bunker vs overpressure. Thus, the curve for a kneeling dummy in Figure 16 was obtained by multiplying the predicted velocities from the curve in Figure 15 by a factor of 0.6.

No velocities were measured for the dummies standing in the face-on fighting bunkers on Dice Throw. However, in the face-on fighting bunkers in the shock-tube experiments, the ratio of the horizontal component of impact head velocity of a standing dummy to the maximum horizontal component of head velocity of a kneeling dummy was found to be 0.84 and 0.87 at incident overpressures of 12 and 20 psi, respectively. Because the two measured ratios were reasonably close together, a constant ratio of 0.85 was assumed for making predictions of impact head velocity for a dummy standing in a fighting bunker vs overpressure. Thus, the curve for a standing dummy in Figure 16 was obtained by multiplying the predicted velocities from the curve in Figure 15 by a factor of 0.85.

Data from previous biological studies (Reference 4) were used in connection with the predicted velocities shown in Figure 16 to obtain the probabilities of impact injury as a function of incident overpressure from a 1-KT yield for personnel in a face-on fighting bunker, Figure 17.

Personnel Shelters

The predicted horizontal component of the center-of-mass velocity for the dummy standing in the jet entering the personnel shelter reached its maximum value within the first 10 inches of displacement, and there was no significant deceleration prior to impact. The curve in Figure 18 shows predicted impact velocity vs incident overpressure for a 1-KT yield. The Dice Throw point was plotted

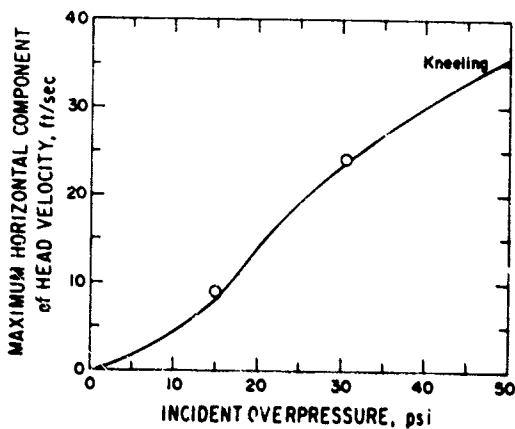


Figure 15. Predicted Maximum Horizontal Component of the Head Velocity of a Dummy Kneeling in a Face-On Fighting Bunker vs Incident Overpressure from a 1-KT Yield. The points show measured values.

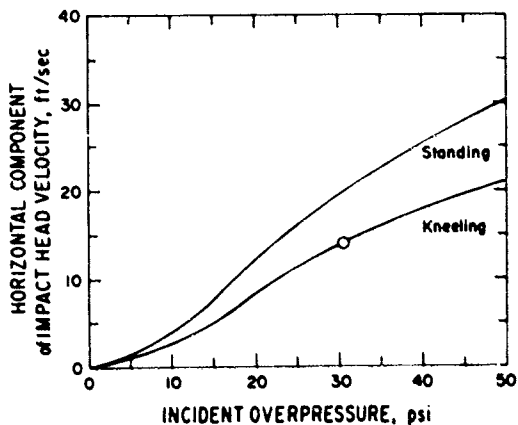


Figure 16. Predicted Horizontal Component of the Impact Head Velocity of a Dummy Standing or Kneeling in a Face-On Fighting Bunker vs Incident Overpressure from a 1-KT Yield. The point shows measured values.

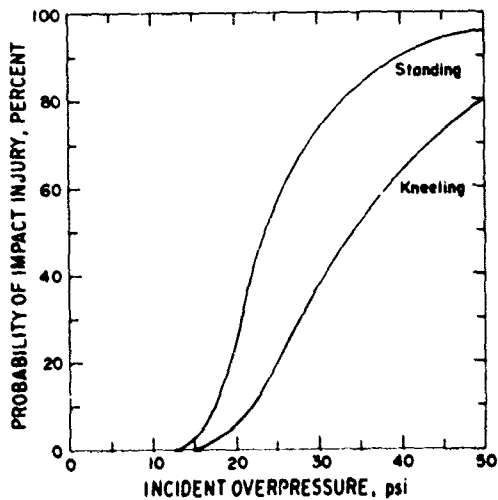


Figure 17. Predicted Probability of Impact Injury to a Person Standing or Kneeling in a Face-On Fighting Bunker vs Incident Overpressure from a 1-KT Yield.

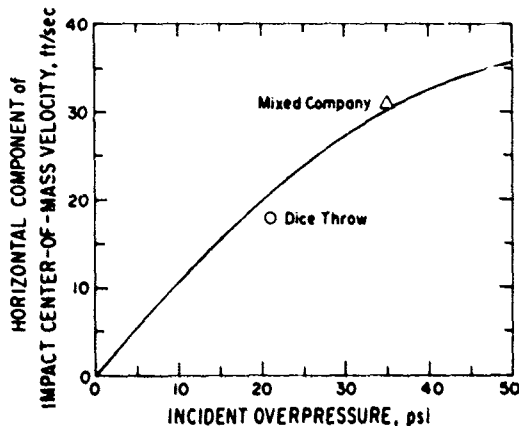


Figure 18. Predicted Horizontal Component of the Impact Center-of-Mass Velocity of a Dummy Standing in the Jet Entering an Underground Personnel Shelter vs Incident Overpressure from a 1-KT Yield. The points show measured values except for the Mixed-Company velocity which was adjusted as described in the text.

at the measured velocity, whereas the Mixed Company point was plotted at double the measured velocity. The reason for doubling the velocity was that (1) the Dice Throw dummy was standing in line with the center of the entryway tunnel such that approximately one-half of its projected area was engaged by the jet, whereas the Mixed Company dummy was standing in line with the edge of the entryway tunnel such that approximately only one-quarter of its projected area was engaged by the jet, and (2) the predictions indicated that the impact velocity should be very nearly proportional to the projected area engaged by the jet.

Data from previous biological studies (Reference 4) were used in connection with the predicted velocities shown in Figure 18 to obtain the probability of impact injury as a function of incident overpressure from a 1-KT yield for occupants standing 5 ft from and directly in line with the entryway tunnel of an underground personnel shelter, Figure 19.

REFERENCES

1. "Personnel Risk and Casualty Criteria for Nuclear Weapons Effects (U)," U. S. Army Combat Development Command, Report No. ACN4260, Fort Bliss, Texas, 2 August 1971. (Confidential)
2. Richmond, D. R., E. R. Fletcher, R. K. Jones and W. S. Jackson, "Airblast Effects Inside Field Fortifications," Mixed Company Event Project LN401, POR 6622-1, Defense Nuclear Agency, Washington, D. C., 18 June 1974.
3. "Field Fortifications," Department of the Army Field Manual, FM 5-15, Headquarters, Department of the Army, Washington, D. C., August 1965.
4. Fletcher, E. R., J. T. Yelverton, R. A. Hutton and D. R. Richmond, "Probability of Injury from Airblast Displacement as a Function of Yield and Range," Topical Report, DNA 3779T, Defense Nuclear Agency, Washington, D. C., 29 October 1975.

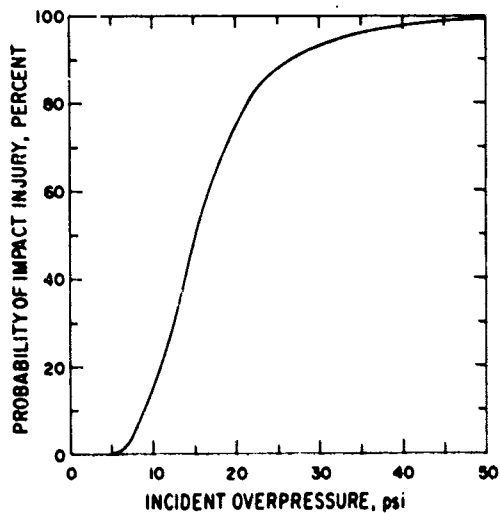


Figure 19. Predicted Probability of Impact Injury to Personnel Standing in the Jet Entering an Underground Personnel Shelter vs Incident Overpressure from a 1-kT Yield.

**30. DYNAMIC RESPONSE OF TWO TYPES
OF GERMAN HOUSE CONSTRUCTION**

by

**C.K. Wiehle, J.R. Rempel, and J.E. Beck
Stanford Research Institute**

/also published as DNA/FC POR 6966/

CONTENTS

OBJECTIVE	1
INTRODUCTION	1
TEST STRUCTURES	1
Description	1
Design	3
Masonry Cavity Test Wall	3
Fachwerk Test Wall	5
Analysis	5
Masonry Cavity Wall	5
Fachwerk Wall	6
Collapse Predictions	6
INSTRUMENTATION	9
CONSTRUCTION	12
Foundation and Floor Slab	12
Non-Responding Walls	12
Masonry Cavity Wall	14
Aboveground Concrete Work	14
Fachwerk (Half-Timber) Framing	16
Ceiling and Roof Framing	16
Fachwerk Brick Masonry	19
Roof Covering	22
TEST RESULTS	22
Free-Field Overpressure	22
Post-Shot Damage Survey	25
Structure No. 1	25
Masonry Cavity Wall	25
Fachwerk Wall	31
Roof System	37
Structure No. 2	37
Masonry Cavity Wall	37
Fachwerk Wall	43
Roof System	46
Structure No. 3	50
Masonry Cavity Wall	50
Fachwerk Wall	50
Roof System	50

Instrumentation	53
Cameras	53
Deflection Gages	53
Total Pressure Gages	55
Side-On Pressure Gages	55
REFERENCES	63

OBJECTIVE

The objective of the SRI program in the Dice Throw event was to investigate the dynamic response and collapse modes for two types of German house construction subjected to air blast loading; the two types were masonry cavity wall and Fachwerk, or half-timber construction. The data from this experiment is of direct interest to the development of the DNA collateral damage methodology.

INTRODUCTION

This report is primarily concerned with the post-shot damage survey, although limited background and construction information is presented for a better understanding of some of the building damage. Because the electronic pressure and deflection data are being digitized preparatory to computer analysis, only preliminary results of the instrumentation is presented at this time. Also, the high speed films of the test have only just been received, and although they have been reviewed they have not as yet been examined in detail.

The detonation occurred at 0800 on October 6, 1976, and re-entry by the SRI damage survey team was made shortly after the area was cleared, and the post-shot damage survey of the three test structures was initiated. The damage survey consisted of a detailed inspection of all masonry walls, timber members, and debris. Post-shot photographic coverage included the undisturbed blast damage, as well as photographs of the details of damage and of reconstructed members considered important for determining the collapse mechanisms.

It should be noted that the information presented in this event report, including any observations or conclusions, must be considered as preliminary and are subjected to possible modification when the complete test data become available.

TEST STRUCTURES

Description

The test structures were approximately 16 ft by 28 ft in plan dimensions and about 20 ft high at the ridge. There were three identical structures, each located at a different range east of ground zero. As shown on Figure 1, Structure No. 1 was located at a range of 1147 ft (7.0 psi predicted free-field overpressure level); Structure No. 2 at 1730 ft (3.5 psi); and Structure No. 3 at 2730 ft (2.0 psi). The front wall of the structures faced west.

Each structure consisted of two adjoining, but distinct test cells constructed on a common reinforced concrete slab cast on grade: one test cell was of masonry cavity wall construction and the other of Fachwerk, or half-timber construction. The masonry cavity wall test cell

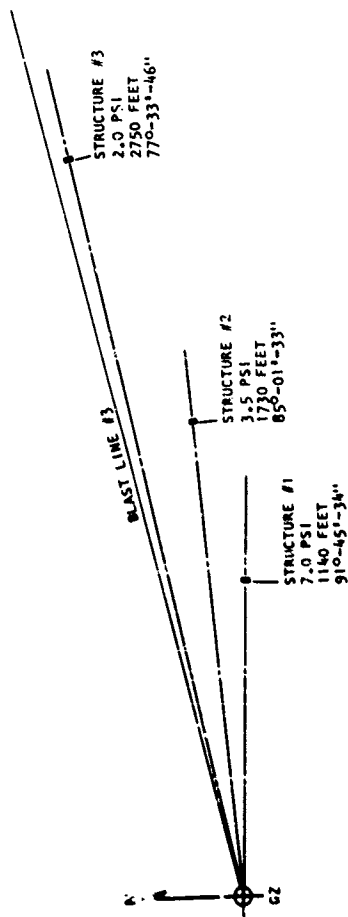


FIGURE 1 LOCATION OF SRI TEST STRUCTURES

consisted of unreinforced brick and concrete masonry unit (CMU) wall panels on the front and one side, and a reinforced concrete ceiling slab. The Fachwerk wall test cell consisted of brick and timber wall panels on the front and one side, and a timber joist ceiling system. The back wall of the test structure and an interior wall separating the two test cells were constructed of reinforced concrete masonry units (RCMU). The test structures were covered by a wood frame gable roof system supporting heavy clay tile roofing. The plan and elevations of the test structures are shown on Figure 2.

Design

The selection of the walls to be included in the field test was based on typical types of West German house construction for which no dynamic response and collapse information was available. One wall type selected was representative of masonry cavity wall construction found in load-bearing wall residences of relatively recent periods, and the other wall type was representative of the traditional Fachwerk (half timber) construction prevalent throughout Germany during previous periods.

Masonry Cavity Test Wall

The design of the masonry cavity wall test panels was similar to the exterior walls used in the "Modern Masonry Wall House" described in Ref. 1. However, as a result of differences in U.S. and West German construction materials, it was necessary to make certain substitutions in the design of the test walls. For example, the red brick commonly used in the U.S. has a width of 3-1/2-in. (9 cm) instead of the 11.5 cm (4.5 in.) prevalent in West Germany. This substitution was felt to be of minor importance because the interior wythe of CMU and not the exterior facing wythe of brick was thought to govern the strength of the wall. Of possibly more importance was the substitution of CMU for the gas concrete blocks used in the interior wythe of the modern German house in Ref. 1. Because gas block is manufactured by a special process and is not available in the U.S., its use in the construction of West German residences was discussed with an SRI consultant (Ref. 2). It was his opinion that although gas concrete and other light weight blocks are being widely used in West Germany today, there are a considerable number of existing buildings with masonry units similar to the CMU used in the U.S. In any event, for the specific type of wall tested, the substitution of CMU for gas concrete blocks was not considered too important because the collapse strength of the wall is primarily a function of the relatively large in-plane forces imposed on the wall by the concrete ceiling slab and heavy roof system rather than of the material properties of the wall itself.

The final design for the masonry cavity test walls is shown on Figure 2. As can be noted, the overall thickness of the wall was about 14 in., and was constructed with a 3-1/2-in. thick exterior wythe of brick, a 7-5/8-in. thick interior wythe of CMU, and a 2-7/8-in. wide cavity.

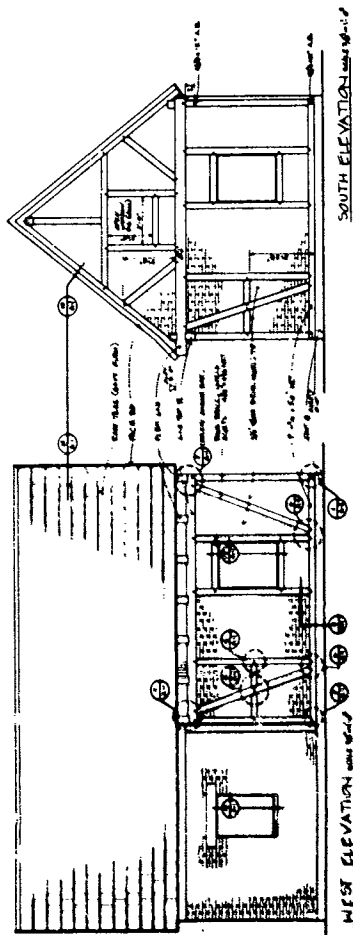
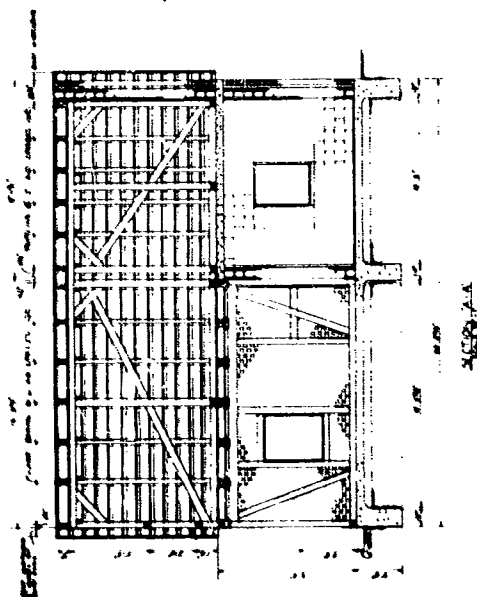
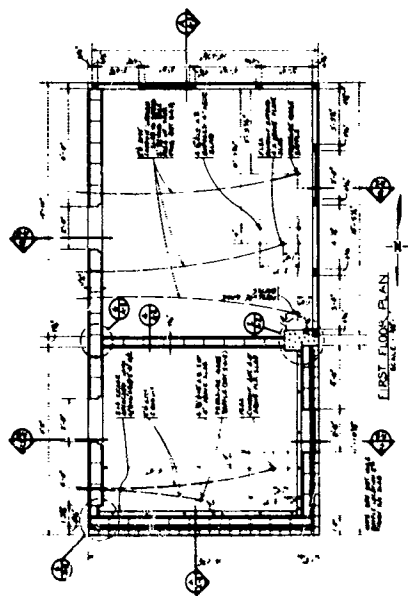


FIGURE 2. PLAN AND ELEVATIONS

Fachwerk Test Wall

The Fachwerk, or half-timber buildings existing in Germany today were built over a period spanning hundreds of years, and consequently were constructed with a variety of sizes and types of timber and masonry materials, and with innumerable patterns or layouts of the timber members. Because it was not possible in a single field test to examine the behavior of all combinations of timber and masonry of interest, a primary goal was to design a test to obtain basic data on the dynamic response and collapse mechanisms of Fachwerk walls that could be used to verify or help develop a prediction model for application to a variety of actual building situations and weapon environments. Also, because of the complexity of Fachwerk construction, it was necessary during the design to include only those details in the test panels that were judged to have significant influence on the response and collapse of the wall under blast loading.

A preliminary design of the test walls was made based on an examination of standard sources of West German construction practices, such as Refs. 3, 4, and 5. The preliminary design was then discussed with the SRI consultant (Ref. 2) and modified to reflect his actual German construction experience. The final design for the Fachwerk test walls is shown on Figure 2. A' posts, diagonals, and braces were 4-3/4-in. sq timbers, and all Fachwerk joints were mortise and tenon, connected with wooden pegs. The masonry in-filled panels were 3-1/2-in. thick brick, and had various spans to provide a range of collapse strengths.

The details of the test structures are shown on the construction drawings and specifications (Ref. 6).

Analysis

A dynamic analysis of the two test walls was required to estimate the relative room size of the masonry cavity wall and Fachwerk test cells, and to estimate the collapse overpressure level of the walls for locating the test structures at the site. The ARL predicted air blast data for the DICE THROW event (Ref. 7) was used for all analyses.

Masonry Cavity Wall

The masonry cavity wall was analyzed using the SRI building evaluation procedure for unreinforced masonry walls (Ref. 8). Although the details of the analytic method will not be presented in this event report, the wall was analyzed as a two-way action wall, fixed on four edges, and with vertical in-plane forces resulting from the reinforced concrete ceiling slab and heavy roof system. Because the methodology had not been developed for cavity wall construction, and because it was thought that the two wythes of brick and CMU would act independently as a result of the large cavity, the analysis was based on the resistance of the CMU wall. Under the assumed behavior the brick wall was found to have negligible blast strength.

Fachwerk Wall

The collapse analysis of Fachwerk walls required the development of an interim resistance function and preparation of the computer program, since this type of wall had not been treated in the previous SRI building evaluation procedure. To estimate the collapse strength of Fachwerk walls required an estimate of the response and collapse of at least the two major components, the in-filled brick panels and the supporting timber posts.

For the analysis of the brick panels it was assumed that a shear failure between the in-filled brick panels and the timber posts would not occur during the initial response of the wall because spikes driven into the timbers and embedded in the mortar between brick courses would prevent a punching shear failure. Instead, it was assumed for the interim mathematical model that the brick panels would develop an initial bending mode, and after flexural cracking would respond in a horizontal arching mode between vertical timber posts. The details of the model are presented in Ref. 9; however, it was assumed that as the masonry panel deflects under lateral load, the in-plane movement of the wall at the supports was resisted by the deformation of the vertical timber posts.

A preliminary flexural analysis of the timber posts that support the brick panels and span between the top and bottom plates, indicated that the posts would develop a slightly greater resistance than the brick panels. Also, because mortise and tenon joints were used to connect posts and plates, a shear failure at the connections was not predicted as would be the case for ordinary wood stud nailed connections. The pre-test predictions for the Fachwerk walls was therefore based on the analysis of the brick in-filled panels.

Collapse Predictions

The SRI pre-shot predictions for the test structures are presented in Figure 3 for the front and side masonry cavity test walls and Figure 4 for the front and side Fachwerk test walls. As can be noted in the figures, the results of the collapse analyses are presented as probability functions. The predicted collapse overpressure is defined as the peak free-field overpressure that results in the incipient collapse of a wall; where incipient collapse implies that the wall is on the threshold of collapse.

For the masonry cavity walls, the predictions on Figure 3 indicate only a slight chance of the front wall reaching incipient collapse at the 2.0 psi level, a 0.98 probability of collapse at the 3.5 psi level, and collapse assured for the front wall at 7.0 psi. For the side wall, the predictions indicate no chance of collapse at the 2.0 psi level, a 0.50 probability of collapse at the 3.5 psi level, and a 1.0 probability of collapse at 7.0 psi.

For the Fachwerk test walls, the collapse predictions of Figure 4 show a greater spread than those for the masonry cavity walls; this is

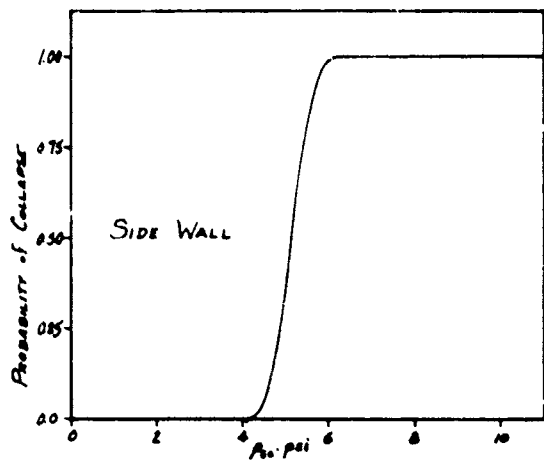
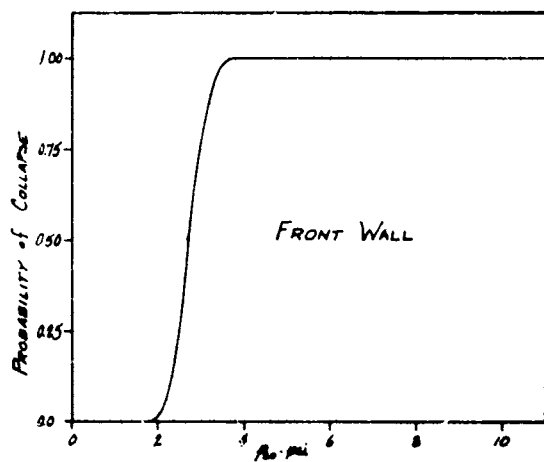


FIGURE 3. COLLAPSE OVERPRESSURE PREDICTIONS FOR MASONRY CAVITY WALL

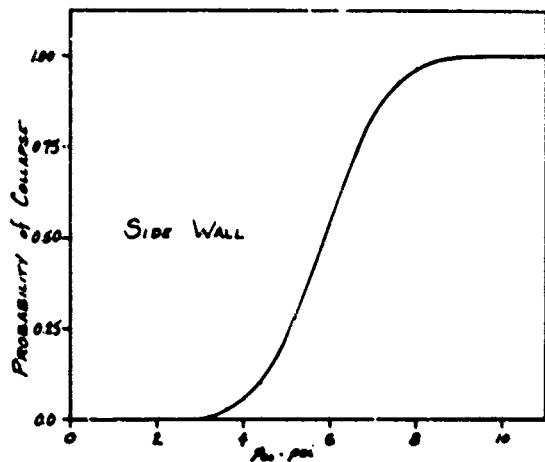
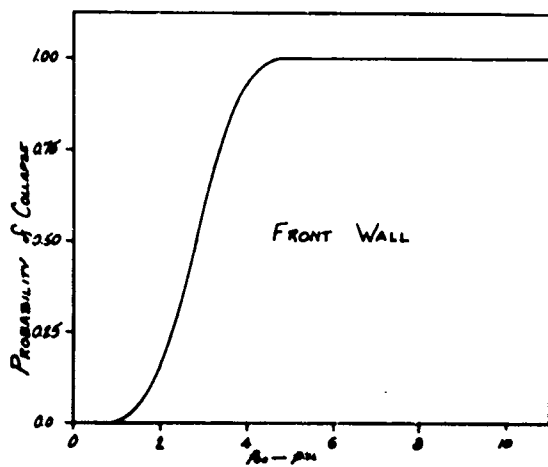


FIGURE 4 COLLAPSE OVERPRESSURE PREDICTIONS FOR 48-IN. WIDE FACED-WALL PANEL

a result of the unknowns involved in the dynamic analysis of Fachwerk walls. Also, the predictions shown on Figure 4 are only for the 48-1/2-in. wide panel adjacent to the window. For the front Fachwerk wall panel, the predictions indicate a 0.15 probability of collapse at the 2.0 psi level, a 0.80 probability of collapse at 3.5 psi, and collapse assumed at the 7.0 psi level. For the side wall, there was no chance of collapse predicted for the 2.0 psi level, only about 0.10 probability of collapse at the 3.5 psi level, and about 0.85 probability of collapse occurring at the 7.0 psi level.

INSTRUMENTATION

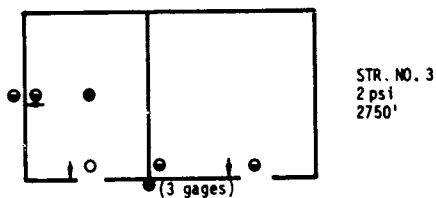
The instrumentation for the three test structures included 35 electronic gages, consisting of 26 pressure-time gages and 9 deflection gages, and 6 high speed cameras. Basically the electronic gages consisted of exterior pressure gages to measure the pressure-time function of the front and side test walls; interior pressure gages to measure the pressure transients and the room-pressure build-up for determining the differential pressure-time loading on the test wall panels; pressure gages to measure the pressure-time on the upper and lower surfaces of the second story (ceiling) concrete slab to determine if a significant pressure differential existed on the slab; and deflection gages to measure the dynamic response of selected wall panels. The gage locations are indicated on Figure 5.

All structures were instrumented identically, except that Structure No. 3 (at 2.0 psi) had two additional head-on pressure gages located in the front face of the reinforced concrete pilaster that separates the masonry cavity and Fachwerk test walls. The purpose of the additional pressure gages was to determine if any pressure anomalies occurred on the exterior surface of the front wall as a result of the 1-ft overhang of the second story floor systems.

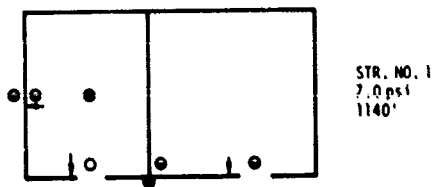
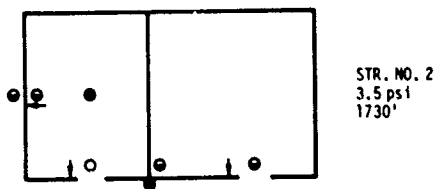
In addition to the electronic instrumentation, two high-speed cameras were installed at each structure location. As noted on Figures 6a and 6b, the cameras were located north and south of each structure at an angle of 50 degrees from the front wall.

The primary purpose of the high-speed cameras was to record the mode of response and collapse mechanism of each wall element, including individual Fachwerk panels. The cameras were to supplement the electronic gage measurements, and to assist in the post-shot analysis by providing a visual record of the initial and final wall break-up and debris transport.

As noted on Figure 6, the Nova cameras were located at Structure No. 1 and the Photonic cameras at Structures Nos. 2 and 3. The Nova cameras, which have the shorter focal length lenses, were located at Structure No. 1 to reduce the distance between camera and structure to minimize any dust or debris problem that could occur at the higher overpressure level.



N



Legend:

- — Side-on p-t gage, ground slab (or grade)
- — Side-on p-t gage, top and bottom of ceiling slab
- — Side-on p-t gage, bottom of ceiling slab
- — Head-on p-t gage, concrete pilaster
- ⊙ — Deflection-time gage, wall mid-height

FIGURE 5 INSTRUMENTATION PLAN

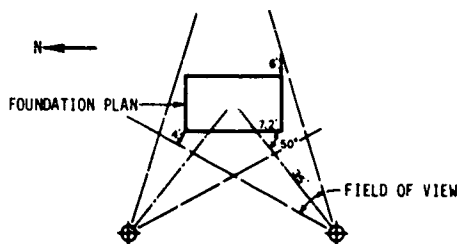


FIGURE 6a NOVA CAMERA LOCATIONS STRUCTURE NO. 1 (7.0 psi)

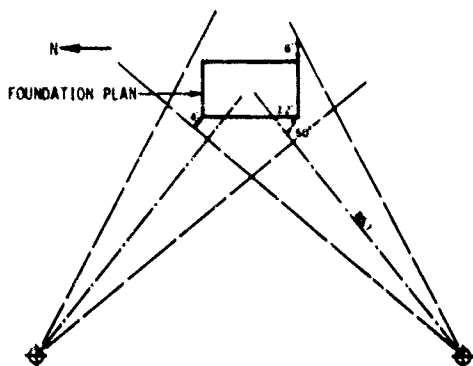


FIGURE 6b PHOTOSONIC CAMERA LOCATIONS STRUCTURES NOS 2 & 3 (3.5 and 2.0 psi)

CONSTRUCTION

All three building sites were worked simultaneously although often similar operations were carried out in sequence from the structure nearest to ground zero (G.Z.) (Structure No. 1) to the farthest structure (Structure No. 3).

Foundation and Floor Slab

Construction began with the excavation for the floor slab to an appropriate depth of 6 in. below natural grade; the floor slab, 28 ft 2-5/8 in. by 15 ft 2-5/8 in. in plan dimensions, was oriented with its long dimension perpendicular to the line of site to G.Z. Footings 14 to 24 in. wide were excavated to a depth of 3 ft below top of slab. Soil under the slab was wetted and compacted with gasoline powered, hand-pushed compactors until soil density to a depth of 6 in. was at least equal to natural density. Approximately 6 in. of heavy sand was then spread and compacted on the area below the floor slab and polyethylene sheeting 0.006-in. thick was placed on top of the sand.

After steel forms were fixed in place and reinforcing steel located and tied, approximately 28 cy of ready-mixed concrete, batched on the Dice Throw test bed, was placed and finished. Final slab thickness varied from 6 to 8 in., and the slab was reinforced in both directions by 3/8-in. steel bars 8 in. on center. In Figure 7 the finishing of the slab is in progress. The figure also shows the apportionment of the slab surface into two rooms of unequal areas, separated by a line of reinforcing bars projecting above the slab. These bars, as well as those in the rear wall shown in the right of the photograph, were grouted into concrete masonry units making up the non-responding portions of the structure.

The slab in the foreground of Figure 7 contains the two Fachwerk test walls on the west and south sides; the cavity walls are in the north room beyond the interior divider wall.

Non-Responding Walls

Heavily reinforced to their full height and solidly grouted (except for the divider wall at Structure No. 1), the RCNU walls were designed to resist the dynamic forces without inelastic response. The interior divider wall contained 8-in. thick RCNU; the rear or eastern wall, 12-in. thick RCNU. Both RCNU walls were tied at their intersection by horizontal reinforcing steel. The rear wall had an access opening 3 ft wide by 4 ft 8 in. high leading into each room; during the shot these openings were closed with heavy wooden doors bolted in place.

The western anchorage for the interior divider wall was a reinforced concrete pilaster approximately 15 by 27 in. in cross section extending the full height of the wall and tied to it by horizontal reinforcing steel.



FIGURE 7 FINISHING REINFORCED CONCRETE FLOOR SLAB

In Figure 8 construction of the RCMU walls is underway. Some of the reinforcing steel for the pilaster projects from the slab at the left end of the divider wall.

Masonry Cavity Wall

After the RCMU walls were laid up to a height of about 4 ft, the masons immediately began work on the first story masonry cavity test walls. Like the RCMU the two wythes of the masonry cavity walls were mortared directly to the floor slab, but no reinforcement was used in the test walls. The cavity walls were anchored at the northeast corner of the RCMU wall by an interlocking CMU bond with the RCMU and by steel masonry ties between brick and CMU. At the pilaster, anchorage was achieved through metal ties and a single column of 8-in. RCMU. (See detailed drawings in Ref. 6.)

As the cavity wall reached the 4-ft height of the RCMU walls, the masons set up scaffolding and continued construction of both the RCMU and the cavity walls. In Figure 9 the cavity walls are seen nearing completion. The Z-ties between the CMU and brick wythes are in place ready for placement of mortar; the anchorage to the RCMU at the northeast corner is seen in the center foreground.

To simulate a substantial floor system in preventing inward sliding of the cavity wall over the floor slab, a nominally 2-by-4-in. wood plate was bolted to the slab directly against the inside face of the cavity wall. In Figure 7 the bolts for this plate may be clearly seen projecting above the slab on a line about 15-1/2 in. in from the edge.

Aboveground Concrete Work

When the masons had finished all first story masonry walls, the pilaster was formed and poured, and five to eight days later the concrete was placed for the 8-in. thick reinforced concrete ceiling slab. While curing, this slab was supported by temporary forms resting on jacks. The finished slab completely covered the masonry cavity wall room and projected 1 ft beyond the front (west) cavity wall. At the time of placing the concrete for the pilaster, the RCMU non-responding walls were filled with cement grout.

The top course of the masonry cavity wall consisted of solid top block and the cavity between the brick and CMU wythes was spanned by a 4-1/2-in. wide strip of sheet metal nailed to the masonry to prevent intrusion of the concrete from the ceiling slab into the cavity. The only bond between the ceiling slab and its supporting walls was that provided by fresh concrete placed on masonry; no mechanical ties were used.

The clear distance between floors was 8 ft 8 in.



FIGURE 8 CONSTRUCTION OF RCMU NON-RESPONDING SUPPORT WALLS



FIGURE 9 CONSTRUCTION OF MASONRY CAVITY TEST WALL

Fachwerk (Half-Timber) Framing

After the aboveground concrete work was complete, carpenters began construction of the timber framework for the Fachwerk walls shown in elevation in Figure 2. Although most of the components were prepared in the contractor's shop in Socorro, it was found necessary to fit some on the job after the major portions of the framework had been put in place. All joinery was mortise and tenon, illustrated in Figure 10. Holes for the pegs were drilled with the timbers joined; tight Douglas fir pegs were then driven in with a plastic mallet. Figure 11 is a photograph of the partially completed timber work on the south wall. The bolts seen in the foreground of Figure 7 are seen again in Figure 11 holding the bottom plate in position (a similar series of bolts fastens the west Fachwerk wall). The projecting portion of the wood pegs were cut off after final adjustments in timber positions were made. The tenon joining a horizontal brace to a diagonal brace is seen in the upper left of the photograph.

As noted above, the Fachwerk test walls bottom plates were anchored to the floor slab. In addition there were four anchor bolts holding vertical timber posts to the non-responding structural elements: two bolts in the pilaster at the north end of the west front wall and two bolts in the 12-in. RCMU at the east end of the south side wall. Since the timber framing was fastened together with mortise and tenon joinery, it was impossible to cast all these bolts into the masonry or concrete. Therefore the bolts projecting from the horizontal surface of the floor slab were cast in place while those on vertical surfaces were expansion type bolts driven into drilled holes through the in-place timber posts. During construction it was found possible to use cast-in-place bolts in vertical surfaces if they were sufficiently high above the horizontal surface, hence on Structures Nos. 2 and 3 some of the upper bolts are cast-in-place.

Ceiling and Roof Framing

With the south and west Fachwerk framing in place, the carpenters erected 6-by-10-in. ceiling joists, one of which served also as the top plate in the Fachwerk south wall. The tenons seen at the top of the posts in Figure 11 fit mortises in this joist.

The joists are held to the top plate of the Fachwerk west wall by 3/4-in. deep notches and by oak dowels 1-1/2 in. in diameter by 5 in. in length. Like the concrete overhead slab, the joists extended beyond the west front wall by 1 ft. At their eastern (back) ends the joists were nailed to a wooden plate bolted to the RCMU.

A false ceiling of 5/8-in. thick plywood was nailed between the joists to carry a 3-1/2-in. deep layer of brick, pictured in Figure 12. The ceiling brick were painted white on the top surface to distinguish them in any post-shot debris from structural brick. After the brick were painted, the attic floor was surfaced with 3/4-in. thick plywood.

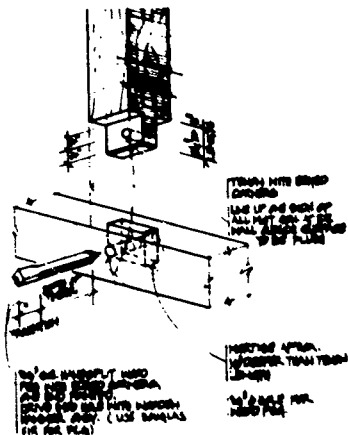


FIGURE 10 TYPICAL MORTISE AND TENON JOINT USED IN FACHWERK FRAMING

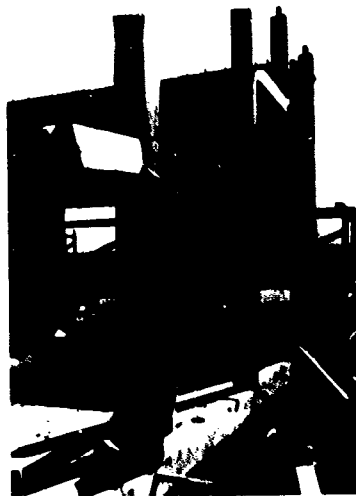


FIGURE 11 PARTIALLY COMPLETED TIMBER FRAMING FOR FACHWERK SOUTH SIDE WALL



FIGURE 12 BRICK IN PLACE BETWEEN CEILING JOISTS

Roof erection began with the two 4-by-6-in. rafters at the north end of the structure and the 6-by-6-in. ridge beam supported on 6-by-6-in. posts. The ridge beams over the two rooms were separate. Rafter spacing was approximately 24 in. on center over the north (cavity wall) room and 30 in. on center over the south (Fachwerk) room and sloped at an angle of 51 degrees to the horizontal. Rafters were fastened at the ridge and at the bottom plate with 8-in. spikes driven into pre-drilled holes. As soon as the roof framing was well underway, the masons were able to continue the north cavity wall in the gable on top of the ceiling slab. In Figure 13 the masons have just mortared the first two CMU courses on top of the reinforced concrete ceiling slab. The attachment of rafter to plate and the bolting of plate to slab is also shown in the photograph; the attachment of rafter to ridge beam was similar to its attachment at the plate. Ridge beam supporting posts were toe nailed at the top into the ridge beam and at the bottom into special plates bolted to the slab. Figure 14 shows an overall view of the work at this stage.

Fachwerk Brick Masonry

While the carpenters were finishing the roof framing and the Fachwerk south gable framing, the masons began filling the half-timber framework. One wythe of common brick in running bond was mortared into each subpanel. In addition to the mortar placed between brick and timber members, 50d nails half driven into the wood and half embedded in approximately every fifth horizontal mortar joint also provided bonding between masonry and timber. Figure 15 is a view from inside the structure showing the masons at work on the first story Fachwerk. The 50d nail at the first course can be seen in the lower central Fachwerk portion of the scene. The plywood false ceiling has been installed between joists. Note that the brick are laid flush with the timber framework on their inner surfaces. Because of the difference in thickness between the brick and timber the outside surfaces are not flush but the brick is substantially inset. In the Fachwerk gable however nominally 4-by-6-in. timber was used for framing so that the brick was flush on both surfaces. A view from outside, Figure 16, shows the inset brick in the first story and the flush brick in the gable.

Figure 16 also shows the different rafter spacing over the two rooms. The ridge beam and plates are not continuous but are cut between the two closely spaced rafters (seventh and eighth from the south or right hand side). The three ridge posts are visible supporting the ridge over the Fachwerk room. Three post were planned for the cavity wall room as well but during construction it was noted that the center post would rest on the position of the upward facing pressure gage in the center of the overhead slab. Therefore, two equally spaced posts were substituted for the single central post. In Figure 16 only two of these four posts over the cavity wall room are in place. Note that the northernmost post over the Fachwerk room is within a few inches of the southernmost post over cavity wall room.

In Figure 16 can also be seen the pre-cast reinforced concrete header spanning the single masonry cavity wall window. A similar header was



FIGURE 13 OVERALL VIEW OF CONSTRUCTION OF
MASONRY CAVITY WALL IN GABLE



FIGURE 14 CONSTRUCTION OF MASONRY CAVITY WALL
IN GABLE ABOVE CONCRETE CEILING SLAB



FIGURE 15 INTERIOR VIEW OF FACHWERK MASONRY CONSTRUCTION

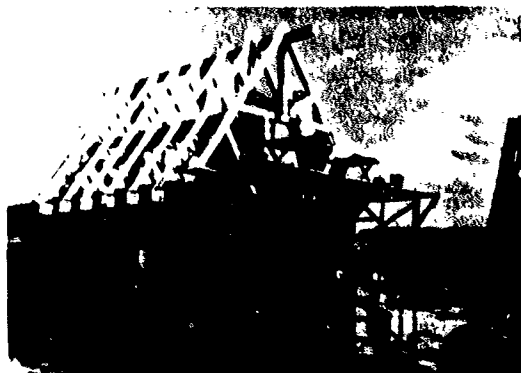


FIGURE 16 MASONRY CONSTRUCTION IN FACHWERK GABLE WALL

built into the CMU wythe of the cavity wall. The sill of this window consisted of two rowlock courses of brick. Wood jambs were nailed to a wood nailing strip tightly wedged into the cavity in the window opening.

All first story windows were glazed with wood window stop holding a single pane of double strength glass; the gable window was not glazed.

Roof Covering

The baked clay roof tile chosen was a European style made in the United States^a weighing 9.35 psf when laid. Each tile was fastened with a single nail to 1-by-2-in. net wood strips laid parallel to the west wall approximately 14 in. on center. The tile overlapped on all four sides (except for the bottom course and end tier). Figure 17 shows a photograph of the roofing operation. The alternation in tile color was done for photographic reasons. (The Fachwerk panel above the front window was later filled with brick.)

The special closure tile manufactured for use at the ridge was omitted for the test structures; a cap of mortar sealed the ridge instead. The tile nailing strips extended past both north and south gable walls to create roof overhangs of approximately 6 in. on the sides.

TEST RESULTS

Free-Field Overpressure

The air blast data obtained in the vicinity of the three SRI test structures included the free-field measurements along blast line No. 3 at ground ranges of 1140 ft (Structure No. 1) and 2750 ft (Structure No. 3), and measurements in the truck area at 1140 ft, 1370 ft, and 2000 ft. In addition, measurements from the pressure gages on the ground surface adjacent to the north wall of each structure, and from the pressure gages mounted on the front surface of each concrete pilaster could be used to estimate the actual free-field overpressure at each structure location.

For the three structure locations, the discrepancies in the peak free-field overpressure data from four sources are given in Table 1. The values shown in the table as estimated overpressures were obtained by curve fitting the actual data over the ranges of most interest; this was necessary where free-field pressure gages are not located at the same ground range as the structure. The values shown as calculated in the table were obtained by using the initial discontinuity of the reflected pulse measured by the head-on pressure gages mounted on the concrete pilaster of each structure. Although the actual free-field overpressure level at each structure cannot be determined with certainty, it is apparent that the overpressure level was slightly less than the predicted value of 7.0 psi for Structure No. 1, was approximately equal to the 3.5 psi predicted value for Structure No. 2, and was a little below the 2.0 psi predicted value for Structure No. 3.

^a Ludowici-Celadon Company, Chicago, Illinois.



FIGURE 17 TILE ROOFING OPERATION

Table 1
PREDICTED AND MEASURED PEAK FREE-FIELD OVERPRESSURES
AT LOCATIONS OF THREE SRI TEST STRUCTURES

Range (ft)	Peak Overpressure (psi)				
	Predicted	Blast Line #3 [†]	Calculated [*]	Outside North Wall	Truck [†] Area
1140	7.0	6.3	6.8	6.7	6.7
1730	3.5	3.6 ^{**}	3.3	3.7	
2750	2.0	2.5	1.7	1.8	

^{*} Calculated from peak reflected peak overpressure at pilaster gage (P-2), assuming perfect reflection. Assumed ambient air pressure = 12.325 psi.

[†] Values reported by letter dated 21 April 1977 from Test Group Director, Dice Throw.

^{**} Estimated.

Post-Shot Damage Survey

The post-shot damage survey started immediately after the test bed was cleared for re-entry. The overall damage to the three test structures can be briefly summarized as follows. Structure No. 1, as shown in Figure 18, experienced a catastrophic collapse of the front cavity wall and a portion of the side cavity wall, and of the front and most of the side Fachwerk wall panels. Structure No. 2, as shown in Figure 19, experienced structural damage to the front cavity wall, although the wall was still in place, and cracking of the side cavity wall. The Fachwerk walls had a partial collapse of the 4-ft wide masonry panels on both the front and side walls, as well as damage to some of the timber members. Structure No. 3, as shown in Figure 20, had only hairline cracking in the cavity walls, and some cracking in the Fachwerk masonry panels.

Figure 18 - 20 also show the post-shot damage to the roof systems of the three test structures. It was apparent from the test that the roof tile was stronger in bending than originally estimated, and the roof framing therefore received much higher dynamic loading than anticipated. This resulted in much greater damage to the roof support members: at Structure No. 1 all front rafters, except the one adjacent to the north cavity wall gable, were fractured; at Structure No. 2 all front rafters, except the two end rafters, were fractured or experienced horizontal splitting; and at Structure No. 3 three front rafters had horizontal splits and three had lifted from the front plate. Details of the damage to each structure is given in the following sections.

Structure No. 1

Masonry Cavity Wall. As can be seen in Figure 21 the brick and CMU on the west front wall were completely collapsed. On the front wall, the only remaining CMU was the bottom course and a portion of the top course that was still adhered to the concrete ceiling slab (Figure 22). The remaining brick on the front wall was a 27-in. vertical section, adjacent to the concrete pilaster, that had rotated inward about 1 ft, three courses of brick along the front above the floor slab, and the top course of brick still bonded to the concrete ceiling slab.

The north side cavity wall was collapsed for a distance of about one-third its length from the front wall as shown in Figure 23. The bottom two courses of CMU, at their intersection with the front wall, were still in place although they had rotated outward and forward about 3/4 in. (Figure 24). Portions of the brick and CMU that were still standing had the Z-ties intact even though the two wythes had rotated about 4 in. outward as a unit (Figure 25). The top course of brick and CMU in the side wall were still bonded to the concrete ceiling slab in the same manner as described for the front wall.

The fracture planes in the top course of CMU and brick in the front wall below the ceiling slab joint are shown in Figure 26; the fractures

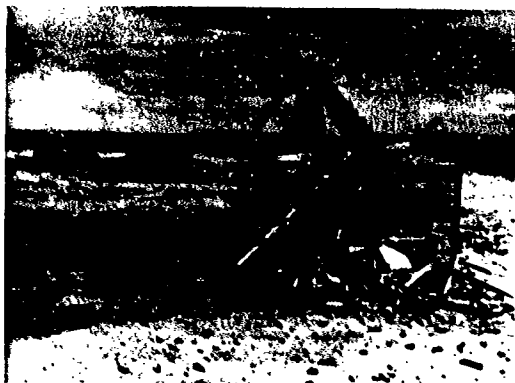


FIGURE 18a POST-SHOT VIEW OF STRUCTURE NO. 1
FROM SOUTH FACHWERK SIDE



FIGURE 18b POST-SHOT VIEW OF STRUCTURE NO. 1 FROM
NORTHWEST MASONRY CAVITY WALL SIDE



FIGURE 19 POST-SHOT VIEW OF STRUCTURE NO. 2
FROM SOUTHWEST FACHWERK SIDE



FIGURE 20 POST-SHOT VIEW OF STRUCTURE NO. 3
FROM SOUTHWEST FACHWERK SIDE

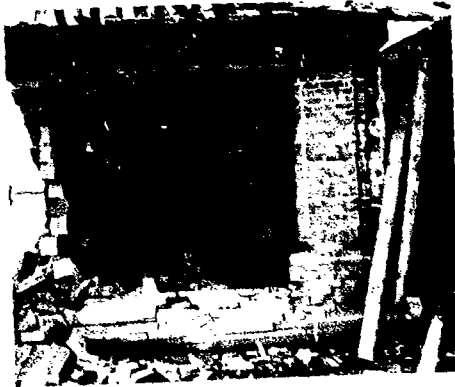


FIGURE 21 COLLAPSED FRONT MASONRY CAVITY WALL STRUCTURE NO. 1

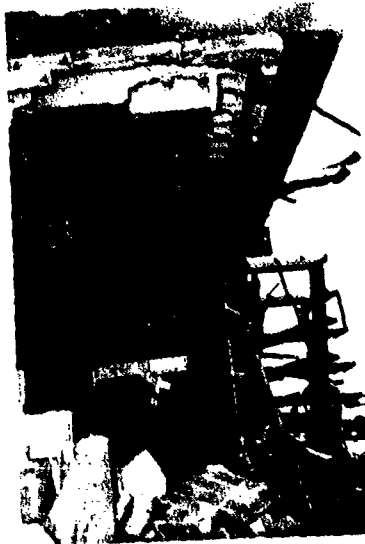


FIGURE 22 END VIEW OF COLLAPSED MASONRY CAVITY WALL STRUCTURE NO. 1



FIGURE 23 PARTIALLY COLLAPSED NORTH SIDE
MASONRY CAVITY WALL STRUCTURE NO. 1



FIGURE 24 FRACTURE AT INTERSECTION OF WEST FRONT AND NORTH
SIDE MASONRY CAVITY WALLS STRUCTURE NO. 1

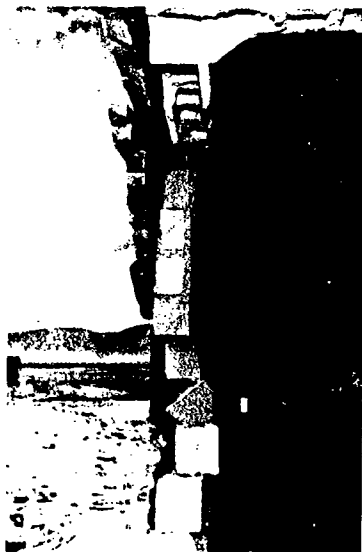


FIGURE 25 OUTWARD ROTATION OF NORTH
MASONRY CAVITY WALL STRUCTURE NO. 1



FIGURE 26 FRACTURE PLANES IN TOP COURSE OF CMU IN FRONT CAVITY
WALL BELOW CONCRETE CEILING SLAB STRUCTURE NO. 1

were similar in the side wall. The fracture pattern on the inner face of the CMU indicates a shear/compression failure, whereas that on the outer face of the CMU indicates a tensile failure. The failure at the mortar joint between bricks, which can also be noted in Figure 26, indicates that the brick wythe failed in tensile bond.

At the connection between the front cavity wall and the concrete pilaster, the fracture pattern in the CMU was as just described for the top course of the CMU at the ceiling slab. The portion of the brick wythe still standing in the front wall exhibited a typical tensile fracture along a vertical section one-half brick in from the concrete pilaster support (Figure 21). A damaged section of the brick, on an approximate diagonal from the upper right corner, indicated compressive spalling.

The bottom course of the CMU in the front wall was still in place in front of the kicker plate. However, as shown in Figure 27, the inner face of the CMU was fractured vertically through the webs, and the top edge of the inner face had rotated inward about 1 in. The remainder of each block was still in place, although the bond between CMU and the bottom mortar bed was broken. Removal of the inner face indicated that the bottom course of CMU in the front wall had also failed in shear/compression at the inner face. The brick along the bottom of the collapsed front wall had failed in tension at the horizontal mortar-to-brick joint.

An examination of the steel Z-ties placed between the brick and CMU wythes showed that many of the ties were undamaged. Of the ties found in the debris, only a few were bent, one was fractured, and one apparently experienced an axial column type buckle. The remainder of the ties found in the debris, as well as those remaining in the damaged walls, appeared in their original condition. It's therefore possible that some of the ties found in the debris were damaged during collapse of the wall.

Because of the condition of the Z-ties, e.g., Figure 28, and because the brick and CMU in damaged but still standing sections of the walls had rotated as a unit (e.g., Figure 25), it is apparent that the steel Z-ties placed on 16-in. centers horizontally and vertically had sufficient strength to transfer the blast forces between the outer brick and inner CMU wythes. As a result of the two wythes acting as a unit, rather than as individual panels, the masonry cavity wall developed a greater resistance to the blast forces than assumed in the analysis. A cursory examination of the test data indicates that the measured velocity of the cavity wall at time of collapse was about two-thirds of the predicted velocity. On the other hand, from the measured wall velocity at collapse, as well as from the distribution of the front wall debris, it is apparent that the free-field overpressure of about 6.5 psi at Structure No. 1 was, as predicted, well above the incipient collapse overpressure for the front masonry cavity wall.

Fachwerk Wall. As can be seen on Figure 29 the brick and timber panels of the west front Fachwerk wall were completely collapsed. The only members remaining near their original positions were the vertical post adjacent



FIGURE 27 FRACTURE IN BOTTOM COURSE OF CMU IN
FRONT CAVITY WALL STRUCTURE NO. 1



FIGURE 28 TYPICAL INTACT Z-TIE EMBEDDED IN BRICK MASONRY
FROM FRONT MASONRY CAVITY WALL STRUCTURE NO. 1



FIGURE 29 COLLAPSED WEST FRONT FACHWERK WALL STRUCTURE NO. 1

to the concrete pilaster and the bottom plate which was fastened with anchor bolts to the concrete floor slab.

On the south side wall, only two of the four Fachwerk panels remained standing; as shown on Figure 30 the two remaining panels were badly damaged. With the collapse of most of the vertical timber supports in the Fachwerk walls, the ceiling and roof systems collapsed onto the floor slab.

The collapse of the Fachwerk wall panels involved at least three primary mechanisms; (1) the deflection and break-up of the brick masonry, (2) the large deflection and fracture of the timber posts, and (3) fracture of the plates at the mortise and tenon connections. There were also other identified collapse mechanisms, which were considered as minor or secondary. An example of a minor mechanism would be the pullout or fracture of the wooden pegs in the mortise and tenon joints. An example of a secondary collapse would be the large vertical deflection of the top plate of the front wall, after the brick and timber posts had collapsed, and the subsequent fracture of the corner post between the front and side Fachwerk walls. An examination of the damage on both Structures No. 1 and 2 (to be discussed subsequently), as well as a preliminary review of the high-speed test movies, indicates that the three mechanisms occurred simultaneously, or if they occurred in a definite sequence it was not apparent from the information examined to date. It is thought at present that if there was a preference for a specific collapse mechanism to occur, then it was more a function of flaws in the materials or construction than large differences in basic structural strength.

The final disposition of the debris in the interior of the room from the front Fachwerk wall panels, such as shown in Figure 31, indicates that the 6.5 psi overpressure level was well above the incipient collapse overpressure of the wall. The timber elements of the front wall were distributed towards the rear of the room, and in several cases were found deposited against the rear RCMU wall. For example, Figure 32 shows the timber post from the left (north) of the window resting against the rear wall with the lintel still attached. The bottom of the post is upward indicating that the post rotated during translation, and timber marks on the wall indicate that the post impacted the rear wall with considerable velocity. Also, the major portion of the bricks from the front wall were found close to the rear wall; in fact, one brick impacted the rear RCMU wall 41 in. above the floor slab, as shown in Figure 33.

A preliminary review of the test movie for Structure No. 1 indicated that as the inward center deflection of the timber posts of the front wall became large, the mortise joints in the bottom plate fractured, except for those at the two end posts. With removal of the bottom support for the posts, the wall panels rotated inward at the bottom under the blast forces. When this occurred, the top plate of the front wall was essentially spanning the distance between the two end posts. Under the influence of the high roof dead loads, and possibly some blast forces, the top plate deflected downward at the center placing an eccentric load on the corner post between the west front and south side Fachwerk walls. The corner post fractured at the top and collapsed outward from the corner.



FIGURE 30 TWO PANELS REMAINED STANDING IN SOUTH
SIDE FACHWERK WALL STRUCTURE NO. 1



FIGURE 31 INTERIOR DEBRIS FACHWERK TEST CELL STRUCTURE NO. 1

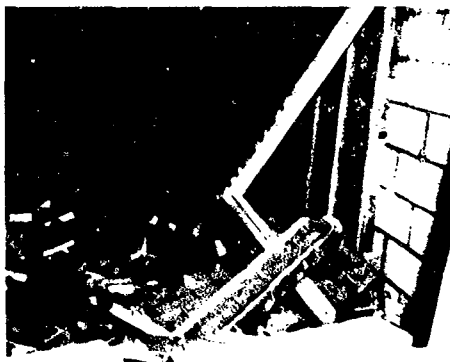


FIGURE 32 INTERIOR DEBRIS FACHWERK TEST CELL STRUCTURE NO. 1



FIGURE 33 BRICK FRAGMENT EMBEDDED IN REAR RCMU WALL 41 INCHES ABOVE FLOOR SLAB AS A RESULT OF IMPACT OF BRICK FROM COLLAPSED FRONT FACHWERK WALL STRUCTURE NO. 1

The initial collapse of the south side Fachwerk wall was similar to the front wall, however, the damage was not nearly as great and the final disposition of the members was different. The test movie indicated that as the inward deflection at the center of the vertical post to the left of the 48-in. wide panel (the first vertical post east of the front wall corner post) became large, the mortise joint in the bottom plate fractured, and the wall panel started to rotate inward at the bottom. However, because the net inward blast force on the side wall was much less than that on the front wall, and even reversed direction during the load cycle, the side wall did not collapse inward as the front wall had done, but rather the inward deflection reached a maximum and then decreased. With the collapse of the corner post, as described above, the two damaged panels in the side wall (those nearest to the front wall) collapsed, with most of the debris being deposited on the outside of the structure.

Roof System. As shown in Figure 29 the roof system over the Fachwerk wall test cell was completely collapsed, and that over the cavity wall test cell was severely damaged but still in place. All roof tile had been removed by the blast and was displaced as far as 121 ft behind Structure No. 1, and 71 ft in front of the structure.

The roof framing over the Fachwerk wall had collapsed onto the test cell as a result of the wall collapse. However, even though all front roof rafters had been fractured by the blast loading, all rear rafters were structurally intact and still nailed to the rear plate (Figure 30).

The roof framing over the cavity wall test cell was approximately in position although skewed, as noted in Figure 34. All front rafters, except the one adjacent to the north side cavity wall gable, had experienced typical flexural fractures near the center of the rafter span. The top portions of the rafters were still nailed to the ridge beam, but were hanging downward, and the bottom portions had rotated around the front plate and were resting on top of the reinforced concrete ceiling slab. Figure 34 also shows that the six rear rafters, four ridge beam posts, and the ridge beam above the masonry cavity wall are all structurally intact but somewhat displaced.

Structure No. 2

Masonry Cavity Wall. Although the front cavity wall was still in place, there was extensive cracking of the exterior wythe of brick as shown in Figure 35. As noted for Structure No. 1, there was also a vertical crack one-half brick in from the concrete pilaster support in Structure No. 2. Another vertical crack was apparent at the juncture of the front and side cavity walls; this crack extended the full height of the wall and was continuous in either the front or side walls. The crack width varied from a small crack at the bottom to about 1/4 in. near the top (Figure 36). The diagonal cracks from the left corners of the wall shown in Figure 35, showed some compressive spalling. It appears that the window jambs wedged



FIGURE 34 DAMAGED ROOF FRAMING ABOVE MASONRY
CAVITY WALL TEST CELL STRUCTURE NO. 1

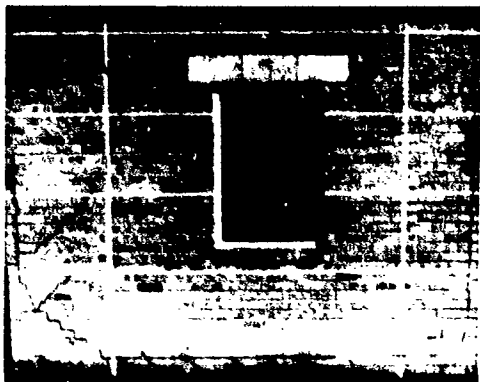


FIGURE 35 CRACKED FRONT MASONRY CAVITY WALL STRUCTURE NO. 2

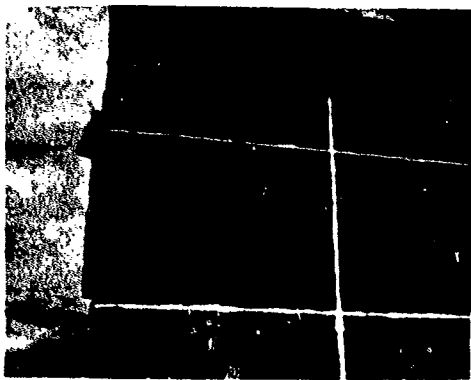


FIGURE 36 CRACK AT CORNER OF FRONT AND SIDE
MASONRY CAVITY WALLS STRUCTURE NO. 2

in the cavity between the two wall wythes provided sufficient stiffness to the wall at the window opening to modify an otherwise fairly classical crack pattern.

Figure 37 shows the crack pattern in the exterior of the north side cavity wall of Structure No. 2; the juncture of the side and front walls is on the right in the figure. Except for the crack at the corner, the cracks in the wall vary in width from about 1/16 in. on the right part of the wall to hairline on the left. Although not discernible in the figure, a portion of the wall above and to the right of the center in Figure 37 was pushed inward about 1/4 in. from its original position.

An examination of the interior surface of the CMU indicated that there was more extensive damage to the front cavity wall than was apparent from the cracks in the exterior surface of the brick. The inner face of the top course of CMU above the window had fractured just below the concrete ceiling slab for a horizontal distance of about 5 ft. The CMU below the fracture had a maximum inward permanent displacement of about 1/2 in. near the center of the fracture as can be seen in Figure 38; the displacement decreased to zero near the ends of the fracture. Also, the portion of the block above the fracture plane was still well bonded to the bottom surface of the concrete ceiling slab. The fracture plane on the inner face of the CMU in the front wall of Structure No. 2, which is shown in Figure 38, was identical to that observed in a like location in Structure No. 1 (see Figure 26).

In addition to the fracture above the window, there was also a gap at the intersection of the CMU in the front and side walls. Figure 39 shows that the side wall, on the right in the photograph, has separated and displaced about 1/2 in. away from the front wall; the figure shows the gap in the second course of CMU below the concrete ceiling slab.

In order to examine for further possible damage to the CMU in the front wall, the window frame was removed to permit inspection of the cavity between the brick and CMU wythes. It was discovered that the horizontal mortar joint under the top course of CMU had failed and that the CMU wythe below the top course had displaced inward about 1/2 in. relative to the top course of CMU, which was obviously still bonded to the concrete ceiling slab. It was therefore apparent that the inner face of the front wall CMU in Structure No. 2 had experienced a compression/shear type of failure and that the top block had split along the webs and horizontal mortar joint in a manner similar to that noted for the bottom course of CMU in the front cavity wall of Structure No. 1 (see Figure 27).

Because of the damage to the front cavity wall CMU just described, the rear surface of the brick wythe was examined in the cavity to determine why the exterior surface of the brick had given no indication of the degree of damage sustained by the CMU above the window. A close examination of the rear brick surface showed that although some additional cracks in the brick were found, there was no evidence that the brick wythe had a permanent displacement of 1/2 in. The top course of bricks was well bonded to the concrete ceiling slab, and there was no detectable slippage along any of the



FIGURE 37 CRACKED SIDE MASONRY CAVITY WALL STRUCTURE NO. 2



FIGURE 38 FRACTURE IN INNER SURFACE OF CMU IN FRONT CAVITY WALL
JUST BELOW THE CONCRETE CEILING SLAB STRUCTURE NO. 2

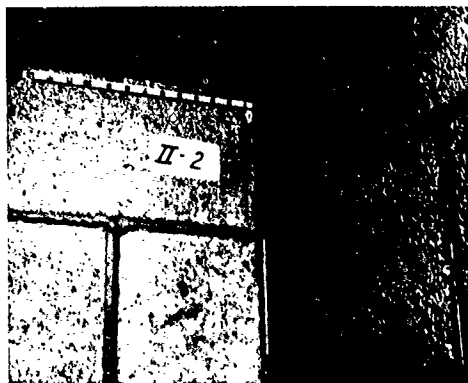


FIGURE 39 GAP AT INTERSECTION OF CMU IN FRONT AND SIDE
MASONRY CAVITY WALLS STRUCTURE NO. 2

mortar joints. However, it was found that some of the Z-ties between the two wythes had slipped in the mortar joints, permitting the two wythes to separate.

From the similarities between the damage sustained by the front cavity wall in Structure No. 2 and the failure modes observed in identical locations in Structure No. 1, it is apparent that the free-field overpressure of about 3.5 psi at the Structure No. 2 location was sufficient to develop the maximum resisting capability of the cavity wall. Furthermore, it is felt that the wall was close to its collapse overpressure, and that an increase in overpressure of as little as 1/2 psi would have produced significantly greater wall displacement and a correspondingly greater damage.

The interior CMU of the north side cavity wall showed crack patterns similar to, but more extensive than, those observed in the exterior brick. Also, the cracks in the CMU were generally wider than found in the brick, being as wide as 1/8 in. in the area towards the front of the wall.

Fachwerk Wall. A view of the damage to the west front Fachwerk wall of Structure No. 2 can be seen in Figure 40. As can be seen in the figure, the masonry in the 48-in. wide panel to the left of the window has been severely damaged with a portion having collapsed onto the floor slab, the masonry in the panel below the window has collapsed, and there is damage to the masonry in some of the other panels. In addition, the tenons are exposed at the bottom of the post and diagonal to the right of the window, indicating a failure of the bottom plate at the mortise joint, and there are splits in the top plate at the joints for both the post and diagonal to the right of the window.

The damage to the south side Fachwerk wall is shown in Figure 40. Although the damage to the 48-in. wide panel to the left of the window appears somewhat similar to that observed for the identical panel in the front wall, the damage to the other masonry panels and timber framing is much less than that observed on the front wall at the same location.

Figures 41 and 42 show in more detail the damage sustained by the west front Fachwerk wall. It is apparent that the bottom plate at the mortise joint to the right of the window fractured, permitting the post and diagonal to displace inward at the bottom with a permanent deflection of about one ft; this deflection probably accounts for the loss of brick below the window. The fracture in the plate is shown graphically in Figure 43, and is a typical failure mode, noted in both Structures Nos. 1 and 2.

The post to the left of the window in Figure 42 split parallel to the grain for its entire height; this is also a typical failure mode often observed in Structure No. 1. The post to the left of the 48-in. wide brick panel, although still in place, sustained a classical bending failure, exhibiting compressive distress on the exterior surface and tensile fracture on the inner surface. In addition, cracking of the inner surface of the bottom plate in the vicinity of the mortise joint for this post indicated



FIGURE 40 DAMAGED WEST FRONT AND SOUTH SIDE
FACHWERK WALLS STRUCTURE NO. 2



FIGURE 41 DAMAGED WEST FRONT FACHWERK WALL STRUCTURE NO. 2



FIGURE 42 OBLIQUE VIEW OF DAMAGED WEST FRONT
FACHWERK WALL STRUCTURE NO. 2



FIGURE 43 TYPICAL FRACTURE IN BOTTOM PLATE AT MORTISE
JOINT WEST FACHWERK WALL STRUCTURE NO. 2

that a fracture of the plate had been initiated which was similar to that observed at other bottom plate mortise joints.

The brick masonry in the 48-in. wide panel on the front Fachwerk wall, shown in Figure 44, was approximately one-half collapsed with the remainder severely damaged. The masonry showed evidence of failure at the mortar joints and compressive spalling of the exterior surface of the bricks.

The final disposition of the debris from the front wall is shown in Figure 45. Although some debris was translated as far as the rear RCMU wall, none was piled against the rear wall and no brick impacted the rear wall above the floor slab as occurred in Structure No. 1. This indicates, of course, a lower brick velocity at time of collapse for Structure No. 2 than for Structure No. 1.

The damage to the south side Fachwerk wall is shown in Figure 46. As can be seen in the figure, the damage to the 48-in. wide brick panel on the side wall is different from that on the front wall in that a large section of the side wall panel, below the collapsed mid-section, is intact although rotated inward at the top. This type of failure mode was probably a result of failing to install one of the masonry-to-timber nails in the right hand post at about the mid-height of the rotated section. The masonry above and below the collapsed portion sustained considerable cracking and spalling of the brick similar to that noted in the front wall panel.

Of the 48 bricks comprising the eight collapsed courses of brick in the 48-in. wide panel in the south side wall, half of the bricks fell on the interior floor slab of the structure and half on the exterior.

The only damage to the side wall timber framing was a vertical split in the post support to the left of the 48-in. wide panel. Although the post was still in place, the split extended from the outer face of the post just below the horizontal brace diagonally upward to the rear face of the tenon at the top of the post.

Roof System. As shown in Figure 40, the front roof system of Structure No. 2 sustained considerable damage. Of the 13 front rafters only the two end rafters adjacent to the north and south gable walls were not damaged. Above the cavity wall test cell five of the front rafters experienced typical flexural fractures near the center of their spans. Of the seven front rafters above the Fachwerk wall test cell, three had flexural fractures, and three had horizontal splitting, but did not fracture. Figure 47 shows an interior view of the damage to the front roof system for Structure No. 2. None of the rafters in the rear portion of the roof were damaged.

Figures 40 and 48 show the damage to the roof tile. Each half of the roof had 12 rows of 43 tiles for a total of 516 tiles. As shown in Figure 40, the front tile was damaged in all sections of the roof, but damage was



FIGURE 44 DAMAGED 48-IN. WIDE PANEL ON FRONT
FACHWERK WALL STRUCTURE NO. 2

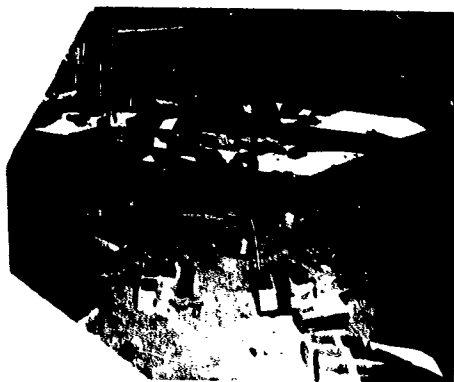


FIGURE 45 DISTRIBUTION OF BRICK DEBRIS FROM FRONT
FACHWERK WALL INTERIOR STRUCTURE NO. 2



FIGURE 46 DAMAGE TO SOUTH SIDE FACHWERK WALL STRUCTURE NO. 2

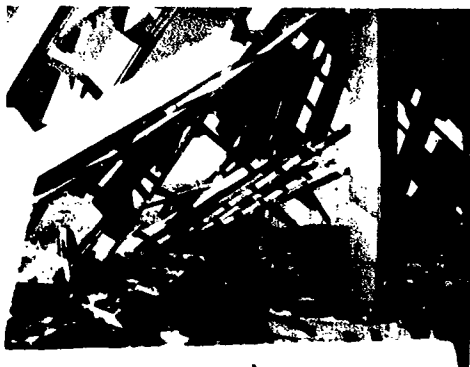


FIGURE 47 INTERIOR VIEW OF FRACTURED FRONT
ROOF RAFTERS STRUCTURE NO. 2

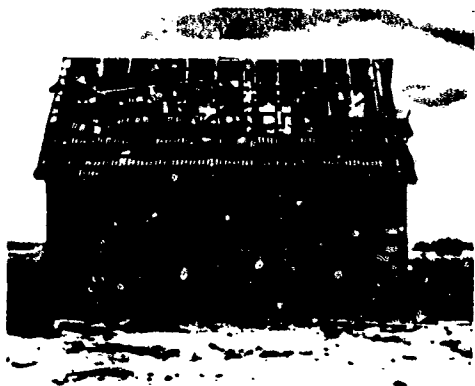


FIGURE 48 REAR VIEW OF DAMAGE TO ROOF TILE STRUCTURE NO. 2

concentrated in the lower courses. A total of 73 percent of the tiles were broken or missing from the front surface. As shown in Figure 48, on the rear half of the roof, in contrast to the front, there was much more damage to the tile on the upper portion of the roof than towards the bottom; in fact, the top three courses down from the ridge were completely destroyed. Although the overall tile damage appears less on the rear than on the front roof, 68 percent of the rear roof tiles were broken or missing.

Structure No. 3

Masonry Cavity Wall. There was only minor damage to the masonry cavity walls of Structure No. 3, shown in Figure 49. The only noticeable crack was a 1/32-in. wide horizontal crack in the brick mortar joint one brick down from the top of the west front cavity wall. All other cracks in the brick and CMU wythes were small or hairline.

Fachwerk Wall. Figure 49 shows the west front and south side Fachwerk walls. Although there was no noticeable damage to any of the Fachwerk timber framing in these walls, there was some cracking of the masonry. In the 48-in. wide panel on the west Fachwerk wall, there was a large crack in the brick masonry to the left of the window opening. As shown in Figure 50, the portion of the wall to the right of the diagonal cracking is displaced inward about 1/4 in. relative to the left portion. Also, the center portion of the masonry panel had about a 1/2-in. permanent inward deflection. Some of the other front wall masonry panels had minor cracks, but all were less than 1/64-in. wide.

The south side Fachwerk wall in Structure No. 3 was generally in good condition with only small or hairline cracks in some of the brick masonry.

Roof System. As shown in Figures 49 and 51 the roof system received only minor damage in Structure No. 3. Of the 13 rafters on the front of the roof, one of the rafters above the cavity test cell and three above the Fachwerk test cell experienced horizontal shear failures near mid-span. In addition, three rafters near the center of the structure lifted above the front roof plate about 3/4 in. There was no noticeable damage to any of the other roof framing members.

Figures 49 and 51 show the minor damage to the roof tile. Of the 516 tiles on the front roof surface, 20 percent were broken or missing. As noted previously for Structure No. 2, the tile damage for Structure No. 3 was also concentrated in the lower courses on the front roof and the upper courses on the rear roof.

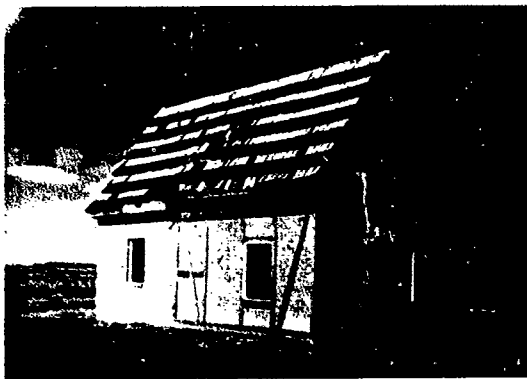


FIGURE 49 POST-SHOT VIEW OF STRUCTURE NO. 3

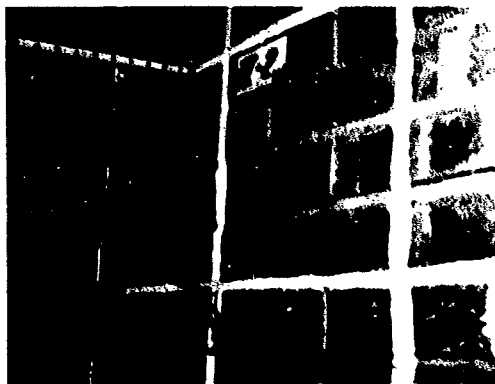


FIGURE 50 DAMAGED 48-IN. WIDE PANEL ON FRONT
FACHWERK WALL STRUCTURE NO. 3

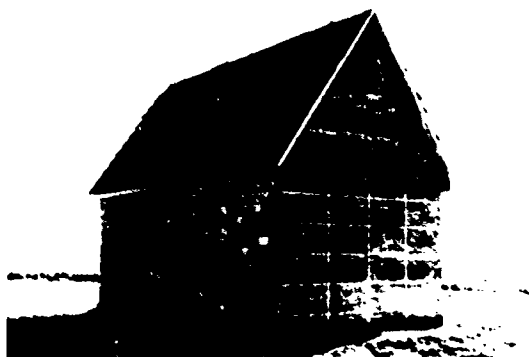


FIGURE 10. DAMAGE TO WEAVER TILE STRUCTURE NO. 3

Electronic Gage Data

For the purpose of measuring (a) air blast loading on test walls and (b) movement or response of these walls, each of the three structures was instrumented with eight pressure and three displacement gages. Two of the pressure gages were outside and the remainder inside the building. All displacement gages were attached to the inner surfaces of walls, one to each of the front and side masonry cavity test walls and one to a single panel of the front (west) Fachwerk wall (4-ft wide panel adjacent to window). Of the two outside pressure gages mounted at each structure one was a total head gage installed in the reinforced concrete pilaster in the front (west) wall facing ground zero; the second gage measured side-on overpressure at the ground surface just outside the north wall. The structure most remote from ground zero (Structure No. 3) contained two additional total head pressure gages in the concrete pilaster. The inside pressure gages measured side-on pressures in floors and ceilings.

All gage information was transferred by cable as FM signals to recording equipment in Instrumentation Park No. 3 approximately 5000 ft east of ground zero. Data reduction was begun by playback through a discriminator to a visicorder, the record from which was digitized on a Benson-Lehner 29E Telereader by an operator who aligned crosshairs on a magnified image of the visicorder trace. The same operator also read calibration steps which had been placed on a separate magnetic tape approximately one week before the detonation.

Simultaneously with the pressure and displacement data, timing information (in IRIG B format) was directly recorded on the magnetic data tape. From this signal absolute times of first response at each gage were read to half a ms. Times relative to the detonation were found from the reported time of detonation: 8 hours 0 minutes 0.048 seconds local time. A summary of the performance of and peak values recorded by the electronic gages is contained in Table 2. Most of the records are noisy, but only two failed to produce useable results.

Cameras

Although the difficult lighting conditions reduced the resolution of the pictures at all structures, only one camera failed to produce useable footage. The northwest camera at Structure No. 1 did not start. All other cameras provided acceptable coverage from the moment of detonation until the negative wind phase brought dust from immediately behind the structure forward to obscure the camera view. By that time the structural response was well defined. Because of the relatively short positive wind duration at the 7 psi free-field overpressure level, this obscuration allowed a shorter viewing time at Structure No. 1 than at the other two structures.

The approximately one millisecond interval between frames permits good temporal resolution of events. Clearly visible are shock arrival and passage over the structure, window breaking, inward deflection of both front and side Fachwerk walls and of front masonry cavity walls, downward

Table 2
ELECTRONIC CABLE RESULTS

Kind of Cable	Location	Structure No. 1		Structure No. 2		Structure No. 3	
		Peak	Comment	Peak	Comment	Peak	Comment
P6	1/4 ft. above the center	6.2 psi	3-step rise	3.2 psi	Mild ringing; 3-step rise	1.7 psi	
P6	1/4 ft. above under window	5.0 psi	3-step action	2.8 psi	Ringing; vortex action	1.5 psi	
D	1/4 ft. above wall	6.0 psi	3-step ends @ 22 ms with saturation	6.0 psi	Full range reached at 22 ms	3.7 psi	Never outward but oscillates about permanent deflection = 0.5 in.
P6	1/4 ft. rising over window	6.3 psi	Strong vortex action; ringing	2.9 psi	Ringing; vortex action	1.3 psi	
P7	1/4 ft. rising, center down	3.3 psi	Disturbed rise; strong ringing	1.8 psi	Ringing	1.1 psi	
P6	1/4 ft. rising, center up	7.3 psi	3-step rise; random noise	3.3 psi	Ringing	2.4 psi	
P6	1/4 ft. inside H wall	6.6 psi	Mark line structure in fiber	2.5 psi		1.3 psi	
P6	1/4 ft. outside H wall	6.7 psi	Secondary peak; permanent deflection @ 68 ms	3.7 psi	Secondary peak	1.8 psi	Secondary peak
D	1/4 ft. above wall	6.0 psi	Disturbed rise; no saturation; slow negative	6.8 psi	Permanent deflection 0.3 in.; never outward	.09 in.	Permanent deflection 0.03 in.; never outward
P	1/4 ft. above wall	6.1 psi	Permanent deflection -0.5 in.; strong oscillation	-0.4 in.	One cycle oscillation; no permanent deflection	.07 in.	Oscillation
P6	Pilaster middle	6.7 psi		7.4 psi		3.6 psi	
P7	Pilaster bottom	---		---		3.4 psi	Record ends @ 70 ms
P7	Pilaster top	---		---		3.3 psi	Record ends @ 65 ms

P6 = 80-ohm overpressure
P7 = 100-ohm overpressure
D = 100-ohm underpressure
P = 100-ohm pressure
C/W = 100-ohm cavity wall room

deflection of the front top plate at Structure No. 1, and stripping of roof tile. At Structure No. 1, the outward collapse of the Fachwerk side wall is just beginning when dust obscuration begins; the inward collapse of the front masonry cavity wall is also not completely visible. Unfortunately, the behavior of the north side cavity wall at Structure No. 1 is not seen at all because of the camera failure.

Deflection Gages

Every deflection gage provided useable information. Those at the front walls of Structure No. 1 quickly reached full range of 6 in. and were destroyed by the wall debris. The gage in the north masonry cavity wall of Structure No. 1 shows at least one cycle of unmistakable oscillation, first inward approximately $1\frac{5}{8}$ in., then outward approximately $2\frac{1}{4}$ in. with a period of approximately 300 ms; there is a permanent outward deflection of approximately $1\frac{1}{2}$ in. The portion of the north wall to which the deflection gage was attached at Structure No. 1 was still standing after the explosion (e.g., see Figure 25).

At Structure No. 2, maximum masonry cavity wall deflections were approximately $\frac{3}{4}$ in. and $\frac{1}{2}$ in. with a single oscillation and no permanent deflection in the north wall. The west front wall did not move outward at all, but stopped moving at 120 ms with a permanent inward deflection of approximately $\frac{1}{4}$ in. The Fachwerk wall panel deflected to full gage range of 6 in. approximately 33 ms after blast arrival.

The Fachwerk front wall at Structure No. 3 deflected inward to a maximum of approximately 3.7 in. in 60 ms, followed by weak oscillation around a permanent inward deflection of approximately $\frac{1}{2}$ in. Period of oscillation is approximately 120 ms. Deflection of the front masonry cavity wall was approximately 0.10 in. peak and 0.02 in. permanent inward. A weak oscillation, amplitude less than 0.1 in. peak, was detected in the record of the north masonry cavity wall at Structure No. 3.

Deflection gage records from Structure No. 2 are reproduced in Figure 52. Zero time corresponds to blast arrival at the west wall.

Total Pressure Gages

All pilaster gages show a seemingly instantaneous jump in pressure followed by a more gradual rise to a maximum some 5 ms later. At Structure No. 1, the initial step is approximately 14.8 psi while the peak is near 16.4 psi. At Structure No. 2, the corresponding pressures are approximately 5.1 and 7.3 psi and at Structure No. 3, 2.8 and 3.6 psi. Clearing of reflected pressure approximately 20 ms after shock arrival is seen at all structures.

The two additional pilaster gages at Structure No. 3 recorded significantly lower peak pressures, i.e., 3.4 and 3.5 psi, than did the central gage and both records go to zero after some 70 ms.

Pilaster gage results for Structure No. 2 are shown in Figure 53.

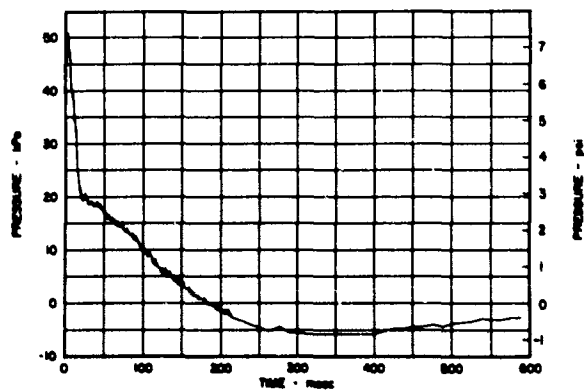


FIGURE 53 TOTAL PRESSURE VERSUS TIME, PILASTER STRUCTURE NO. 2

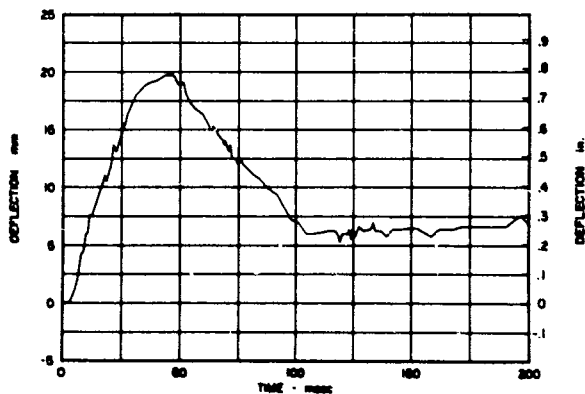


FIGURE 52a DEFLECTION VERSUS TIME, WEST FRONT
MASONRY CAVITY WALL STRUCTURE NO. 2

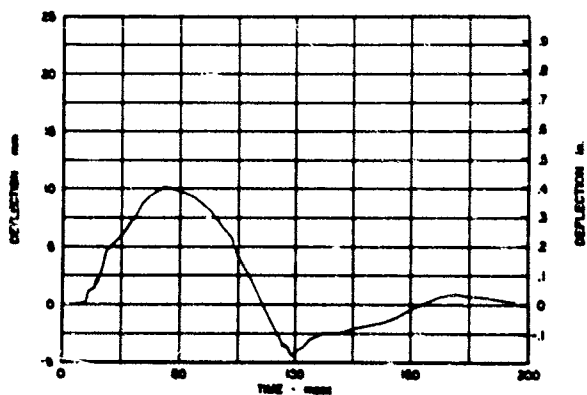


FIGURE 52b DEFLECTION VERSUS TIME, NORTH SIDE
MASONRY CAVITY WALL STRUCTURE NO. 2

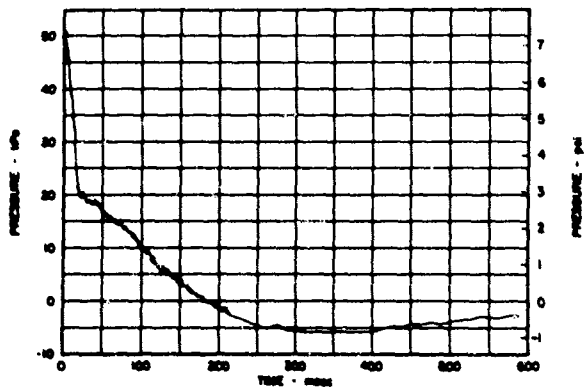


FIGURE 53 TOTAL PRESSURE VERSUS TIME, PILASTER STRUCTURE NO. 2

Side-On Pressure Gages

The ground level gages just outside the north walls all showed an initial step. Unlike the total pressure at the pilaster, this outside side-on pressure showed no significant rise following the discontinuity.

At this time, no attempt has been made to infer shock speed by measuring the time interval between shock arrival at the front wall and at the gage outside the north wall.

All outside side-on pressure gages show a secondary shock arrival approximately 18 ms behind the main shock. The secondary shock, including an accompanying pressure decline, interrupts the normal free-field pressure decay behind the main shock. Normal positive phase pressure is recovered after 30 to 50 ms.

A record from the outside north wall side-on gage at Structure No. 2 is shown in Figure 54. Zero time is shock arrival at the pilaster gage of the same structure.

The interior pressure gages, all installed flush with horizontal surfaces, showed a generally gradual build-up of pressure followed by a decline and negative pressure phase patterned after what is seen in free-field records. Gages inside the Fachwerk room all recorded maximum pressures close to free-field values reached after a 50 to 60 ms rise time. In the masonry cavity wall room maximum pressures were approximately 20 percent lower than in the adjacent Fachwerk room, but rise times were quite similar. Records show some pressure fluctuations which have not been studied yet. In particular, a decline interrupting pressure build-up at the two gages in each structure near windows appears to be associated with vortex formation at the window edge. There is a gradual intensification of this effect when comparing the pressure record from Structure No. 3, where it is weak, to Structure No. 1, where it is strong. Relatively large irregularities in the rising interior pressures at the two interior gages remote from windows of Structure No. 1 are seen also; these irregularities appear much weaker in the other two structures.

The differential pressures across the midpoint of the ceiling slabs show downward pressure approximately twice the upward at all structures.

Pressure traces from the interior gages at Structure No. 2 appear in Figure 55. Zero time in all figures corresponds to shock arrival at the pilaster gage.

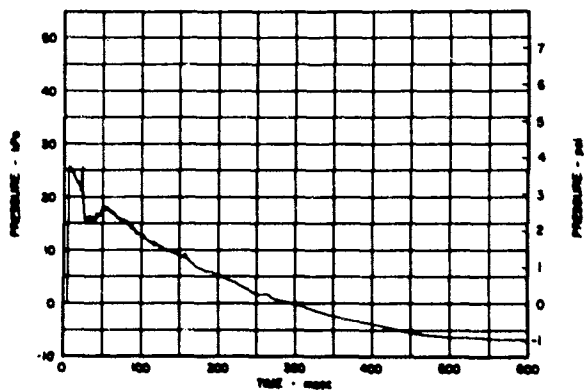


FIGURE 54 PRESSURE VERSUS TIME, OUTSIDE NORTH
SIDE WALL STRUCTURE NO. 2

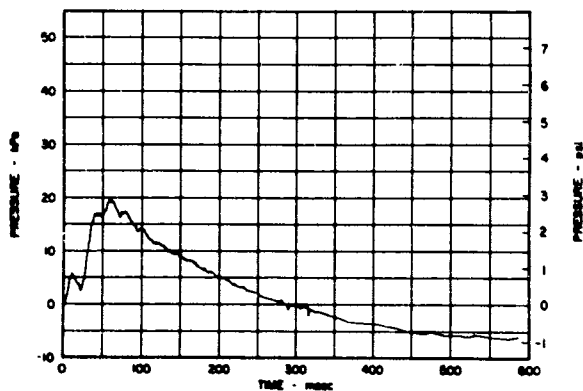


FIGURE 55a PRESSURE VERSUS TIME, FACHWERK ROOM BELOW WINDOW STRUCTURE NO. 2

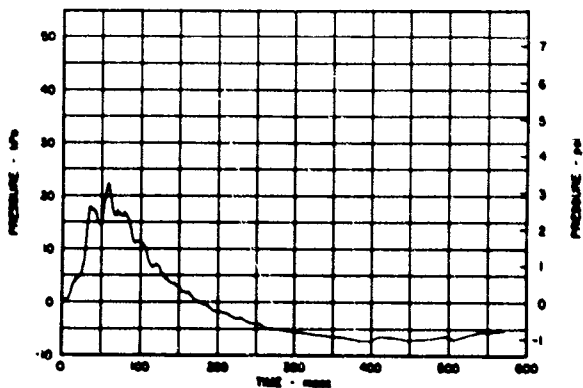


FIGURE 55b PRESSURE VERSUS TIME, FACHWERK ROOM NORTHWEST CORNER STRUCTURE NO. 2

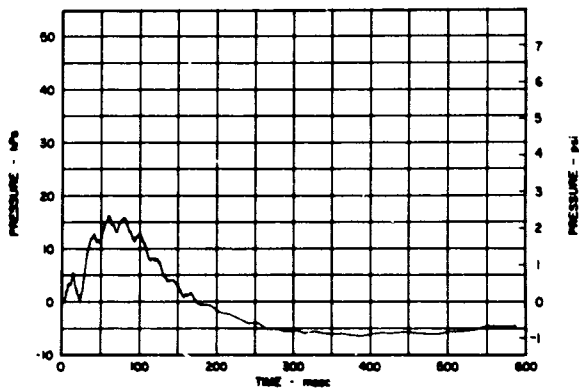


FIGURE 55c PRESSURE VERSUS TIME, MASONRY CAVITY WALL ROOM ABOVE WINDOW STRUCTURE NO. 2

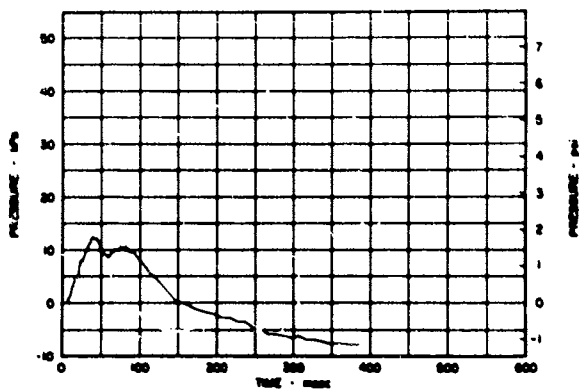


FIGURE 55d PRESSURE VERSUS TIME, MASONRY CAVITY WALL ROOM CENTER OF CEILING STRUCTURE NO. 2

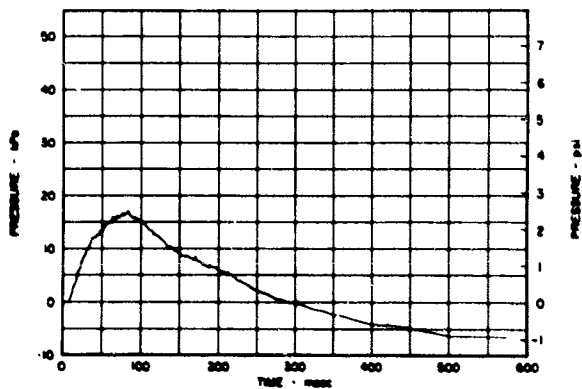


FIGURE 55e PRESSURE VERSUS TIME, MASONRY CAVITY WALL ROOM, BESIDE NORTH WALL STRUCTURE NO. 2

REFERENCES

1. SRI Progress Report to Defense Nuclear Agency, February 20, 1976.
2. Hermann J. W. Zillgens, A.I.A., Architect, San Diego, CA.
3. Mittag, Martin, Baukonstruktionslehre, C. Bertelsmann Verlag/Gütersloh, 1958.
4. Hart, Franz, Baukonstruktion für Architekten, Julius Hoffman Verlag/Stuttgart, 1950.
5. Ebinghaus, Hugo, Der Hochbau, Fachbuchverlag Dr. Pfanneberg & Co./Giessen, 1958.
6. SRI Drawings 4269-1, -A1, -A2, and -A3, and Specification for "Masonry Cavity Wall and Half Timber Wall Test Structures," for DICE THROW, June 10, 1976.
7. "Airblast Predictions for DICE THROW," Ballistics Research Laboratory, enclosure to FCTNOT letter of 9 March 1976 from Captain T. V. Edwards, USAF, Technical Director, DICE THROW.
8. Wiehle, C. K., and J. L. Bockholt, "Existing Structures Evaluation, Part IV: Two-Way Action Walls," (for Office of Civil Defense), Stanford Research Institute, Menlo Park, California (September 1970).
9. SRI Progress Report to Defense Nuclear Agency, September 20, 1976.

31. TEST SUMMARY - NBDS OPTICAL MEASUREMENTS

by

M. Oberst

Sandia Laboratory Albuquerque

TEST SUMMARY - NBDS OPTICAL MEASUREMENTS

BACKGROUND AND OBJECTIVES

A Nuclear Burst Detection System (NBDS) sensor station and central processing console (CPC) were fielded at Dice Throw. The objective of the experiment was to utilize NBDS equipment to measure the azimuth and time history of an optical event and thereby demonstrate capabilities of the NBDS. The equipment used consisted of a tripod mounted sensor station, a prototype junction box, a hand held display, hard wired communications, van mounted CPC and a motor-generator set. The equipment was located at WEAP site, 13,280 feet from ground zero.

In order to accomplish the stated measurements, certain modifications were required to prevent system rejection of the event as non-nuclear and to allow full-time history recording. The sensor station changes involved elimination of the EMP coincidence requirement and modification of software to transmit the time history of any optical trigger received. The CPC software was modified to allow receipt and printing of time history messages and to provide the capability of a quick-look data plot. Elimination of the EMP coincidence discriminant introduced a problem of false triggers whenever the sun entered the field-of-view (FOV) of the sensor station. This, together with the 8:00 AM shot time necessitated the use of a sun shade. A 4 x 5 foot sheet of masonite was erected on a portable tower approximately 33 feet from the sensor station. The center of the shade was located at 103° true azimuth (EAST from NORTH) and 10° elevation such that it blocked the sun for a sufficient period around shot time to allow the optical measurement to be made.

TIME HISTORY MEASUREMENT

Attachment 1 and 2 show the Dice Throw data as printed out and plotted by the CPC. The amplitude is by level detector (LD) value and time is by sample number. Since both scales are only quasi-logarithmic, one simple conversion factor does not apply. However, when point by point conversions are applied, the time history as shown in attachment 3 results. For comparison purposes, attachment 4 is a plot of data taken at Dice Throw with an older style instrument (not saturation) and attachment 5 is a plot of data taken with an instrument fielded at WEAP site as part of a USAFTAC experiment. All three plots (attachments 3 through 5) compare favorably.

AZIMUTH MEASUREMENT

Attachment 6 shows a top view of one of the NBDS sensor station azimuth detectors. The azimuth is measured as the ratio of light received by the azimuth channel to that received by a reference channel. The ratio, encoded as a number between zero and 1023, is a measure of the angle from the channel ambiguity. The ambiguity was set for Dice Throw at 9° south of due west. The true azimuth (EAST from NORTH) of Dice Throw was 55° placing it at a NBDS azimuth of 206°. Since NBDS sensor stations are designed to receive scattered light (FOV +4° to +10°), a correction factor is computed and applied at the CPC. This correction of 12° indicates an expected azimuth reading of 194° (NBDS) or 552 counts. A look at the bottom of attachment 1 shows the actual azimuth reading obtained was 731 counts* or 257° (NBDS). The indicated azimuth error is 257° minus 194° equals 63°. Attachment 6 diagrams and summarizes the various angles.

A post-shot analysis of the NBDS sensor station azimuth capability revealed a sensitivity to light at vertical angles below 4° which was previously considered negligible. At the close range of Dice Throw, the direct light component received at these low vertical angles becomes comparable to the scattered component received from the intended FOV. This direct component tends to shift the measured azimuth toward higher ratios and is sufficient to account for the Dice Throw azimuth error. Unfortunately, the sensitivity of the calculations to certain measured values is such that an exact direct light correction cannot be achieved. Dice Throw, therefore, does not permit a good estimate of NBDS sensor station optical azimuth accuracy.

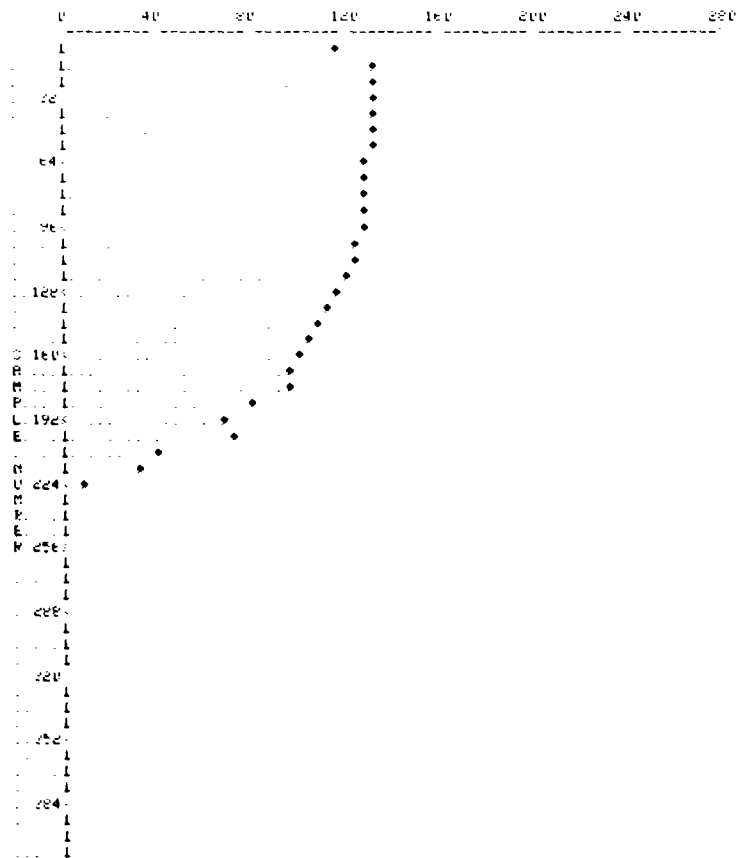
SUMMARY

The operation of the NBDS sensor station, hand-held display, junction box, CPC and the associated algorithms developed for Dice Throw performed as expected. The objective of measuring optical time history was accomplished. The objective of measuring sensor azimuthal accuracy could not be determined. Unexpected results were obtained due to the sensor sensitivity to the direct light component at vertical angles less than 4°.

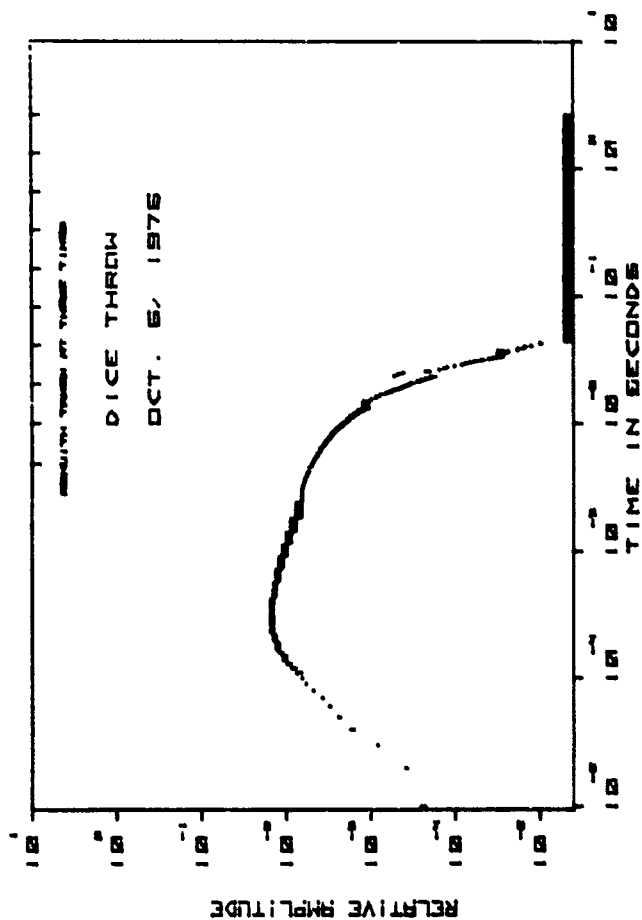
*This azimuth is selected from the 12 obtained since it was based upon the highest amplitude signal.

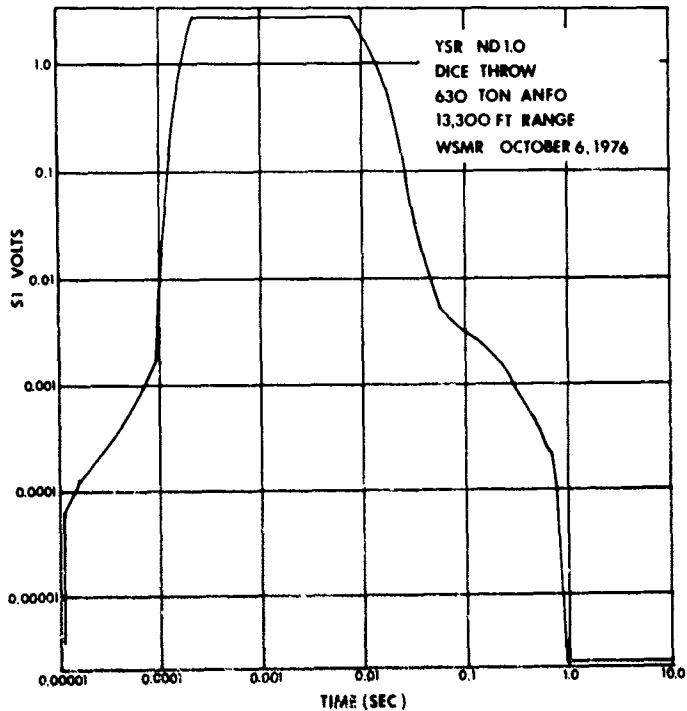
PL

DECIMAL LEVEL

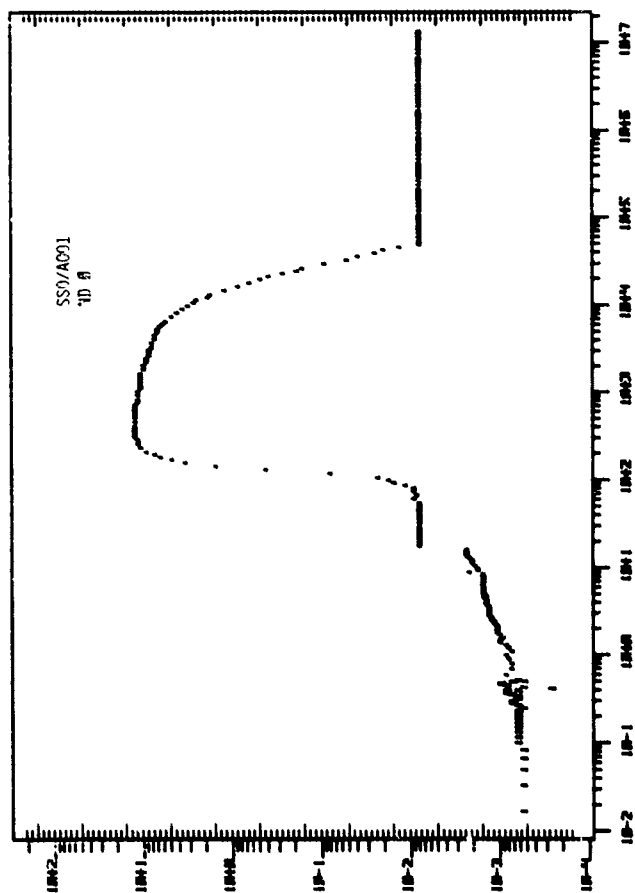


Attachment 2





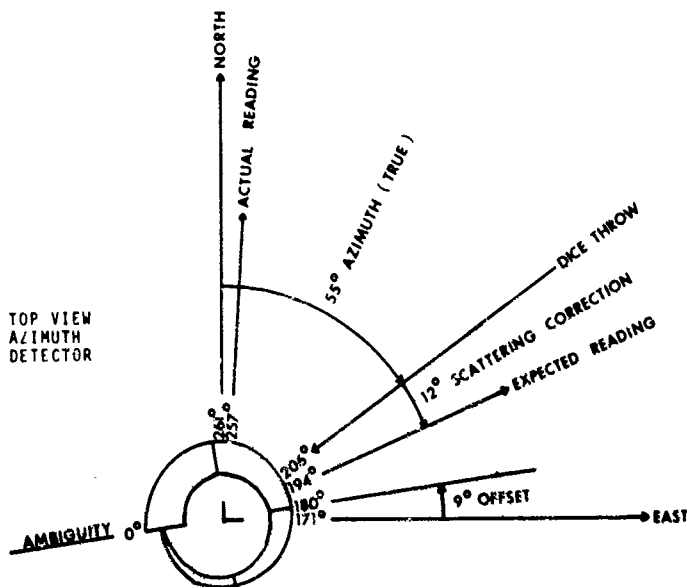
Attachment 4



Attachment 5

AZIMUTH RELATIONSHIPS

DICE THROW



	RATIO	READING	ANGLE FROM AMBIGUITY	ANGLE FROM NORTH
DUE NORTH	.73	742	261°	0°
ACTUAL READING	.71	731	257°	4°
TRUE DICE THROW	.57	689	206°	55°
EXPECTED READING	.54	552	194°	67°
	.50	512	180°	81°
	.48	486	171°	90°
DUE EAST			0°	261°
SYSTEM AMBIGUITY	0 or 1	0 or 1023		

TEST SUMMARY - NBDS/MAST ASSEMBLY

OBJECTIVE

The purpose of this experiment was to demonstrate structural capability of the NBDS/mast system exposed to a blast environment. Nuclear blast survivability is a part of the NBDS design criteria and Dice Throw provided the best opportunity for evaluating this requirement.

ANALYSIS

Pretest analysis of the NBDS/mast system indicated several problem areas. The analysis was performed with the use of the SHELL-SHOCK computer code. This is a SLA in-house code used for predicting the response of structures to dynamic loads. The code can combine a variety of springs, masses, and shell and solid elements. The mast was divided into 50 shell elements, the NBDS package into 11 masses, and the effect of the guy wires were simulated by linear springs.

The suspected problem areas were the high loads in the guy wires, unsupported mast length, the joint at the base of package, and the optical base.

Early calculations indicated that the three guy wire systems showed excessively high loads in the cables and also an unsupported length of 20' brought the tube close to yielding. We, therefore, recommended a four guy system. The four guy system still indicated high loads in the 1/8" cables and larger diameter cables appeared to be desirable. We were attempting to provide a non-yielding cable system, in order to assure vertical alignment. This meant installing larger ground anchors and cables. The top cables were 5/16" diameter and the others were 1/4" diameter. The intended design should have provided the desired characteristics, except the cable clamps did not perform anywhere near the capacity of the cables. Two cables failed prematurely because of large slippage in the cable clamps. In fact, nearly all the cables showed clamp slippage.

The dynamic analysis also indicated a whipping effect of the NBDS package. A very high moment is induced at the joint and the base plate was modified to sustain this load. Although no fractures were predicted, the yielding would be substantial to cause misalignment of the NBDS package.

The last area of concern was the optical base. The base was made of a laminated glass-phenolic and this type of

material usually exhibits a large coefficient of variation (10 value). Although failure was not predicted, we did want to establish this design for a blast environment.

TEST RESULTS

The results of the experiment show we met our intended objectives. The NBDS base plate and optical support survived the blast environment. Preliminary pressure traces indicate that predicted overpressure (5 psi) was achieved. No instrumentation was installed in this experiment. Camera coverage was provided.

The camera was located about 80' from the mast centerline and provided a field of view of almost the entire mast and cables (See Figure 1). The films showed blast arrival time at 660 msec and the predicted time was 660 msec. (Further times are referenced to structural response times and $t = 0$ is at shock arrival.) The mast centerline shows about 5" lateral displacement at 10 msec. Other displacements were too small for resolution up to 80 msec. At this time, a forward guy broke at the #3 level and freed the upper center portion of the mast. A peak displacement occurred at 160-175 msec and was on the order of 26".

The actual displacement was probably larger than this since there is a degree of freedom away from the camera. Also, during this time the actual dynamic pressure is very low ($\sim .25$ psi). The positive phase duration of the overpressure lasted for 315 msec compared to a predicted 291 msec.

The tower itself did not fail or yield. In the post-test configuration, the tower was leaning forward because of the weight of the heavier cables. When the broken cables were returned to the anchors, the mast returned to its pre-test configuration. If the cables had been standard issue, we suspect the tower would return to the vertical position.

It was noted, that similar communication masts in another test area all showed cable yielding or stretching as well as ground anchor displacements 2-3 inches. Because the cables were light-weight, most of the towers righted themselves. It would appear that the stronger cable system is not needed and we recommend that the standard 1/8" cables be continued as the most desirable design.

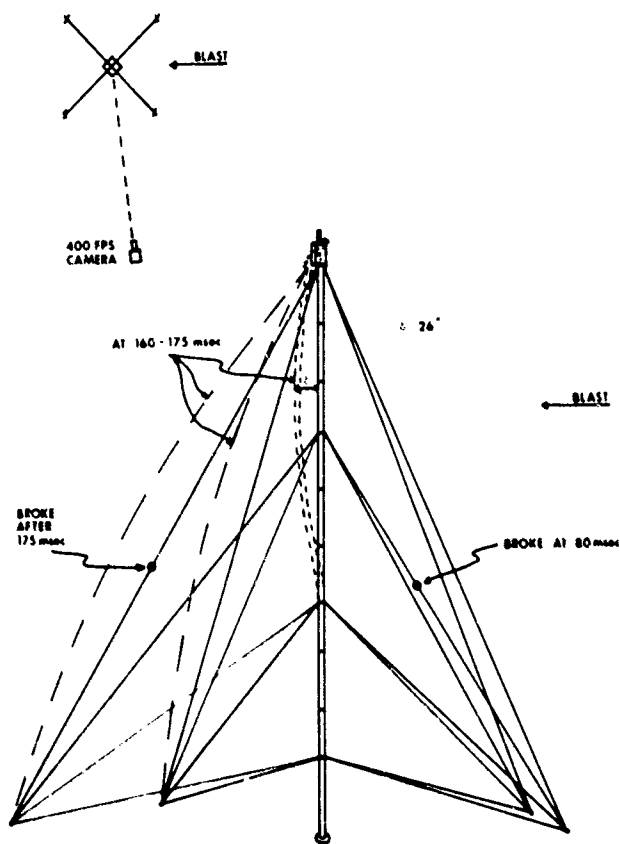


FIGURE 1. DICE THROW - NBDS/MAS: CONFIGURATION

**32. RESULTS OF THE SPECIAL FORCES
COMMUNICATIONS EXPERIMENT
AT THE DICE THROW MAIN EVENT**

by

**Capt. Alexander F. Wojcicki
SOC, USAOCCS**

INTRODUCTION

DICE THROW offered a unique opportunity to gain experimental data on the operational characteristics of Special Forces-peculiar radio sets in desert and nuclear blast environments. Additionally, quantitative data on g-loading to failure of certain critical radio components was desired; experience had indicated that the AN/PRC-74B was more prone to failure than the AN/GRC-109 during the conduct of parachute operations.

OBJECTIVES

Overall objectives of the experiment were:

1. To evaluate Special Forces communications techniques in a desert environment.
2. To evaluate the response of low-powered amplitude-modulated (AM) radio sets and associated antennas and power supplies to air blast and shock at low overpressures (1.0 psi predicted).
3. To evaluate shock response of critical components at selected higher overpressures.

CONDUCT AND RESULTS OF THE LOW OVERPRESSURE EXPERIMENT

1. At the low overpressure site, a variety of antenna/radio combinations were evaluated using authorized frequencies in the 2,000 to 15,000 MHz range. Termination point for all radio traffic was the 7th Special Forces Group Operational Base at Fort Bragg, North Carolina. Two contact a day were planned, with continuous operation from T-120 minutes to T-45 minutes and from T-.75 minutes to T+60 minutes. The following antennas and radios were tested:

- a. Antennas: $\frac{1}{4}$ -wave di-pole, inverted 'L', inverted 'V', slant wire, and multiple wave long wire.
- b. AN/GRC-109, G43 generator, manual morse (CW) mode.
- c. AN/GRC-109, G43 generator, AN/GRA-71 burst code device mode.
- d. AN/GRC-109, .125 kW generator, manual CW mode.
- e. AN/GRC-109, .125 kW generator, AN/GRA-71 burst code device mode.
- f. AN/PRC-74B, BA-4386, manual morse mode.
- g. AN/PRC-74B, BA-4386, AN/GRA-71 burst code device mode.

2. Data to be obtained included: determination of most effective system, measurement of dB degradation of signal transmitted through the burst cloud,

measurement of gross deformation of antenna masts or breakage of antennas, detection of visible damage to radio sets, and determination of GO/NO GO condition of each radio and antenna.

3. Radio operators were on site at the time of detonation to transmit message traffic immediately after detonation and to evaluate the systems. Seventeen personnel, including control and safety personnel, were on the test bed at time of detonation. Permission for personnel to remain on-site was obtained from the Test Group Director, once written approval from The Office of the Surgeon General was granted.

4. Results:

a. Actual overpressures at the experiment site were 1.3-1.5 psi for exposed personnel and equipment, rather than the 1.0 psi predicted. Overpressure values are taken from RRL gauge line -1 at 1522 m/5000 ft.

b. Communications circuits between the test bed and the Special Forces Operational Base were not established during the experiment period. It is believed that the cause was low frequency propagation probabilities for the assigned frequencies at the time of detonation.

c. No damage to any portion of the antenna array, to any of the radio components, or to any of the power supplies was noted after detonation.

d. No injuries of any kind occurred among personnel on-site. No one noticed a sensation of ringing in the ears after detonation (all personnel wore over-the-ear hearing protectors.)

CONDUCT AND RESULTS OF THE HIGH OVERPRESSURE EXPERIMENT

1. The high overpressure phase of the experiment was conducted by BRL in the C³ area. One AN/PRC-74B and one T-784 transmitter (AN/GRC-109) were placed on ground at the 7.3 psi predicted overpressure level; one T-784 transmitter at the 5.0 psi predicted level; and one AN/PRC-74B at the 3.0 psi predicted level. It was believed that the equipment at the 7.3 psi level would fail, thereby providing a proven 'gate', or overpressure/g-load-ing factor above and below failure. Instrumentation included wired accelerometers attached at the longitudinal plane center of mass. Accelerometers were uni-axial, and oriented horizontally, perpendicular to the plane tangent to the incident shock wave.

2. Results:

a. Overpressure levels were less than predicted. None of the radios suffered visible damage and all were operational post-detonation. Consequently, only those components at the highest overpressure levels were analyzed.

b. AN/PRC-74B (did not fail)

- (1) Static overpressure..... 6.0 psi
- (2) Dynamic overpressure..... .98 psi
- (3) System mass/surface area exposed..... .01 kg/cm²
- (4) Translation distance..... 63.5 in
- (5) Maximum delta-g..... 84.0 g
- (6) Maximum delta-g/delta-t..... 655/.45 (g/ms)

c. T-784

- (1) Static overpressure..... 6.0 psi
- (2) Dynamic overpressure..... .98 psi
- (3) System mass/surface area exposed..... .13 kg/cm²
- (4) Maximum delta-g..... 386 g
- (5) Maximum delta-g/delta-t..... 386/.50 (g/ms)

CONCLUSIONS

1. Effective communications in a desert environment are difficult to attain with the AN/PRC-74B and AN/GRC-109 radio sets.

2. Present generation Special Forces communications equipment is able to withstand air blast and shock at a level of 1.5 psi without damage. Critical components can withstand 6.0 psi without damage.

3. At a given overpressure level, the AN/PRC-74B exhibits a much greater shock response than the T-784 transmitter.

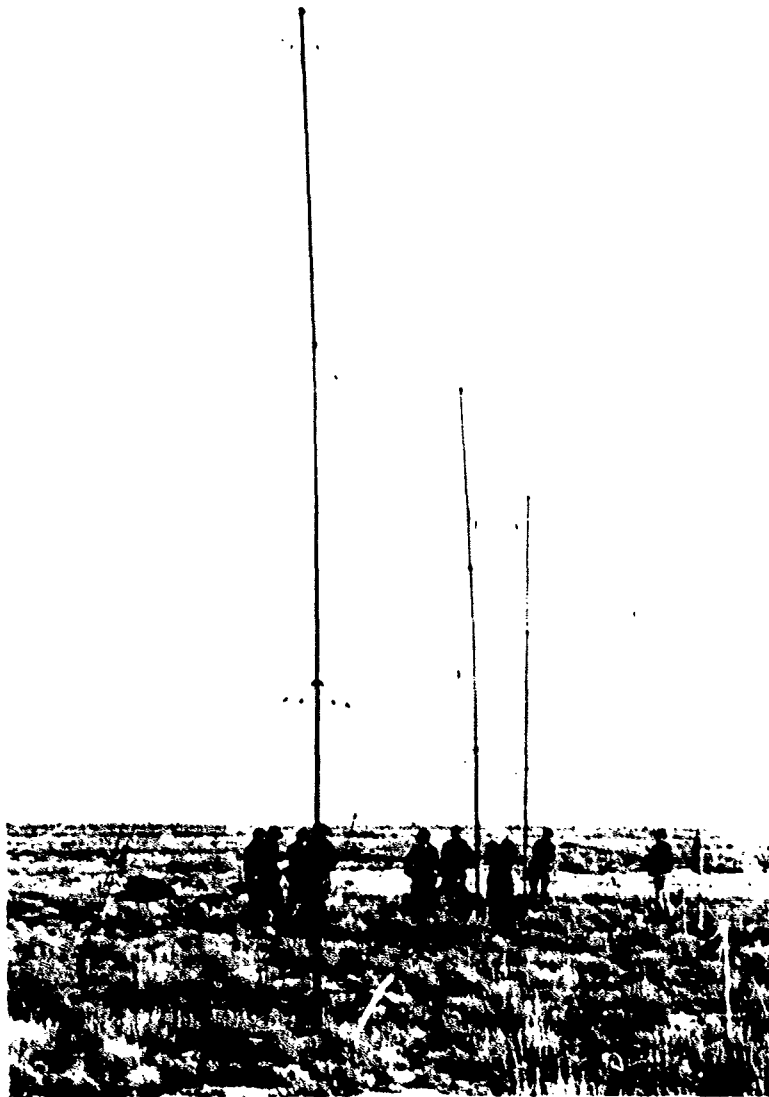


Figure 1. Post detonation view of 1.5 psi experiment site.



Figure 2. Post-detonation operation of AN/PRC-74B radio set with AN/GRA-71 burst code device.

33. CRATER AND EJECTA ENHANCEMENT STUDIES

by

R.W. Henny

Air Force Weapons Laboratory

and

G.D. Jones

Civil Engineering Research Facility

To be published as FOR 696

DISTRIBUTION LIST

DEPARTMENT OF DEFENSE

Director
 Defense Advanced Research Project Agency
 ATTN: Strategic Tech. Office
 ATTN: NMRO
 ATTN: Technical Library

Director
 Defense Communications Agency
 ATTN: NMCSSC Code 510

Defense Documentation Center
 Cameron Station
 12 cyATTN: TC

Director
 Defense Intelligence Agency
 ATTN: DT-1C Nuc Eng Branch
 ATTN: DT-2 Wpns & Sys Div
 ATTN: DI-7D

Director
 Defense Nuclear Agency
 ATTN: DDST
 ATTN: TISI Archives
 3 cy ATTN: TITL Technical Library
 ATTN: STSP
 ATTN: SPAS
 ATTN: Maj. William A. Alter
 ATTN: Maj. E. Neal Gunby
 ATTN: Tom Kennedy
 ATTN: Maj. Edmund Mueller
 ATTN: LTC Edwin T. Still
 ATTN: SPSS
 ATTN: SPTD

Director
 Defense Research & Engineering
 ATTN: SGSS (OS)
 ATTN: AD/ET J. Persh

Commander
 Field Command
 Defense Nuclear Agency
 ATTN: FCTMD
 ATTN: FCTMOT
 ATTN: FCTMOF
 ATTN: FCPR
 ATTN: FCT
 ATTN: Capt. V.A. Alvarez
 ATTN: Capt. R.G. DeRaad
 ATTN: Noel Gantick
 ATTN: Lt. C. Klimmek
 ATTN: LCDR J.D. Strode
 ATTN: Maj. J.F. Bestgen

Director
 Joint Strat Lgt Planning Staff JCS
 ATTN: JLPW-2
 ATTN: JPTM
 ATTN: JPTP

Chief
 Livermore Division Field Command DNA
 Lawrence Livermore Laboratory
 ATTN: FCPRL

Explosive Safety Board
 ATTN: Dr. Thomas Zaker

The Pentagon
 ATTN: J-5 Plans & Pol Planning & Prgm Div
 ATTN: J-5 Plans & Policy Nuc Div

Studies Analysis and Gaming Agency
 Joint Chiefs of Staff
 ATTN: SDEB

Director
 Defense Civil Preparedness Agency
 ATTN: Michael A. Pachuta

Director
 National Security Agency
 ATTN: Edward Butala (MS11)
 ATTN: William DeBoy (MS11)

Commander
 902 Military Intelligence Group
 ATTN: Col. Hassel L. Parker

DEPARTMENT OF THE ARMY

Director
 PMO Advanced Tech Center
 ATTN: ATC-T Melvin T. Capps
 ATTN: Marcus Whitfield

Program Manager
 BMD Program Office
 ATTN: DACS-BMT John Shea
 ATTN: DACS-BM2
 ATTN: DACS-BM2-D Julian Davidson
 ATTN: DACS-BMT Clifford E. McLain

Commander
 BMD System Command
 ATTN: BDMSC-TEN Noah J. Hurst

Deputy Chief of Staff for Resch Dev & Acq
 Department of the Army
 ATTN: Technical Library

DEPARTMENT OF THE ARMY, continued

Deputy Chief of Staff for Operations & Plans
Department of the Army
ATTN: Director of Nuclear Plans & Policy

Commander
U.S. Army Electronics Command
ATTN: Robert Frieberg

Commander
SOL USAOCCS
ATTN: Capt. Alexander L. Wojcicki

Commander
Harry Diamond Laboratories
ATTN: DRXDO-RBH James H. Gwaltney
ATTN: DRXDO-TF Robert B. Oswald, Jr.
ATTN: DRXDO-TI, Technical Library
ATTN: DRXDO-NP
ATTN: L. Belliveau
ATTN: W. Vault

Commander
Picatinny Arsenal
ATTN: Al Loeb
ATTN: SARPA-ND-C-T Donald Miller
ATTN: SARPA-FR-E Louis Avrami
ATTN: SMUPA-MD Henry Opat

Director
TRASANA
ATTN: R.E. Dekinder, Jr.

Commander
White Sands Missile Range
ATTN: Richard Dysart
ATTN: Dale W. Green

Director
U.S. Army Ballistic Research Labs
ATTN: J.H. Keefer, DRDAR-BLE
ATTN: DRXBR-X, Julius J. Meszaros
ATTN: DRXRD-BVL, William J. Schuman, Jr.
ATTN: Richard Vitali
ATTN: DRXBR-TB, J.T. Frasier
ATTN: Robert E. Eichelberger
ATTN: Technical Library, Edward Baicy
ATTN: W.D. Allison
ATTN: N. Ethridge
ATTN: Col. R. Gomez
ATTN: A. Gupta
ATTN: J. Jacobson
ATTN: V. King
ATTN: C. Kingery
ATTN: R. Mayerhofer
ATTN: R. Pearson
ATTN: R.L. Peterson
ATTN: E. Quigley
ATTN: R.J. Raley
ATTN: R.E. Reisler
ATTN: E. Roecker
ATTN: D.L. Rigotti
ATTN: R. Schumacher
ATTN: R. Shelton
ATTN: J. Sullivan
ATTN: W. Taylor
ATTN: G. Teel
ATTN: G. Watson
ATTN: M. Wiherle

Director
U.S. Army Engineer Waterways Experiment Station
ATTN: Technical Library
ATTN: James Ballard
ATTN: Jimmy P. Balsara
ATTN: William Flathau
ATTN: William L. Huff
ATTN: Adam A. Rula
ATTN: James Watt
ATTN: LTC Ronald R. Kaufmann

Commander
U.S. Army Materiel & Mechanics Research Center
ATTN: DRXMR-IHI, John F. Dignam

Commander
U.S. Army Materiel Development & Readiness CMD
ATTN: DRXDE-D, Lawrence Flynn
ATTN: Technical Library

Commander
U.S. Army Missile Command
ATTN: DRSMI-XS, Chief Scientist
ATTN: DRS-RKP, W.B. Thomas
ATTN: DRSMI-RRR, Bud Gibson

Commander
U.S. Army Nuclear Agency
ATTN: MONA-SA
ATTN: MONA-WE
ATTN: CDC-NVA
ATTN: ATCA-NAW
ATTN: Maj. John Uecke
ATTN: Maj. Alan Lind

U.S. Army Satellite Communications Agency
ATTN: Eugene Caulfield

Commander
U.S. Army Armament R&D Command
ATTN: Alvin Flugel (DRDAR-LCW)
ATTN: Martin A. Ravotto (DRDAR-LCS-W)
ATTN: Daniel Waxler (DRDAR-LCS-W)

DEPARTMENT OF THE NAVY

Chief of Naval Material
ATTN: MAT 0323, Irving Jaffe

Chief of Naval Operations
ATTN: Code 604C3, Robert Piacesi
ATTN: Code 604C4, Robert A. Blaise
ATTN: OP 62
ATTN: OP 981

Chief of Naval Research
ATTN: Technical Library

Director
Naval Research Laboratory
ATTN: Code 2600, Technical Library
ATTN: Code 7770, Gerald Cooperstein
ATTN: Code 5180, Mario A. Persechino

Commander
Naval Sea Systems Command
ATTN: 0333A, Marlin A. Kinna

DEPARTMENT OF THE NAVY, continued

Officer-in-Charge
Civil Engineering Laboratory
Naval Construction Battalion
ATTN: Technical Library

Officer-in-Charge
Naval Surface Weapons Center
ATTN: Code WA07, Carson Lyons
ATTN: Code WR10, Joseph Petes
ATTN: Code WA501 Navy Nuclear Programs Office
ATTN: Michael Swisdak
ATTN: Phillip Peckham

Commanding Officer
Naval Weapons Evaluation Facility
ATTN: Lawrence R. Oliver
ATTN: Peter Hughes
ATTN: Rudolf Friedberg

Director
Strategic Systems Project Office
ATTN: NSP-272

Commander
Naval Facilities Engineering Command Headquarters
ATTN: Technical Library

Naval Sea Support Center
Fleet Support Office
ATTN: LCDR E.W. Edgerton

DEPARTMENT OF THE AIR FORCE

Commandant
AF Flight Dynamics Laboratory, AFSC
ATTN: FXG

AF Geophysics Laboratory, AFSC
ATTN: Chan Touart

AF Materials Laboratory, AFSC
ATTN: LPH Gordon Griffith
ATTN: MBE George E. Schmitt
ATTN: MBE Donald L. Schmidt
ATTN: MAS
ATTN: T. Nicholas
ATTN: LTM

AF Rocket Propulsion Laboratory, AFSC
ATTN: RTSN G.A. Beale

AF Weapons Laboratory, AFSC
ATTN: DYS
ATTN: Al Sharp
ATTN: SAB
ATTN: DYT
ATTN: DYV
ATTN: Dr. Ninge
ATTN: SUL
ATTN: Lt. Joel C. Bradshaw
ATTN: Susan Check
ATTN: Steve Melzer
ATTN: Charles Needham
ATTN: Maynard A. Plamondon
ATTN: LTC James Warren
ATTN: Harry Webster
ATTN: NTO
ATTN: Technical Review

Air Force Institute of Technology, AFIT
ATTN: Library, AFIT

Headquarters
Air Force Systems Command
ATTN: XRT0
ATTN: SOSS

Commander
Arnold Engineering Development Center
ATTN: AOA

Commander
ASD
Key ATTN: EWES D. Ward

Commander
Foreign Technology Division, AFSC
ATTN: TOPTN
ATTN: PDBG
ATTN: TDFBD, J.D. Pumphrey

HQ USAF/RD
ATTN: RDQSM
ATTN: RD
ATTN: RDQ
ATTN: RDPM

HQ USAF/XO
ATTN: XOSS

SAMSO/DY
ATTN: DYS

SAMSO/MN
ATTN: MNH
ATTN: MNH
ATTN: Capt. Thomas Edwards

SAMSO/RS
ATTN: RST
ATTN: RSS
ATTN: RSSE

Commander in Chief
Strategic Air Command
ATTN: XOBM
ATTN: XPQM
ATTN: Maj. Ronald W. Bashant
ATTN: XPFS
ATTN: DOXT

U.S. ENERGY RESEARCH & DEVELOPMENT ADMINISTRATION

Division of Military Application
ATTN: Doc. Con. for Res. & Dev. Branch

University of California
Lawrence Livermore Laboratory
ATTN: G. Stahle, L-24
ATTN: C. Joseph Taylor, L-92
ATTN: Joseph B. Knox, L-216
ATTN: Joseph E. Keller, Jr., L-125
ATTN: Bernard Hayes

U.S. ENERGY RAD ADM., continued

Los Alamos Scientific Laboratory

ATTN: Doc. Control for Robert Skaggs
ATTN: Doc. Control for R. Dingus
ATTN: Doc. Control for John McQueen
ATTN: Doc. Control for J.W. Taylor
ATTN: Doc. Control for R.S. Thurston

Sandia Laboratories

Livermore Laboratory

ATTN: Doc. Control for Technical Library
ATTN: Doc. Control for H.L. Norris, Jr. N151

Sandia Laboratories

ATTN: Doc. Control for Thomas B. Cook
ATTN: Doc. Control for R.R. Boade
ATTN: Doc. Control for Albert Chahai
ATTN: Doc. Control for M. Cowan
ATTN: Doc. Control for Jack Reed
ATTN: Doc. Control for Normal Breazeal
ATTN: Doc. Control for Technical Library

Director

Oak Ridge National Laboratory

ATTN: Dr. C. Kearny, Bldg. 4500n

DEPARTMENT OF DEFENSE CONTRACTORS

Acurex Corporation

ATTN: J. Huntington
ATTN: J. Courtney
ATTN: C. Nardo
ATTN: R. Rindal

Aerospace Corporation

ATTN: W. Barry
ATTN: R. Mortensen
ATTN: Richard Crolius, A2-RM1027
ATTN: H. Blaes
ATTN: W. Mann
ATTN: Robert L. Strickler
ATTN: J. McClelland

Analytic Services, Inc.

ATTN: Jack Selig

AVCO Research & Systems Group

ATTN: John Gilmore, J400
ATTN: Document Control
ATTN: John E. Stevens, J100
ATTN: William Broding
ATTN: George Weber, J230

Battelle Memorial Institute

ATTN: Technical Library
ATTN: E. Unger
ATTN: Merwyn R. Vanderlind

Boeing Company, The

ATTN: Edwin York
ATTN: Robert Holmes
ATTN: Robert Dyrdaahl
ATTN: Brian Lempriere
ATTN: Jay C. Pyle
ATTN: Roland Carlson

Boeing Wichita Company

ATTN: L. Swaney

Brown Engineering Company, Inc.

ATTN: Ronald Patrick

California Research & Technology, Inc.

ATTN: Ken Kreyenhagen

Chrysler Defense Division

ATTN: R.L. Smith

Calspan Corporation

ATTN: M.S. Holden

Dayton, University of

Industrial Security Super KL-505

ATTN: Hallock F. Swift
ATTN: D. Gerdman

Denver, University of

Colorado Seminary, Denver Research Institute

ATTN: John Wisotski
ATTN: Larry L. Brown

Effects Technology, Inc.

ATTN: Richard Parisse
ATTN: Robert Wengler

EG&G, Inc.

Special Projects Div.

ATTN: Robert Ward

Electromechanical Systems of New Mexico, Inc.

ATTN: R.C. Shunk

Ford Aerospace & Communications Operations

ATTN: P. Spangler

General Electric Company

Space Division

ATTN: A. Martellucci
ATTN: Phillip Cline
ATTN: G. Harrison
ATTN: Daniel Edelman
ATTN: Carl Anderson

General Electric Company

TEMPO-Center for Advanced Studies

ATTN: DASIAU

General Electric Company

TEMPO-Center for Advanced Studies-Albuquerque

ATTN: Gerald Perry

General Electric Company

TEMPO-Center for Advanced Studies-Bel Air

ATTN: E.J. Bryant

General Research Corporation

P.O. Box 3587

ATTN: T. Stathacopoulos

Institute for Defense Analyses

ATTN: Joel Bengston
ATTN: IDA Librarian

Ion Physics Corporation

ATTN: Robert D. Evans

DEPT. OF DEFENSE CONTRACTORS, continued

Kaman Avidyne

Division of Kaman Sciences Corp.

ATTN: L.S. Criscione
ATTN: Ray Reutimick
ATTN: Norman P. Hobbs

Kaman Sciences Corporation

ATTN: Donald C. Sachs
ATTN: Thomas Meagher
ATTN: John R. Hoffman
ATTN: Frank H. Shelton
ATTN: John Keith

Ken O'Brien & Associates

ATTN: Richard Cronk

Lockheed Missiles & Space Co., Inc. - Sunnyvale

ATTN: R. Walz, Dept. 81-14

Lockheed Missiles & Space Co., Inc. - El Segundo

ATTN: T.R. Fortune

Lockheed Missiles & Space Co., Inc. - Palo Alto

ATTN: F.G. Borgardt

Lovelace Foundation for Medical Education
and Research

ATTN: D.R. Richmond
ATTN: R.O. Clark
ATTN: E.R. Fletcher

Martin Marietta Aerospace
Orlando Division

ATTN: William A. Gray, MP-61
ATTN: Laird Kinnaird
ATTN: Gene Aiello
ATTN: James M. Potts, MP-61

McDonnell Douglas Corporation

ATTN: E.A. Fitzgerald
ATTN: R.J. Reck
ATTN: H. Hurwicz
ATTN: H.M. Berkowitz
ATTN: J.F. Garibotti
ATTN: L. Cohen

National Academy of Sciences

ATTN: National Materials Advisory Board

ATTN: Donald G. Groves

New Mexico, University of
Civil Engineering Research Facility

ATTN: Glen Jones
ATTN: Golden Lane
ATTN: Stephen Pickett

Northrop Corporation

ATTN: Don Hicks

Pacific-Sierra Research Corp.

ATTN: Gary Lang

Physics International Company

ATTN: Doc. Control for James Shea
ATTN: Doc. Control for Technical Library

Prototype Development Associates, Inc.

ATTN: John McDonald
ATTN: John Slaughter

R&D Associates

ATTN: I.A. Field
ATTN: Cyrus P. Knowler
ATTN: Paul Rausch
ATTN: Jerry Carpenter
ATTN: Harold L. Brode
ATTN: William R. Graham, Jr.
ATTN: Edward Chapyak
ATTN: Henry Cooper
ATTN: Albert L. Latter

RCA Corporation

ATTN: L. Van Keuren, Bldg. 13-5-2

RAND Corporation, The

ATTN: J.J. Mate

Raytheon Company

ATTN: Library

Science Applications, Inc. - La Jolla

ATTN: Olan Nance
ATTN: W. Yengst
ATTN: John Warner
ATTN: Dwane Howe
ATTN: G. Ray

Science Applications, Inc. - El Segundo

ATTN: Carl Swain
ATTN: Lyle Dunbar
ATTN: G. Burghart

Science Applications, Inc. - McLean

ATTN: William R. Seebaugh
ATTN: William M. Layson
ATTN: Michael McDonnell

Southern Research Institute

ATTN: C.D. Pears

SRI International

ATTN: Philip J. Dolan
ATTN: D. L. Huestis
ATTN: George R. Abrahamson
ATTN: Herbert E. Lindberg
ATTN: Donald Curran
ATTN: Carl Wiehle
ATTN: Alan A. Burns

Systems, Science and Software, Inc.

ATTN: G. A. Gurtman
ATTN: Russell E. Duff

Terra Tek, Inc.

ATTN: Sidney Green

TRK Defense & Space Systems Group- Redondo Beach

ATTN: Peter Brandt, EI-2006
ATTN: Peter K. Dal, RI/2170
ATTN: R.K. Piebuch, RI/2078
ATTN: Thomas G. Williams
ATTN: D.H. Baer, RI-2136
ATTN: I.E. Alber, RI-1008
ATTN: W.W. Wood

DEPT. OF DEFENSE CONTRACTORS, continued

TRW Defense & Space Systems Group - San Bernardino
ATTN: William Polich
ATTN: E.Y. Wong, 527/712
ATTN: L. Berger
ATTN: Earl W. Allen, 520/141
ATTN: V. Blankenship

Admiralty Surface Weapons Establishment
Ministry of Defence
United Kingdom
ATTN: W.D. Delany

British Embassy
Washington, DC
ATTN: ACOW

FOREIGN

Embassy of Australia
Washington, DC
ATTN: Office of the Defence Science Attaché

Royal Fortification Administration
Stockholm, Sweden
ATTN: Dr. Eddy Abrahamsson
ATTN: Brig. Gen. Gunnar Noren

National Defense Research Institute
Stockholm, Sweden
ATTN: H. Axelsson

Defence Research Establishment Suffield
Ralston, Alberta, Canada
ATTN: Clayton Coffey
ATTN: Allan W.M. Gibb
ATTN: G.A. Grant
ATTN: R.M. Heggie

Infrastructure Staff
Federal Republic of Germany
ATTN: Col. Rottgerkamp
ATTN: LTC Hermann Pahl
ATTN: Eberhard Bachmann

Ernst-Mach Institute
Federal Republic of Germany
ATTN: Dr. Heintz Reichenbach
ATTN: Gerhard Gurke

Office of Test & Development
Norwegian Defence Construction Service
Oslo, Norway
ATTN: Arne Skjeltorp

National Defence HQ
Directorate of Maritime Activities and Research
Quebec, Canada
ATTN: Ole R. Bezemer

Technologisch Laboratorium (TNO)
Rijswijk, Netherlands
ATTN: H.J. Pasman

Federal Ministry of Defense
Federal Republic of Germany
ATTN: LTC D. Bruegmann
ATTN: R. Schilling
ATTN: L. F. Hentschel

Military Attache Staff
Embassy of the Federal Republic of Germany
ATTN: Col. Rudolf Eriemann

Federal Republic of Germany Liaison Office
Alexandria, VA
ATTN: Herman Pfrenge